

MIocene TO RECENT STRATIGRAPHY, STRUCTURAL
ARCHITECTURE AND TECTONIC EVOLUTION OF THE
ANTALYA BASIN, EASTERN MEDITERRANEAN SEA

FATMA İSTAR İSLER

**MIOCENE TO RECENT STRATIGRAPHY, STRUCTURAL ARCHITECTURE
AND TECTONIC EVOLUTION OF THE ANTALYA BASIN,
EASTERN MEDITERRANEAN SEA**

by

© Fatma İřtar İřler

A thesis submitted to the
School of Graduate Studies
in partial fulfilment of the
requirements for the degree of
Master of Science

Department of Earth Sciences
Memorial University of Newfoundland

December - 2003

Abstract

The Miocene-Recent structural and sedimentary evolution of the Antalya Basin south of Turkey in the eastern Mediterranean Sea is delineated using detailed interpretation of ~900 km of high-resolution multi-channel seismic reflection profiles. Three seismic stratigraphic units are identified. Unit 1 is Pliocene-Quaternary in age and is characterized by a strongly reflective acoustic package which shows considerable lateral continuity. Unit 2 consists of an acoustically transparent package with few coherent reflectors: it represents the Messinian evaporite succession. Unit 3 is early-late Miocene but pre-Messinian in age and is defined by an acoustically reverberatory package which shows moderate lateral continuity.

Detailed interpretation and mapping of the seismic reflection profiles showed that the structural architecture of the Antalya Basin is characterized by 4-5 northwest-southeast trending anticline-syncline pairs. The anticlines are invariably cored by north-dipping, south-verging thrusts, thus representing ramp anticlines with the synclines between thrust culminations representing piggy-back basins. Temporal and spatial relationship of these large-scale structures and the stratigraphy and growth stratal architecture of Units 1-3 successions clearly document a two-phase history for the Miocene to Recent kinematic evolution of the Antalya Basin. The first phase of deformation occurred in the Miocene and affected the entire Antalya Basin. It involves the northwest-trending, southwest-directed fold-thrust structures in Unit 3. A fundamental change in the kinematic regime occurred during the transition from the late

Miocene to early Pliocene, when the strain was strongly partitioned both temporally and geographically. The second phase of deformation occurred in the early-Pliocene to Recent. Structures associated with this phase of deformation consist of (1) northwest-trending listric extensional faults involving the Pliocene-Quaternary succession as well as the similarly trending transtensional faults involving the Miocene to Pliocene-Quaternary successions, which occupy the northern portion of the study area extending from the present-day shoreline to the innermost portion of the deep Antalya Basin, (2) re-activated Miocene thrusts involving the Pliocene-Quaternary successions, which occupy the northern and central segments of the Antalya Basin, and (3) northwest-trending transpressional structures involving the Miocene to Pliocene-Quaternary successions, which occupy the southern segment of the deep Antalya Basin. The northern extensional/transtensional faults exhibit concurrent activity with the re-activated Miocene thrusts of the imbricate fold-thrust belt. These faults are interpreted to develop in relation to the westward displacement of the Tauride block as the eastern segment of the Aegean-Anatolian Microplate initiated its westward escape in the latest Miocene to early Pliocene, which continued during the Pliocene-Quaternary and still persists today. By contrast, the southern transpressional fault activity is interpreted to be related to the choking of the subduction along the Cyprus Arc as a result of the collision of the Eratosthenes Seamount with Cyprus during the early Pliocene to Recent.

Acknowledgment

I would like to take this opportunity to thank a number of people who contributed significantly to the flowering of this master's thesis.

I would like to express my sincere gratitude and appreciation to my supervisors, Ali E. Aksu, Jeremy Hall and Tom J. Calon for providing me with the unique opportunity to be a part of the most exciting Eastern Mediterranean Sea Project. I also would like to thank them for their expert guidance, thought-provoking ideas, mentorship at all levels during the development of this thesis. Their valuable companionship is gratefully acknowledged. I further wish to thank Ali E. Aksu, Jeremy Hall and the Faculty of Graduate Studies for their financial support during the duration of this research.

I wish to acknowledge my appreciation for Sharon Deemer and Tony Kocurco for their much-appreciated advice, tremendous help and valuable insight during the geophysical data processing stage of the thesis. I also would like to thank Paul Barnes for performing the successful processing of the geophysical data acquired during the 1991 and 1992 Eastern Mediterranean Project Survey. I wish to acknowledge my thanks to Landmark for providing the software used during the processing of the seismic data.

I would like to thank Doğan Yaşar and the crew of R/V Koca Piri Reis for their valuable assistance during the data acquisition stage of this thesis. I would like to further thank Doğan Yaşar for his continuous support throughout this master's project.

I wish to express my appreciation to my dear friends for their tremendous support and for sharing this exciting experience with me. I would like to express my sincere

gratitude for Ali Aksu for encouraging and inspiring me to start this wonderful journey.

Thank you for walking with me all the way through, watching me from a distance when I was able to walk by myself and raising me when I stumbled.

I would like to extend my gratitude and thanks to my brother Bursin, mom Güzide, dad Rıdvan, my grandmother Nunuş and grandfather Ekrem for their life-long love, care and affection, which gave me the courage and passion to pursue my dreams.

Table of Contents

Abstract	i
Acknowledgment	iii
List of Figures	vii
 Chapter 1 - Introduction	 1
1.1. Tectonic Framework	1
1.2. Antalya Basin	6
1.3. Stratigraphy of Onland Basins	10
1.4. Objectives	15
1.5. Bathymetry	16
1.6. Global Positioning System Data on Modern Deformation	19
1.7. Seismicity	23
 Chapter 2 - Data acquisition	 31
2.1. The Seismic Reflection Method	31
2.2. The Acquisition Parameters and the Geometry of the Survey	33
 Chapter 3 - Marine seismic data processing	 38
3.1. Trace editing	39
3.2. Amplitude recovery	41
3.3. Field Geometry and CMP Sorting	45
3.4. Deconvolution	46
3.5. Bandpass filtering	48
3.6. Velocity Analysis, Normal Moveout Correction and Trace Muting	52
3.7. Common Midpoint (CMP) Stacking	68
3.8. Migration	71
3.8.1. General Overview	71
3.8.2. Kirchhoff Time Migration	79
 Chapter 4 - Seismic stratigraphy and chronology	 85
4.1. Unit 1: Pliocene-Quaternary	85
4.2. Unit 2: Late Miocene (Messinian)	89
4.3. Unit 3: Miocene (pre-Messinian)	91
 Chapter 5 - Late Miocene ridges and the intervening Pliocene-Quaternary basins	 92
5.1. Late Miocene Ridges	92
5.1.1. Ridges ϵ_1 and ϵ_{11}	92
5.1.2. Ridge ϵ_2	106
5.1.3. Ridge ϵ_3	112
5.1.4. Ridge ϵ_4	119

5.1.5. Ridge ε_5	126
5.1.6. Locally Emerging Ridges (referred to as $\varepsilon_x, \varepsilon_y, \varepsilon_{13}, \varepsilon_{12}, \varepsilon_{31}$)	129
5.1.6.1. Ridge ε_{12}	129
5.1.6.2. Ridge ε_x	130
5.1.6.3. Ridge ε_{31}	130
5.1.6.4. Ridge ε_y	131
5.1.6.5. Ridge ε_{13}	132
5.2. Pliocene-Quaternary Basins	132
5.2.1. Shelf and Slope Basins	133
5.2.2. Abyssal Basins	139
5.2.2.1. Basin β_1	139
5.2.2.2. Basin β_{1a}	146
5.2.2.3. Basin β_2	147
5.2.2.4. Basin β_3	152
5.2.2.5. Basin β_4	155
5.2.2.6. Basin β_5	159
5.2.2.7. Basin β_6	162
Chapter 6 - Structural geology of the Antalya Basin	166
6.1. Domain 1	168
6.2. Domain 2	182
6.2. Domain 3	195
Chapter 7 - Discussion	202
7.1. Kinematic evolution of the Antalya Basin	202
7.1.1. Miocene (pre-Messinian)	204
7.1.2. Messinian	206
7.1.3. Pliocene-Quaternary	210
7.2. Correlations with western Cyprus	217
7.3. Previous Models and Comparisons with the Author's Model	222
Chapter 8 - Conclusions	232
References	235
Appendix	243

List of Figures

CHAPTER 1

1.1	Tectonic map of the eastern Mediterranean	2
1.2	Bathymetric map of the eastern Mediterranean	7
1.3	Tectonic map of the Isparta Angle	8
1.4	Stratigraphy of the Antalya Basin	11
1.5	Global Positioning System velocity field	21
1.6	Seismicity of the eastern Mediterranean	25
1.7	Fault plane solutions of major earthquakes in eastern Mediterranean	29

CHAPTER 2

2.1	Reflection geometry of a seismic wave	32
2.2	Common-mid-point shooting technique	34
2.3	Seismic reflection shooting geometry	37

CHAPTER 3

3.1	Marine seismic data processing flow chart	40
3.2	Noisy traces	42
3.3	Recording shifts and correction	43
3.4	Recording time delay and correction	44
3.5	Noisy shot gather	50
3.6	Amplitude spectrum of the shot gather shown in Figure 3.5	51
3.7	Shot gather shown in Figure 3.5 after filtering	53
3.8	Amplitude spectrum of the filtered shot gather	54
3.9	Velocity analysis display methods	57
3.10	Shot gather panel showing under-corrected events	59
3.11	Shot gather panel showing over-corrected events	60
3.12	Shot gather panel showing flattened events	61
3.13a	Velocity analysis panels using supergather of 20 CDPs	63
3.13b	Velocity analysis panels using supergather of 5 CDPs	64
3.14	Velocity analysis panels - 48 channel	66
3.15	Velocity analysis panels - 16 channel	67
3.16	Example of a near trace gather and a stack section	70
3.17	Example of a near trace gather and a stack section	72
3.18	Example of a near trace gather and a stack section	73
3.19	Example of a stacked section	74
3.20	Example of a migrated section	75

3.21	Example of a stacked section	76
3.22	Example of a migrated section	77
3.23	Post-stack migration technique	80
3.24	Kirchhoff time migration principle	83

CHAPTER 4

4.1	Seismic character of Unit 1	86
4.2	Stratigraphic correlation chart	88
4.3	Seismic character of Units 2 and 3	90

CHAPTER 5

5.1	Map showing the distribution of basins and ridges in Antalya Basin	93
5.2	Map showing the distribution of the Pliocene-Quaternary sediments	94
5.3	Seismic reflection profile showing major ridges and basins	96
5.4	Seismic reflection profile showing major ridges and basins	97
5.5	Seismic reflection profile showing major ridges and basins	98
5.6	Seismic reflection profile showing major ridges and basins	99
5.7	Seismic reflection profile showing major ridges and basins	100
5.8	Seismic reflection profile showing major ridges and basins	101
5.9	Seismic reflection profile showing major ridges and basins	102
5.10	Seismic reflection profile showing major ridges and basins	103
5.11	Seismic reflection profile showing major ridges and basins	104
5.12	Seismic reflection profile showing major ridges and basins	109
5.13	Seismic reflection profile showing major ridges and basins	110
5.14	Seismic reflection profile showing major ridges and basins	111
5.15	Seismic reflection profile showing major ridges and basins	113
5.16	Seismic reflection profile showing major ridges and basins	115
5.17	Seismic reflection profile showing major ridges and basins	116
5.18	Seismic reflection profile showing major ridges and basins	118
5.19	Seismic reflection profile showing major ridges and basins	120
5.20	Seismic reflection profile showing major ridges and basins	122
5.21	Seismic reflection profile showing major ridges and basins	123
5.22	Seismic reflection profile showing major ridges and basins	125
5.23	Seismic reflection profile showing major ridges and basins	127
5.24	Seismic reflection profile showing major ridges and basins	134
5.25	Seismic reflection profile showing major ridges and basins	135
5.26	Seismic reflection profile showing major ridges and basins	136
5.27	Seismic reflection profile showing major ridges and basins	138
5.28	Seismic reflection profile showing major ridges and basins	140

5.29	Seismic reflection profile showing major ridges and basins	141
5.30	Seismic reflection profile showing major ridges and basins	142
5.31	Seismic reflection profile showing major ridges and basins	143

CHAPTER 6

6.1	Map showing major structural elements in Antalya Basin	167
6.2	Seismic reflection profile showing structures and faults	170
6.3	Seismic reflection profile showing structures and faults	171
6.4	Seismic reflection profile showing structures and faults	172
6.5	Seismic reflection profile showing structures and faults	174
6.6	Seismic reflection profile showing structures and faults	175
6.7	Seismic reflection profile showing structures and faults	177
6.8	Seismic reflection profile showing structures and faults	178
6.9	Seismic reflection profile showing structures and faults	179
6.10	Seismic reflection profile showing structures and faults	181
6.11	Seismic reflection profile showing structures and faults	183
6.12	Seismic reflection profile showing structures and faults	184
6.13	Seismic reflection profile showing structures and faults	185
6.14	Seismic reflection profile showing structures and faults	186
6.15	Seismic reflection profile showing structures and faults	189
6.16	Seismic reflection profile showing structures and faults	190
6.17	Seismic reflection profile showing structures and faults	191
6.18	Seismic reflection profile showing structures and faults	192
6.19	Seismic reflection profile showing structures and faults	196
6.20	Seismic reflection profile showing structures and faults	197
6.21	Seismic reflection profile showing structures and faults	198
6.22	Seismic reflection profile showing structures and faults	200

CHAPTER 7

7.1	Tectonostratigraphic chart	203
7.2	Major tectonic elements of northern Cyprus	205
7.3	The N-reflector	207
7.4	Messinian subunit 2a	209
7.5	The M-reflector	211
7.6	Growth strata wedges	213
7.7	Growth strata wedges	214
7.8	Seismic reflection profile	215
7.9	Seismic reflection profile	218
7.10	Seismic reflection profile	219

CHAPTER 1. Introduction

1.1. Tectonic Framework

The present-day tectonic framework of the eastern Mediterranean is controlled by the last phase of collision between the African and Eurasian Plates, and the displacement of smaller Aegean-Anatolian, Syrian-Arabian, and Black Sea-Caucasus Microplates (Fig. 1.1). The boundary between the Syrian-Arabian Microplate and the African Plate is delineated by the north-south trending sinistral Dead Sea Fault zone, which developed as the result of the opening of the Red Sea to the south in the Miocene. The northward movement of the Syrian-Arabian Microplate and its eventual collision with the Eurasian Plate in the late Miocene-early Pliocene resulted in the closure of the southern arm of the Neothetys Ocean (i.e. the Bitlis Ocean) and the suturing along the Bitlis-Zagros Suture zone of southeast Turkey and northwest Iran (Şengör and Yılmaz, 1981). This collision initiated the westward tectonic escape of the Aegean-Anatolian Microplate along two major transform fault systems (Şengör, 1991). The North Anatolian Fault zone extends from the Karlıova triple junction in eastern Turkey westward into the Marmara Sea and Aegean Sea, forming a gently arcuate dextral strike-slip fault system delineating the northern boundary between the Aegean-Anatolian Microplate and the Black Sea-Caucasus Microplate (Fig. 1.1). The sinistral East Anatolian Fault zone defines the southeastern boundary of the Aegean-Anatolian Microplate. It extends from the Karlıova triple junction toward the southwest, tracing the northwestern fringes of the Bitlis-Zagros Suture zone. This fault zone meets the sinistral Dead Sea Fault zone and the northeast

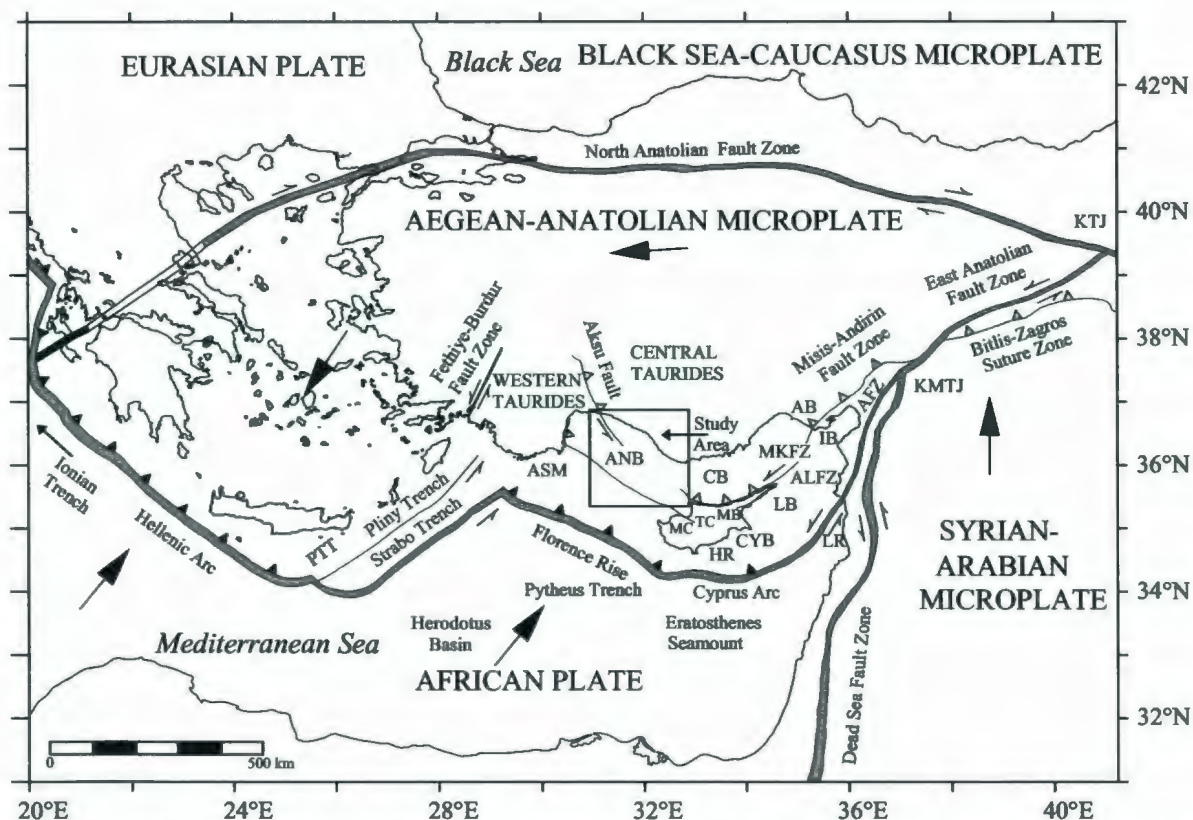


Fig. 1.1. Simplified tectonic map of the eastern Mediterranean Sea (modified from Aksu et al., 1992). PTT- Ptolemy Trench, KTJ- Karlova Triple Junction, MB- Mesaoria Basin, MC- Mamonia Complex, TC- Troodos Complex, LB- Latakia Basin, MKFZ- Misis-Kyrenia Fault Zone, IB- Iskenderun Basin, AFZ- Amanos Fault Zone, KMTJ- Kahramanmaraş Triple Junction, CYB- Cyprus Basin, CB- Cilicia Basin, LR- Latakia Ridge, HR- Hecateus Ridge, ASM- Anaximander Seamounts, ANB- Antalya Basin. Large arrows show plate motion relative to fixed Eurasian Plate. Subduction zones are shown by double lines with filled triangles positioned on the overriding plate. Major thrust faults are shown by single lines with hatched triangles on the hanging wall. The strike-slip faults are displayed by half arrows showing the directions of relative displacement.

continuation of the Cyprus Arc, the Amanos Fault zone, at a triple junction near the town of Kahramanmaraş. The southern boundary of the Aegean-Anatolian Microplate with the African Plate west of the Kahramanmaraş triple junction is defined by two large, crustal-scale arcuate structures: the Cyprus Arc in the east and the Hellenic Arc in the west (Fig. 1.1).

In its easternmost segment the Cyprus Arc is defined by the southwest-northeast-trending Nahr el Kebir graben of southwestern Syria. This structure can be readily traced to the southwest where it connects with the northeast-trending Tartus Ridge (Ben Avraham et al. 1995), which in turn links with the similar trending Latakia Ridge, and further connects with the east-west trending Cyprus Arc situated between the Eratosthenes Seamount and Cyprus. Further to the west, the Cyprus Arc is delineated by the southeast-northwest-trending Florence Rise, north of the Pytheus Trench, a prominent deep which consists of a series of small elongate basins (Hsü et al., 1978). The Florence Rise is a large accretionary wedge developed as the result of prolonged northeast subduction of the African Plate beneath the Aegean-Anatolian Microplate (Woodside, 1977). Eratosthenes Seamount is a bathymetric high situated on the edge of the African Plate, south of Cyprus. Drilling results clearly indicate that the seamount consists of Cretaceous-Miocene carbonate successions (Robertson, 1998), which overly an intermediate-thickness attenuated continental crust (Makris et al., 1983). Eratosthenes Seamount is presently colliding with Cyprus, thus constricting the subduction along this segment of the Cyprus Arc (Robertson, 1998). The now-sutured Hecateus Ridge north of

the Cyprus Arc and the Mamonia and Troodos Complexes of Cyprus suggest that the process of microplate accretion has been a common process in the evolution of the Island of Cyprus. Along the Florence Rise portion of the Cyprus Arc, subduction is more obvious, marked by moderate seismic activity, whereas in the east there is little or no evidence for subduction and seismicity does not clearly delineate the plate boundary (Woodside, 1976, 1977; Nur and Ben Avraham, 1978; Ben Avraham et al., 1978; Şengör, 1979; Dewey and Şengör, 1979; Rotstein and Kafka, 1982; Kempler and Ben Avraham, 1987; Ambraseys and Adams, 1993; Oral et al., 1995; Vidal et al., 2000).

The Hellenic Arc defines the western boundary of the convergence between the African Plate and the Aegean-Anatolian Microplates. It can be traced along the Ionian Trench which extends from the northwestern Ionian Sea to the southeast, encircles the southern shores of Crete and swings to the northeast, where it links with the three prominent sinistral strike-slip fault systems along the Ptolemy, Pliny and Strabo Trenches. These trenches are defined by several very narrow and deep bathymetric depressions consisting of several isolated elongate basins. Their onshore extension in Turkey is represented by the sinistral strike-slip Fethiye-Burdur Fault zone (Fig. 1.1).

The Hellenic Arc joins the Cyprus Arc across a major morpho-tectonic element, the Anaximander Seamounts (Fig. 1.1). Similar to Eratosthenes, these are not seamounts *sensu-stricto*, but so named because of their morphological similarities with seamounts. The Anaximander Seamounts consist of three main bathymetric highs that rise ~2000 m above the deep abyssal plain of the Antalya and Herodotus Basins, reaching relatively

shallow depths of less than 1000 m (Fig. 1.1).

Several horse-tail-like sinistral strike-slip faults splay from the East Anatolian Fault zone and extend toward the southwest from the Kahramanmaraş triple junction. The Amanos Fault zone is one of the most prominent of these splays which defines the eastern boundary of the Amanos Mountains. It can be readily traced to the eastern shores of the Mediterranean Sea where it joins with the prominent arcuate Amanos-Larnaka Fault zone (Hall et al., submitted). From here the Amanos-Larnaka Fault zone is traced across the southern margin of the Troodos Complex, swinging to the northwest and extending into the Antalya Basin (Calon et al., submitted a, b).

The Misis-Andirin Fault zone is another important splay of the East Anatolian Fault zone and extends toward the southwest into the Misis Mountains of southern Turkey (Fig. 1.1). This structure can be readily traced into the prominent northeast trending Misis-Kyrenia Fault zone (Aksu et al., 1992; submitted) and then to the east-west trending Kyrenia Range of northern Cyprus (Calon et al., submitted a). Further west the Misis-Kyrenia Fault swings toward the northwest and continues into the Antalya Basin. The Misis-Kyrenia and the Amanos-Larnaka-Troodos lineaments form two crustal-scale arcuate elements running parallel to the general trend of the Cyprus Arc. Several basins evolved between these three lineaments, including the Adana and Cilicia Basins in the north and the Iskenderun, Latakia and Mesaoria Basins in the centre and the Cyprus Basin in the south (Fig. 1.1). These lineaments and basins clearly extend westward into the Antalya Bay, and constitute the core tectonic elements of this thesis.

1.2. Antalya Basin

The present-day Antalya Basin is a predominantly marine depocentre, situated between the Cyprus Arc (Florence Rise) in the south and the Taurus Mountains (Taurides) of southern Turkey in the north (Fig. 1.1). It is bounded to the east by the Anamur-Kormakiti zone (Anastasakis and Kelling, 1991), a bathymetric rise which separates the Antalya and Cilicia Basins (Fig. 1.2). In the west the Antalya Basin is bounded by the Beydağları Mountains and the Anaximander Seamounts which are pronounced bathymetric highs immediately south of the Lycian Nappes and the Antalya Complex (Antalya Nappes) of southwestern Turkey (Fig. 1.2; 1.3). The seamounts are situated at the northeastern edge of the Ptolemy-Pliny-Strabo Trenches of the Hellenic Arc and the northwestern extremity of the Florence Rise (Fig. 1.1).

The Taurus Mountains of the southern Anatolia comprise a prominent segment of the Alpine orogenic belt. This mountain chain separates into two branches, the southwest-northeast oriented western branch and the southeast-northwest oriented eastern branch, defining the limbs of the Isparta Angle (Blumenthal, 1969). Thus, the Isparta Angle is a north-facing-convex triangular-shaped region, which limits the northwestern onland extension of the marine Antalya Basin (Fig. 1.3). It is bounded to the west by an allochthonous unit, the Lycian Nappes, representing Permian to Tertiary northwest-verging thrust succession of deep and shallow water sediments, and extensive Late Cretaceous ophiolites (Okay, 1989). The Fethiye-Burdur Fault zone (Fig. 1.1) is a wide

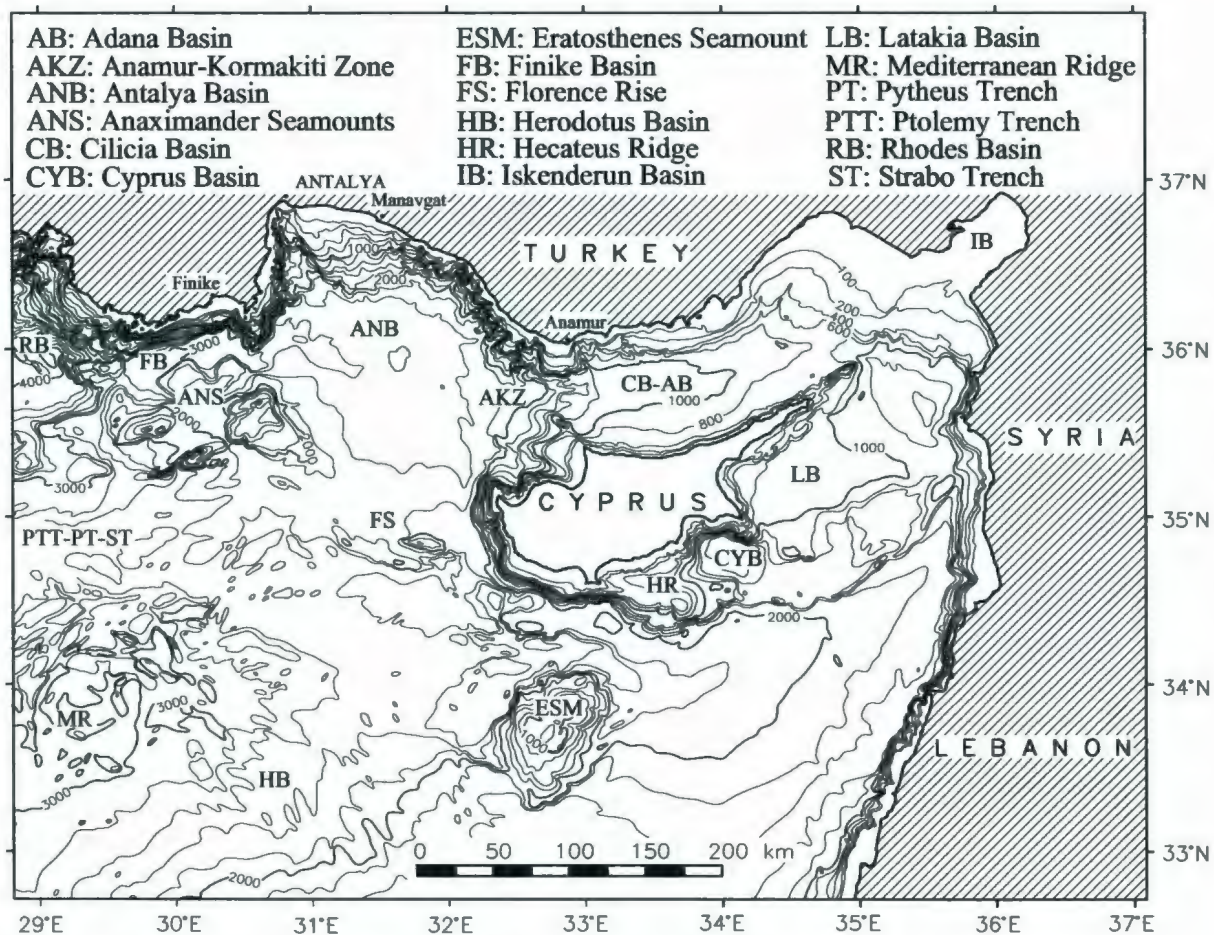
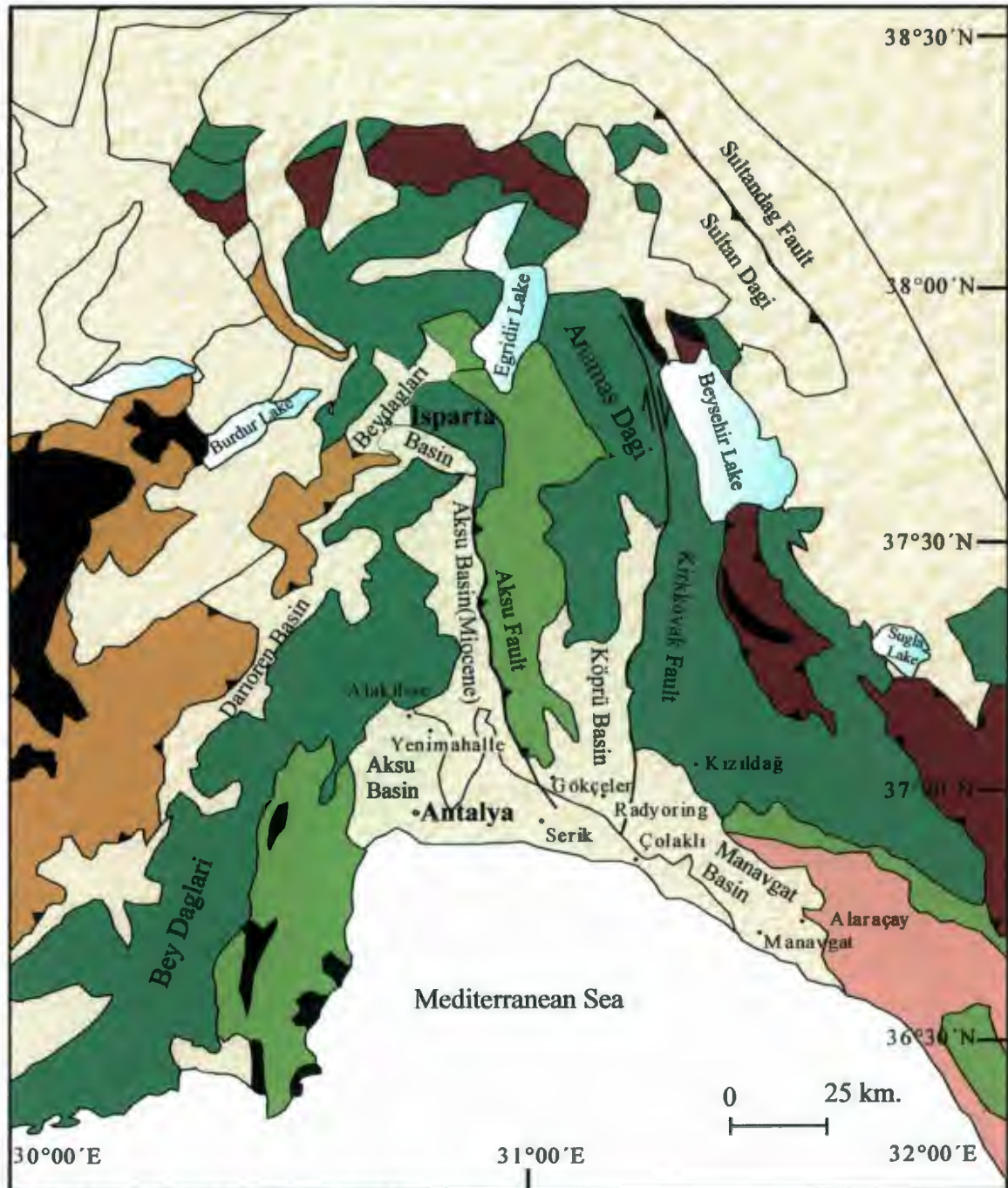


Fig. 1.2. Bathymetric chart of the eastern Mediterranean (modified from Aksu et al, 1992).



- BEYDAĞLARI-ANAMAS-AKSEKİ AUTOCHTHONE
- ANTALYA NAPPES
- BEYŞEHİR-HOYRAN-HADİM NAPPES
- LYCIAN NAPPES
- ALANYA MASSIF
- OPHIOLITE NAPPES
- NEOGENE DEPOSITS

Fig. 1.3. Map showing distribution of tectonic elements and major faults in Isparta Angle (compiled from Senel, 1997).

belt characterized by sinistral strike-slip faults with considerable normal dip-slip component, and marks the western margin of the Isparta Angle, linking it with the Ptolemy-Pliny-Strabo Trenches to the southwest (Şaroğlu et al., 1987; Price and Scott, 1994; Barka et al., 1997). The Isparta Angle is bounded to the east by an allochthonous unit, the Beyşehir-Hoyran-Hadim Nappes (Fig. 1.3), a Permian-Tertiary carbonate, siliciclastic and minor ophiolitic succession (Monod, 1977), with the Sultandağ thrust (Fig. 1.3) defining the northeastern margin of the region (Şaroğlu et al., 1985; Barka et al., 1997).

The basement of the Isparta Angle mainly consists of two autochthonous units: the Beydağları Platform in the west and the Anamas-Akseki Platform in the east (Robertson and Woodcock, 1986; Dilek and Rowland, 1993). The Beydağları Platform consists of predominantly Jurassic to Miocene platform carbonates (Poisson, 1977), whereas the Anamas-Akseki Platform (Monod, 1977) (= the Geyikdağı Platform of Özgül, 1984) constitutes platform carbonates of Cambrian (Dumont, 1976) to Eocene (Özgül, 1984; Monod, 1977) age. The Antalya Complex (Antalya Nappes) is an allochthonous Mesozoic shallow-water carbonate succession that originated in the basin between these two major autochthonous units (Poisson et al., 1984). It was thrust over the Beydağları Platform in the west and the Anamas-Akseki Platform in the east during the late Cretaceous-early Paleocene. The Paleozoic metamorphic Alanya Massif occurs in the southeastern part of the Isparta Angle, and overthrusts the Antalya Complex in an eastward direction (Dilek, 1993).

During the Miocene, the western limb of the Isparta Angle, including the Beydağları Platform experienced a 30° counterclockwise rotation (Kissel and Poisson, 1987; Morris and Robertson, 1993), whereas the eastern limb, the Anamas-Akseki Platform, experienced a 40° clockwise rotation since the Eocene (Kissel et al., 1990). Thus, the Isparta Angle experienced a late Miocene phase of compression, also known as the Aksu Phase, with coeval eastward and westward thrusting along the western and eastern limbs, respectively (Barka et al., 1997).

1.3. Stratigraphy of Onland Basins

The Isparta Angle contains several large interconnected Miocene depocentres, including the Darıören, Beydağları, and Antalya Basins, and a single Pliocene-Quaternary depocentre the Aksu Basin (Fig. 1.3). The Antalya Basin includes several smaller depocentres, such as the Aksu, Köprü and Manavgat Basins.

The Darıören Basin evolved in the Miocene as a foreland basin associated with the flexural loading of the lithosphere during the emplacement of the Lycian Nappes (Hayward, 1984). The basin fill consists of an Aquitanian to Langhian succession of continental and/or shallow-marine conglomerates of the Aksu Formation (Tepekli Conglomerate), which displays progressive onlap over the Antalya Nappes, overlain by patch and fringe reefs of the Langhian Oymapınar Formation, which in turn is overlain by a thick succession of mainly Burdigalian to lower Langhian marls and turbidites of the Geceleme Formation sourced from the Lycian Nappes (Fig. 1.4; Akay and Uysal, 1985;

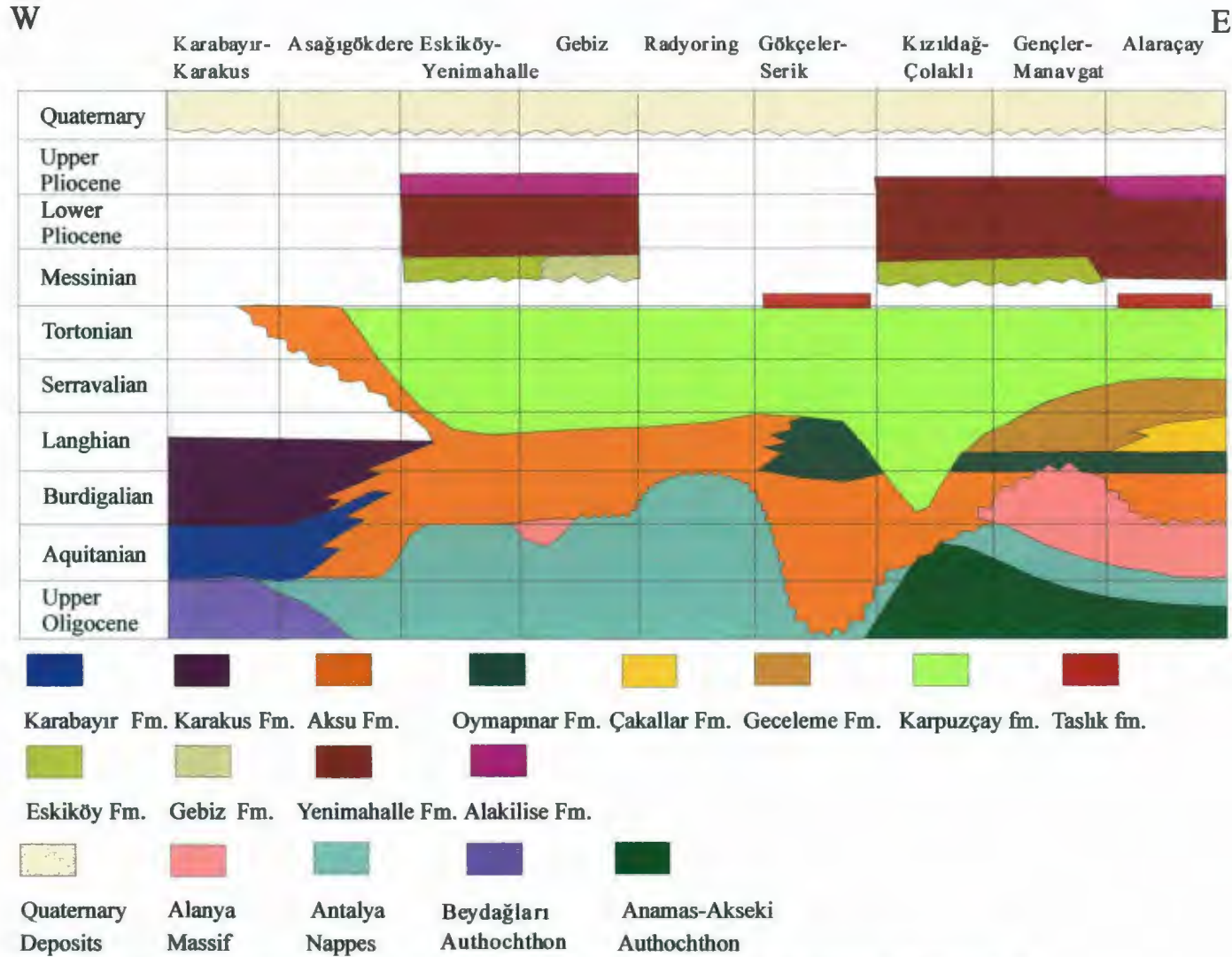


Fig. 1.4. The composite columnar section showing the variation of stratigraphy from west to east in Isparta Angle (modified from Akay et al., 1985).

Akay et al., 1985).

The basal succession in the Beydağları Basin consists of lower Aquitanian shallow-water algal limestones of the Karabayır Formation, which show progressive onlap over the Beydağları autochthon and the Antalya Nappes (Fig. 1.4; Akay et al., 1985). The upper portion of the Karabayır Formation consists of deep-water limestones with abundant pelagic microfauna and flora. It is conformably overlain by the Burdigalian-Langhian Karakuş Formation (= Kısmen Güneyce Formation of Akbulut, 1977), a siliciclastic unit consisting of sandstone-calcareous siltstone interbeds at the base, grading into conglomerate with limestone lenses (Fig. 1.4; Akay et al., 1985).

In the Miocene Aksu, Köprü and Manavgat Basins (Fig. 1.3), the basal succession consists of upper Oligocene-Langhian continental-marine conglomerates of the Aksu Formation (= Tepekli Formation of Monod, 1977; Beşkonak Formation of Eroskay, 1968) which regionally displays a progressive onlap over the Beydağları and Anamas-Akseki Platforms, the Antalya and Lycian Nappes, as well as the Karakuş Formation in the Beydağları Basin (Fig. 1.4; Akay et al., 1985; Kocabıyıköğlu et al., 2000). Locally, the Aksu Formation is conformably overlain by the Langhian to Burdigalian Oymapınar Formation, a variable lithology ranging from algal and patch reef facies in the northwest of the Isparta Angle to pelagic limestone facies succession in the southeast (Fig. 1.4; Akay and Uysal, 1985; Kocabıyıköğlu et al., 2000). In the Manavgat Basin, the Langhian-Serravallian age deep-water marls, calcareous siltstones and sandstone-shale alternations of the Geceleme Formation conformably overlies the Oymapınar Formation (Akay et al.,

1985). Here, the breccias of the Çakallar Formation (Akay et al., 1985; = Çakallar Member of Kocabıyıkoglu et al., 2000) are locally intercalated in the lower portion of the Geceleme Formation. Toward the west, the Geceleme Formation is either conformably overlain by or locally displays lateral contacts with the lower segment of the Karpuzçay Formation. The Karpuzçay Formation consists of a Serravallian-Tortonian siliciclastic turbidite and debris flow succession (Akay et al., 1985); it is also known as the Aksuçay Formation (Akbulut, 1977), Manavgat molasse (Monod, 1977), Kargı molasse (Poisson, 1977), Beşkonak Formation (Eroskay, 1968) and Kayabaşı Formation (Hadımlı, 1968). During the Tortonian, shallow-water clastic limestones, including colonial corals were locally developed within the Isparta Angle (i.e. Gebiz Limestone). The Taşlık Formation locally conformably overlies the Karpuzçay Formation. It consists of a lower calcareous siltstone unit, a middle silty limestone unit and an upper gypsum-bearing pebbly conglomerate unit. It is Messinian in age (Fig. 1.4).

The Pliocene-Quaternary Aksu Basin developed in the early Pliocene in the southern part of the Isparta Angle. The Pliocene succession rests with a marked angular unconformity over the Karpuzçay Formation, but shows a progressive onlap over the autochthonous block along the fringes of the basin (Fig. 1.4). The succession includes the Eşiköy Formation, a basal conglomerate-sandstone unit of early Pliocene age (Kocabıyıkoglu et al., 2000), conformably overlain by the predominantly marine deltaic shales and mudstones of the lower-upper Pliocene Yenimahalle Formation (Akay et al., 1985), and the conglomerates and sandstones of the upper Pliocene Alakilise Formation

(Akay et al., 1985). Debris flow and alluvial fan deposits (i.e. Kemer Fanglomerates of Glover and Robertson, 1998) originating from the Taurus Mountains encircling the Isparta Angle are intercalated with the Yenimahalle Formation (Fig. 1.4; Akay and Uysal, 1985). During the uppermost Pliocene and early Pleistocene, extensive cold, fresh-water carbonates (travertine), known as the Antalya Tufa, were deposited mainly in the western portion of the Isparta Angle and is overlain by the fluvial Belkış conglomerates (Fig. 1.4; Akay and Uysal, 1985; Glover and Robertson, 1998).

Except for a small number of regional studies no systematic survey was carried out within the Antalya Basin, thus the detailed tectonic architecture of the region is poorly documented, and the role of the basin within the Miocene to Recent kinematic evolution of the eastern Mediterranean is not fully understood. Woodside (1977) used widely-spaced single-channel marine seismic reflection profiles to note the character of the Florence Rise, and Anaximander Seamounts, the northward tilting and subsidence of the Antalya and Finike Basins and the apparent continuation of the Strabo Trench south of the Florence Rise and suggested that the regional tectonics around the Antalya Basin is characterized by the underthrusting of the Aegean-Anatolian Microplate by the African Plate. However, he also argued that the limited seismic activity in the region, and the absence of both volcanism and a clearly defined trench along the Florence Rise probably indicate that active subduction probably ended within the past 5 million years (my). Sage and Letouzey (1990) used a small number of regional multi-channel seismic reflection profiles shot by the Institut Français du Pétrole and identified two internally parallel south-

facing fragmented thrust belts within the Antalya Basin. They interpreted these thrusts as the southern extension of the Alpine orogenic arc, comprising of a pile of nappes, which became emplaced in several phases from upper Cretaceous to Recent. They indicated that these nappes include lower Cretaceous ophiolitic material, such as the Lycian Nappes, and pointed out that the thrust belts constitute the basement of many offshore basins with an Oligocene to Recent fill, including the Antalya Basin.

1.4. Objectives

The multi-channel seismic data used in this study were acquired in 1992 and 2001 and a systematic processing sequence has been applied to prepare the data for interpretation. Consequently, several structural and isochron maps are produced to delineate the regional distribution and variation of the geological structures and the stratigraphic sequences within the study area.

The geophysical objectives of this thesis are :

- 1) to determine the appropriate parameters for the processing of the multi-channel seismic data in Antalya Bay,
- 2) to evaluate the effects and success of each individual processing step,
- 3) to process the data to the final image so as to make the profiles look as similar to the real subsurface geology as possible.

The geological objectives of this thesis are:

- 1) to construct a detailed tectonic architecture for the eastern Antalya Basin and to

- provide correlations between the onshore and offshore features in the study area,
- 2) to produce detailed maps of tectonic/salt-related structures and to delineate their role in the Miocene to Recent deformation observed within the basin,
 - 3) to interpret the role of the Antalya Basin within the Miocene to Recent kinematic evolution of the eastern Mediterranean.

1.5. Bathymetry

Antalya Basin is a deep embayment in the eastern Mediterranean Sea, situated between the Florence Rise in the south and the Turkish coastline in the north and west (Fig. 1.2). It is connected to the Cilicia Basin in the east by a prominent shallow, north-south trending bathymetric high, referred to as the Anamur-Kormakiti zone (Fig. 1.2). In the southwest the Antalya Basin is bounded by the Finike Basin and the Anaximander Seamounts.

The continental shelf surrounding the Antalya Basin is generally narrow in the western segment of Antalya Bay but widens considerably to ~10 km widest along the northwestern corner of the bay, becoming progressively narrower (~5 km) along the eastern shores, seaward of the towns of Anamur and Manavgat (Fig. 1.2). The shelf-slope break occurs at approximately 100-150 m water depth, with gentle slopes (5-7°) leading to the floor of the Antalya Basin at >2000 m (Fig. 1.2). The steepest slopes of up to 9° are found along the western margin of Antalya Bay. In the east a single broad canyon connects the Cilicia and Antalya Basins. The slope face is dissected by numerous

submarine canyons feeding submarine fans. The canyon heads cut the shelf producing an undulating topography along the shelf break. Along the upper slope several smaller tributary channels join to form larger canyons, hundreds of metres wide. Along the lower slope region, single large canyons split where each distributary channel progressively loses its expression toward the abyssal plain. The slope to rise transition occurs between 1500-1900 m water depths, and is defined by a notable reduction in slope gradient. The abyssal plain in Antalya Basin is a nearly flat-lying zone ranging in depth between 2000 - 2400 m.

The Mediterranean Ridge is a continuous arcuate feature that can be traced from the northwestern Ionian Sea to the southeast of Cyprus. The Hellenic Arc runs parallel to the western portion of the Mediterranean Ridge and is delineated by a series of parallel and *en-echelon* ocean basins, differing from the typical expression of a conventional subduction arc marked by a single, fairly continuous trench. The Ptolemy, Pliny and Strabo Trenches from west to east, represent the eastern portion of the Hellenic trench system and each consists of several southwest-northeast-trending elongate depressions. The Ptolemy and Pliny Trenches are very prominent with depths varying from 2000 to 3630 and 2000 to 4450, respectively. The Strabo Trench is less pronounced with a shallower depth in the southwest (~2800 m) that becomes deeper (~3200 m) towards the northeast, where it gradually plunges into the deep Rhodes Basin, ~4700m (Fig. 1.2). The Pytheus Trench, a chain of southeast elongate depressions, lies along the south of Rhodes Basin, Anaximander Seamounts and Florence Rise and links with the Cyprus Trench (the physiographic expression of central Cyprus Arc) to the south of Cyprus. The Cyprus

Trench is situated between Cyprus and the Eratosthenes Seamount and extends eastward where it merges into the >1000 m deep Cyprus Basin. The western portion of the trench is narrower compared to its broad character in the east and it appears disturbed associated with the surrounding prominent bathymetric highs (e.g. Eratosthenes Seamount and Hecateus Ridge). The shallow basins located north of the subduction zone represent forearc basins with the volcanic arc situated in the central Aegean Sea (e.g. Milos and Santorini) and central Turkey (e.g. Erciyas and Hasan Dağı). Finike Basin is an east-west-elongated depression, situated between the southern Turkey in the north and the Anaximander Seamounts in the south. It becomes shallower towards east, where it merges with the abyssal plain of Antalya Bay through a gentle slope. To the northeast, it links with the Turkish shore through a steep shelf, bisected by submarine canyons at some localities, while to the north, the transition to southern Turkey occurs also through a steep shelf but with a mostly undisturbed character. Finike Basin is separated from the Rhodes Basin to the west, which is a >4400 m deep depression located southeast of the Island of Rhodes, via a prominent bathymetric high reaching a depth of ~2050 m. Southward, the floor of the Finike Basin climbs up to the Anaximander Seamounts through a gentle slope.

The Anaximander Seamounts are situated to the southwest of the Antalya Basin, immediately south of the Finike Basin (Fig. 1.2). They consist of several large bathymetric highs, separated by narrow, sinuous depressions. The highest peak, at 1022 m depth, is situated in the western portion and displays a westsouthwest-eastnortheast orientation. It is connected to the southwest-northeast-trending, 973 m deep central peak through a

relatively wide plateau of 1800 to 2000 m depth. The eastern peak is 927 m deep and shows a general southwest-northeast orientation. It lies on the abyssal plain as a separate feature and shows transition to the central seamount through a 2000-2200 m deep narrow canyon.

The subduction zone to the south of Antalya Bay is represented by the Cyprus Arc. The features along the arc are more significant in the westward portion compared to the fairly undisturbed eastern portion. The Florence Rise is situated south of the Antalya Bay and west of the Island of Cyprus. It forms a notable east-west trending bathymetric feature that rises from the abyssal plain to a depth of 1559 m. Eratosthenes Seamount is a north-south trending sub-rectangular high immediately south of Cyprus, rising to a depth of 966 m above the adjacent abyssal plain.

Various morpho-tectonic features observed in the eastern Mediterranean reflect the complexity of the region. The regional distribution and character of these features are prominent in the analysis of the tectonic processes since they comprise evidence of previous and recent tectonic activity.

1.6. Global Positioning System Data on Modern Deformation

The Global Positioning System (GPS) provides a precise measurement of continental motion and deformation. These, in turn, contribute to the understanding of the rheological models of the continental lithosphere and the forces causing the active deformation (Reilinger et al., 1997). The analysis of the movement vectors shown in

Figure 1.5, suggests that the Syrian-Arabian Microplate is moving north-northwest at a rate of about 25 mm/year, the African Plate is moving northward at a rate of about 10 mm/year and the Aegean-Anatolian Microplate is rotating counterclockwise with an internal deformation of <2 mm/year, relative to Eurasian Plate (DeMets et al., 1990, 1994). The movement of African Plate relative to the Arabian-Syrian Microplate is accommodated along the sinistral slip of the Dead Sea Fault. The rotation of the Aegean-Anatolian Microplate is accommodated along the dextral North Anatolian Fault and its extension into the Aegean Sea (i.e. the North Aegean Trough) in the north, and along the sinistral East Anatolian Fault in the east.

Continental blocks tend to escape from collisional zones to prevent the subduction of continental material and to reduce the topographic elevation (McKenzie, 1970; Şengör, 1979; Jackson and McKenzie, 1988; Jackson, 1992). The westward movement of the Aegean-Anatolian Microplate is a prime example of a tectonic escape, in this case resulting from the collision of the Syrian-Arabian Microplate with the Eurasian Plate along the Bitlis-Zagros Suture zone, in eastern Turkey.

Jackson and McKenzie (1984) measured the earthquake slip vectors along the North Anatolian Fault and obtained an Euler vector with a rotation pole of 14.6° N, 34° E and rate of 0.64° /my for the Anatolian segment of the Aegean-Anatolian Microplate and Eurasian Plate. Accordingly, they suggest that the western Aegean segment of the microplate is separated from the eastern Anatolian segment of the microplate by a north-south oriented extension zone and added that the intensity of earthquakes in western

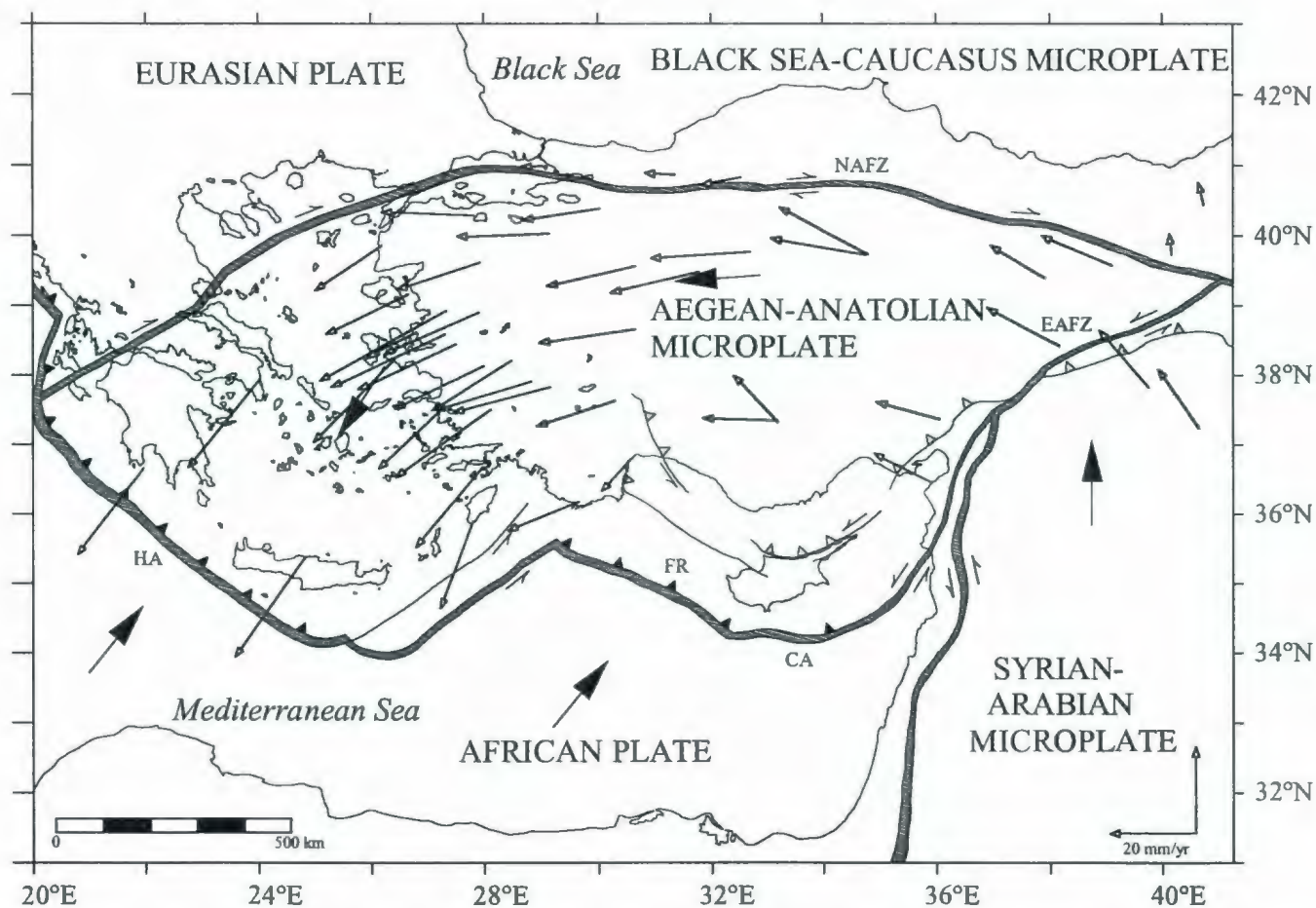


Fig. 1.5. Global Positioning System (GPS) horizontal velocities measured relative to Eurasia in the period 1988-1994 (modified from Reilinger et al. (1997) and Robbins et al. (1995). NAFZ- North Anatolian Fault Zone, EAFZ- East Anatolian Fault Zone. HA, Hellenic Arc, FR- Florence Rise, CA- Cyprus Arc. Large arrows show plate motion relative to fixed Eurasian Plate. Subduction zones are shown by double lines with filled triangles positioned on the overriding plate. Major thrust faults are shown by single lines with hatched triangles on the hanging wall. Strike-slip faults are displayed by half arrows showing the directions of relative displacement.

Turkey compared with the non-seismic character of the central Turkey provides support for this two-microplate hypothesis. Taymaz et al. (1991) obtained a similar Euler vector, only with a change in the rotation rate (0.78° /my). However, Reilinger et al. (1997), derived two Euler vectors: one using only ten GPS stations located in the central portion of the Anatolian segment of the microplate and the other using all the stations south of North Anatolian Fault zone and west of East Anatolian Fault zone, which indicate rotation poles and rates of $29.2 \pm 0.8^\circ$ N, $32.9 \pm 0.4^\circ$ E, $1.3 \pm 0.1^\circ$ /my and $31 \pm 0.8^\circ$ N, $32.2 \pm 0.4^\circ$ E, $1.7 \pm 0.2^\circ$ /my, respectively. These two Euler vectors imply a statistically negligible difference and point a pole position situated near the Sinai Peninsula. Based on the similarity of these Euler vectors, Oral et al. (1995), and Reilinger et al. (1997) suggested that the rotation of the Aegean-Anatolian Microplate may be better characterized by a single plate model. In this model, the Aegean-Anatolian Microplate displays little deformation in the east and a notably increasing deformation toward the Hellenic Arc, resulting in north-south extension in the southeastern Aegean region.

The Euler poles of Reilinger et al. (1997) display a 14° shift to the north from those calculated by Jackson and McKenzie (1984) and Taymaz et al. (1991). This shift in the pole position denotes a smaller radius of curvature for the rotation of Aegean-Anatolian Microplate relative to Eurasian Plate. Based on the examination of the curvature of the North Anatolian Fault, Westaway (1994) suggested that a rotation curvature for the Aegean-Anatolian Microplate must exist along the trace of this fault to accommodate the observed geometry. The rotation curvature obtained by Reilinger et al.

(1997) overlaps the trace of the North Anatolian Fault along the eastern-central portion but deviates toward south from the western portion. Using the earthquake focal mechanisms and the geological maps, Barka and Kadinsky-Cade (1988), Barka et al. (1997) noted a change from a strike-slip and extensional character to a more complex system of restraining and releasing bends along the North Anatolian Fault, towards the west. This change in the character of North Anatolian Fault may explain the deviation of the fault from the rotation pole estimated by Reilinger et al. (1997).

Systematic analysis of the GPS velocity field based on a fixed Eurasian Plate shows a counterclockwise rotation of the Aegean-Anatolian Microplate with an increase in the horizontal velocities towards west-southwest (Fig. 1.5). The high velocities observed in the southwestern part of the microplate is interpreted to occur as a result of the southward retreat of subduction of the African Plate along the Hellenic Arc (McClusky, 2000).

The evaluation of the GPS data generally supports McKenzie (1970)'s earlier ideas on the deformation field in the eastern Mediterranean. The counterclockwise rotation of the Aegean-Anatolian Microplate relative to Eurasia suggested by the GPS measurements provides a better understanding of the geological architecture in Antalya Bay, and is further discussed later.

1.7. Seismicity

The Alpine-Himalayan belt is a prominent zone of active seismicity where

earthquakes are generated along the boundaries between the larger Eurasian, African and Indo-Australian Plates and several smaller Syrian-Arabian and Aegean-Anatolian Microplates. The boundary between the African and Eurasian Plates in the easternmost Mediterranean, including the Aegean Sea is fairly complex, and this region is considered as the most active portion of this zone of seismicity. The seismicity map shown in Figure 1.6 constitutes the data from the Kandilli Observatory, Earthquake Research Institute-KOERI, and International Bathymetric Chart of the Mediterranean- Seismicity-IBCM-S.

A number of large historical and recent earthquakes provide valuable information on the character of the recent tectonic activity in the eastern Mediterranean region (Barazangi and Dorman, 1969; Ambraseys, 1970; McKenzie, 1970, 1972; Nowroozi, 1971; Comninakis and Papazachos, 1972; Papazachos, 1973; Büyükaşikoğlu, 1980; Rotstein and Kafka, 1982). The seismicity in eastern Mediterranean Sea generally increases from east to west (Fig. 1.6). The focal depth distribution of earthquakes with magnitudes greater than 4 reveal that the hypocenters >50 km are mainly concentrated in the region of the Hellenic Arc, the Florence Rise, the Anaximander Seamounts including the Finike Basin, the Adana-Iskenderun Basins, the southern regions of Cyprus and along the volcanic arc in central Anatolia. Earthquakes with epicenters <50 km are concentrated along the North Anatolian Fault, the East Anatolian Fault and in the onshore extension of the Antalya Bay, the Isparta Angle. Three recent major earthquakes have occurred along the western flank of the Isparta Angle in 1914 ($M=7$), 1971 ($M=6.2$) and 1957 ($M=7$), whereas the eastern flank does not appear to be seismically active. In central Anatolia

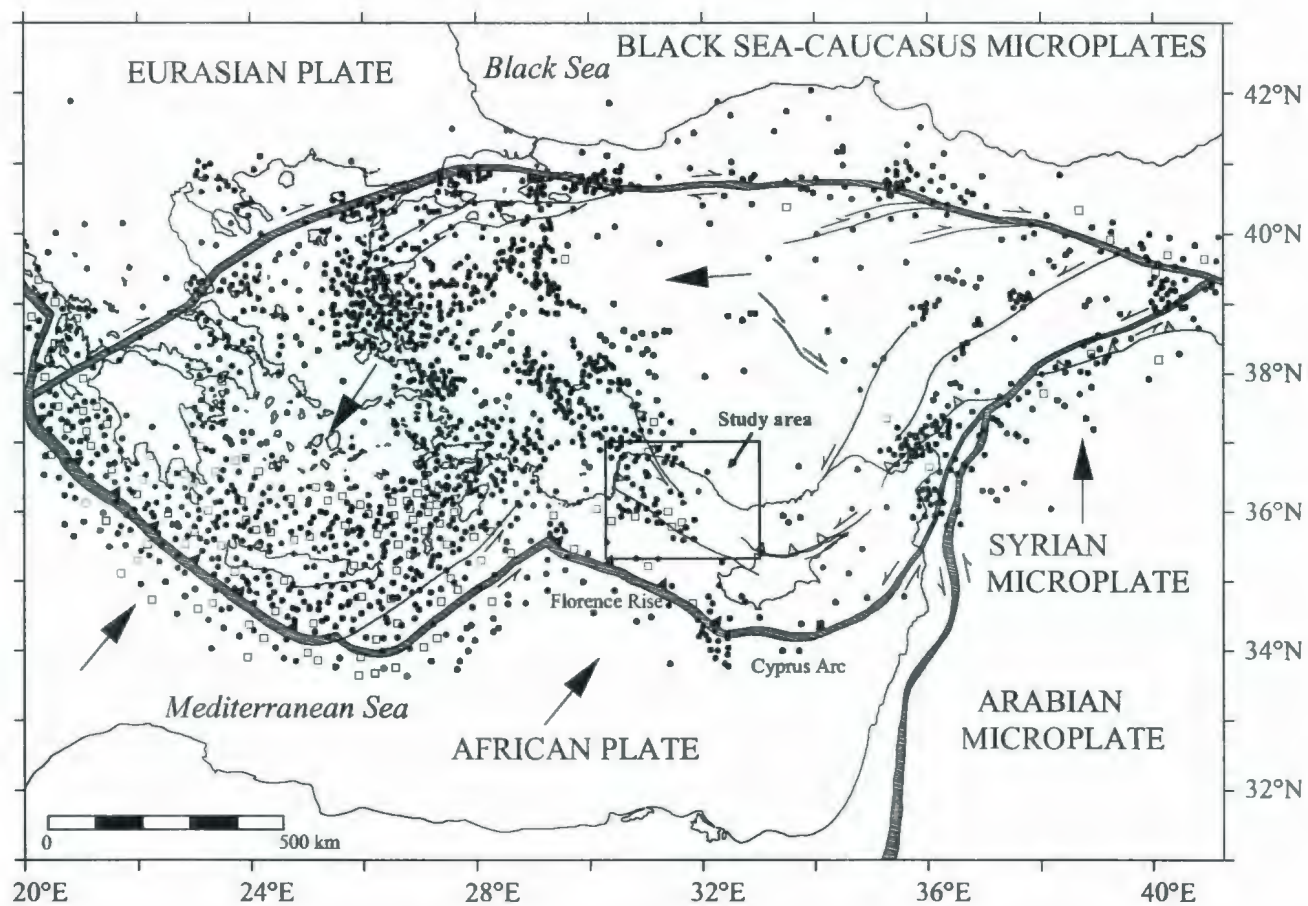


Fig. 1.6. Seismicity map of the eastern Mediterranean showing the distribution of earthquake epicentres with magnitudes >4 , compiled using data from Kandilli Observatory Earthquake Research Institute, and International Bathymetric Chart of the Mediterranean- Seismicity-IBCM-S. Focal depths <50 km and >50 km are represented by filled circles and open squares, respectively. Large arrows show plate motion relative to fixed Eurasian Plate. Subduction zones are shown by double lines with filled triangles positioned on the overriding plate. Major thrust faults are shown by single lines with hatched triangles on the hanging wall. Strike-slip faults are displayed by half arrows showing the directions of relative displacement.

both historical and recent earthquakes suggest a lower seismic activity compared to western Anatolia (Ambraseys, 1970;1988; Ambraseys and Finkel, 1987; Barka et al., 1997). The most important earthquakes in this area are the 1938 Kırşehir earthquake with a magnitude of 6.8 (Parejas and Pamir, 1939; Ketin, 1969; Barka et al., 1997) and the three historical earthquakes that occurred in 1668, 1717 and 1835 (Ambraseys and Finkel, 1987; Öztin and Bayülke, 1990). Western Turkey is characterized by high seismic activity, with several large earthquakes delineating the master faults of the east-west trending graben systems, such as the 1899 Büyük Menderes, 1928 Torbalı, 1955 Balat, 1969 Simav, 1970 Gediz and 1995 Dinar earthquakes. Little or no seismic activity is observed in the southern part of central Anatolia (including the Mut Basin).

The boundary between the African Plate and the Aegean-Anatolian Microplates can be seismically traced from the Ionian Sea in the west across the Hellenic Arc, Florence Rise-Cyprus Arc into the Bitlis-Zagros Suture zone in the east (Fig. 1.6). The Hellenic Arc subduction zone, including the Ptolemy, Pliny and Strabo Trenches along its western margin is seismically very well defined by a narrow, north-concave belt of shallow, intermediate and deep earthquakes, with a prominent Benioff zone. The Florence Rise and Cyprus Arc can also be traced seismically as another north-concave belt, but with a notably lower seismicity. The absence of unequivocal oceanic crust in the Levantine Basin (McKenzie, 1972) and the lower earthquake activity strongly suggest that the continental fringes of the African Plate are beginning to collide with the Aegean-Anatolian Microplate, and that the small continental fragment, the Eratosthenes Seamounts is choking the

subduction zone (Robertson, 1998). Rotstein and Kafka (1982) used the recent earthquake data to suggest that a continuous zone of seismicity east of the Anaximander Seamounts defines the northern boundary of the African Plate. Seismic reflection data clearly document the presence of a prominent northeast-trending ridge (i.e. Tartus Ridge, Ben Avraham et al., 1995) which defines the northern boundary of the African Plate with the Syrian-Arabian Microplate in the east and the Aegean-Anatolian Microplate in the north. The Tartus Ridge links the Cyprus Arc with the Dead Sea Fault and the East Anatolian Fault on a triple junction near the town of Kahramanmaraş (Figs. 1.1 and 1.6; Ben Avraham et al., 1995; Vidal et al., 2000). In southeastern Turkey, the plate boundary is characterized by two southwest-northeast oriented, internally parallel zones of seismicity. The southern zone lies along the Bitlis-Zagros Suture zone, while the northern lesser zone correlates with the present-day trace of the East Anatolian Fault.

A few earthquakes are concentrated in the Antalya Basin, some occurring at depths of ~150 km. There are sufficient number of permanent stations to control the error in the locations of the epicenters and the stations are close to the earthquakes to provide a fairly reliable depth information. Rotstein and Kafka (1982) plotted two cross sections of seismicity across the Antalya Bay, where seismicity data show a zone of earthquake foci deepening northward into the Antalya Basin. A similar landward increase in the focal depths of earthquakes is recognized in the vicinity of Rhodes, along the Hellenic Arc (Richter and Strobach, 1978). Considering this similarity, the pattern of the sub-crustal seismicity in Antalya Basin, representing earthquakes with foci >50 km may be interpreted

as delineating a possible continuing subduction zone.

The analysis of seismicity in the eastern Mediterranean provides a better understanding of the past and recent tectonic processes that control the movement of the African and Eurasian Plates and the reorganization of the smaller microplates (i.e. Aegean-Anatolian and Syrian-Arabian Microplates). The focal depth distribution of the earthquakes together with the associated fault plane solutions contributes greatly to the interpretation of the complex geological structures in the area.

Fault plane solutions obtained from the earthquake data, which consist of the azimuth angles of the stations with respect to the epicenter and the initial direction of the P waves recorded at those stations, shows evidence of a complex deformation in the eastern Mediterranean (Fig. 1.7). The major fault activity obtained from the fault plane solutions of earthquakes in the Iskenderun and Adana Basins reveals a predominantly strike-slip character. A similar strike-slip character is also recognized along the North Anatolian Fault and East Anatolian Fault zones. In the western portion of the North Anatolian Fault, the strike-slip character is accompanied by a distinct normal slip component. In western Turkey normal fault activity occurs along several well defined graben systems. The Antalya Basin and the area to the south and southwest of Cyprus is characterized by both reverse and normal faulting with a strike-slip component. The fault plane solutions from the Harvard Seismology Centroid-Moment Tensor (CMT) database (from 1976 to 2002) shown on Figure 1.7 are of the earthquakes with magnitudes equal and greater than 4.

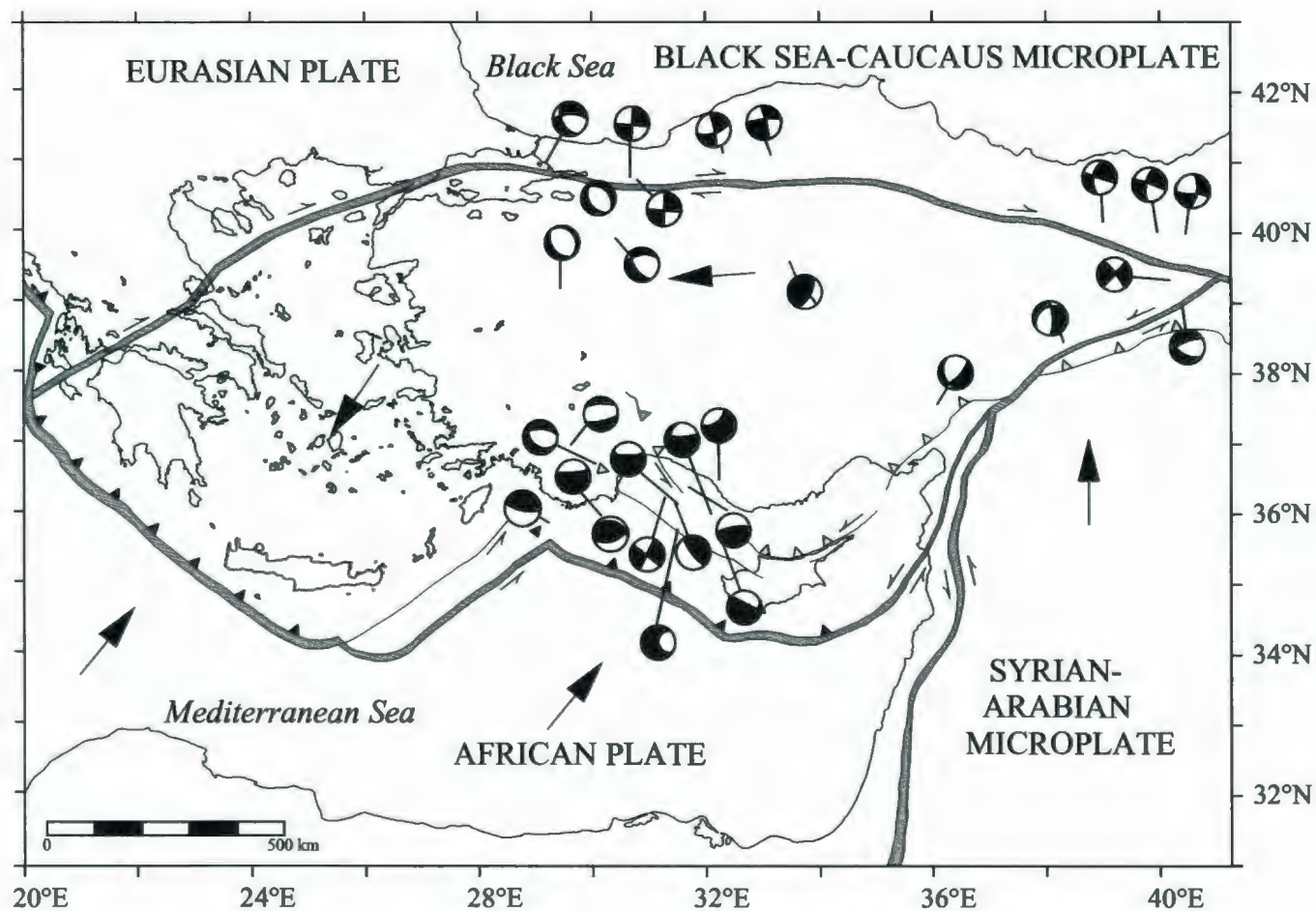


Fig. 1.7. Fault plane solutions (lower hemisphere projection) for major earthquakes in the eastern Mediterranean region (compiled from Jackson et al., 1984 and Harvard CMT Catalog). The active subduction zones are marked by double lines with arrow heads positioned on the overriding plate. The major thrust faults are shown by single lines with arrow heads on the hanging wall. The strike-slip faults are displayed by half arrows showing the directions of relative displacement.

The regional and focal depth distribution of earthquakes in relation to the plate boundaries is very important in delineating the role of Antalya Bay within the tectonic processes that control the eastern Mediterranean. The information provided by the fault plane solutions helps to note the character of the fault activity in the study area, providing a tool to compare with what is shown by the seismic data.

CHAPTER 2. Data Acquisition

2.1. The Seismic Reflection Method

The seismic reflection method involves measuring the two-way-traveltime of the seismic waves from the source to the receivers. Figure 2.1 shows the reflection geometry of a seismic wave path in the case of a dipping reflector in a homogeneous and isotropic medium. Here, h stands for the shortest source-reflector distance, α stands for the dip of the reflector, x is the lateral source-receiver distance and v is the average velocity of the medium. Note that the angle of reflection (β_1) is equal to the angle of incidence (β_2). From Figure 2.1 the traveltime (t) can be derived by applying the cosine law to the triangle ACH,

$$|CR|^2 = |SR|^2 + |SC|^2 - 2 |SR| |SC| \cos (90^\circ + \alpha), \quad (2.1.1)$$

where,

$$\begin{aligned} |CR| &= |SA| + |AR| \\ &= vt. \end{aligned}$$

Consequently, one can rewrite the equation (2.1.1):

$$\begin{aligned} v^2 t^2 &= x^2 + 4h^2 - 4hx \cos (90^\circ + \alpha) \\ &= x^2 + 4h^2 + 4hx \sin \alpha, \end{aligned} \quad (2.1.2)$$

which, when reorganized, denotes the expression of a hyperbola with the axis of symmetry at $x = -2h \sin \alpha$,

$$[v^2 t^2 / (2h \cos \alpha)^2] - [(x + 2h \sin \alpha)^2 / (2h \cos \alpha)^2] = 1. \quad (2.1.3)$$

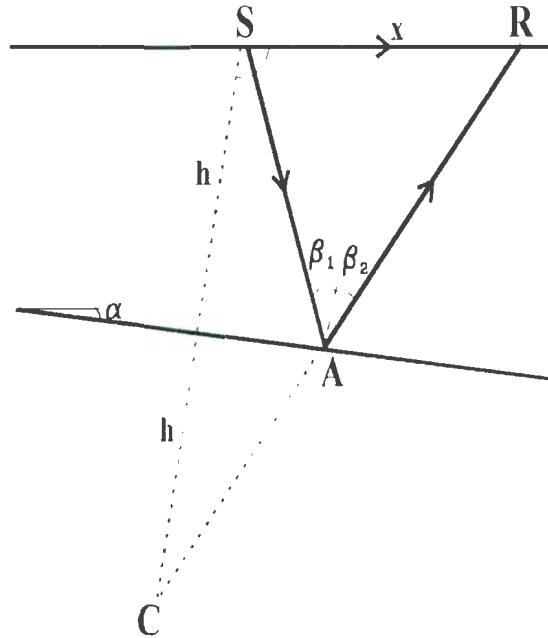


Figure 2.1. A schematic display of a path of a reflecting seismic ray traveling in an isotropic and homogeneous medium.

The travelttime function, which corresponds to a tilted hyperbola, is constrained by the physical properties of the subsurface media (in terms of the propagation velocity of the seismic waves), the depth and dip of the reflector as well as the source-receiver distance.

Reflection requires media with distinct acoustic impedance contrasts. The acoustic impedance (AI) of a medium is expressed by its mass density (ρ) and velocity (v),

$$AI = \rho v. \quad (2.1.1)$$

The reflectivity coefficient (RC) determines the amount of seismic energy which will be reflected from an interface and can be expressed as a function of acoustic impedances.

The reflection coefficient depends upon angle of incidence. For normal incidence,

$$RC_{12} = \rho_1 v_1 - \rho_2 v_2 / \rho_1 v_1 + \rho_2 v_2. \quad (2.1.2)$$

The reflected seismic waves are then detected by the hydrophones and the voltages induced are transferred to the recorder. After pre-amplification (with or without filtering) the analog signals are passed to an analog-to-digital converter. The digital signals are recorded on a magnetic digital tape in industry-standard SEG D format.

2.2. The Acquisition Parameters and the Geometry of the Survey

Approximately 900 km of multi-channel seismic reflection profiles were collected in the Antalya Basin during 1992 and 2001, using the Memorial University of Newfoundland multi-channel seismic acquisition system on the R/V *Koca Piri Reis* of the Institute of Marine Sciences and Technology, Dokuz Eylül University, İzmir, Turkey. During acquisition, the common-mid-point shooting technique (Figure 2.2) was used, allowing redundant sampling of a given reflector, where the multiplicity of subsurface coverage is given by.

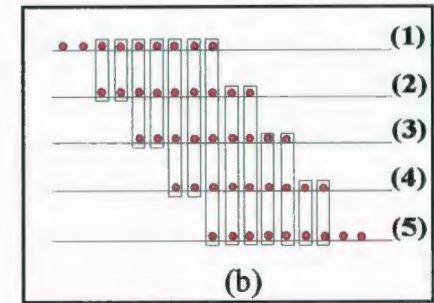
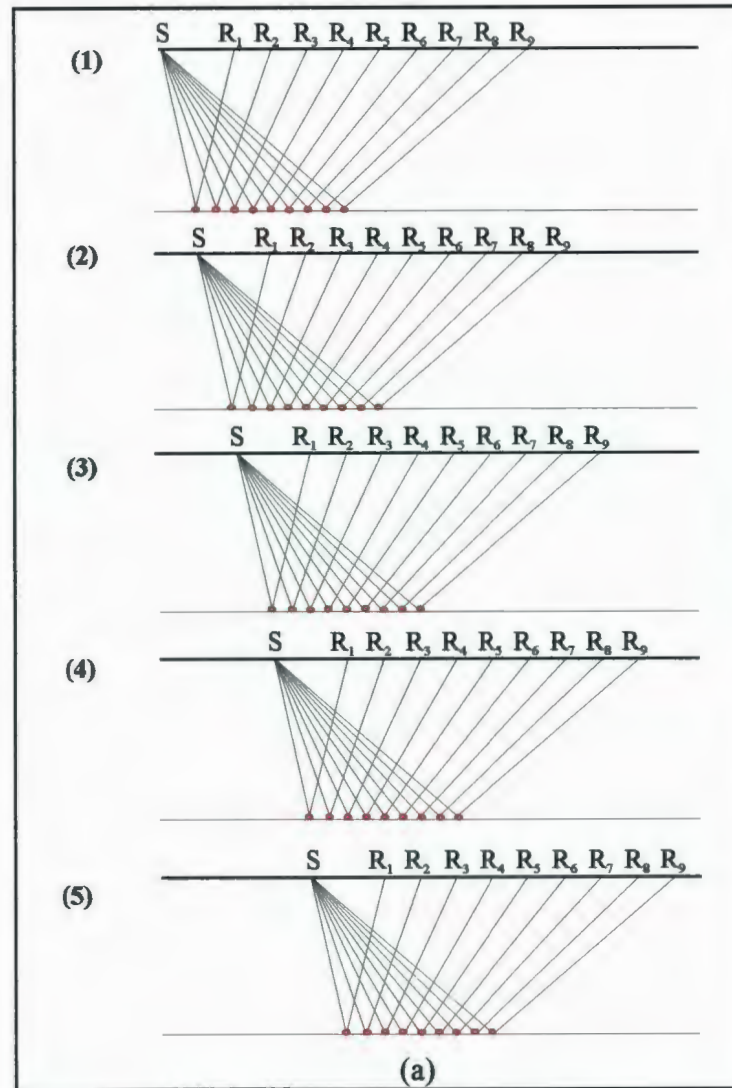


Fig. 2.2. (a) Common-mid-point (CMP) seismic acquisition configuration; (b) resultant multiple subsurface coverage(i.e. Fold)

$$\text{Fold} = 1/2 (\text{Number of channels (Hydrophone Group Interval / Shot Interval)}).$$

The source consisted of a Halliburton sleeve gun array, employing gun sizes of 40, 20 and 10 cubic inch. In 1992, the total volume varied between 70 and 120 cubic inches, but typically 90 cubic inch (1475 cm^3), whereas in 2001, the total volume was typically 200 cubic inch (3278 cm^3). The design bandwidth of the full 200 cubic inch source is approximately flat over 50-250 Hz.

During 1992 and 2001, shots were fired every 25 m, and reflections were detected by the nearest 12 channels of Litton 48 x 12.5 m multi-channel streamer (1992) and the full Teledyne 48 x 12.5 m multi-channel streamer (2001). The signals were transferred to the amplifiers where 36 dB (1992 and 2001) initial gain was applied. The amplified signal was filtered using a low-cut frequency of 8 Hz, with 18 dB/OCT slope (1992 and 2001). The resultant 3-fold (1992) and 12-fold (2001) data were recorded digitally for three seconds below the sediment-water interface (with delay after shooting dependent on water depth) at 1 millisecond sample rate, on optical diskettes using a DFS V seismograph (1992) and on DAT tapes using OYO DAS-1 seismograph (2001). Both 1992 and 2001 multi-channel data were processed at the Memorial University of Newfoundland, with automatic gain control, short-gap deconvolution (only 1992 data), velocity analysis, normal move-out correction, stack, filter (typically 50-200 Hz bandpass), migration, and adjacent trace summing (only 1992 data). Data from 1992 were processed using STARPAK software; data from 2002 were processed using ProMAX (Courtesy of

Landmark Graphics Corporation). Despite the low source volume and low fold, reflections are imaged to 2 seconds two-way time below seabed, even in 2 km water depth.

Most of the 1992 and 2001 profiles were collected in a northeast-southwest direction which is perpendicular to the general trend (strike) of the geological structures in the area. Two tie-lines were shot extending in a west northwest-east southeast direction across the bay and intersecting the rest of the profiles. The resultant coverage constitutes a grid with line separation of around 7.5 km (see Appendix). The details of the shooting geometry for both 1992 and 2001 data are shown in Figure 2.3.

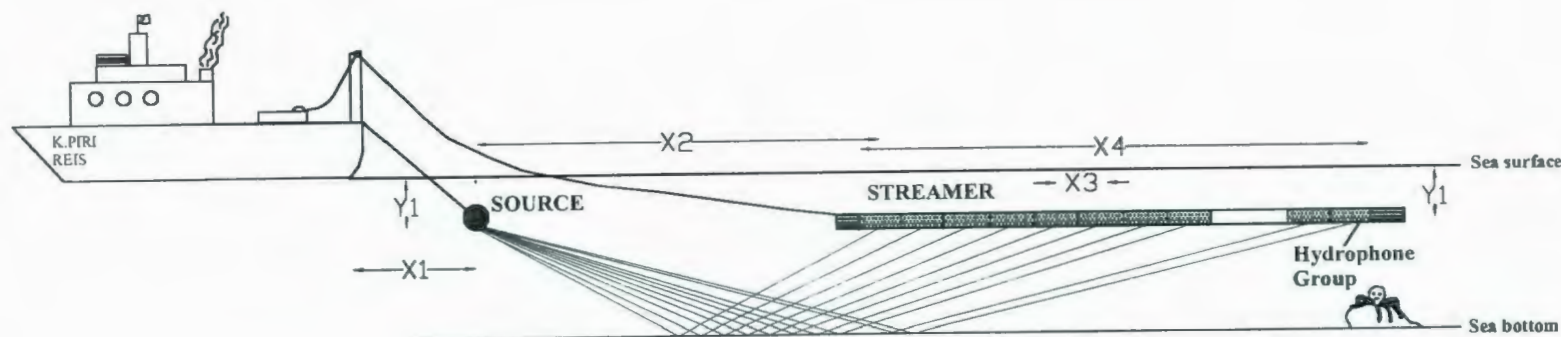


Figure 2.3. The shooting geometry for 1992 and 2001 seismic surveys; values separated by '/' correspond to the acquisition parameters used during 1992 and 2001 surveys, respectively.

Stern to source (X_1): 50 m. / 37 m.

Source to center of first hydrophone group (X_2): 37.5 m. / 95 m.

Hydrophone group interval (X_3): 12.5 m. / 12.5 m.

Active streamer length (X_4): 200 m. / 600 m.

Source and streamer depth (Y_1): 3 m. / 3 m.

CHAPTER 3. Marine Seismic Data Processing

The aim of seismic data processing is to enhance the signal to produce interpretable seismic sections that are closest to the true image of the subsurface. A seismic record contains random and coherent noise as well as primary reflections. The noise may dominate the data particularly at greater depths below the surface because of decreasing signal levels caused by inelastic attenuation. The random noise can originate from various sources including electrical noise from the recording instruments, strumming noise caused by the vibration of the streamer in water due to towing speed, general vessel noise originating from propellers, generators, compressors and the wave noise caused by the rough sea conditions. The coherent noise, on the other hand, occurs most commonly in the form of multiple reflections originating from secondary reflections from the interfaces, monofrequency waves generated by a.c. electrical power lines, and low frequency waves with low amplitudes originating from the cable. One of the most important aspects of data processing is to suppress the noise in order to increase the signal-to-noise ratio. The most common noise suppression methods are filtering, deconvolution and stacking. After the noise component is minimized and stacking is performed, migration is applied to the data to move the dipping reflectors to their true subsurface locations and to collapse diffraction hyperbolae.

Data processing is performed based on a number of assumptions originating from the premise that the medium in which the wave propagation takes place is homogeneous and isotropic. For example, the stacking process assumes hyperbolic moveout, whereas

migration is based on the assumption of zero-offset wavefield. These assumptions generally are not satisfied by the complex structure of the subsurface. However, seismic processing can be successfully used in subsurface data although with a loss of efficiency, because the processing algorithms are designed to deal with some deviations from these assumptions.

A conventional marine seismic data processing flow chart is given in Figure 3.1. The success of each process on the chart depends on the reliability of the previous stages as well as the parameters defined within each step.

The processing of the Antalya Basin seismic data were performed using the Landmark-ProMAX software.

3.1. Trace Editing

The trace editing process for the Antalya Basin seismic data consisted of: (1) renumbering shot files, (2) removing bad traces, (3) correcting anomalous time shifts, and (4) removing static time delays.

A number of duplicate shot files were recognized in the header values. It was not possible for the processing job to be executed when two shots were designated the same file number. Thus, the duplicate shot files were removed and the subsequent shot files were renumbered sequentially. There were approximately 12 noisy traces, distributed

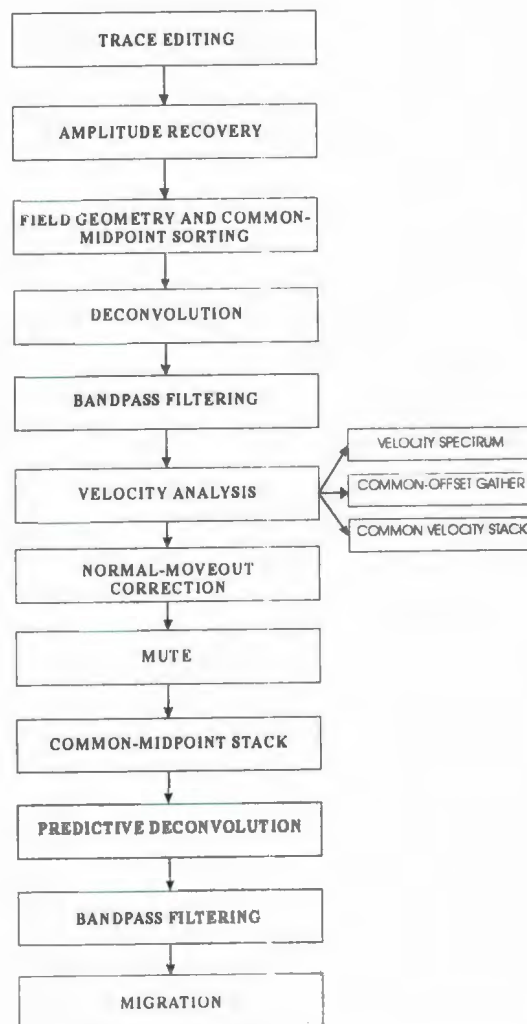


Figure 3.1. A conventional marine seismic data processing flow.

randomly along the streamer (Figure 3.2). The noise was probably generated within the hydrophone array either associated with the portions of the streamer exposed on the sea-surface due to rough sea conditions or malfunctioning birds (streamer depth controller), garbage trapped around birds or air bubbles trapped within the streamer. In order to achieve a higher signal-to-noise ratio, these traces were zeroed. In spite of the fact that deleting the traces decreases the fold on the stacked section, a compromise had to be made to preserve a reasonable signal-to-noise ratio.

A saw-tooth expression of the seabed reflection appeared occasionally on near trace gathers (Fig. 3.3a). This probably arises from malfunctioning of the firing system. They were corrected by shifting up each shot gather with the amount of time required (Fig. 3.3b). However, the non-periodical behavior at some localities, particularly along steeply dipping structures, made the correction very difficult and in some cases impossible.

Record time delays varying between 500-3000 ms (depending on the water depth) were applied during data acquisition in deep water regions in order to maximize useful data in the 3-second recordings (Fig. 3.4a). The data were shifted downward with the amount of the delay to place the reflections to their original arrival times (Fig. 3.4b). The -200 ms source delay was subtracted while defining the amount of shift for correction.

3.2. Amplitude Recovery

During wave propagation from a point source, the amplitude of the wave decays in proportion to the radius of the wavefront, an attenuation mechanism known as spherical

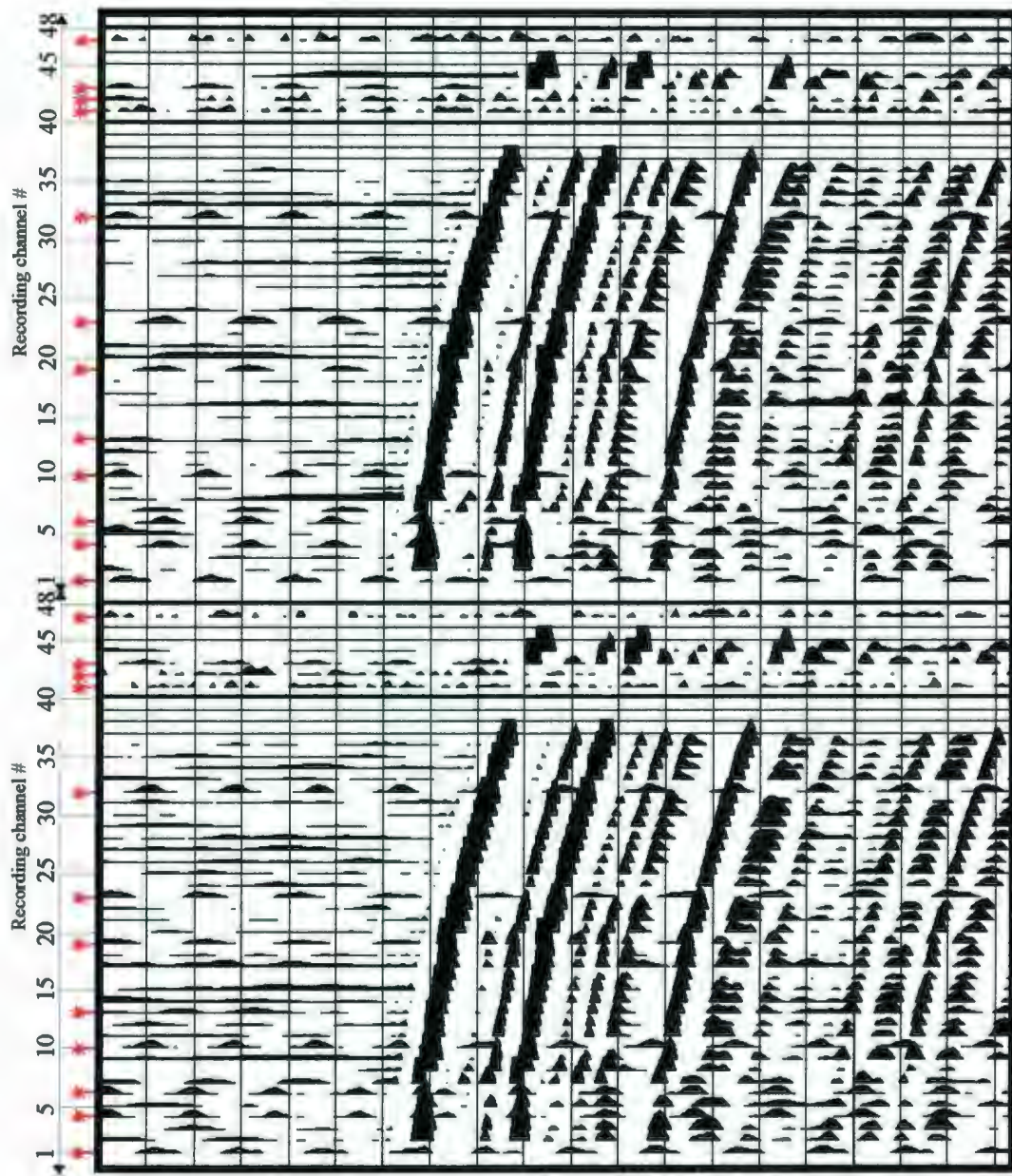
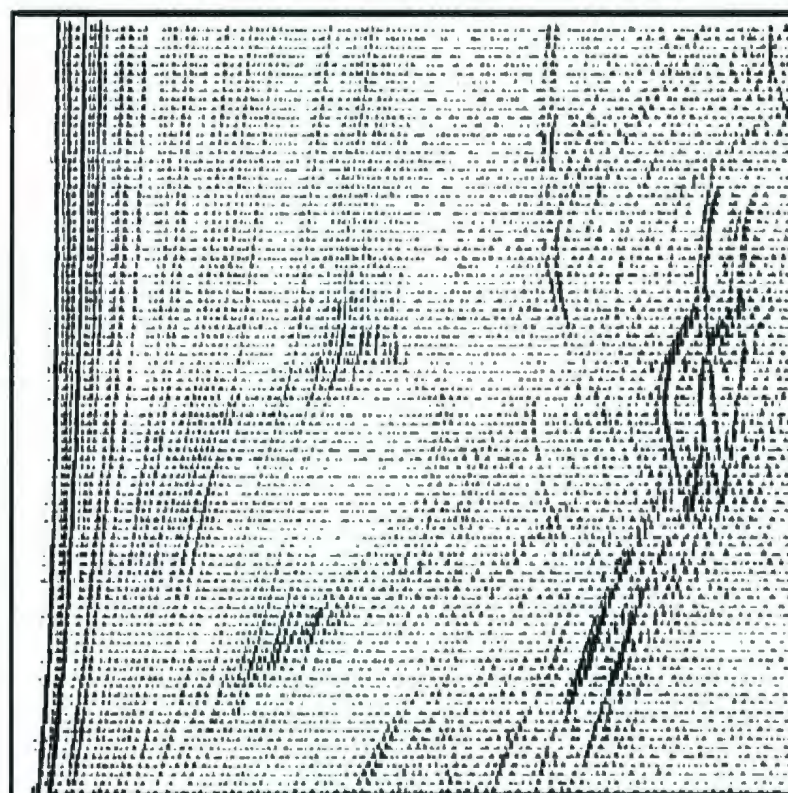
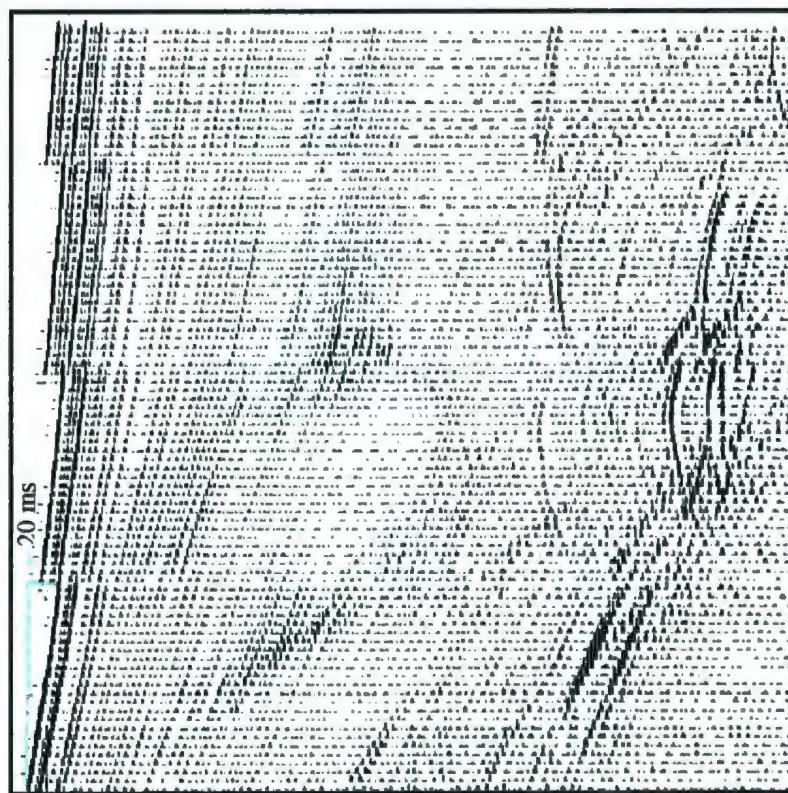


Fig. 3.2. Two consecutive shot gathers. The noisy channels are marked by *.



(b)



(a)

Fig. 3.3. Seismic reflection profile showing the recording shifts: (a) before and (b) after the correction.

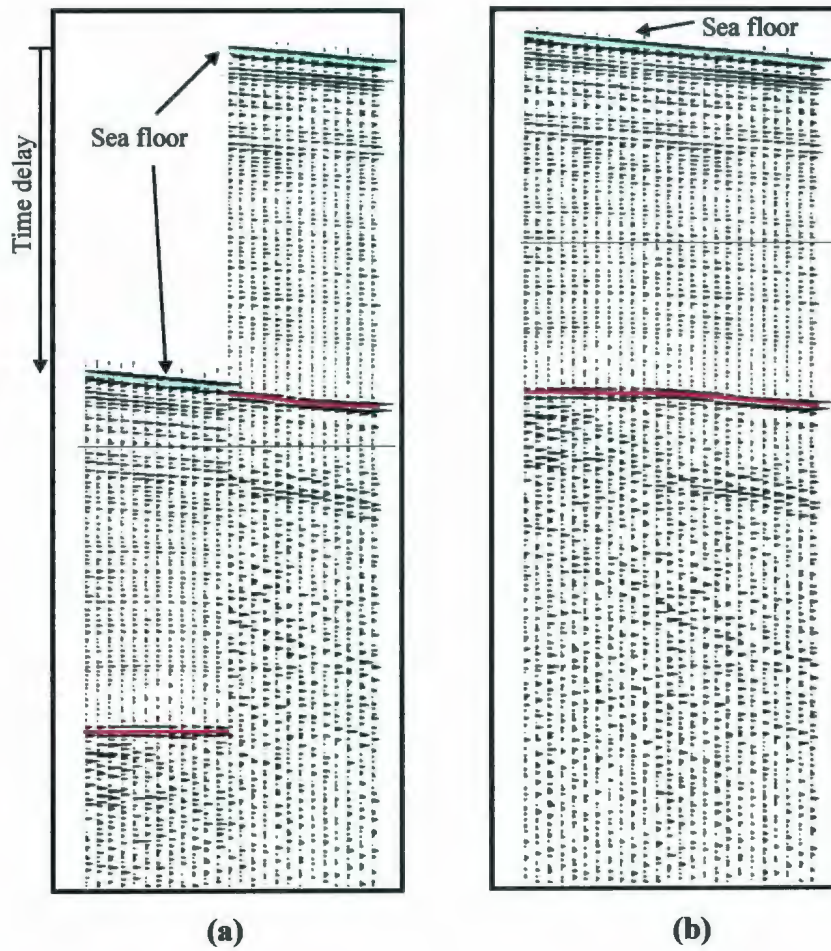


Fig. 3.4. Seismic reflection profile (near trace gather) showing the recording time delays: (a) before and (b) after the correction.

divergence. The velocity, which generally increases with depth, amplifies this effect. The pore fluids in the media, through which the waves are propagating, consume part of the wavefield energy, which also is recognized as amplitude losses in the deeper portions of the seismic section. Thus, the more porous the medium and the longer the raypath, the more the attenuation. It has to be noted that high frequency waves are absorbed more than the low frequency waves.

The penetration achieved on the Antalya Basin seismic data has not been high enough to recognize a decay in the amplitudes below the seabed due to absorption or even spherical divergence (not so surprising in deep water). A gain recovery technique, known as the Automatic Gain Control (AGC) with a sliding time window, was applied to the data after stacking for display purposes. The scale factor used in the gain function was calculated by picking the amplitude of the middle sample in each sliding window and taking the inverse of it. The width of the window was selected as 500 ms because a broad sampling interval has been sufficient to give the desired result - overall even signal level but retaining local high amplitudes of stronger reflections.

3.3. Field Geometry and CMP Sorting

Accurate introduction of the shooting geometry to the dataset is crucial in terms of reliable results in the subsequent processes, such as velocity analysis. The positions of the source and receivers were defined by carefully determining several parameters including the minimum and maximum offset, the shot and receiver intervals, and the sailing azimuth.

Missed shots or misfired shots were treated to match the data with the observer's log. After the geometry information was incorporated with the data, the originally acquired shot and receiver coordinates were transformed to midpoint and offset coordinates by assigning each trace to the midpoint between the associated shot and receiver locations, a process known as common-mid-point (CMP) sorting. Consequently, traces corresponding to the same midpoint were assembled to form a CMP gather, where the number of traces represent multiple coverage (i.e. the fold of the data). Note that, a common-depth-point (CDP) is equal to a CMP in the case of a horizontal reflector. However, it is common to use the term CDP to refer to a CMP even in the presence of dipping reflectors, which is the case in the ProMAX processing software.

3.4. Deconvolution

The recorded seismic wavelet can be considered as a product of convolution of the basic wavelet with the impulse response of the subsurface media through which the wave propagates. If the basic wavelet is a spike, then the recorded wavelet represents the impulse response of the Earth.

The received signals differ from the source signature because of several factors such as hydrophone response, recording filters and surface reflections. Deconvolution is designed to convert each of the received, reflected repetitions of the source wavelet into a spike, by broadening the spectrum (spiking deconvolution) and by attenuating the multiple reflections, whose periods are predictable (predictive deconvolution) There are

several assumptions made during the derivation of the deconvolution algorithms: (1) the medium consists of horizontal and flat layers with no lateral velocity variations, (2) the initial wavelet is minimum phase (its energy is concentrated at the front), (3) the source wavelet is stationary, (3) the data is free of noise, and (4) the primary reflections have a random character (Hatton et al., 1986).

The attempts to apply deconvolution to the Antalya Basin seismic data did not give satisfactory results because (1) the source wavelet generated by the airgun array did not satisfy the assumption of minimum phase, and (2) the seabed reflection was already represented by a fairly short wavelet (if not a single peak) on the sections, which did not critically necessitate spiking deconvolution for identification. Furthermore, the fact that spiking deconvolution does not only introduce more high frequency energy to the seismic data but also boosts the high-frequency noise, made the technique less favorable in this case. The water depth in most of the Antalya Basin is too high for the images to suffer seriously from seabed multiples within the recording time. Therefore, there has been no need for performing predictive deconvolution along most of the profiles. Even in the slope region, predictive deconvolution has not been applied because it fails to be efficient due to the presence of non-flat reflectors and less than two multiple repetitions within the prediction window

3.5. Bandpass Filtering

Bandpass filtering is a frequency filtering technique used to eliminate the low and high frequency noise that exists in the seismic data. It is designed to pass the frequencies corresponding to the reflections while suppressing the frequencies associated with the noise. The pass band is marked by low-cut and high-cut frequencies between which the amplitude response of the filter is equal to unity.

Frequency filtering modifies the amplitude spectrum of a wavelet but maintains its phase. It is performed by multiplying the amplitude spectrum of the filter with that of the seismic wavelet. The output of the process is the seismic data including only the frequencies included within the pass band of the filter.

The amplitude spectrum of an ideal band-pass filter has a rectangular shape marked by low- and high-cut frequencies on each side. The Fourier transform necessary for the filtering algorithm requires a continuous function, hence, the sharp corners of the filter causing discontinuities must be smoothed. In addition, the steep sides of the filter may generate a ringing response (thus diminishing resolution) because of sampling a continuous function with a finite number of Fourier coefficients. The ringing, which deforms the wavelet and adds tails to the central peak in the time domain, results in uneven amplification of frequencies in the pass band. In order to limit the unwanted effects of ringing, steep filter slopes can be replaced by gentle slopes. This can extend the effective pass band further from the desired low- and high-cut frequencies, hence leaving some frequencies associated with noise in the pass band. However, it is a reasonable

compromise when compared with the ringing effect. The final optimized Ormsby filter is represented by a trapezoid in the amplitude spectrum. The broader the band width of a filter, the more compressed the wavelet in the time domain, hence, the more the temporal resolution; usually, at least two octaves in the pass band is considered desirable.

The Nyquist frequency is the highest frequency present in a digital waveform and given by

$$F_{nyq} = 1 / 2\Delta t$$

where Δt stands for the temporal sampling rate. In order to prevent aliasing of the signal (frequency folding), the high-cut frequency has to be smaller than that of the Nyquist frequency.

On the shot gathers shown in Figure 3.5, the seabed reflections are recognized at 3370 ms at the near offset. The wavelets associated with noise are clearly visible above the seabed, where there is no interference with the primary energy. Frequencies of 50-60 Hz, and around 4 Hz are prominent. By comparison, dominant frequencies of the reflections appear to be around 150 Hz. The amplitude spectrum of these shot gathers is given in Figure 3.6. Both displays suggest a frequency range of 40 Hz to 180 Hz for the primary reflections. Therefore, based on the observed frequencies on the shot gather and the frequencies suggested by the amplitude spectrum, it was decided to filter the data with an Ormsby filter, a trapezoidal bandpass filter, using the following parameters: low-cut frequency of 40 Hz, high-cut frequency of 180 Hz, low- and high-frequency slopes cutting the frequency axis at 20 Hz, and 220 Hz, respectively. The filtered data and their

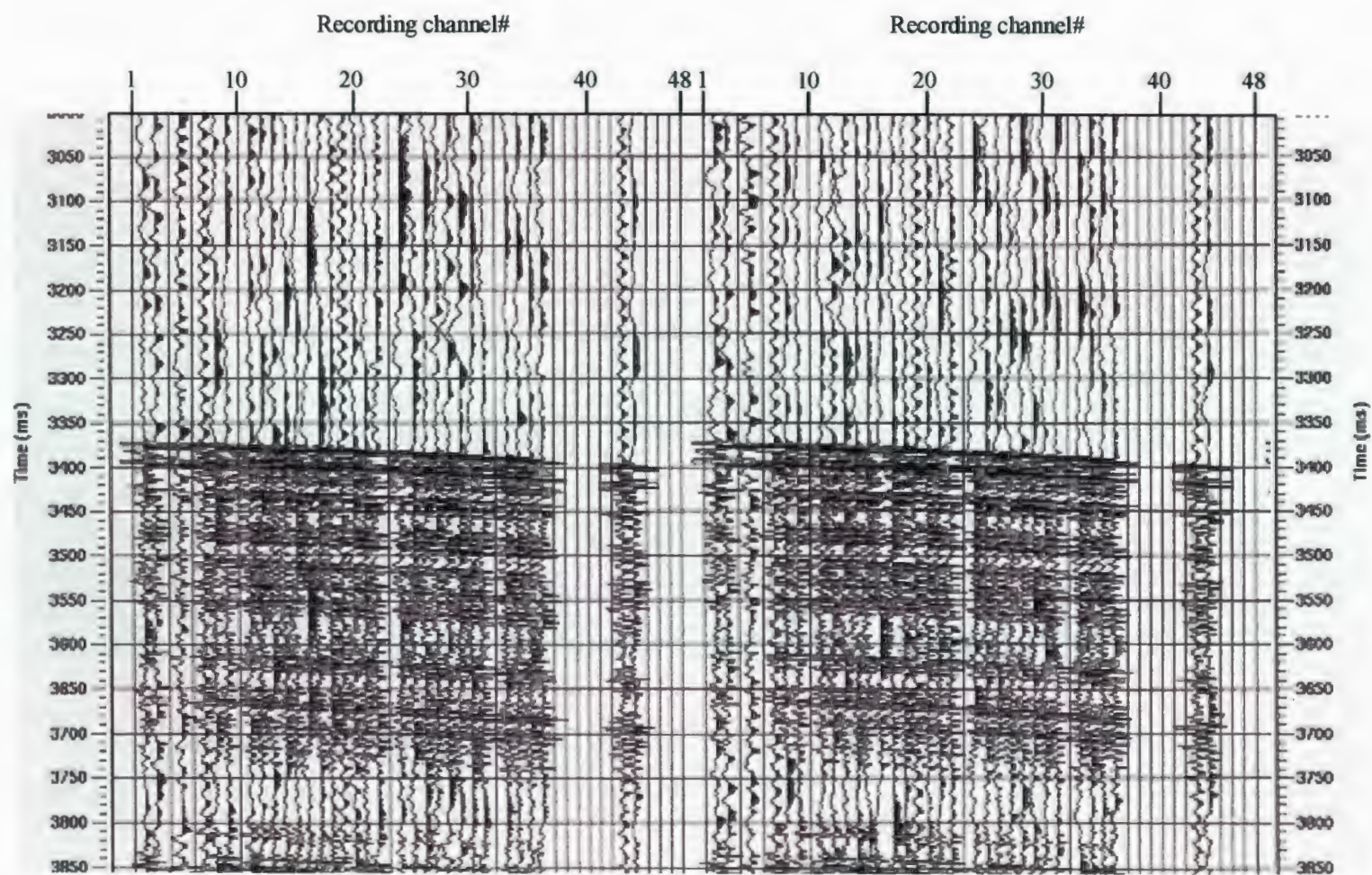


Fig. 3.5. Two consecutive shot gathers. The wavelets associated with noise are visible above the sea floor at 3370 ms.

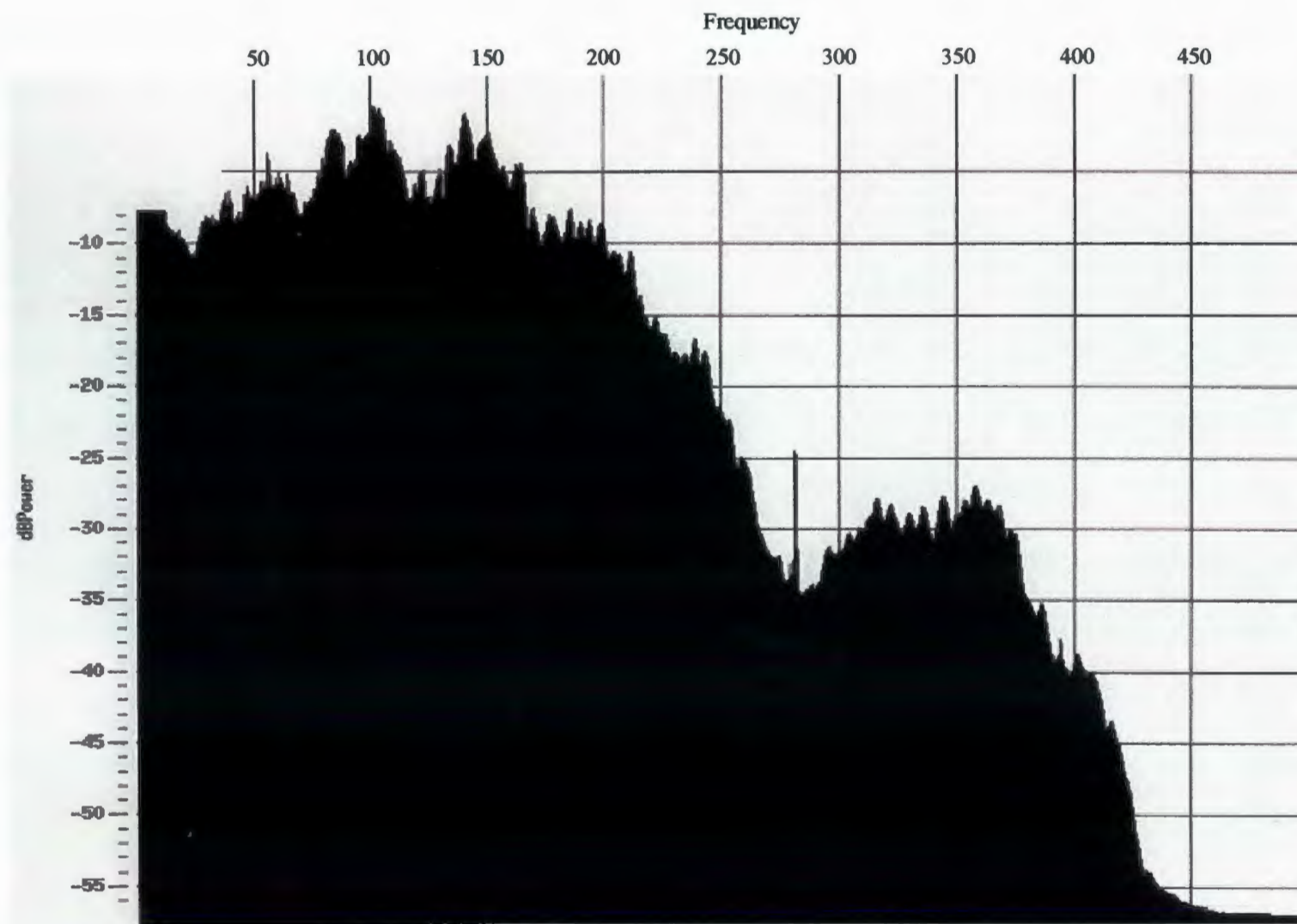


Fig. 3.6. Amplitude spectrum of the shot gathers shown in Figure 3.5.

amplitude spectrum show the success in the enhancement of the primary energy (Figs. 3.7 and 3.8).

3.6. Velocity Analysis, Normal Moveout Correction and Trace Muting

The quality of seismic imaging highly depends on the accuracy of the velocities used during processing. Velocity analysis is performed based on the variation of normal moveout (NMO) with travel time with the assumption of hyperbolic reflection t - x trajectories. It is usually applied to CDP gathers because of the reasonable hyperbolic alignment they display. The estimated velocities are then used to eliminate the time delay associated with the finite distance between the source and the receiver in the CDP gather, a process known as the NMO correction.

The equation (2.1.3) can be rewritten for the case of a horizontal reflector

$$t^2 / (2d/v)^2 - x^2 / 4h^2 = 1$$

and when it is expanded to the binomial series, traveltimes can be written retaining the first couple of terms,

$$t = 2h/v + x^2/4vh \quad (3.6.1)$$

Furthermore, because $2h/v = t_0$, equation (3.6.1) can be re-written as

$$\begin{aligned} t &= t_0 + x^2/2v^2 t_0 \\ \Delta t_{\text{NMO}} &= t - t_0 = x^2/2v^2 t_0 \end{aligned} \quad (3.6.2)$$

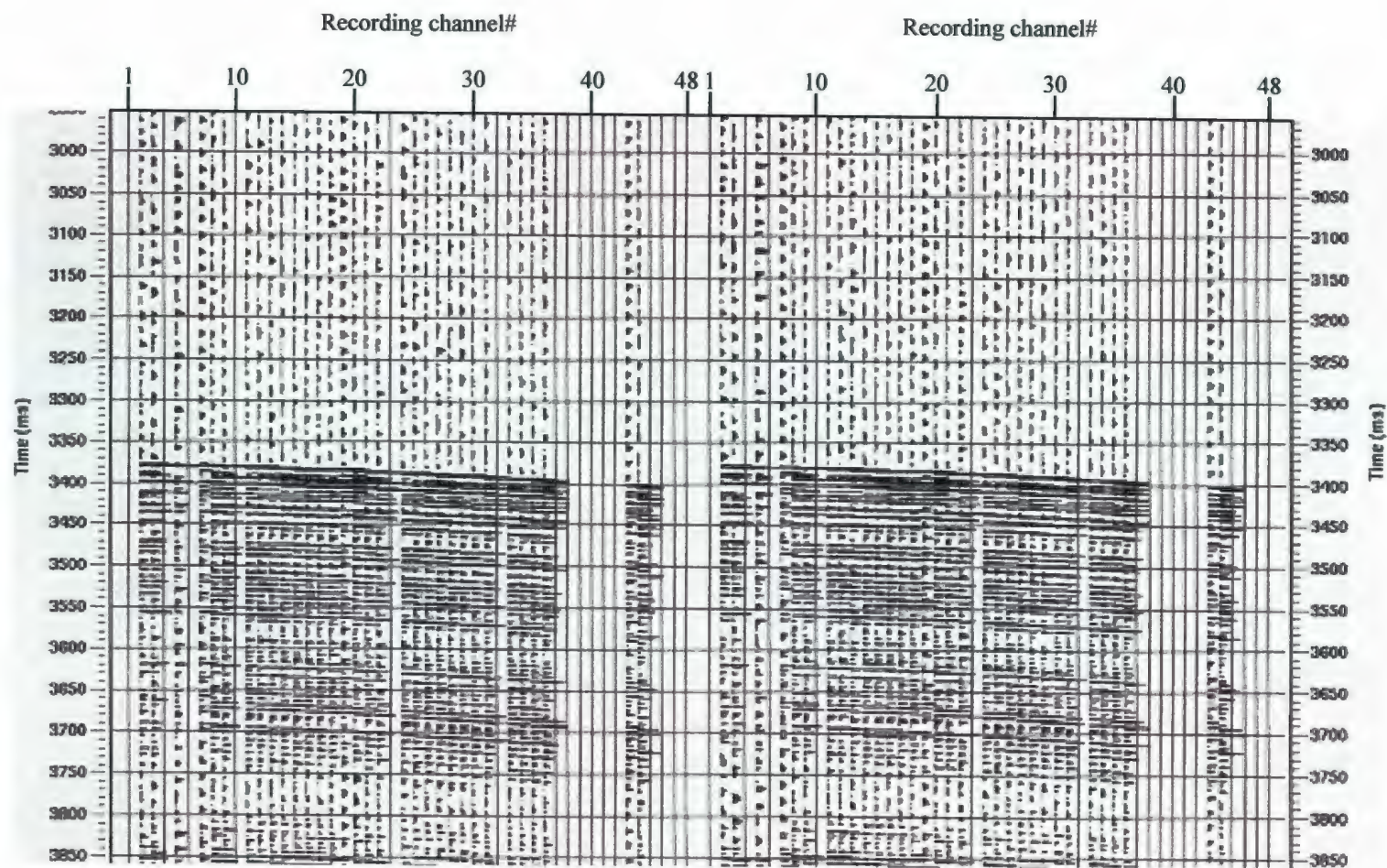


Fig.3.7. Two consecutive shot gathers in Fig. 3.5 after the application of Ormsby Bandpass Filter. Note that frequencies associated with noise are suppressed.

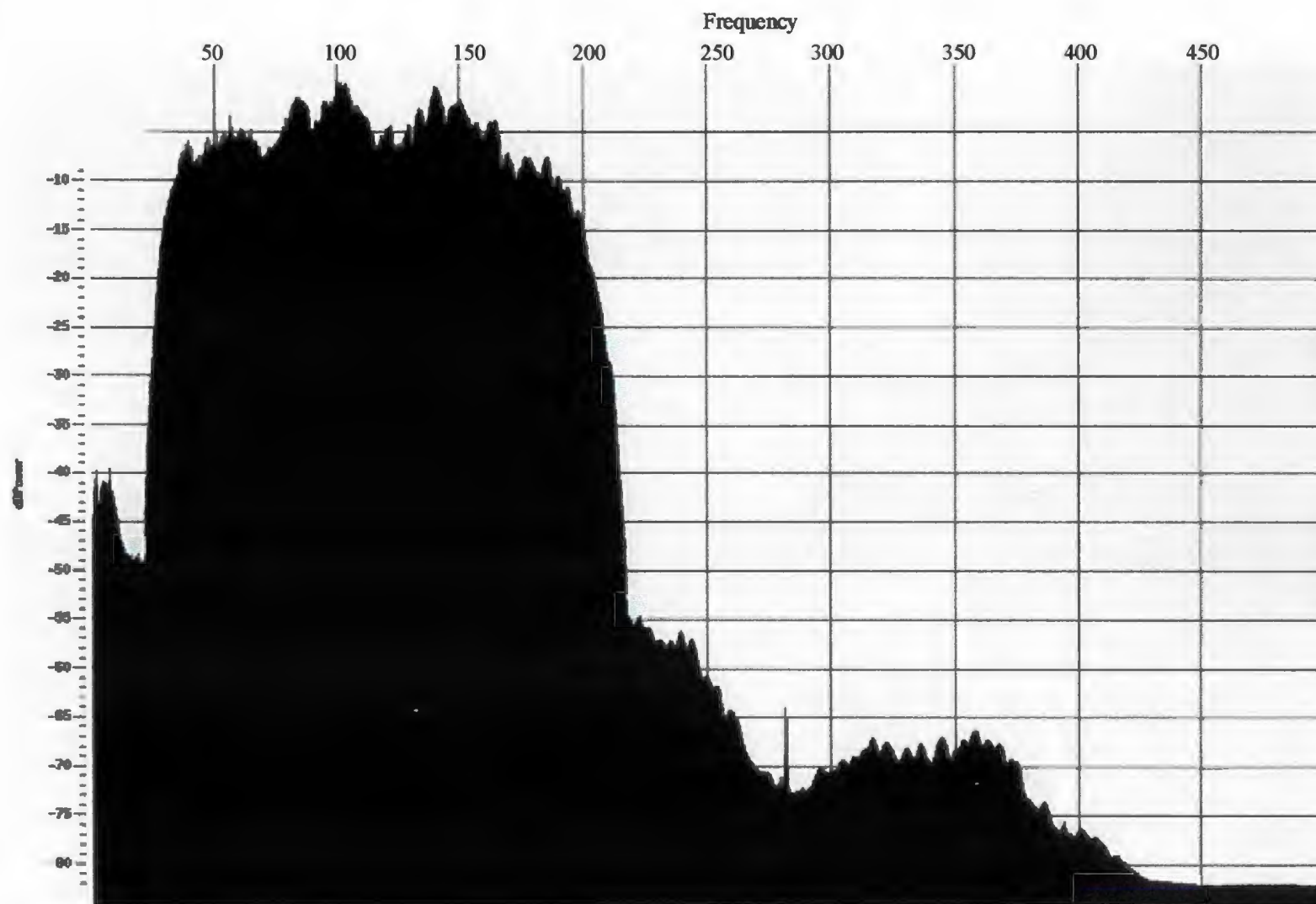


Fig. 3.8. Amplitude spectrum of the shot gathers shown in Figure 3.7.

Equation (3.6.2) shows that the magnitude of the normal moveout is directly proportional to the offset, x , and inversely proportional to velocity, v , and the vertical traveltime, t_0 . Thus, normal moveout is more pronounced for reflections associated with shallow reflectors as well as those received at far offsets.

The velocities that can be derived from seismic data are the root-mean-square (rms) velocities, which are related to the interval velocities in the Dix equation (Dix, 1981). NMO velocity, stacking velocity and rms velocities are considered equal in the case of a short spread length relative to the reflector depth. Velocity generally tends to increase with depth due to increasing confining pressure and increasing sediment density associated with dewatering and lithification. In addition, sediment type and porosity also affect the velocity. The less porous the medium, the higher the velocity (i.e., the velocity is higher in limestone than shale).

In order to increase the signal-to-noise ratio, a supergather with a set of adjacent CDPs that sample a full range of offsets is formed prior to the application of the velocity analysis. The range of velocities to be used in the analysis is limited by the minimum and maximum expected velocities. The maximum stacking velocity must be defined to include the high velocities associated with steeply dipping events and off-plane reflections. The distance interval for velocity analysis must be small enough to sample the lateral changes in the subsurface. Assignment of velocity functions to CDPs between the velocity pick locations are achieved by bilinear interpolation. The number of CDPs to sum in the gather, semblance, and velocity function stack panels, aims to maximize the signal-to-noise

ratio and to provide a viable vertical and horizontal resolution of the semblance peaks.

There are several methods used to derive stacking velocities from seismic data, including velocity spectrum (based on contoured semblance), common offset gathers and common velocity stacks (Fig. 3.9):

The velocity spectrum is determined by the measurement of coherency among the traces in a NMO-corrected CDP gather, using a range of constant velocities. The semblance method of measuring the coherency is performed by using the cross-correlation of traces in a CDP gather. The formula for semblance is given by

$$\text{Semblance} = \frac{\sum_{i=1}^N \left[\sum_{j=1}^M a_{ij} \right]^2}{\sum_{i=1}^N \sum_{j=1}^M a_{ij}^2}$$

where, a_{ij} corresponds to the amplitude of the i th time sample on trace j , N stands for the number of time samples and M is the number of traces. Because this technique is based on the correlation of traces rather than the lateral continuity of stacked events, the semblance velocity spectrum panel yields good resolution in both velocity and time and allows the identification of multiple reflections as well as providing a reasonable stacking velocity function. The display is usually in the form of semblance contours on a time-versus-velocity graph, where the peaks indicate the maximum coherence, from which the

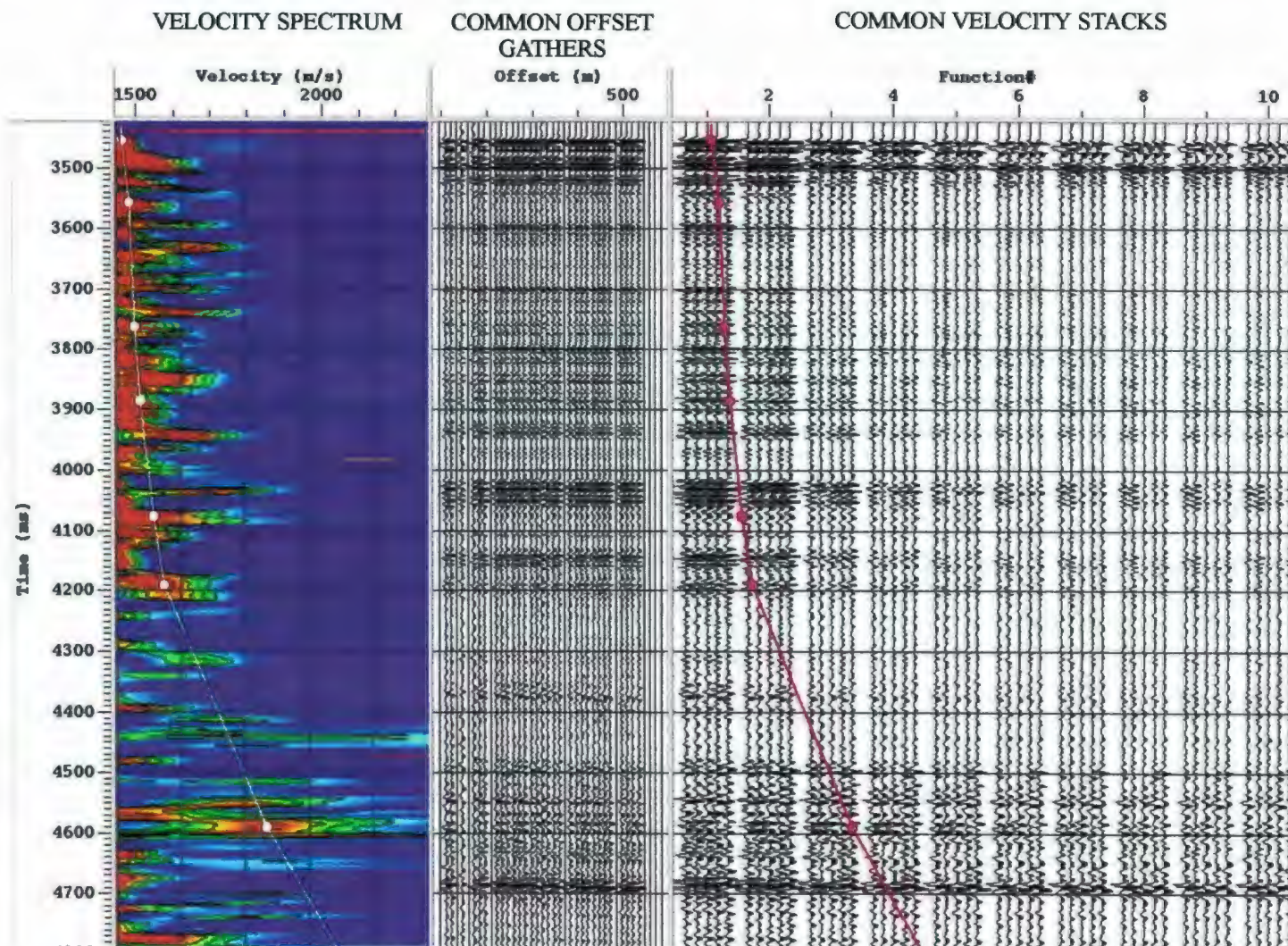


Fig. 3.9. Velocity analysis display showing the methods used to derive stacking velocities (e.g. velocity spectrum, common offset gathers and common velocity stacks).

optimum stacking velocities can be derived for an event at a given time. However, this technique does not give optimum results for data containing complex structures.

The gather panel is achieved by forming a common-offset-stacked gather of a number of CDPs and observing the effect of NMO correction using a specified range of velocities. If the velocities used in the removal of normal moveout are greater (or smaller) than the primary stacking velocities then hyperbolae corresponding to events appear undercorrected (or overcorrected) (Figs. 3.10 and 3.11). Finally, the velocities, which are able to flatten the hyperbolae on the gather are picked as the stacking velocities (Fig. 3.12). Note that multiple reflections are more distinguishable on the common offset gather compared to a stack. On the semblance panel, particularly at the portions where a decay in the resolution occurs, this property of gather panel is very useful in separating the peaks associated with the primary reflections from that of the multiple reflections.

The velocity function stack (VFS), also known as the constant velocity stack (CVS), is done by correcting the normal moveout of a specified number of CDPs using either a set of constant velocities or time-variant velocity functions and then stacking them. The stacked traces are then displayed on a time-velocity plot side by side. Consequently, the appropriate stacking velocities for each event are picked according to the events that stand-out with high amplitudes and show lateral continuity. Because the method uses the lateral continuity of the events, it works well for extracting the velocity function from the data containing complex geological structures.

The factors that control the accuracy of the velocity estimates are: (1) spread

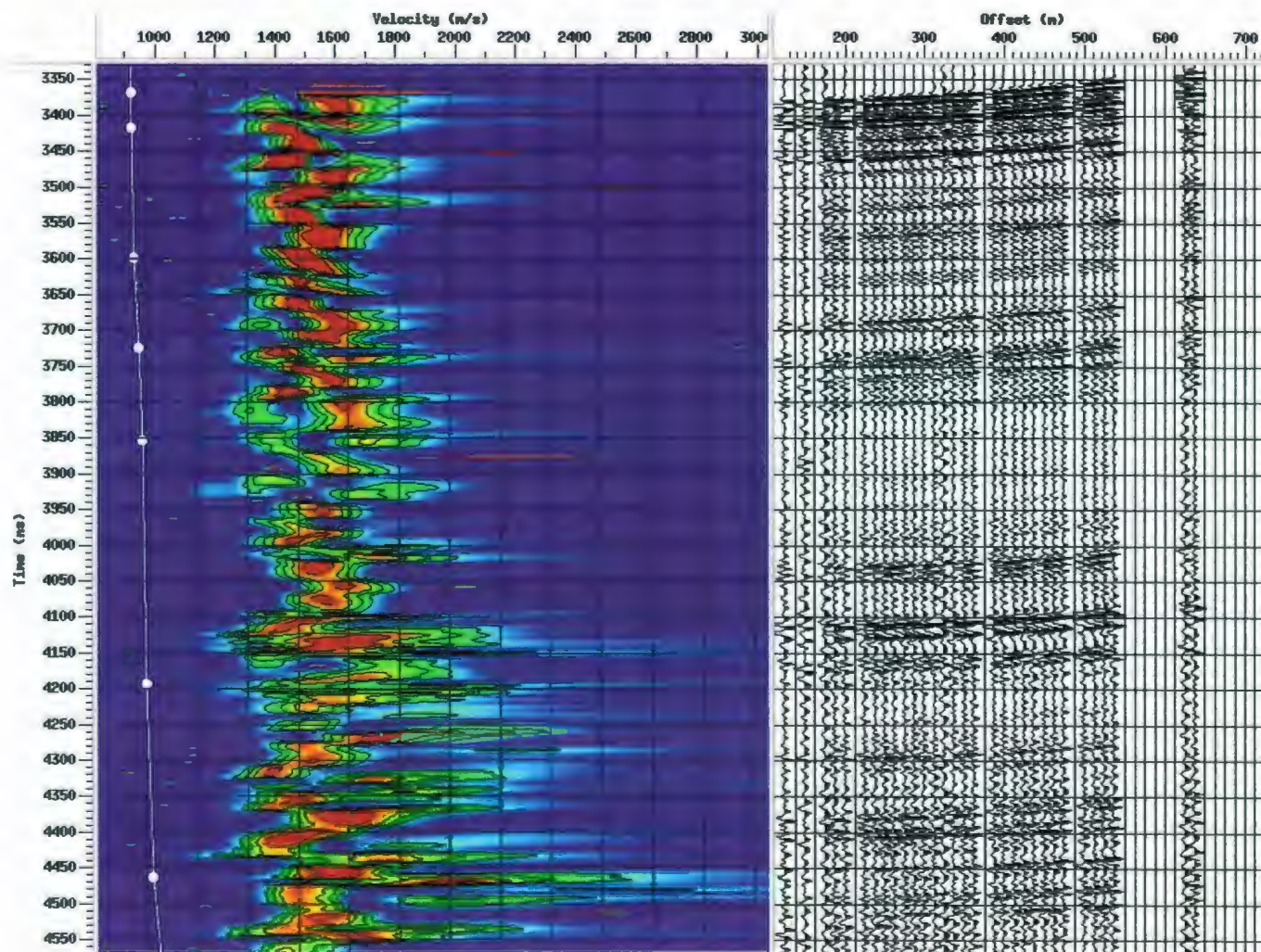


Fig. 3.10. Gather panel displayed next to the semblance panel. White line corresponds to the velocities. Note that the events on the gather panel appear overcorrected when velocities smaller than the primary stacking velocities are picked.

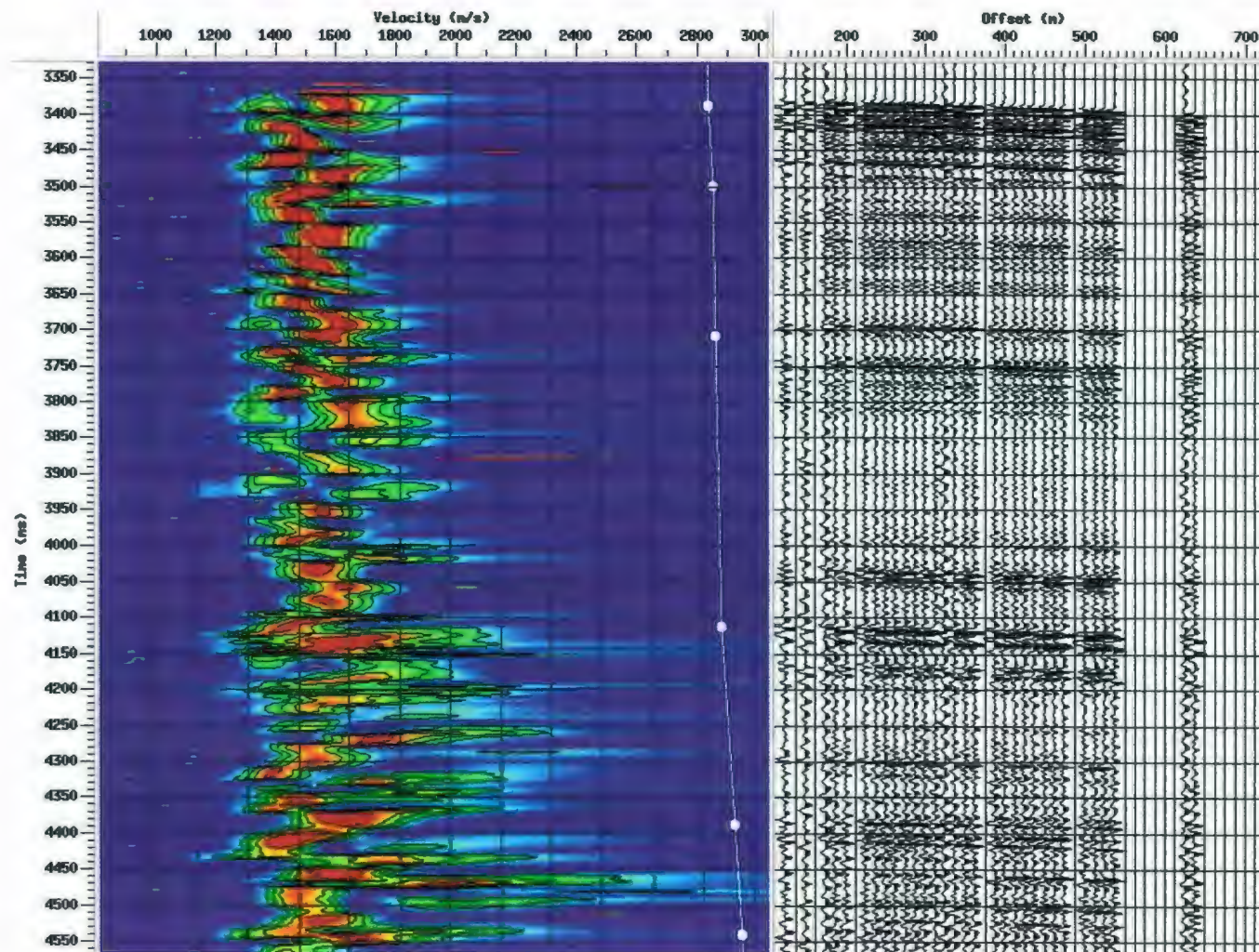


Fig. 3.11. Gather panel displayed next to the semblance panel. White line corresponds to the velocities. Note that the events on the gather panel appear undercorrected when velocities greater than the primary stacking velocities are picked.

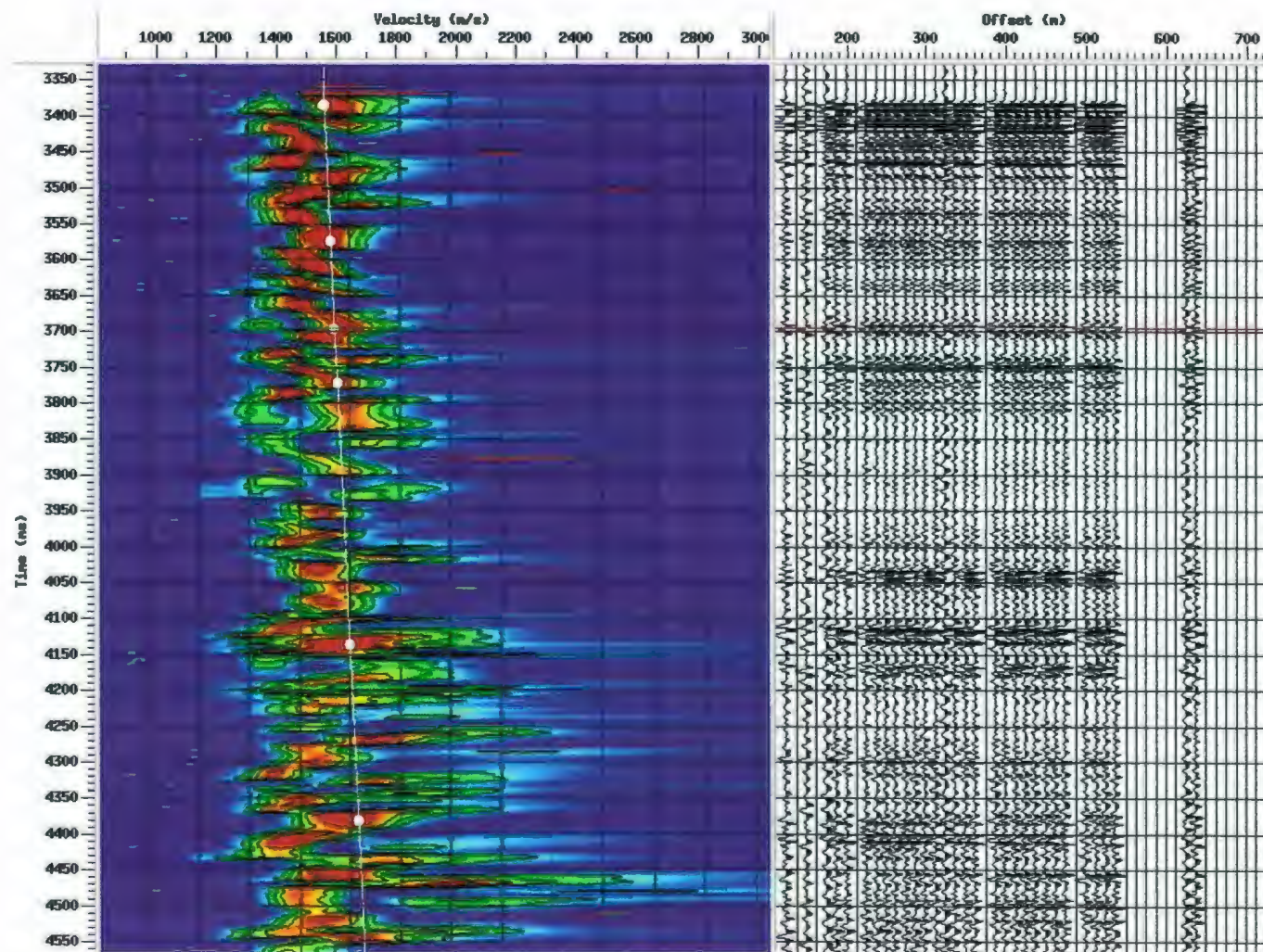


Fig. 3.12. Gather panel displayed next to the semblance panel. White line corresponds to the velocities. Note that the events on the gather panel appear flat when the primary stacking velocities are picked.

length, (2) stacking fold, (3) signal-to-noise ratio, (4) muting, (5) time gate length, (6) velocity sampling, (7) choice of coherency measure, (8) true departures from hyperbolic moveout, (9) bandwidth of data (Yilmaz, 1987). The velocity analysis is applied to filtered data because higher S/N yields better resolved peaks on the panels. Long offsets provide good velocity resolution because of the reasonable moveout and contribution from various offsets. However, the NMO stretch, a stretching of the waveshape yielding a decrease in the frequencies, occurs at far offsets as a result of NMO correction. It causes suppression of shallow events and thus, should be removed. While determining the optimum NMO stretch mute, it has to be considered that the more the data included into the stack, the higher the S/N, hence, the better the velocity resolution. In the absence of far offset data, a decrease in the velocity resolution occurs particularly at the deeper portions of the section where the moveout is small. For a good temporal resolution on the velocity spectrum, the time gate window length must be defined depending on the dominant period recognized. The velocity increment has to be small enough to sample every velocity variation in the data. The presence of distorted hyperbolae possibly originating from the complex structures also makes it difficult to pick the correct stacking velocities.

During the velocity analysis of the profiles from the Antalya Basin, a supergather including 5 CDPs was generated in order to increase the signal-to-noise ratio and to provide a viable vertical and horizontal resolution of the peaks. Figures 3.13a and 3.13b show two different velocity analysis panels calculated based on using a supergather of 20

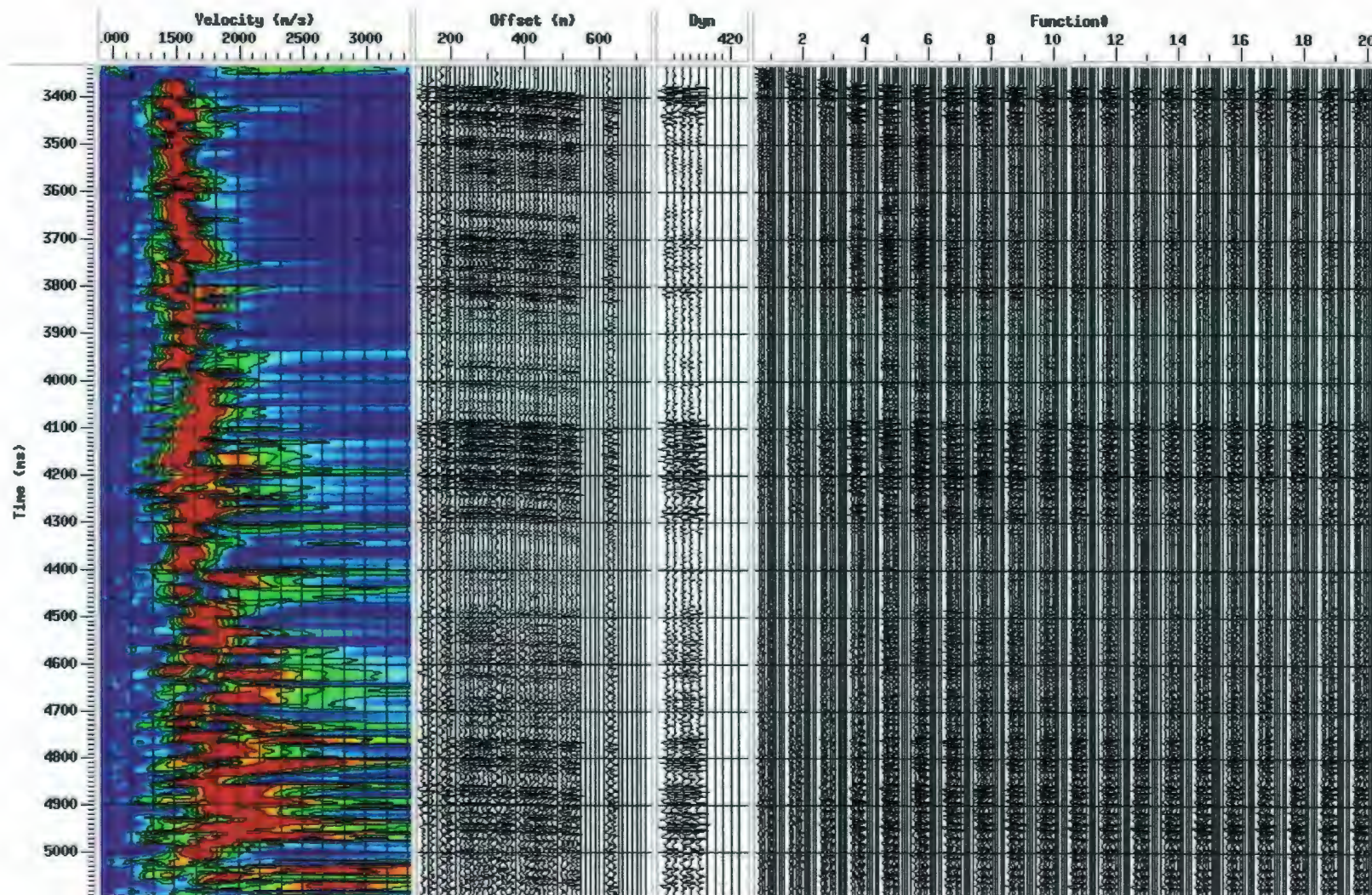


Fig. 3.13a. Velocity analysis display calculated by generating a supergather including 20 CDPs.

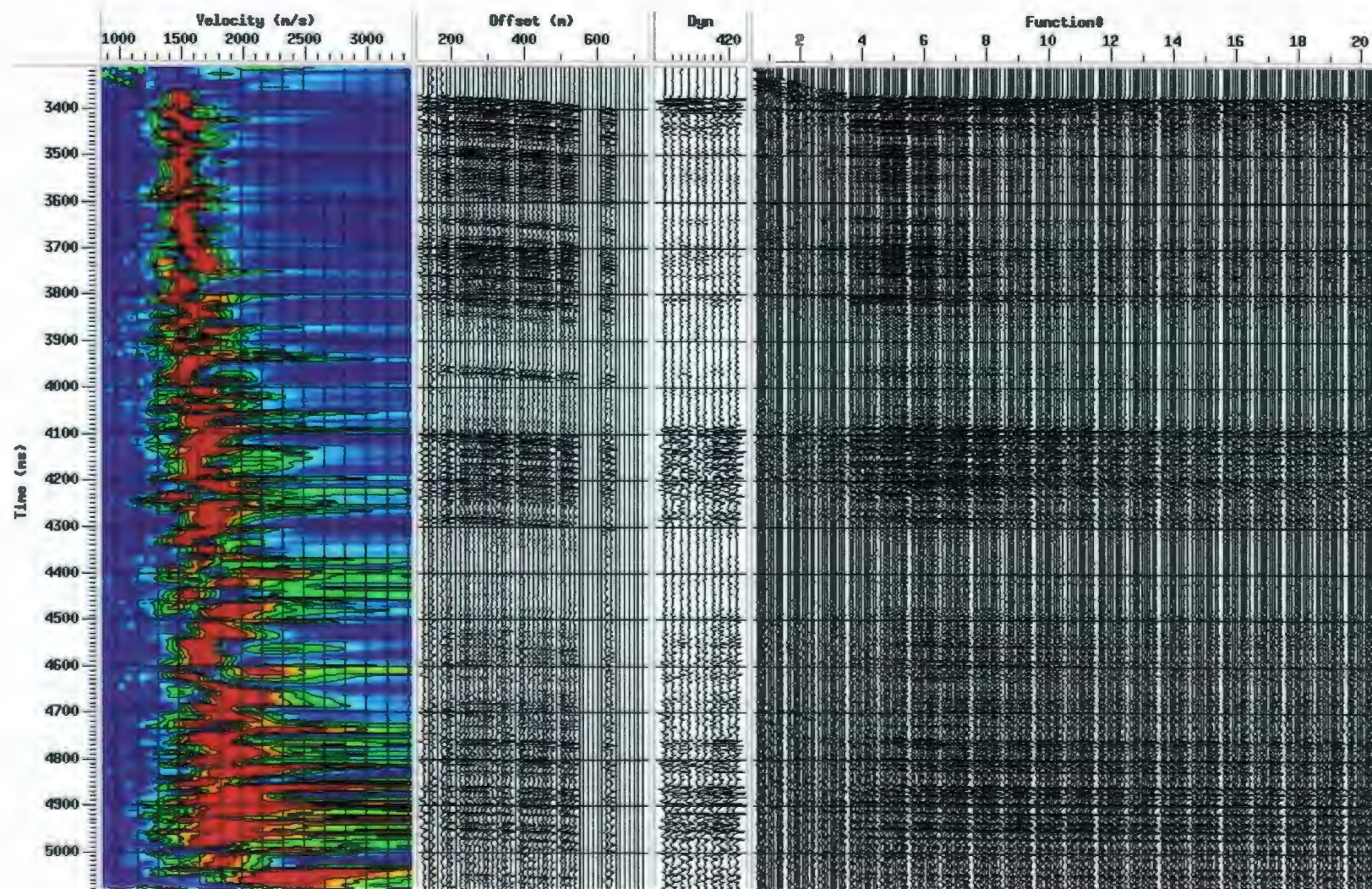


Fig. 3.13b. Velocity analysis display calculated by generating a supergather including 5 CDPs.

and 5 CDPs, respectively. Note the higher S/N and resolution on the panels corresponding to the supergather with 5CDPs. The minimum and maximum expected stacking velocities were defined as 1500 m/s and 3500 m/s, respectively. The lateral sampling interval was selected to be every 100 or 200 CDPs, depending on the complexity of the area. The semblance sample interval was selected as 5 ms, five times the temporal sampling rate of the dataset and the semblance calculation window, which controls the temporal smoothing, was defined as 10 ms. Consequently, the number of semblance calculations to perform in the specified velocity range was selected to be 500, and was increased in areas where more velocities were needed for a reasonable lateral resolution on the semblance panel. An automatic trace muting is performed to remove a more than 30 percent of NMO stretch at shallow times and far offsets.

The fact that the streamer length is very small compared to the water depth yields insignificant moveouts, resulting in an overall fairly broad range of velocities that are able to stack the events. The velocity analysis panels corresponding to the 48-channel 2001 data and the 16-channel 1992 data are displayed in Figures 3.14 and 3.15, respectively. On the 2001 data, the sharp semblance peaks, the well aligned hyperbolas on the gather panel and the high amplitude, continuous appearance of events on VFS panel, are recognized in the shallow portions of the data due to greater moveout at shallow depths. Note the continuous decrease in velocity resolution starting at 3950 ms and extending to 4700 ms (Fig. 3.14). The stacking velocities below this time are represented by very broad semblance peaks and by the events that hardly show any alignment on the gather and VFS

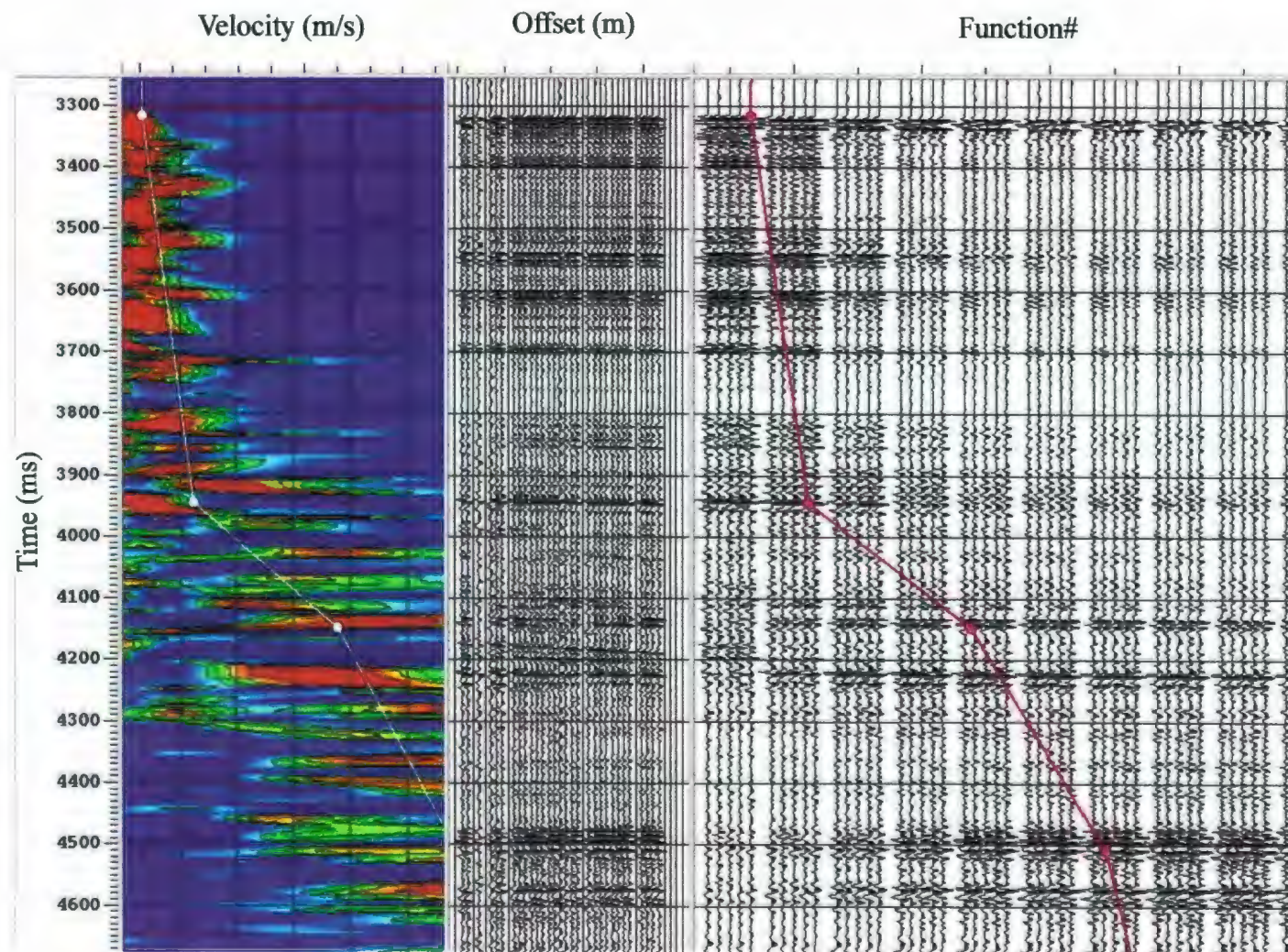


Fig. 3.14. Velocity analysis display corresponding to the 48-channel 2001 data.

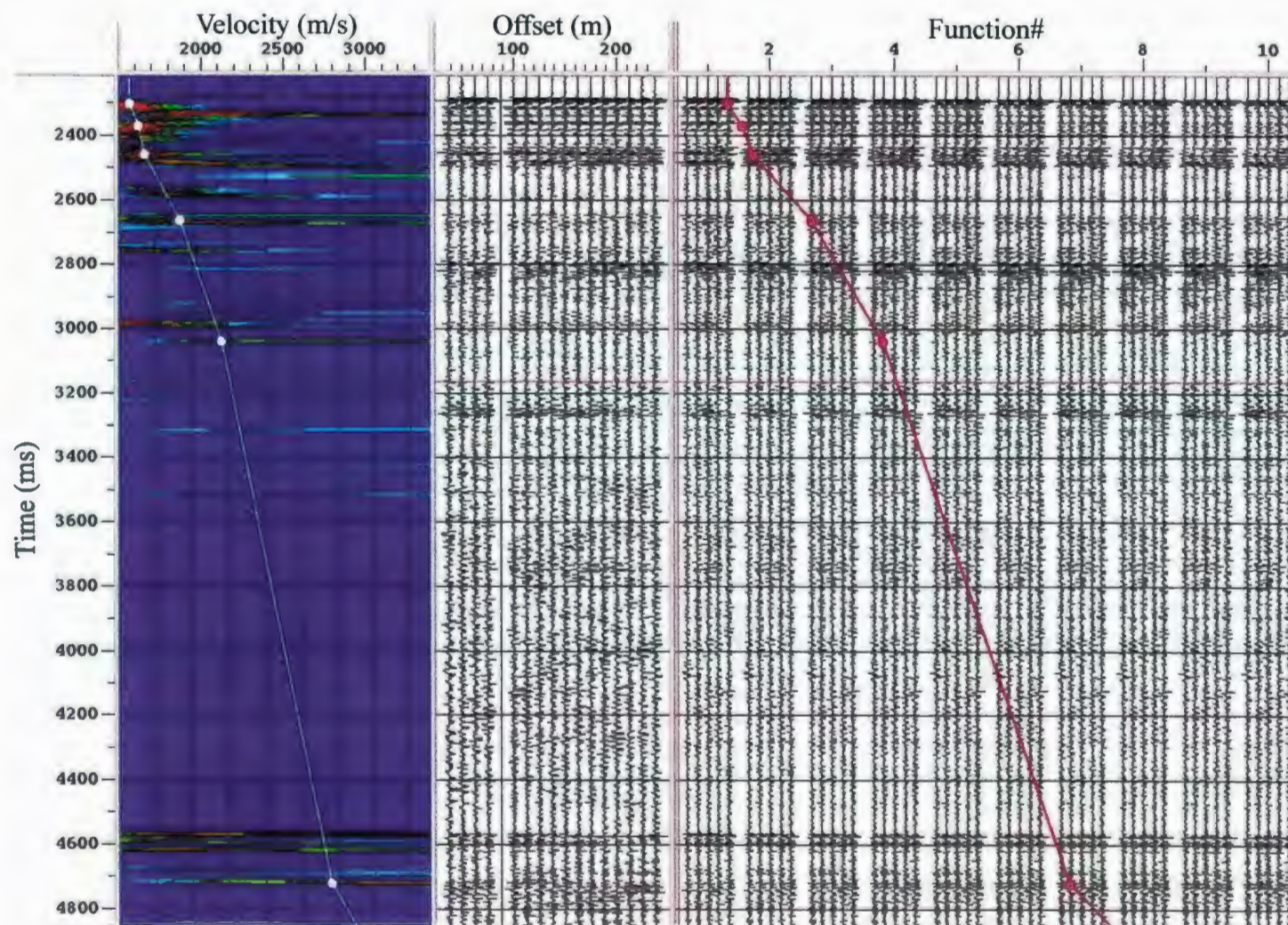


Fig. 3.15. Velocity analysis display corresponding to the 16-channel 1992 data.

panels. On the 1992 data, the offset is too short to recognize any significant variations in NMOs, hence, the resolution on the panels is fairly poor even in the shallow portions (Fig. 3.15).

3.7. Common Midpoint (CMP) Stacking

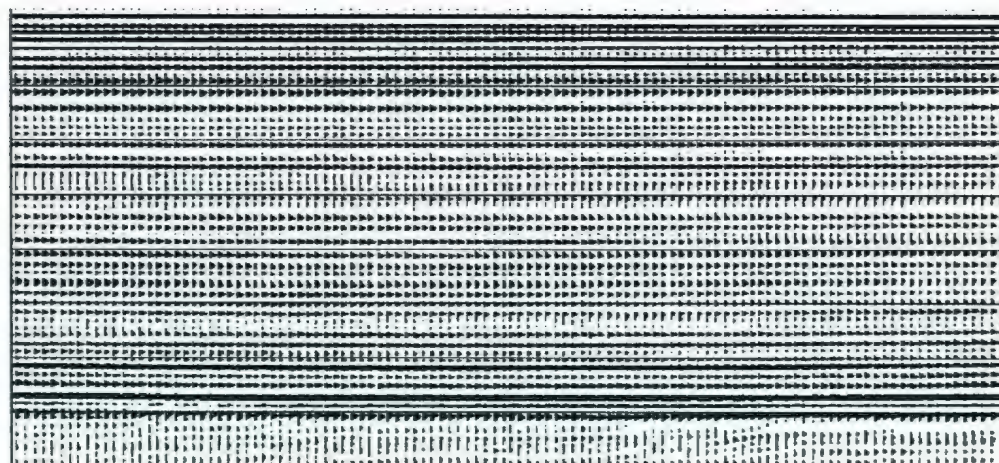
Common midpoint stacking is based on summing the traces in a NMO-corrected CMP gather, in which each primary reflection should occur at the same time on each trace. The traces in a CMP gather corresponding to various offsets are summed at each time sample to give a single trace, equivalent to zero offset, on the stacked section. The most common trace summing technique, mean amplitude summing, involves calculating the mean value of the amplitudes at each temporal sampling interval among the traces within a CMP gather. The mean is given by

$$\text{Mean}(t) = \frac{1}{N} \sum_{i=1}^N s_i(t)$$

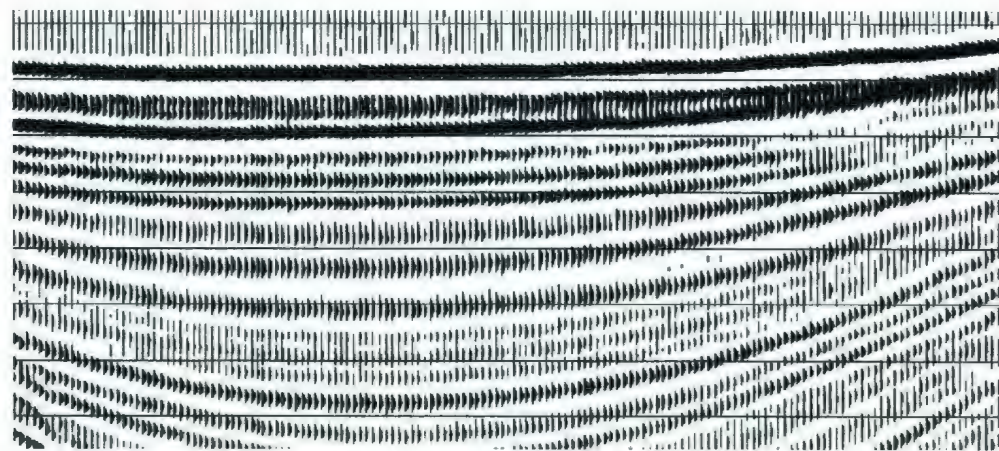
where $s_i(t)$ stands for the sample amplitude on trace i , at a given two-way-travel time, t , and N represents the multiplicity. Here, normalizing the sum with the scalar of $1/N$ aims to preserve the reflection amplitude levels during stacking. There are other methods such as median and weighted trace summing, which may also be used depending on the noise level of the data.

Stacking is one of the most efficient steps in data processing in terms of improving the data quality. It not only compresses the dataset but also attenuates both random and coherent noise. The primary reflections tend to have less NMO than the multiple reflections. For a primary and multiple reflection arriving the receiver at zero offset at the same time, the NMO of the primary reflection is less than the multiple because a greater portion of the travel path of a multiple reflection is confined to the shallow part of the subsurface. Hence, its propagation velocity is lower compared to the primary reflection, which penetrates into the deeper, higher velocity media. As a result of NMO correction using the velocities estimated via velocity analysis, the hyperbolae corresponding to the primary reflections are flat in time while the multiple reflections remain undercorrected. During CMP stacking, the aligned primary reflections will add up constructively, yielding high amplitudes, while the undercorrected multiple reflections will not show amplitudes that stand out on the stacked section. The random noise, because of its uncorrelable character from trace to trace, will also be attenuated by the stacking process (i.e., the signal-to-noise ratio being enhanced by $n^{1/2}$, where n is the stacking fold).

A near trace gather and a stack section of a range of shots are displayed in Figure (3.16). Note that, on the stack section reflectors stand out more distinctly and an improvement in the signal-to-noise ratio is recognized.



(a)



(b)

Fig. 3.16. (a) A near trace gather and (b) a stacked section.

3.8. Migration

3.8.1. General Overview

On a stacked seismic image, dipping reflectors appear at slightly incorrect locations with respect to the location of the sources and receivers, and diffraction hyperbolas occur where there are discontinuities along the reflectors. Migration is the processing technique used for moving these reflectors to their true subsurface locations and collapsing the diffraction hyperbolae, which as a result produces a seismic record with a reasonable spatial resolution that accurately illustrates the geological setting of the subsurface (Figs. 3.17 and 3.18). A dipping reflector, when migrated, moves in the updip direction and appears steeper and shorter. Synclines are represented by bowties on the stacked sections if their curvature is greater than that of incident wave fronts. Migration restores these bowties to synclines by moving the flanks in an updip direction (Figs. 3.19-3.22). When migrated, anticlines become smaller while synclines broaden. The size of the migrated structures is constrained by the velocities used for migration (i.e. the higher the velocities, the more the migration, and hence, the more pronounced the updip displacement). The lateral and vertical displacements of reflectors that occur during migration have to be taken into consideration while determining the profile length and recording time. If either of them is too short, then, the true or pseudo locations of the reflectors may not be represented on the seismic section due to limited imaging space.

The accuracy of the migration is controlled by a number of factors such as: the proximity of stacked section to zero-offset section, the S/N, and the quality of the

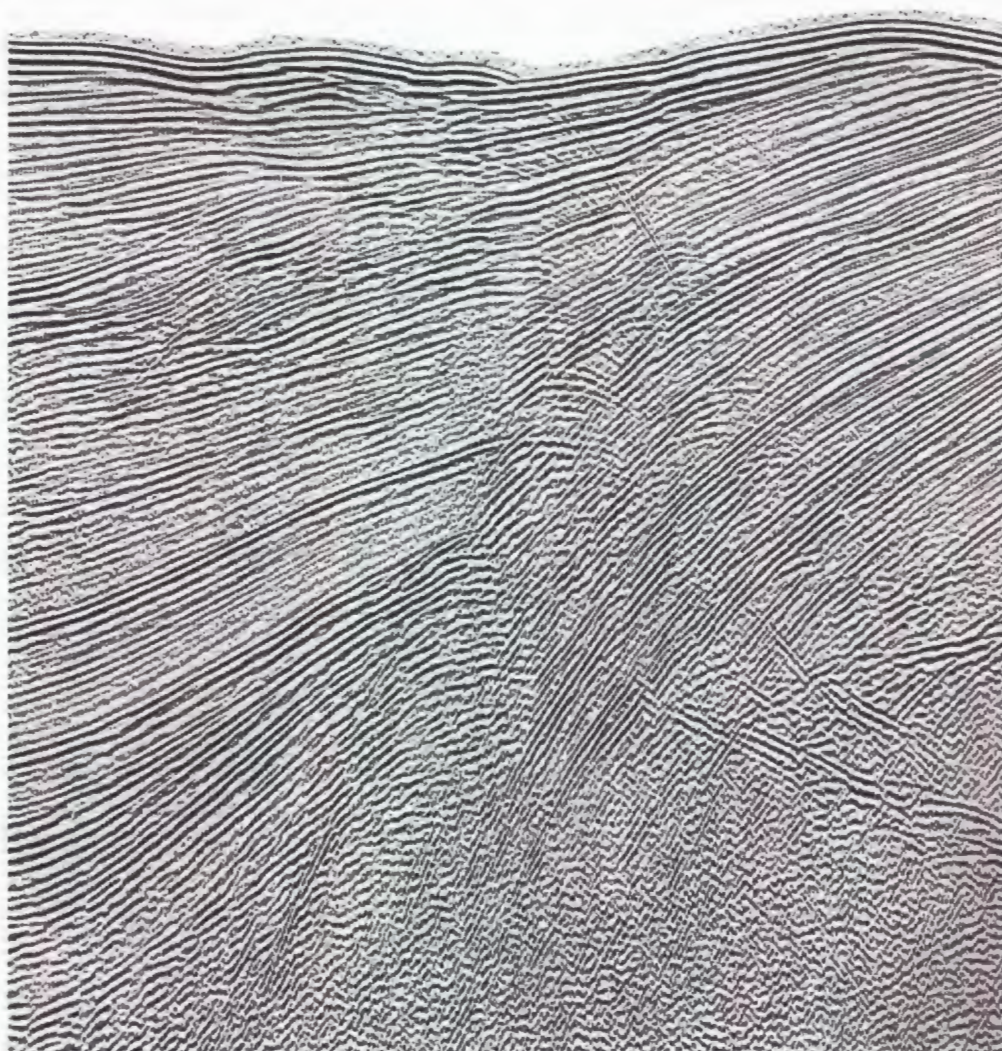


Fig. 3.17. Stacked seismic reflection profile. Note several diffraction hyperbolae concentrated in the central portion of the profile.

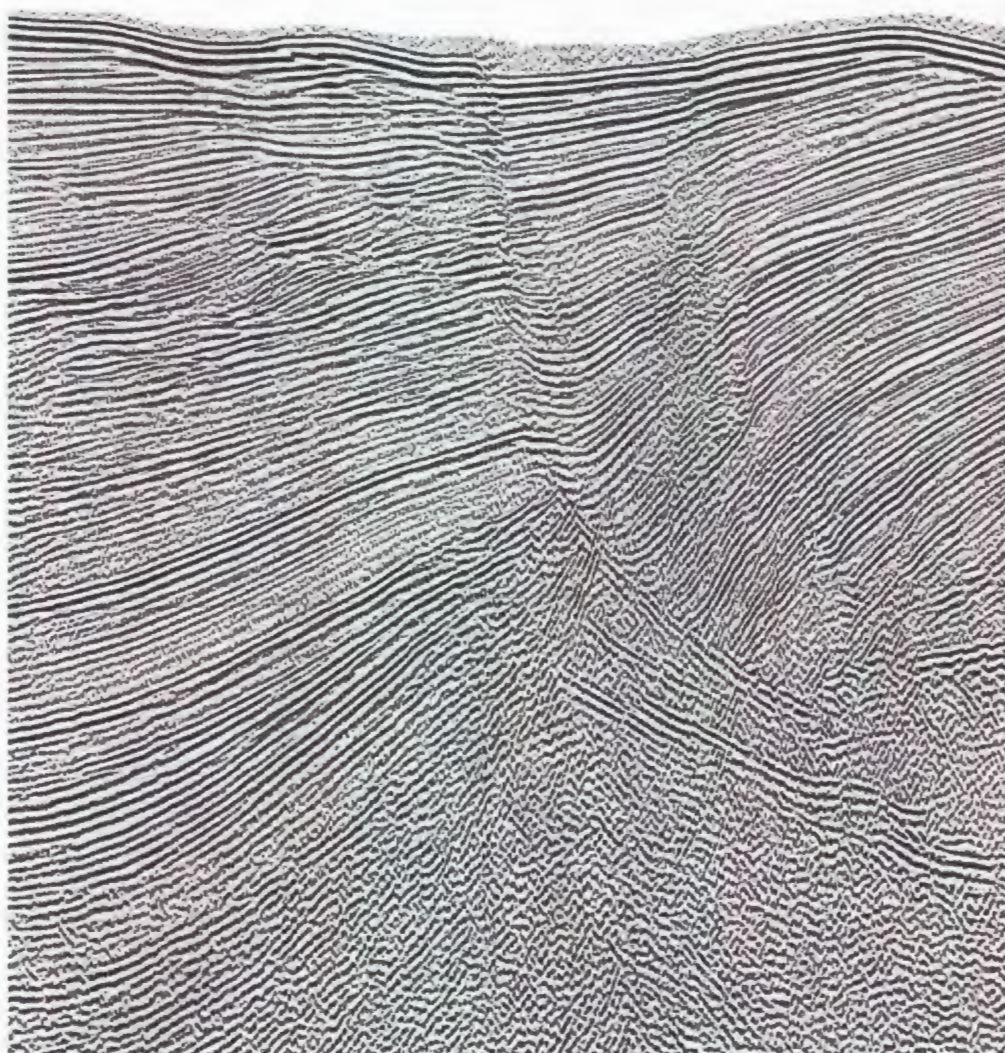


Fig. 3.18. Seismic reflection profile shown in Figure 3.17 after the application of Kirchhoff Time Migration. The diffraction hyperbolae are collapsed and the reflector discontinuities representing faults are clearly imaged.

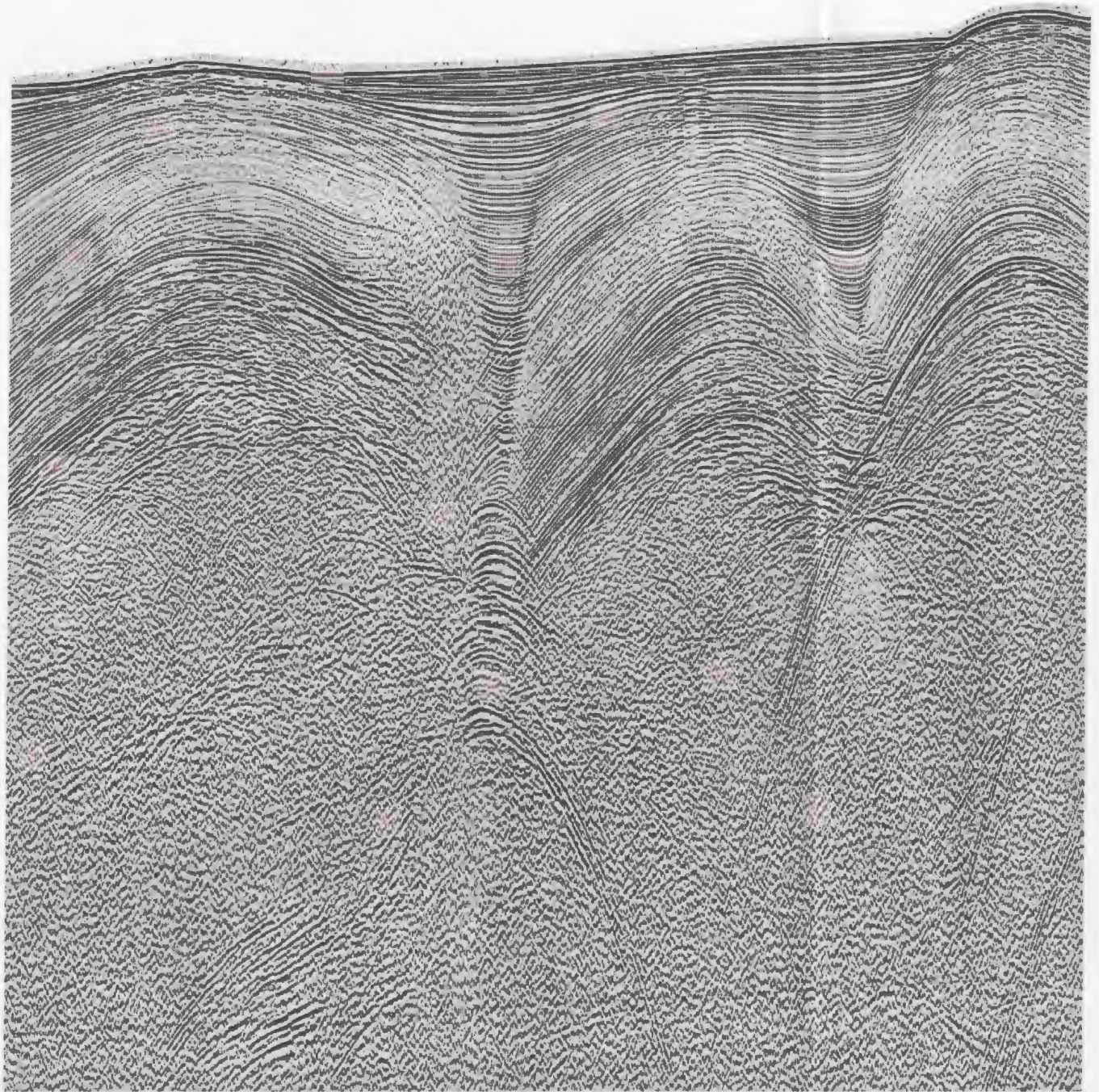


Fig. 3.19. Stacked seismic reflection profile. Note the presence of bowtie geometries.

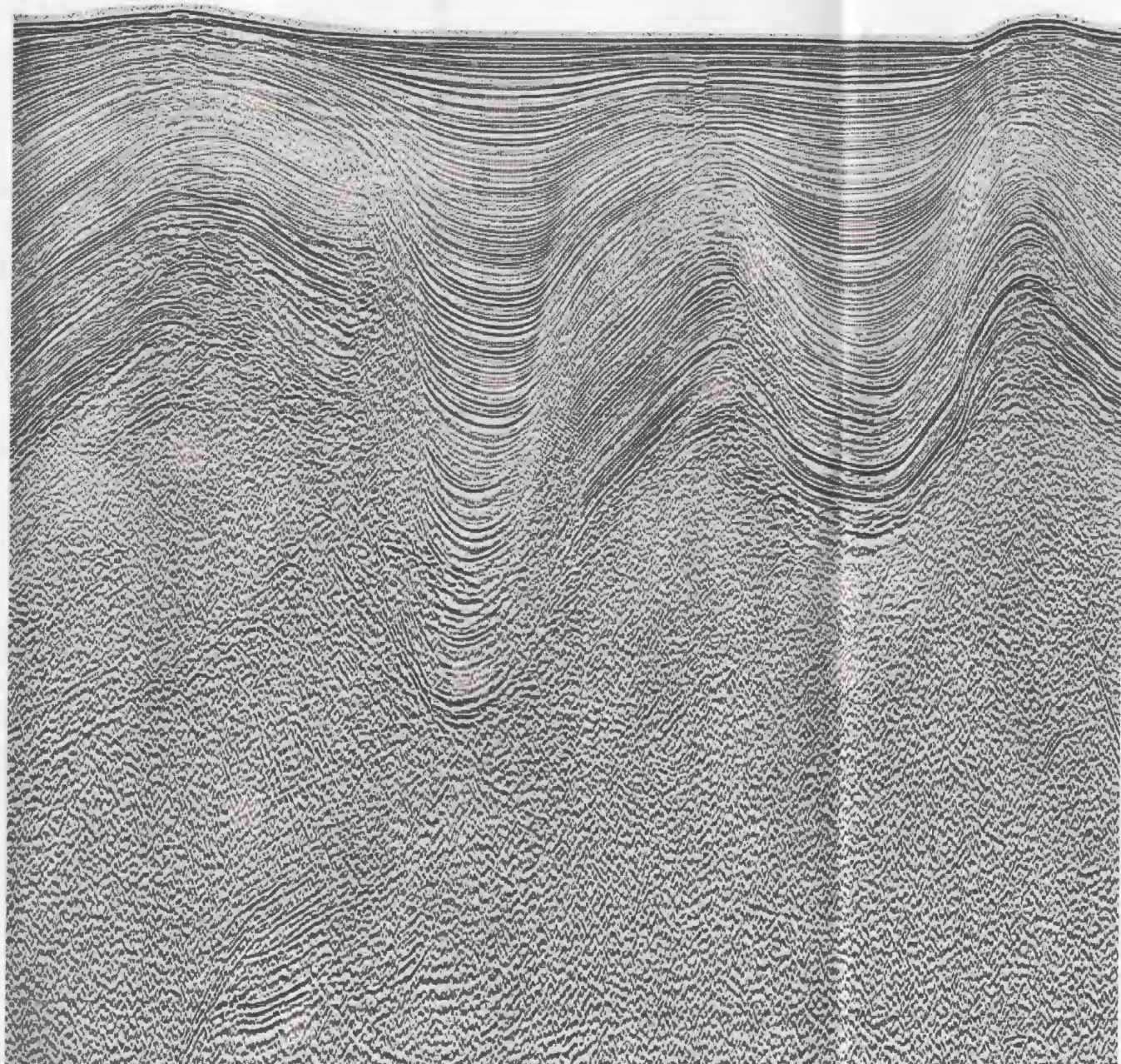


Fig. 3.20. Seismic reflection profile shown in Figure 3.19 after the application of Kirchhoff Time Migration. Bowties are restored to synclines. Also note that the anticlines appear smaller while the synclines are broader.

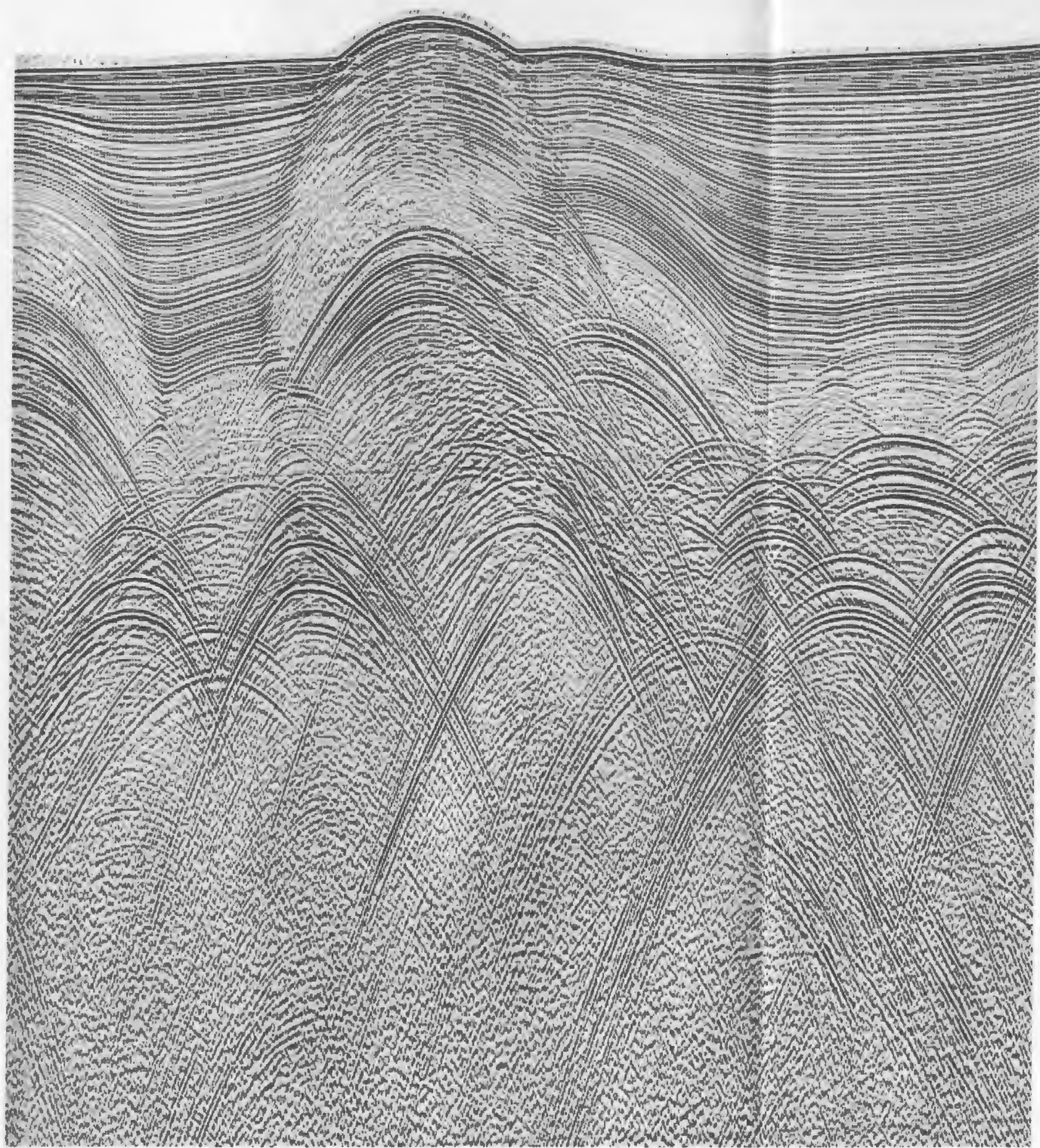


Fig. 3.21. Stacked seismic reflection profile. Note the presence of bowtie geometries.

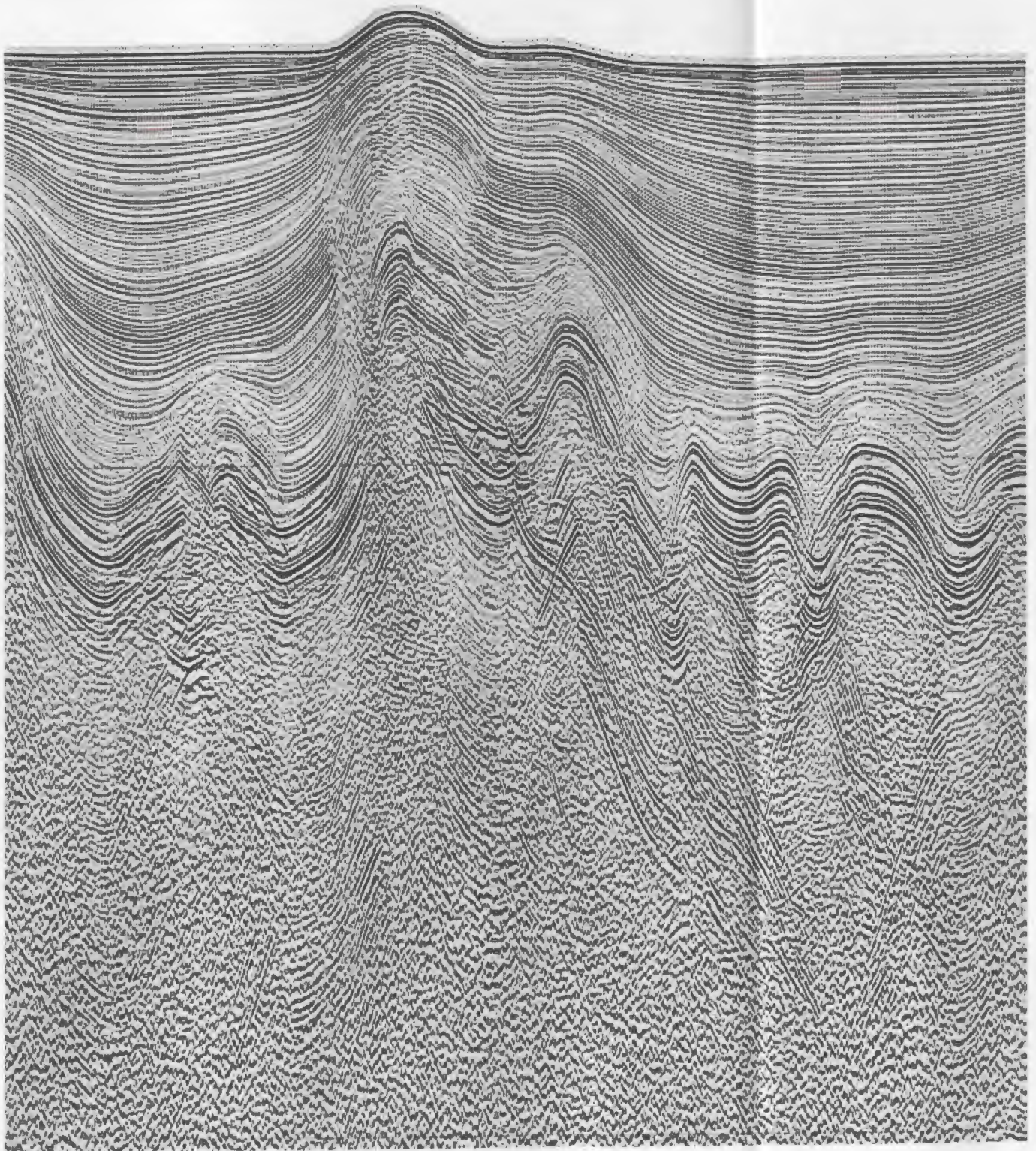


Fig. 3.22. Seismic reflection profile shown in Figure 3.21 after the application of Kirchhoff Time Migration. Bowties are restored to synclines. Also note that the anticlines appear smaller while the synclines are broader.

velocities used during migration. The technique is based on the assumption that the stacked section is equivalent to a zero-offset section. However, in the presence of strong multiples and conflicting dips, this assumption is no longer valid. Thus, a decay in the efficiency of the migration occurs. Migration does not make a distinction between the primary reflections and noise, hence, when a seismic section is migrated all events undergo the same process. In datasets with low S/N, the migration of the noise component, particularly at deep portions, results in the generation of smearing effects, which in turn, decreases the spatial resolution. The precision of stacking velocities estimated through velocity analysis are generally limited due to several reasons as mentioned in the previous section. Furthermore, migration velocities, represented by the medium velocities, may vary from the stacking velocities (i.e. dipping events and off-plane diffractions require higher velocities than the medium velocities to stack properly)

Migration can be performed either before or after stacking as well as in several domains, such as space-time, space-frequency, wave-number-time or wave-number-frequency. Migration before stack is performed on common-offset gathers and has the ability to migrate the events of different dips arriving at the same time. However, the sensitivity to lateral velocity variations and the high computational time it requires, makes migration before stack less favored than migration after stack. Additionally, migration before stack is most needed in areas with conflicting dips, where the assumption of proximity of a stacked section to a zero-offset section is likely to be violated. Above all, having a stacked section to compare with the migrated section is helpful because the

velocities used during migration are not highly reliable. Depth migration has the ability to yield good results in areas with strong lateral velocity variations. However, it is very sensitive to velocity errors compared to migration in the time domain. Therefore, if the estimated velocities are not highly reliable, which is usually the case, then time migration tends to give better results. Figure 3.23 summarizes the most commonly used post-stack migration techniques with their particular advantages and disadvantages.

3.8.2. Kirchhoff Time Migration

Kirchhoff migration is an integral solution to the wave equation, hence, is considered as a wave equation migration technique. It uses an exploding-reflector model recording geometry equivalent to a zero-offset recording geometry, where the exploding sources are located along the reflectors while the receivers are at CMP locations distributed along the profile on the surface. Note that, the recorded time for zero-offset seismic record is two-way-traveltime while for exploding-reflector model seismic record it is one-way travel time. To make these recording geometries comparable, one can use the half of the true medium velocity for the exploding-reflector model.

A scalar wave equation for the exploding-reflector model is given by,

$$\frac{\partial^2 u}{\partial x^2} + \frac{\partial^2 u}{\partial z^2} = \frac{1}{v_h^2} \frac{\partial^2 u}{\partial t^2}$$

Migration Name	Category	Type	Velocity	$V_{(x)}$	$V_{(v/z)}$	Steep Dip	Run Time
Memory Stolt F-K	F-K	Time	$V_{RMS}^{(x,t)}$	Poor	Poor	Fair	0.2
Phase Shift	Phase Shift	Time	$V_{INT}^{(t)}$	None	Good	Good	1.0
Steep-Dip Explicit FD	F-D (70 deg)	Time	$V_{INT}^{(x,t)}$	Fair	Good	Good	21.0
Time	(50 deg)	Time	$V_{INT}^{(x,t)}$	Fair	Good	Fair	10.0
Fast Explicit FD Time	F-D	Time	$V_{INT}^{(x,t)}$	Fair	Good	Fair	9.6
Explicit FD Depth	F-D	Depth	$V_{INT}^{(x,z)}$	Good	Good	Good	21.7
Kirchhoff Depth	Kirchhoff/Im	Depth	$V_{INT}^{(x,z)}$	Fair	Good	Good	7.3
	Explicit	Depth	$V_{INT}^{(x,z)}$	Good	Good	Good	12.0
	Mult. Arr.	Depth	$V_{INT}^{(x,z)}$	Excel.	Excel.	Excel.	64.0
Kirchhoff Time	Kirchhoff	Time	$V_{RMS}^{(x,t)}$	Fair	Good	Good	14.6
Reverse-Time T-K	Reverse Time	Time	$V_{INT}^{(t)}$	None	Good	God	2.5

Fig. 3.23. Chart summarizing the character of poststack 2D migration techniques (modified from Yilmaz, 1985).

where v_h is equivalent to the half of the medium velocity. This equation is based on the assumption that the medium consists of horizontal and flat layers and that there are no lateral velocity variations. The stacked seismic data represent the value of the generated wavefield at the surface and the related function is given by $u(x,0,t)$. Having recorded $u(x,0,t)$, one can calculate the wavefield function recorded using the exploding-reflectors model at a depth of z , which is $u(x,z,t)$. Here, the method used for obtaining $u(x,z,t)$ is called wavefield extrapolation. At $t=0$, the wavefronts have the same shape as the reflectors according to Huygens' principle and a distortion in the resemblance is observed for higher values of t . Setting $t=0$ in $u(x,z,t)$, which means extrapolating the wavefield backward in time to $t=0$, gives the migrated depth-section represented by $u(x,z,0)$. Conversion to a migrated time section can simply be done by replacing z with $vt/2$.

An hyperbola in the $x-t$ (time) domain corresponds to a point in $x-z$ (depth) domain for constant velocity isotropic medium. The reflectors in the time domain are considered to be consisting of adjacent points that act as Huygen's secondary sources, each represented by a hyperbolic traveltime trajectory. On a CMP-stacked dataset, it is possible to calculate the diffraction hyperbola at a given sample point on a trace by using the appropriate velocity function. Assuming a horizontally layered velocity model, the velocity function used to compute the traveltime trajectory is the rms velocity at the apex of the hyperbola at time $t(0)$ (Yilmaz, 1987). Kirchhoff time migration (diffraction summation migration) is based on summing the trace values along the diffraction hyperbolas that are generated at each diffraction point on the reflectors and consequently,

collapsing them so that the sums are placed at the apexes (Fig. 3.24). The result of the summation along the hyperbola which is placed at the apex appears as a large amplitude point on the migrated time section, if the apex is a reflector point in depth. If not, then, the random values of points on traces along the hyperbola tend to cancel each other as a result of summing. By migrating the sample points at each datum on the time section, one obtains a migrated time section. The depth section can be obtained simply by performing a time to depth conversion.

The Kirchhoff time migration technique is based on the assumption that the media of interest consist of horizontal layers with no lateral velocity variations and the stacked section to be migrated is equivalent to a zero-offset section. However, it does not mean that the technique is not applicable to the subsurface which is both vertically and laterally inhomogeneous. Because, due to the random distribution of the reflector dip values, the errors caused by the assumption of horizontal layers are likely to cancel each other statistically.

The aperture width is defined as the lateral extent of a diffraction hyperbola. It is ideally defined to be larger than twice the horizontal distance of migration of the steepest dip (Yilmaz, 1987). In the case of small aperture width, the steep flanks of the diffraction hyperbola will not be spanned and migration will behave as a dip filter, discriminating against steep dips. Whereas, if the aperture width is too large, then, the steeply dipping random noise will be included in the migration and will be displaced in an updip direction, which in turn, will result in decreasing the quality of the overlying data. Thus, data with

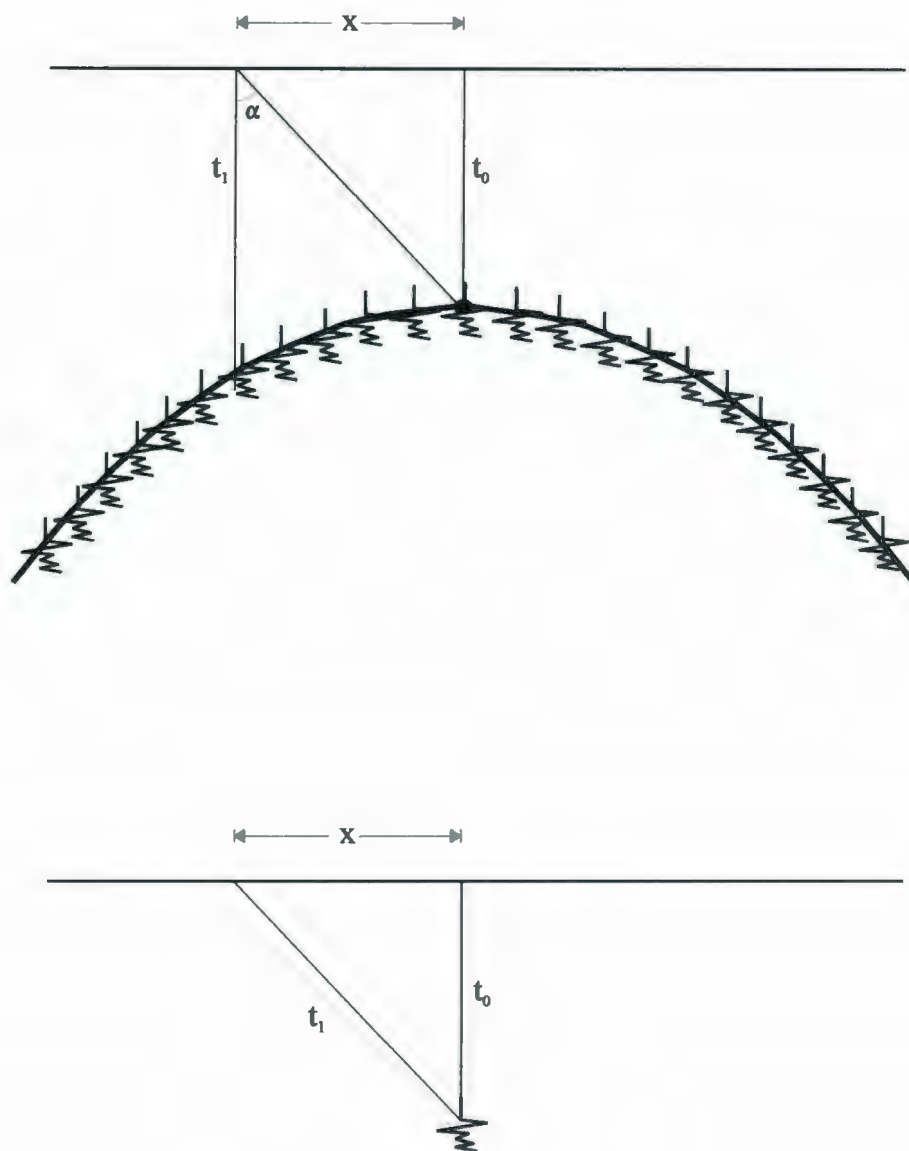


Fig. 3.24. Principle of Kirchhoff Time Migration. Trace values along the diffraction hyperbola are summed and placed at the apex (modified from Yilmaz, 1987).

low S/N is more sensitive to deviations from the appropriate aperture width. The velocity of the medium and the maximum dip to migrate constrain the aperture width (i.e. the higher the velocity, the larger the aperture width, the smaller the dip to migrate, the narrower the aperture width). Therefore, deep events require wider aperture compared to shallow events with the same dip, in the usual case of velocity increasing with depth.

The Kirchhoff migration algorithm applies amplitude and phase corrections compensating for several attenuation mechanisms including the spherical divergence to enable equal contribution to summation along the hyperbolic trajectory from events appearing at various travel times. The technique has the advantages of: (1) migrating events with steep dips up to 90° , (2) can handle moderate lateral velocity variations, (3) is efficient when velocity varies vertically.

During the migration of the Antalya Basin profiles, the Kirchhoff time migration was performed. The stacking (or rms) velocities obtained through velocity analysis, when used in migration, resulted in overmigrated hyperbolas particularly at deeper portion of the section. The appropriate migration velocities, which were successful in collapsing the hyperbolas, were determined by performing a number of tests. It was not possible to suggest a regular percentage to be subtracted from the stacking velocities to achieve the migration velocities. Instead, migration velocities were assigned based on their ability to attenuate the diffraction hyperbolas, at each sample point on the selected CDPs.

CHAPTER 4. Seismic Stratigraphy and Chronology

The Antalya Basin seismic profiles show four seismic stratigraphic units defined by distinct reflectors. The age of these units are determined by incorporating the exploration well data provided by Turkish Petroleum (unpublished data; see Fig. 1.3 for the location of the wells) and by seismically correlating with the units in the adjacent areas (i.e. Adana, Mesaoria, Iskenderun, Cilicia, Latakia and onland Antalya Basins).

4.1. Unit 1: Pliocene-Quaternary

Unit 1 comprises the youngest succession recognized within the Antalya Basin. It is seismically characterized by strong reflections, which suggest high acoustic impedance differences (Fig. 4.1). The reflectors within the succession are considerably continuous and parallel, and can be traced throughout the profiles. A distinct reflector, named as the "M reflector" by Ryan (1969), forms the lower boundary of the sequence. A subunit with a weak, transparent and discontinuous seismic expression is recognized at the base of the Pliocene-Quaternary package.

The thickness of Unit 1 varies significantly through the study area. It is thickest along the center of the basins and shows thinning towards the bathymetric highs and the Turkish coast. The reflectors mostly show onlap against these bathymetric highs as well as the underlying Miocene and older successions. The basal transparent subunit can be traced along the profiles without any significant thickness variations.

The well data suggest a composition of Pliocene-Quaternary age siliciclastic

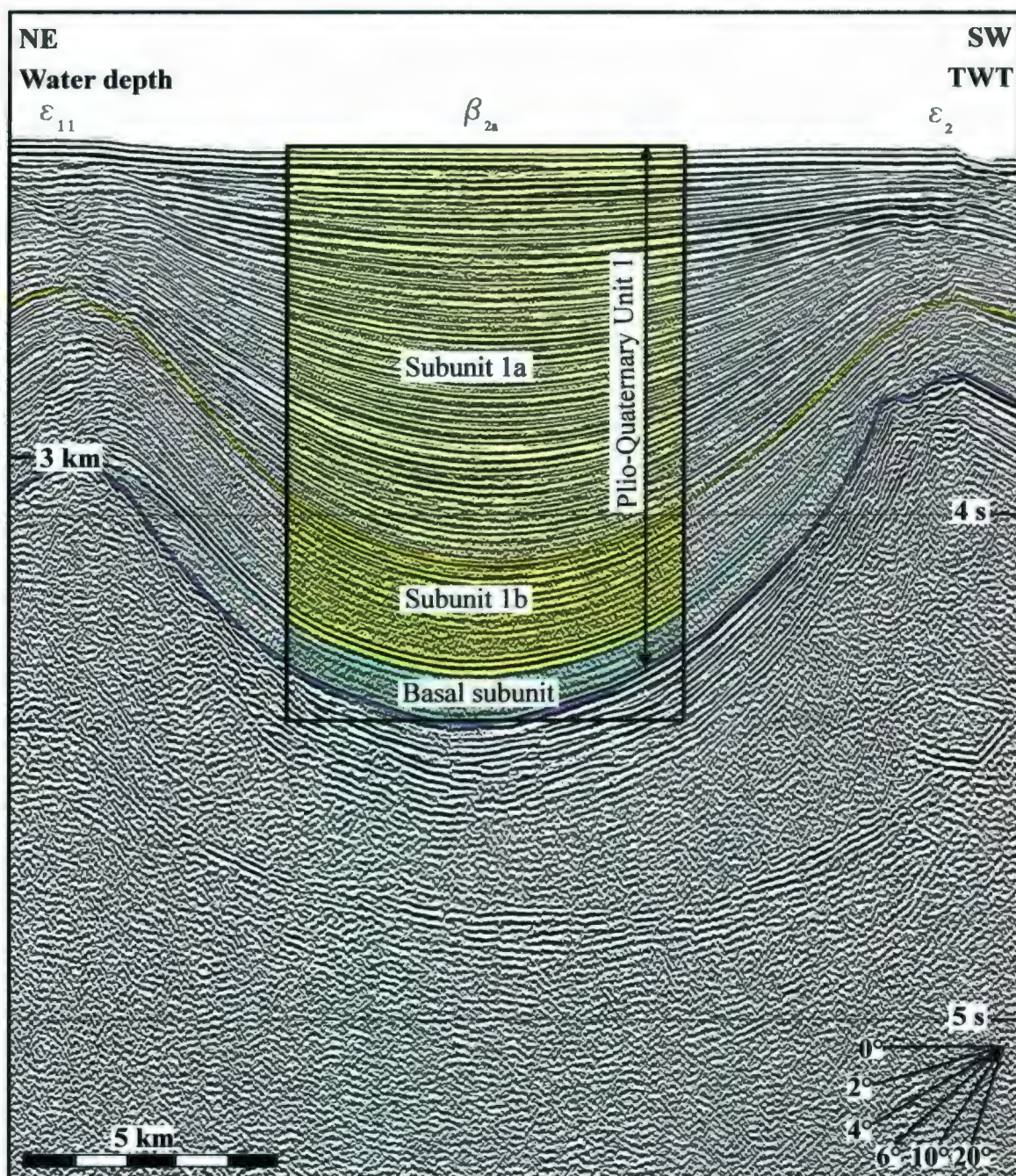


Fig. 4.1. Seismic reflection profile showing the seismic character of Unit 1 strata.

- Top middle Plio-Quaternary subunit
- Top basal Plio-Quaternary subunit
- M-reflector

successions for Unit 1. This unit is correlated on the basis of age with the Pliocene Yenimahalle and Alakilise formations, including the Pleistocene Antalya Tufa and Belkış conglomerate of the onland Aksu Basin (Akay and Uysal, 1985; Akay et al., 1985; Flecker et al., 1998; Karabıyıkoglu et al., 2000). Unit 1 is further correlated with the Kuranşa and Handere/Aktepe formations of the Iskenderun, Inner Latakia, Cilicia and Adana Basins and the Athalassa, Kakkaristra, Apalos and Nicosia formations of the Mesaoria Basin (Fig 4.2). Across the shallow shelves, Unit 1 is characterized by a wedge of south-prograding oblique reflectors.

The basal subunit is correlated with Yenimahalle Formation based on the well data in Antalya Basin, and is further tentatively correlated with the early Pliocene Mirtou Formation of the Kyrenia Range, Nicosia Formation of the Mesaoria Basin and the Handere and Aktepe formations of the Adana, Iskenderun and Inner Latakia basins (Fig. 4.2). Two packages are recognized within the portion of Unit 1 overlying the transparent basal subunit: subunit 1a, subunit 1b. Subunit 1b is the succession that immediately overlies the transparent subunit (Fig. 4.2, Calon et al., submitted a). It has a remarkably strong and continuous seismic expression and shows progressive onlap against the thrust panels. Subunit 1a comprises the seismically weak and transparent upper sequence and also shows progressive onlap over the backlimb and forelimb of the thrust panels. The only unconformities recognized within Unit 1 are the ones associated with the growth of faults and salt diapirs.





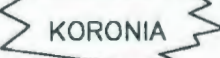
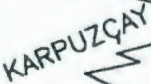

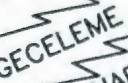

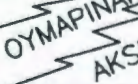






		SEISMIC UNITS	ANTALYA ¹ BASIN	ADANA ² CILICIA ³ BASINS	MESAORIA BASIN ⁴	KYRENIA MOUNTAINS ⁵
QUATERNARY		Unit 1	 ANTALYA TUFU	KURANŞA	APALOS KAKKARISTRA ATHALASSA	 ATHALASSA
PLIOCENE			ALAKILISE	HANDERE	NICOSIA	MIRTOU
			YENIMAHALLE			
MIOCENE	MESSINIAN	Unit 2	TAŞLIK	ADANA Gr.	KALAVASOS	LAPATZA
	TORTONIAN	Unit 3	 GEBİZ	 KUZGUN	 KORONIA	
	SERRAVALIAN		 KARPUZÇAY	 GÜVENÇ	PAKHNA	KYTHREA GROUP
	LANGHIAN		 GECELEME	 CINGÖZ		
	BURDIGALIAN		 OYMAPINAR	 KARISALI		
	AQUITANIAN		 AKSU	 GILDIRLI	TERRA	
				 FAKIRCA		
	OLIGOCENE	Unit 4			LEFKARA	LAPITHOS GROUP
EOCENE			KARSANTI			
PRE-EOCENE BASEMENT			ANTALYA COMPLEX	ALADAG COMPLEX	TROODOS COMPLEX	EXOTIC ELEMENTS

Figure 4.2. Stratigraphy of the onland Antalya Basin showing correlations between marine seismic stratigraphic units and the sedimentary successions in the adjacent Cilicia, Adana, Mesaoria Basins and Kyrenia Range compiled using (1) Akay et al., 1985; Kocabiyikoglu et al., 2000; (2) Yalçın and Görür (1984), Kozlu (1987); (3) Turkish Petroleum Corporation, unpublished data; (3) Kozlu (1987), Yılmaz et al (1988); (4) Robertson et al. (1995); (5) Weiler (1964), Cleintaur et al. (1977), Robertson et al. (1995)

4.2. Unit 2: Late Miocene (Messinian)

Unit 2 consists of weak and mostly discontinuous reflectors underlying the M-reflector (Fig. 4.3). The base of this unit is represented by a strong reflector, the N-reflector, which is only locally imaged on the seismic profiles due to a decrease in resolution in the deeper portions of the sections. The architecture within the sequence is difficult to identify, however, a number of folds truncated by the M-reflector are recognizable. Unit 2 varies in thickness from 100-1300 ms. The interaction of faulting and diapirism control the thickness variations throughout the study area. Based on the well data, it is suggested that Unit 2 is composed of Messinian age halite alternating with lesser quantities of anhydrite and limestone (Turkish Petroleum Corporation, unpublished data). This succession can be correlated with the sporadic minor evaporites over the Tortonian reefal limestones (Gebiz Limestone) of Karpuzçay Formation in the onland Aksu, Köprü, and Manavgat basins (Akay and Uysal, 1985, Akay et al., 1985) and further, with the lower Adana Group/Haymaseki Formation of Iskenderun, Inner Latakia, Adana and Inner Cilicia basins and the Lapatza and Kalavastos formations of Mesaoria Basin and the Kyrenia Range, respectively (Fig. 4.2). Unit 2 thins and pinches out across the slope of the Turkish coast. Towards the shelf, where the Messinian evaporites are missing, M-reflector is still present, but in this case it overlies an older succession. Two packages are recognized within Unit 2: subunit 2a, subunit 2b (Fig. 4.3). Subunit 2a, where present, immediately underlies the M-reflector. It has a strong seismic expression with continuous and parallel reflectors. Subunit 2a shows progressive onlap against the older structural

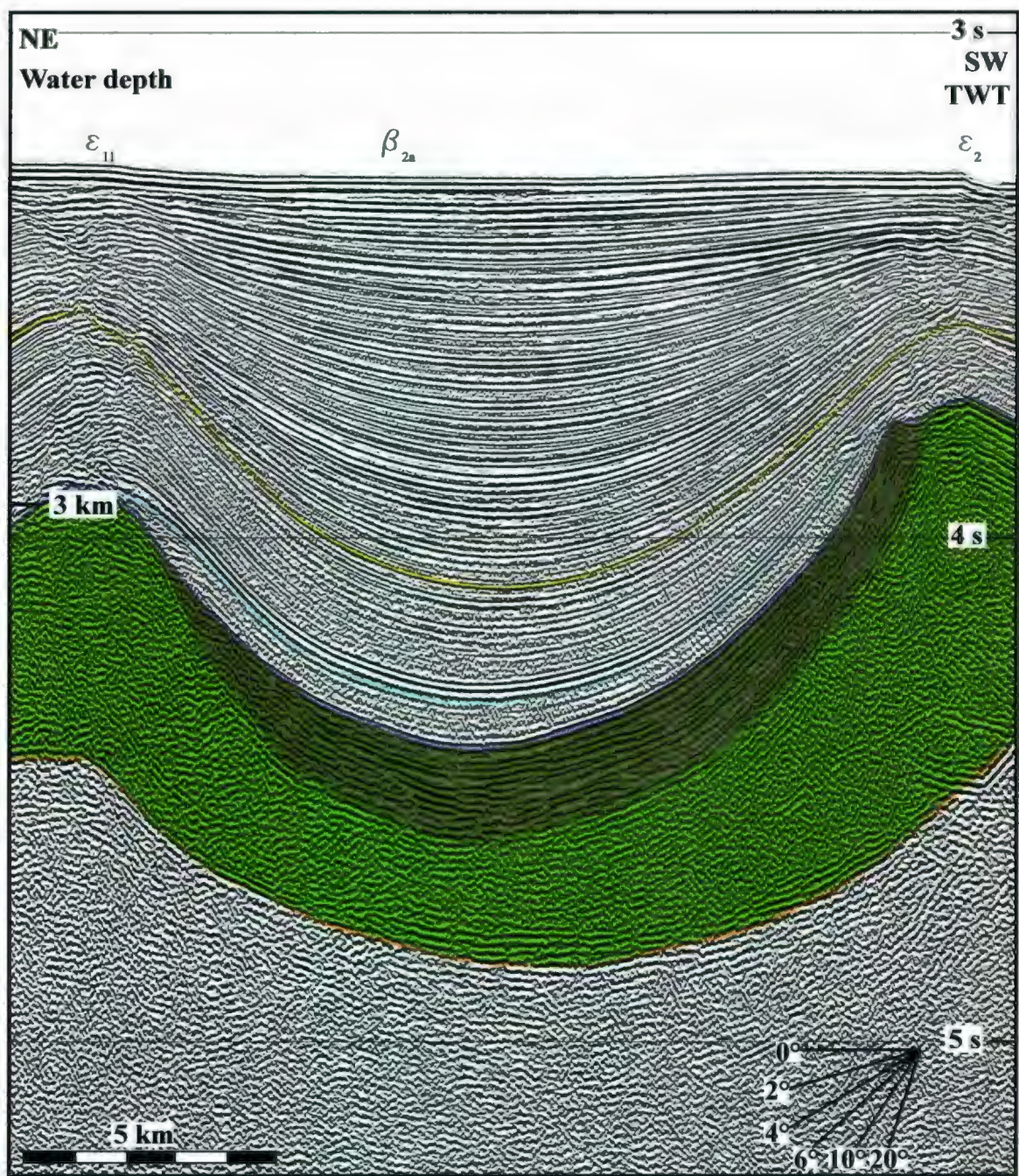


Fig. 4.3. Seismic reflection profile showing the seismic character of Units 2 and 3 strata.

- | | |
|--------------------------------------|------------------------------|
| — Top middle Plio-Quaternary subunit | ■ Upper evaporite subunit 2a |
| — Top basal Plio-Quaternary subunit | ■ Lower evaporite subunit 2b |
| — M-reflector | — Top Unit 3 |

highs. Subunit 2b comprises the seismically weak and transparent sequence, which either underlies subunit 2a, or shows an intercalating relationship with subunit 2a (see Fig. 6.11). Where subunit 2a is absent, subunit 2b immediately underlies the M-reflector.

4.3. Unit 3: Miocene (pre-Messinian)

Unit 3 is characterized by weak reflections, which are mostly discontinuous but locally show moderate lateral continuity (Fig. 4.3). The upper boundary of Unit 3 coincides with the base of Unit 2 when present. Across the shelf and parts of the upper slope where Unit 2 is absent, the M-reflector comprises the upper boundary. The lower boundary is either not well-defined due to decreasing resolution with depth and difficulties in imaging structures below the high velocity evaporites or lies deeper beneath the imaged portion of the subsurface. Unit 3 is tentatively correlated with the Aquitanian-Serravallian Tepekli, Oymapınar and Geceleme formations and the predominantly Tortonian Karpuzçay Formation of the onland Aksu, Köprü and Manavgat basins (Akay and Uysal, 1985; Akay et al., 1985; Flecker et al., 1998; Karabıyıkoglu et al., 2000). It is further correlated with the Pakhna and Koronia formations as well as the Kythrea Group of northern Cyprus (Bagnall, 1960; Follows and Robertson, 1990). Unit 3 probably also correlates with the predominantly siliciclastic successions of the Aslantaş, İsalı, Karataş and Kızıldere formations of the Andırın Block and Misis Mountains, and the Fakırca, Girdili, Karaisalı, Cingöz, Güvenç and Kuzgun formations of the Adana and Cilicia basins (Fig. 4.2, see also Aksu et al., submitted).

CHAPTER 5. Late Miocene Ridges and the Intervening Pliocene-Quaternary Basins

The morphotectonic framework of the Antalya Basin is characterized by the broadly undulating morphology of the M-reflector which shows 100-1500 ms elevation difference between adjacent crests and troughs. Detailed examination of seismic reflection profiles shows that this corrugated morphology is the expression of deeper and much larger fold structures, which delineate a number of internally parallel, broadly northwest-southeast-trending anticlines (referred to as late Miocene ridges) and synclines (referred to as Pliocene-Quaternary basins).

5.1. Late Miocene Ridges

The ridges define large, northwest-southeast-trending, generally non-cylindrical anticlines delineated by the morphology of the M-reflector, as well as the internal architecture of the Messinian evaporites of Unit 2 and the late Miocene (mainly Tortonian) succession of Unit 3. The crestal hinge lines of these anticlines form broadly curvilinear map traces which show doubly-plunging trajectories. Figures 5.1 and 5.2 show the areal distribution of these ridges, referred to as ε_1 to ε_5 , which are described below in terms of their internal stratigraphic architecture below the M-reflector.

5.1.1. Ridges ε_1 and ε_{11}

Ridges ε_1 and ε_{11} form a large, generally double-crested anticlinal structure situated

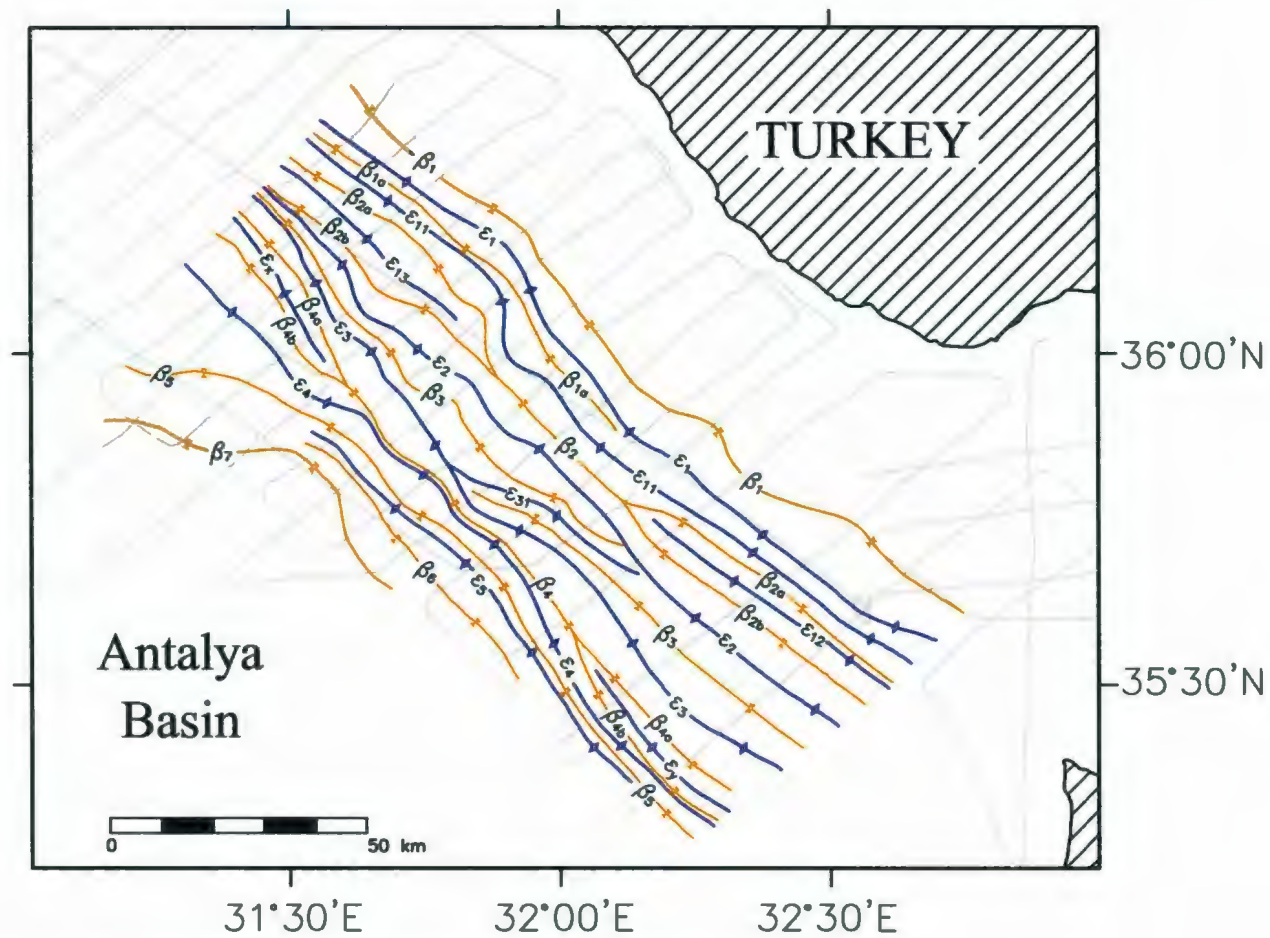


Fig. 5.1. Map of the Antalya Basin showing the axes of basins and ridges.

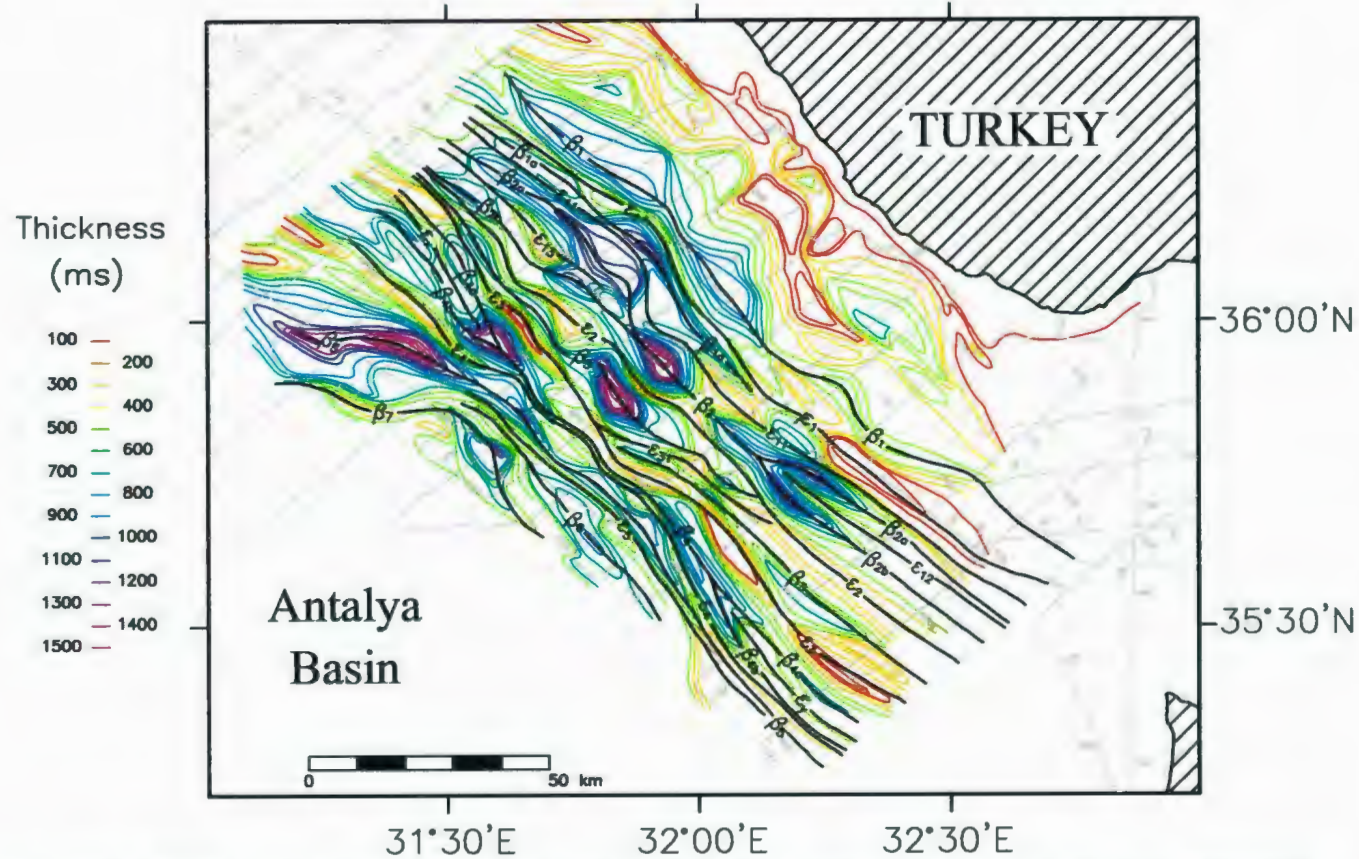


Fig. 5.2. Map of the Antalya Basin showing the axes of basins and ridges posted on Plio-Quaternary isochrone contours. Apparent thicknesses (time from sea floor to M-reflector) in ms are two way time. Contour interval is 100 ms.

seaward of the base of Turkish continental slope (Figs. 5.1, 5.2). In the western portion of the study area, they are clearly separated from one another, with the smaller basin β_{1a} nestled between these two ridges (Figs. 5.1, 5.3). The crest(s) of the structure rises 200-600 ms above the floors of both basin β_1 in the north and basin β_2 in the south (Figs. 5.3-5.11), where the structure creates a <100 ms-high minor rise on the sea floor (e.g. Fig. 5.3). The upper evaporite subunit 2a is thickest beneath the floor of the Pliocene-Quaternary basin β_1 , and shows a dramatic thinning toward the continental slope and the crestal area of ridge ϵ_1 (Figs. 5.3-5.5). The thinning is accomplished by convergence of internal reflectors within subunit 2a, as well as truncation on the lower subunit. The lower evaporite subunit 2b underlies subunit 2a, or the M-reflector. The evaporite subunits 2a and 2b in the crestal region of the ridges ϵ_1 and ϵ_{11} as well as beneath basins β_1 , β_{1a} display highly variable thicknesses on the seismic reflection profiles as traced from northeast to southwest (Figs. 5.3- 5.5). Unit 2 is largely absent across the continental shelf and slope, and the depositional edge of the unit which is delineated by the merger N and M unconformities occurs near the base of slope. The occurrence of thin and strongly reflective, but discontinuous reflector packages at the level of the M-reflector may indicate the presence of salt welds (Jackson and Cramez, 1989). This suggests that, at least locally, the depositional edge of salt may have been situated higher on the slope, and that salt was withdrawn from this region toward the deeper portion of the basin. The morphotectonic architecture of the core of ridges ϵ_1 and ϵ_{11} in the western portion of the study area is characterized by two linked, south-verging asymmetric fold structures

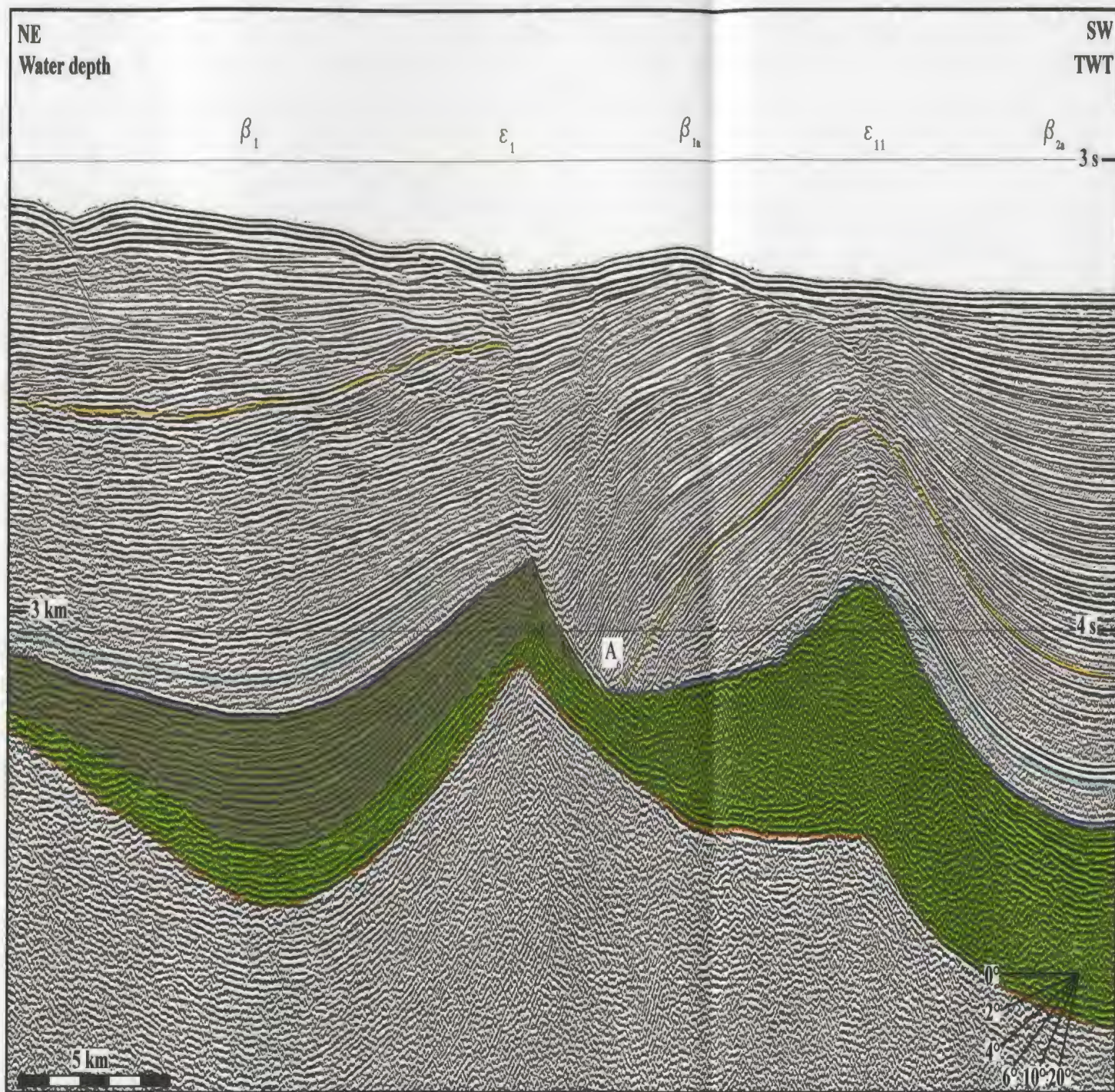
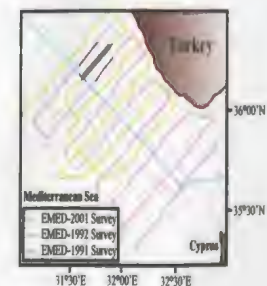


Fig. 5.3. Seismic reflection profile (FIX 495-506).

- Top middle Plio-Quaternary subunit
- Top basal Plio-Quaternary subunit
- M-reflector
- Upper evaporite subunit 2a
- Lower evaporite subunit 2b
- Top Unit 3



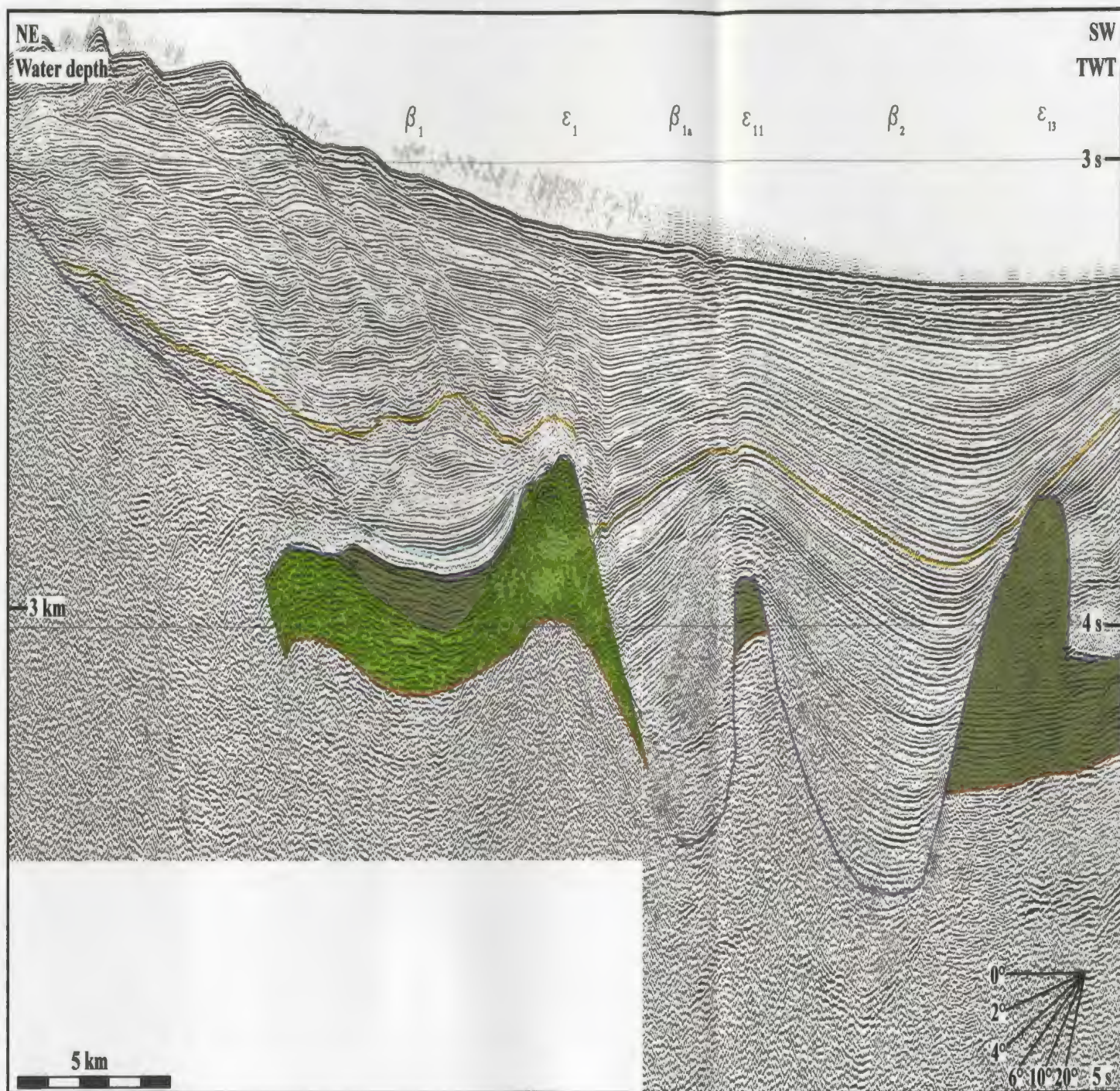
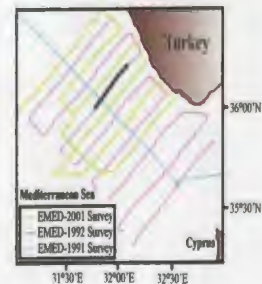


Fig. 5.4. Seismic reflection profile (FIX 1879-1897).

- Top middle Plio-Quaternary subunit
- Top basal Plio-Quaternary subunit
- M-reflector
- Upper evaporite subunit 2a
- Lower evaporite subunit 2b
- Top Unit 3



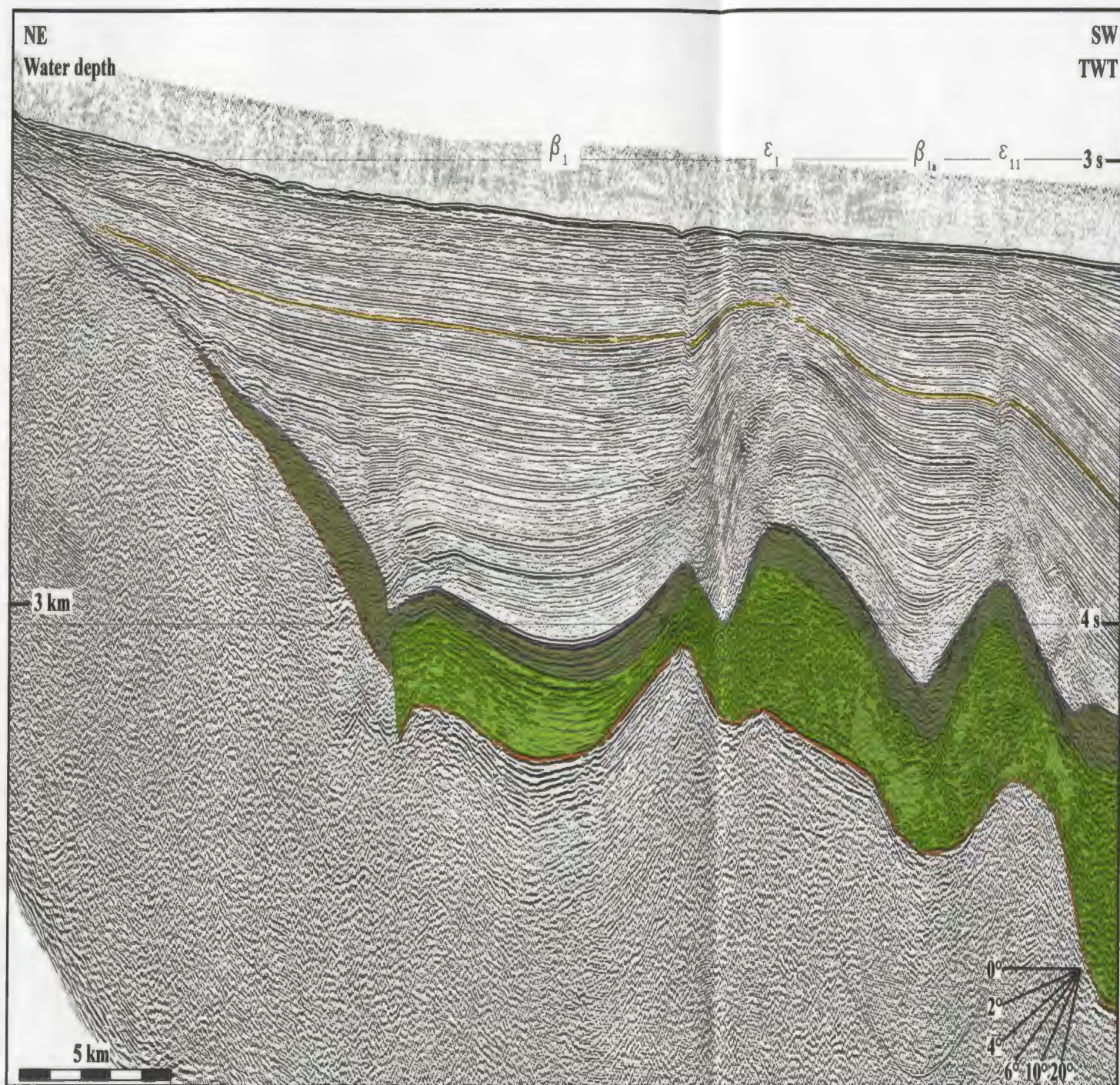
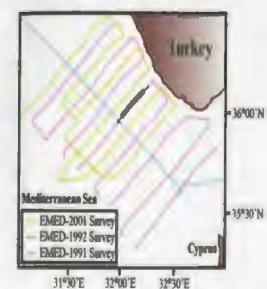


Fig. 5.5. Seismic reflection profile (FIX 1813-1828).

- Top middle Plio-Quaternary subunit
- Top basal Plio-Quaternary subunit
- M-reflector
- Upper evaporite subunit 2a
- Lower evaporite subunit 2b
- Top Unit 3



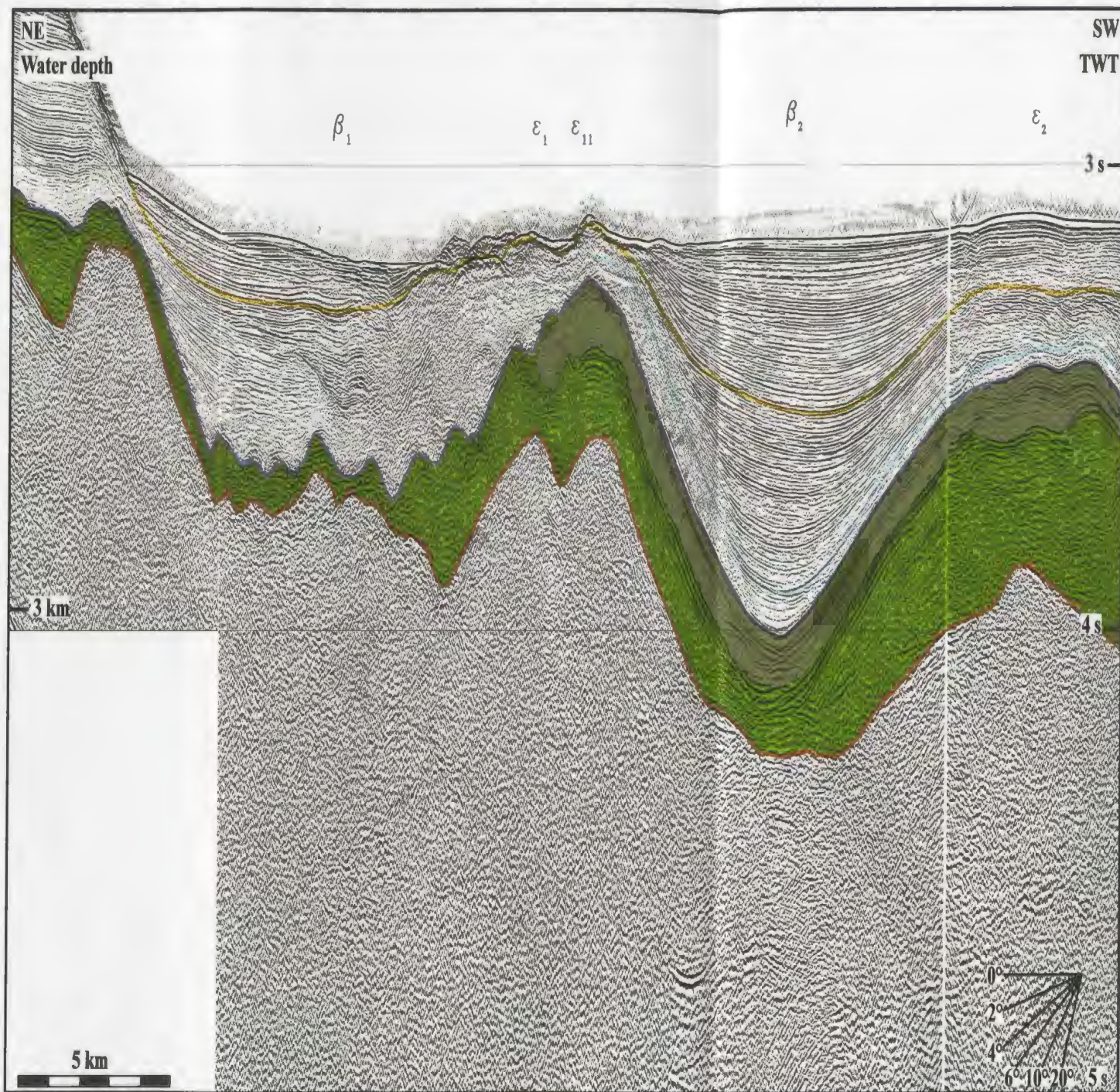
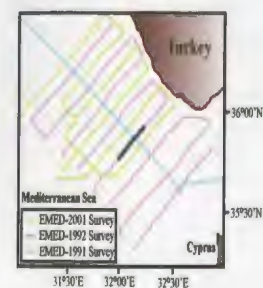


Fig. 5.6. Seismic reflection profile (FIX 1767-1781).

- Top middle Plio-Quaternary subunit
- Top basal Plio-Quaternary subunit
- M-reflector
- Upper evaporite subunit 2a
- Lower evaporite subunit 2b
- Top Unit 3



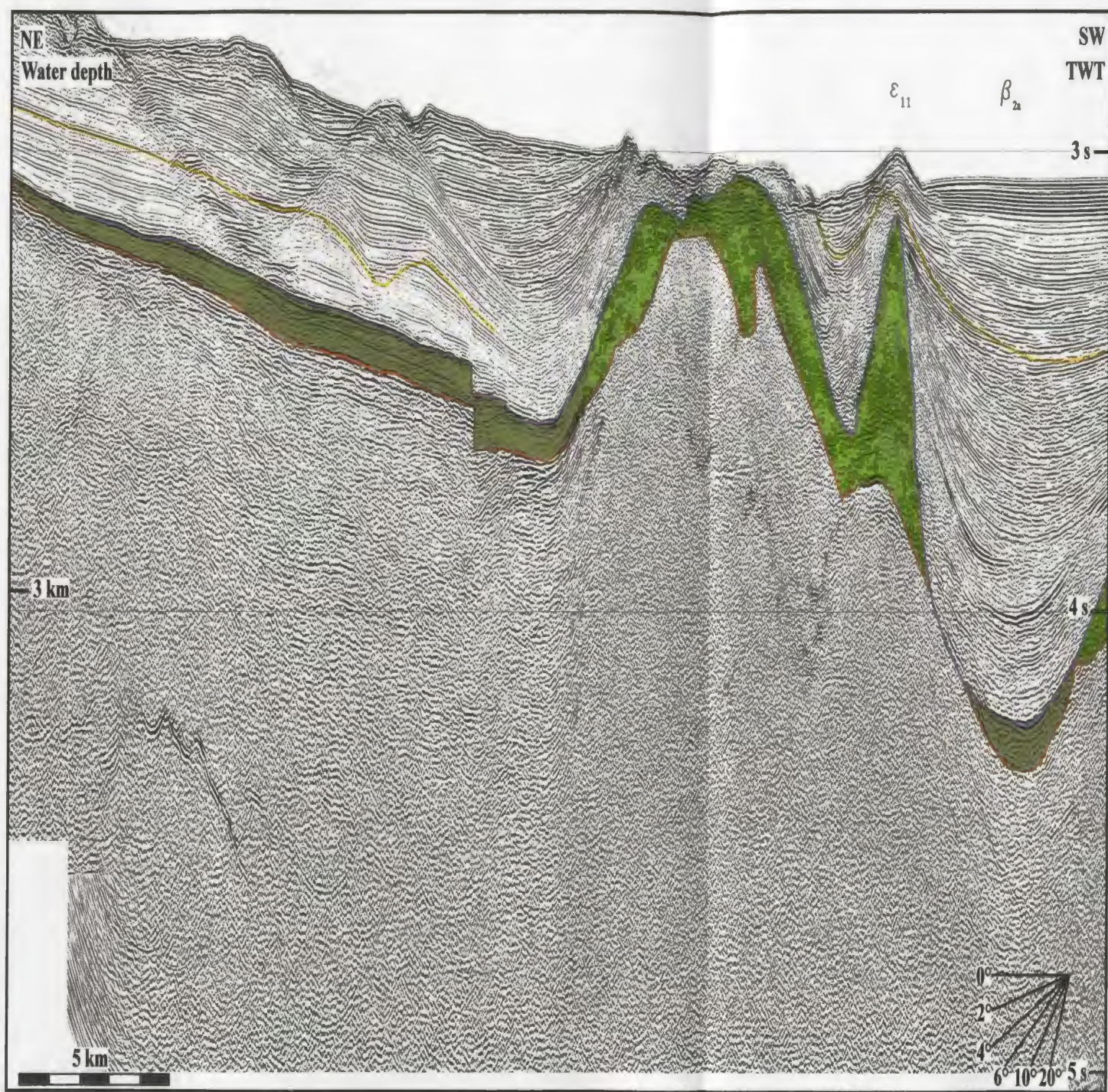
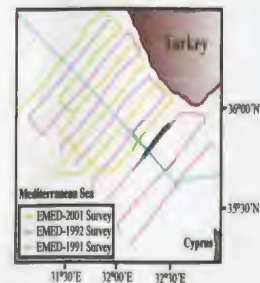


Fig. 5.7. Seismic reflection profile (FIX 1704-1723).

- Top middle Plio-Quaternary subunit
- Upper evaporite subunit 2a
- Top basal Plio-Quaternary subunit
- Lower evaporite subunit 2b
- M-reflector
- Top Unit 3



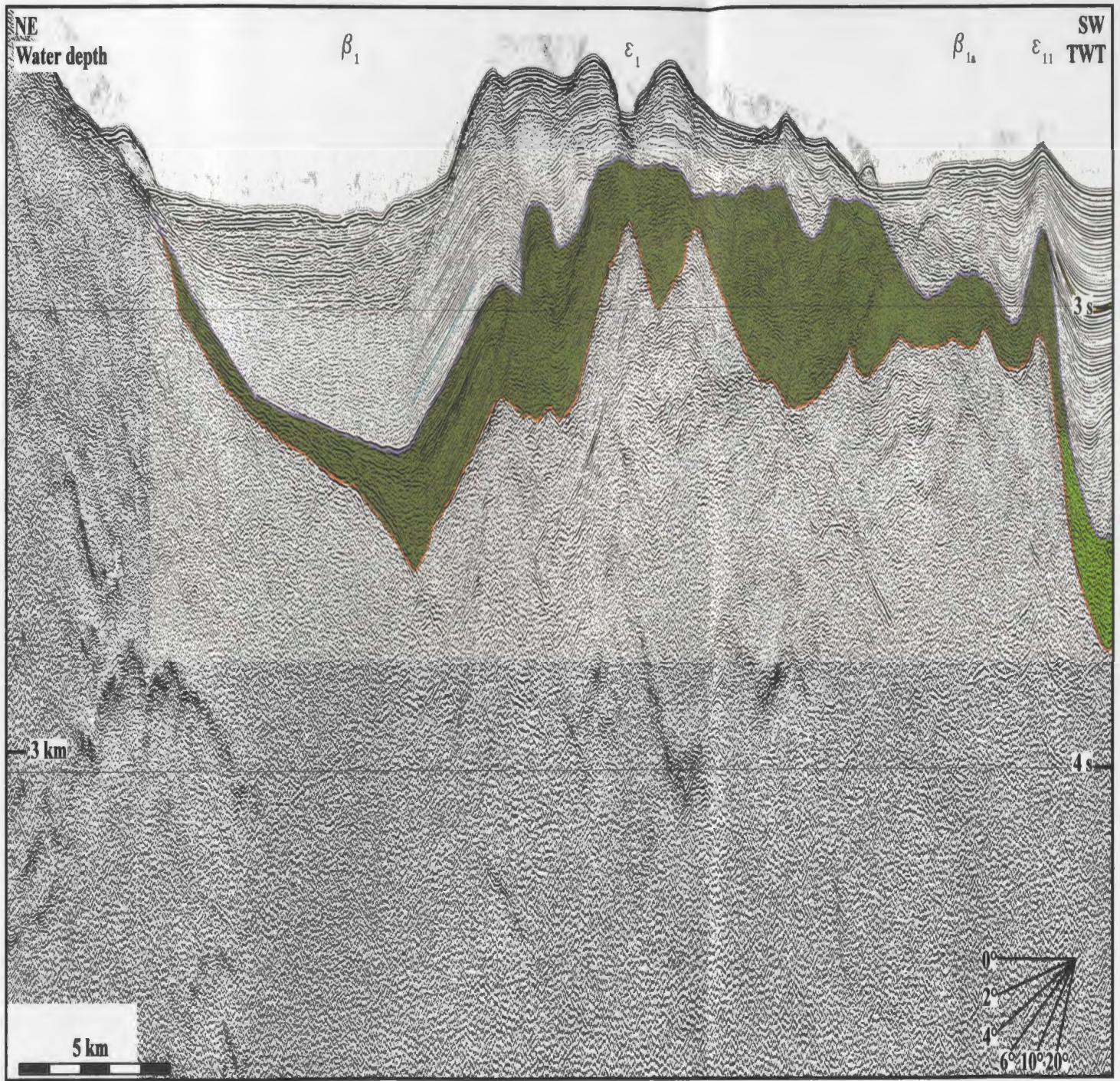
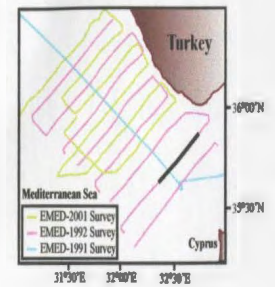


Fig. 5.8. Seismic reflection profile (FIX 1653-1667).

- Top middle Plio-Quaternary subunit
- Top basal Plio-Quaternary subunit
- M-reflector
- Upper evaporite subunit 2a
- Lower evaporite subunit 2b
- Top Unit 3



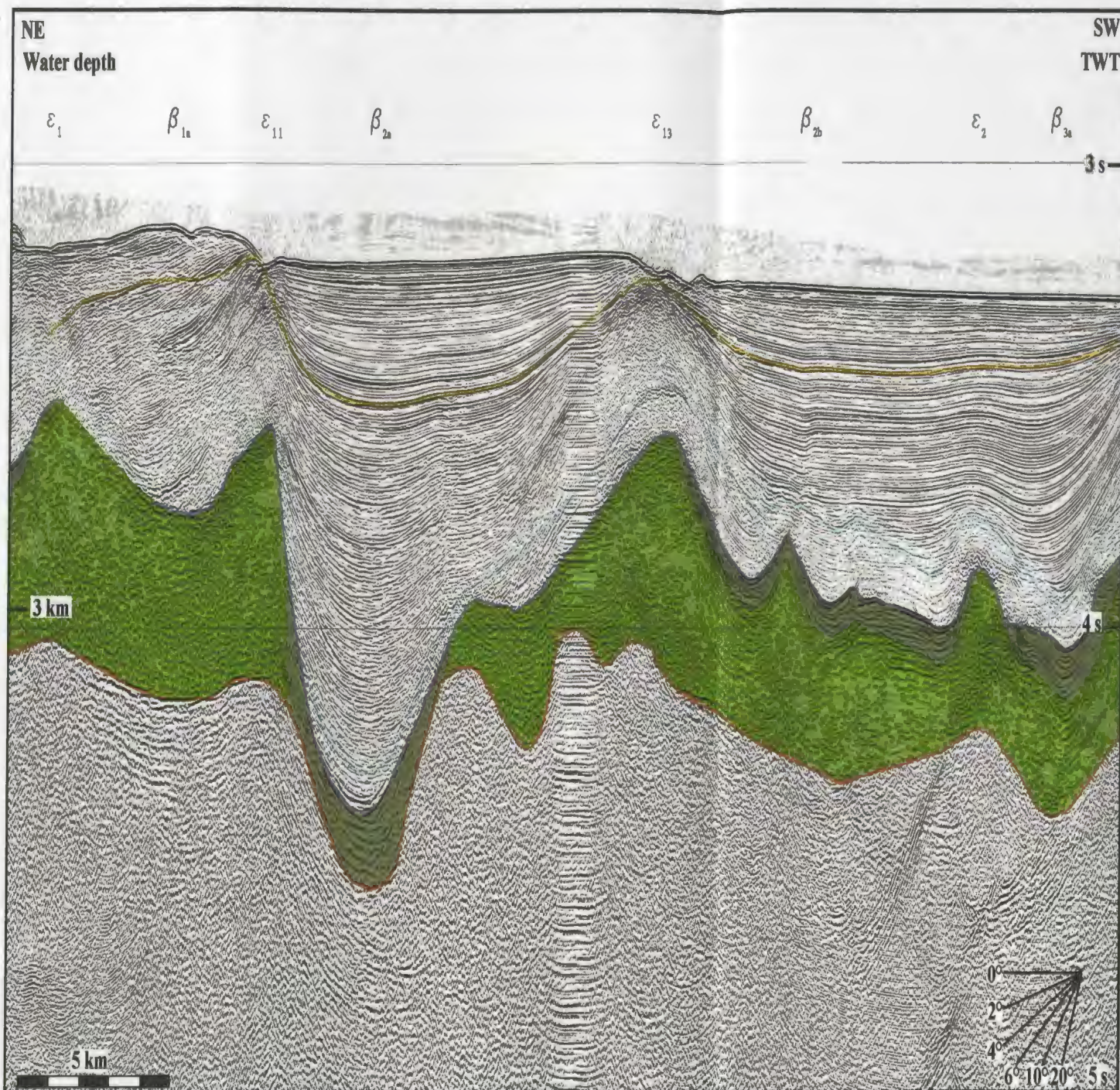
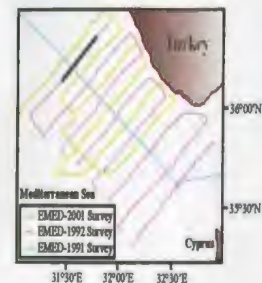


Fig. 5.9. Seismic reflection profile (FIX 1933-1948).

- Top middle Plio-Quaternary subunit
- Top basal Plio-Quaternary subunit
- M-reflector
- Upper evaporite subunit 2a
- Lower evaporite subunit 2b
- Top Unit 3



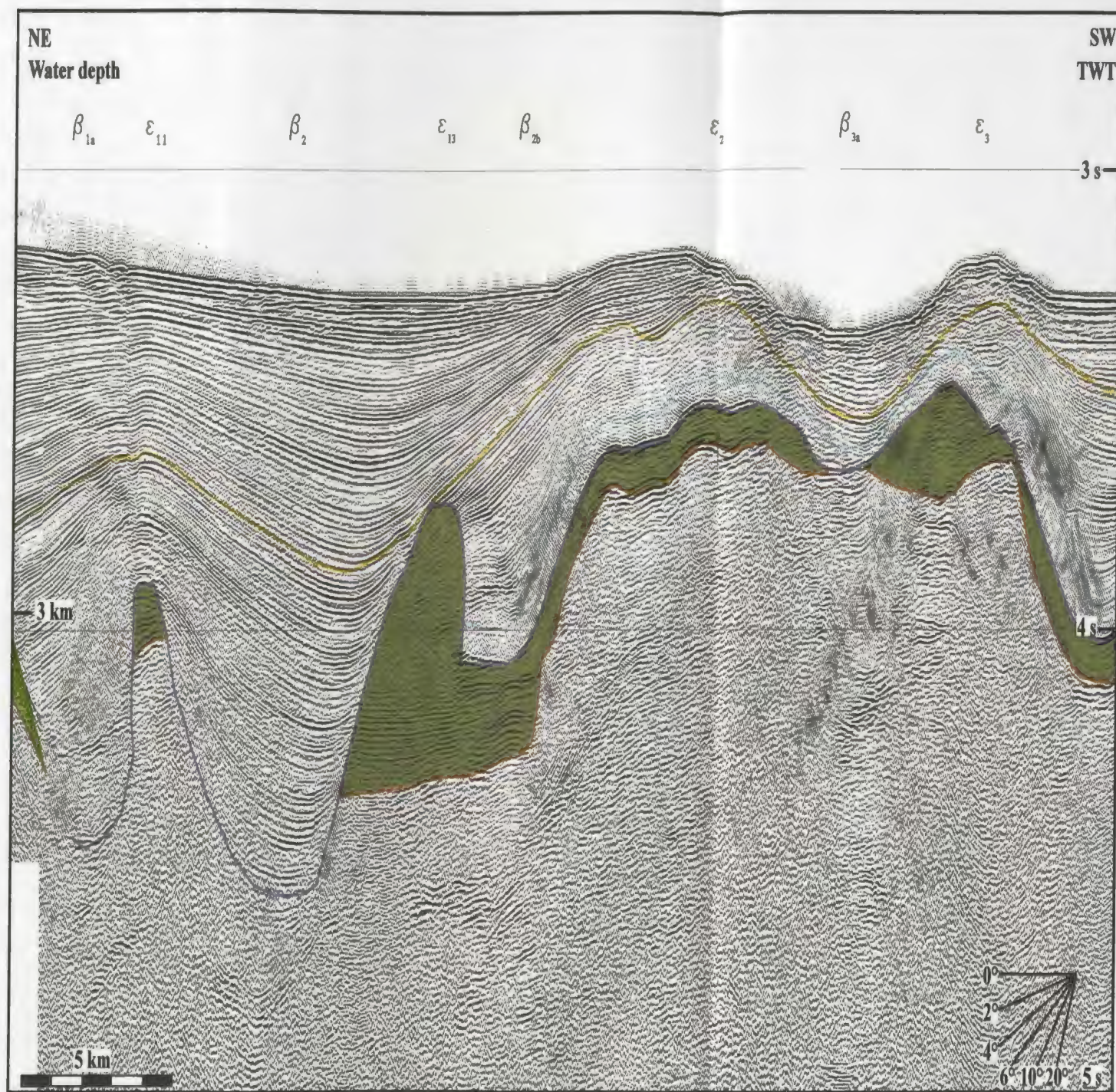
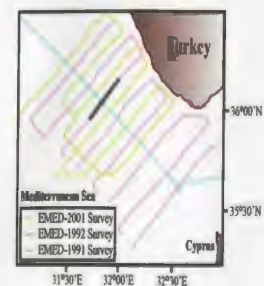


Fig. 5.10. Seismic reflection profile (FIX 1870-1888).

- Top middle Plio-Quaternary subunit
- Upper evaporite subunit 2a
- Top basal Plio-Quaternary subunit
- Lower evaporite subunit 2b
- M-reflector
- Top Unit 3



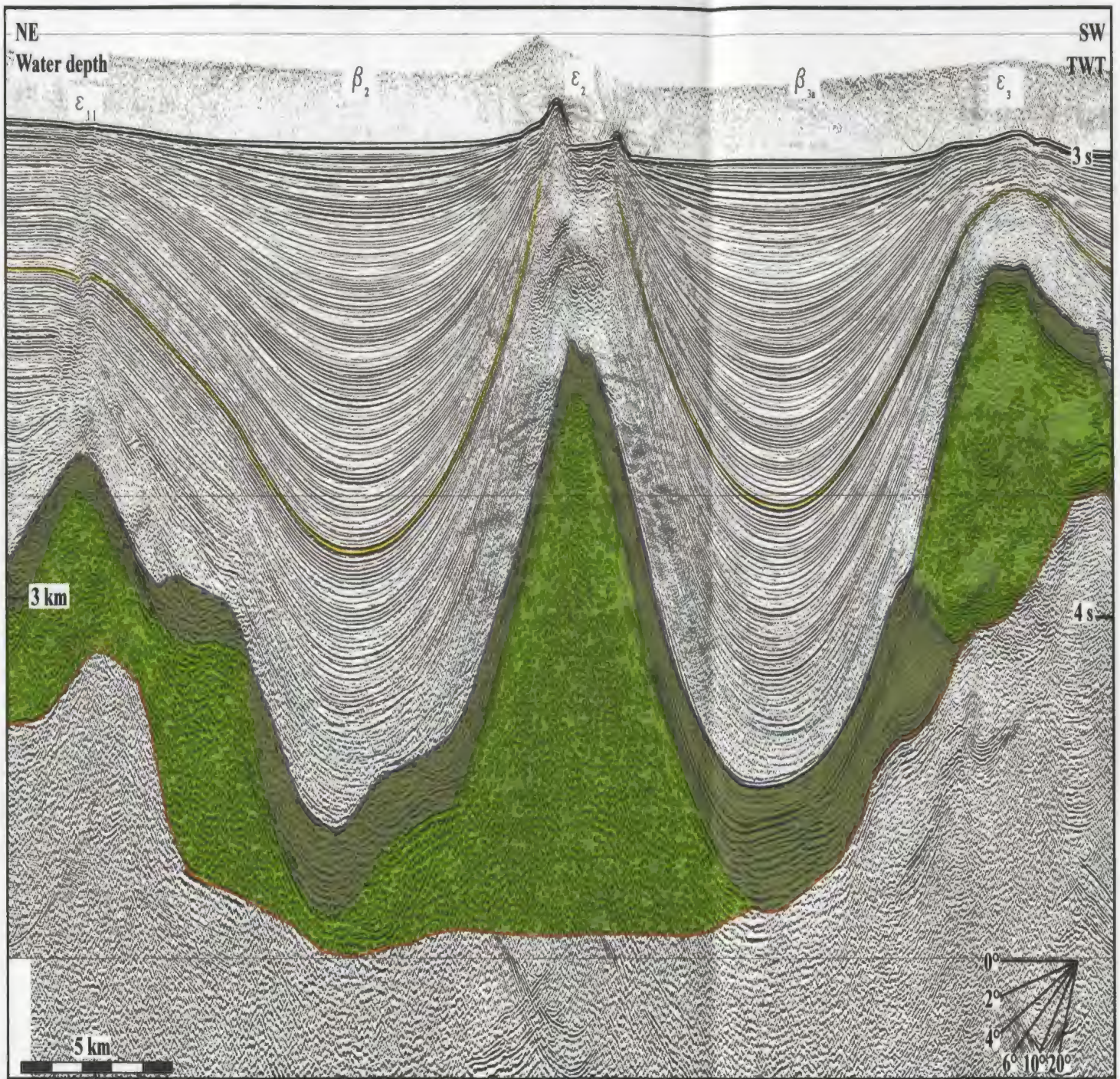
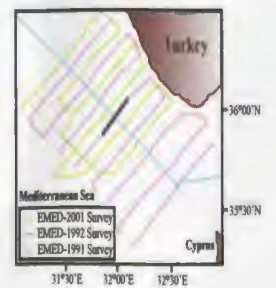


Fig. 5.11. Seismic reflection profile (FIX 1820-1835).

- Top middle Plio-Quaternary subunit
- Top basal Plio-Quaternary subunit
- M-reflector
- Upper evaporite subunit 2a
- Lower evaporite subunit 2b
- Top Unit 3



consisting of long gently north-dipping back limbs and shorter, steeper south-dipping forelimbs, with the crestal hinge line of the anticlines defined by the folds in Unit 3 strata occurring beneath the apex of fold delineated by the M-reflector (Figs. 5.3-5.5). The gently north-dipping back limbs of these folds trace beneath the Pliocene-Quaternary basin β_1 . Here, the axial hinge lines defined by the strata of Unit 3, Unit 2 and Unit 1 are remarkably coincident, suggesting a longer term stability of the basins and ridges (e.g. Fig. 5.3).

In the eastern portion of the study area, ridges ϵ_1 and ϵ_{11} merge to form a massive multi-crested anticlinal structure, with basin β_{1a} forming an uplifted perched depression over the southern fringe of the anticline (Figs. 5.1, 5.6-5.8). The height of the structure ranges from 600-900 ms to 1200 ms, with a very prominent sea floor expression, where the combined ridges ϵ_1 and ϵ_{11} stands from 100-350 ms above the adjacent sea floor (Figs. 5.6-5.8). Here, the upper and lower evaporite subunits 2a and 2b form a nearly uniform, ~200 ms-thick drape over the extensively folded strata of Unit 3 across the large composite ridge $\epsilon_1 + \epsilon_{11}$ (Figs. 5.6-5.8). In the eastern portion of the study area, the base of the evaporite unit is not always well delineated in seismic profiles and Unit 3 shows few coherent reflections (e.g. Fig. 5.6). Further to the east, the evaporite unit shows a dramatic thinning and disappearance (i.e., probable depositional edge) below the M-reflector along the lowermost portion of the continental slope (e.g. Figs. 5.7, 5.8). Here, Unit 3 is well imaged below the base evaporite within the complexly-folded structures of composite ridge $\epsilon_1 + \epsilon_{11}$, and the reflectors within Unit 3 delineate a series of tight folds.

5.1.2. Ridge ϵ_2

Ridge ϵ_2 is an anticlinal structure situated to the south of composite ridge $\epsilon_1 + \epsilon_{11}$ (Figs. 5.1, 5.2). In the westernmost portion of the study area, it appears as a minor structure rising <100 ms high above the adjacent basin floors, where basins β_{2b} and β_{3a} form a large composite depocentre extending between ridges ϵ_{13} and ϵ_3 (Fig. 5.9). Here, the upper evaporite subunit 2a forms an approximately 100 ms-thick, nearly uniform blanket extending across the floor of the composite basin, including ridge ϵ_2 , but shows a marked thinning and pinch-out along the flanks of ridges ϵ_1 and ϵ_{11} (Fig. 5.9). The lower evaporite subunit 2b defines a thick package that underlies subunit 2a across ridge ϵ_2 as well as beneath the adjacent basins (Fig. 5.9). The base of subunit 2b is marked by an erosional unconformity, delineated by a moderately continuous reflector, which truncates the folded strata of Unit 3, while its upper boundary is delineated by highly continuous, strong reflectors of the lowermost subunit 2a. The internal architecture of Unit 3 across composite basins β_{2b} and β_{3a} , including ridge ϵ_2 is delineated by a series of folds, giving the unit a gently corrugated appearance. The folds exhibit long, gently north-dipping back limbs, and shorter and steeper south-dipping forelimbs (Fig. 5.9).

Further to the east, the crestal region of ridge ϵ_2 rapidly ascends and becomes a very prominent structure, rising ~ 800 ms and 300 ms above the floors of basins β_{2b} and β_{3a} , respectively, and creating a ~ 150 ms-high expression on the sea floor (Fig. 5.10). Here, the lower evaporite subunit 2b is absent and the upper evaporite subunit 2a forms a <100 ms-thick package that directly overlies Unit 3. Across the crest of ridge ϵ_2 , subunit

2a immediately overlies Unit 3 and shows a south-directed thinning and pinch-out by erosional truncation at the M-unconformity. Subunit 2a is thickest beneath the floors of adjacent basins and shows a dramatic thinning toward ridge ϵ_2 , which is accomplished by convergence of reflectors as well as abutting against the underlying strata of Unit 3. The internal architecture of the core of ridge ϵ_2 is defined by a very prominent fold structure. This structure is clearly tilted toward the northeast and consists of a >1200 ms-thick package of gently northeast-dipping reflectors which are truncated along the southern portion of ridge ϵ_2 against a more steeply northeast-dipping surface that rises to the base of M-reflector along the central axis of basin β_{3a} . The reflectors within this tilted block are also truncated at the northeastern portion of ridge ϵ_2 by the M-unconformity (Fig. 5.10).

In the central portion of the study area, ridge ϵ_2 stands as a relatively narrow, but high amplitude structure (Fig. 5.11). It exhibits a symmetrical cross-sectional geometry rising ~1100 ms from the floors of basins β_2 and β_{3a} and creates two prominent erosional step-like expression on the sea floor (Fig. 5.11). The upper evaporite subunit 2a is thickest beneath the axes of the adjacent basins and shows a rapid thinning towards ridge ϵ_2 . The lower evaporite subunit 2b appears as a triangular body which underlies subunit 2a in the crestal area of ridge ϵ_2 (Fig. 5.11). Here, the boundary between these two subunits is marked by the abrupt change in seismic character. Beneath basins β_2 and β_{3a} , subunit 2b appears to be missing and Unit 3 underlies the upper evaporite subunit 2a, the base of which is marked by strong reflectors. In the central portion of the study area, only a very small portion of Unit 3 is imaged in seismic profiles, thus the internal architecture of

this succession cannot be fully delineated using the existing seismic reflection profiles (Fig. 5.11). Further to the east, ridge ϵ_2 becomes wider and displays an asymmetrical cross-sectional geometry with a long, gently northerly-dipping back limb, and a shorter and steeper southerly-dipping forelimb. The structure rises 550 ms and 100 ms from the floors of basins β_2 and β_{3a} , respectively (Fig. 5.12). The upper evaporite subunit 2a extends with a uniform thickness across the crest of ridge ϵ_2 , as well as beneath the adjacent basin floors, although a mild thickening is observed toward basin β_2 (Fig. 5.12). In the crestal region of ridge ϵ_2 and beneath basin β_{3a} it overlies a lenticular package of lower evaporite subunit 2b. Whereas, beneath the floor of basin β_2 in the north, subunit 2b shows a pinch out and the upper evaporite subunit 2a immediately overlies Unit 3 (Fig. 5.12). The boundary between the two evaporite subunits as well as between subunit 2a and Unit 3 is well-defined by strong and continuous reflectors. The architecture of Unit 3 across ridges ϵ_2 and ϵ_1 , including the intervening subbasins β_{3a} and β_{3b} , is characterized by a prominent asymmetric fold structure which display a long northerly-dipping back limb and a notably short southerly dipping forelimb (Fig. 5.12). Internally Unit 3 defines a north-dipping, north-thickening homoclinal succession, which shows clear growth in its middle-upper portion. However, the uppermost strata of the unit are variably but notably erosionally truncated by the reflector which defines the base of subunit 2b (Fig. 5.12).

In the eastern portion of the study area, ridge ϵ_2 remains as a prominent asymmetrical structure, although its amplitude varies considerably rising 100-750 ms and ~200 ms from the floor of basins β_{2b} and β_{3a} , respectively (Figs. 5.13, 5.14). The

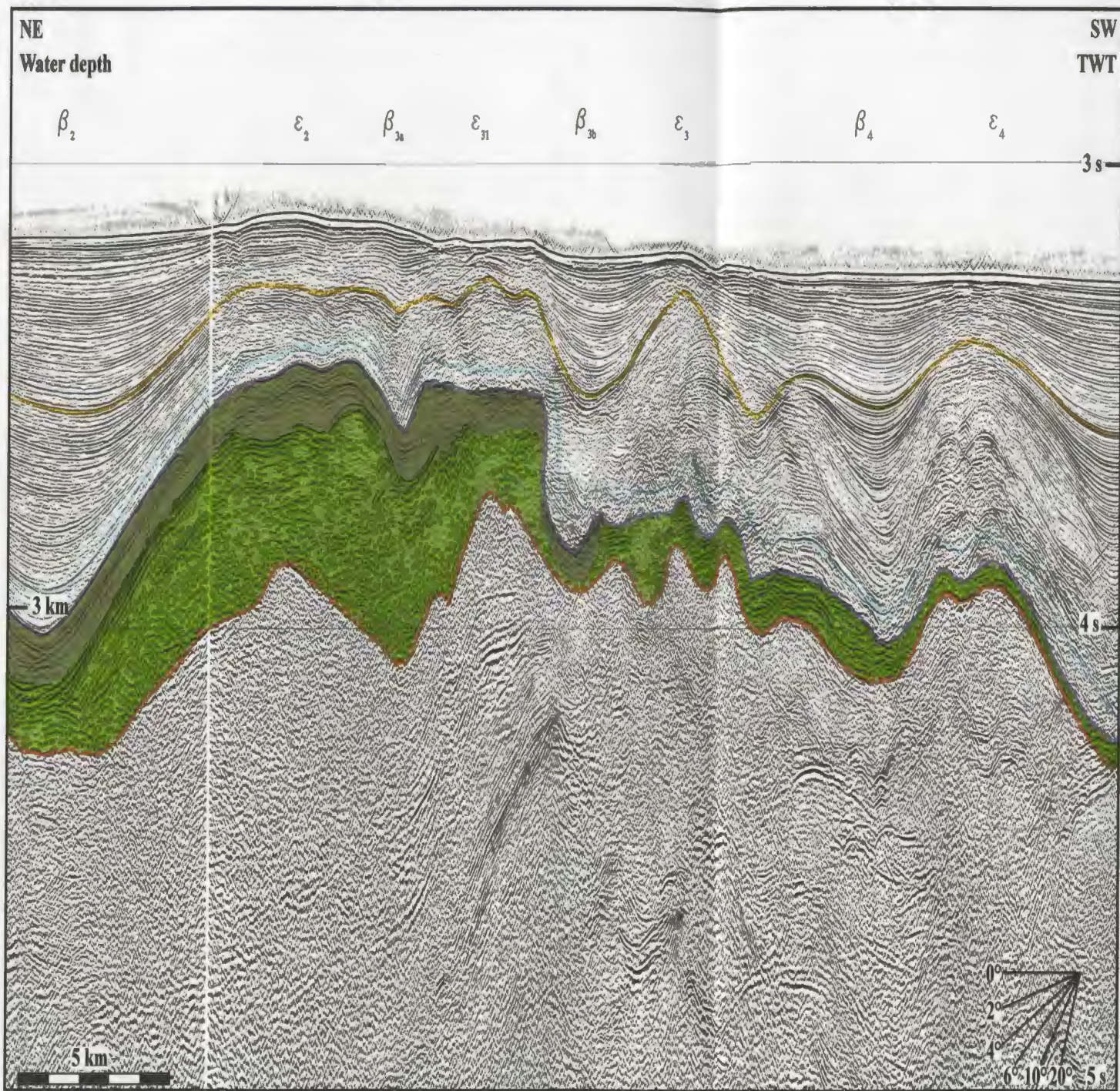
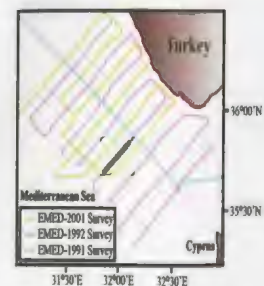


Fig. 5.12. Seismic reflection profile (FIX 1757-1772).

- Top middle Plio-Quaternary subunit
- Top basal Plio-Quaternary subunit
- M-reflector
- Upper evaporite subunit 2a
- Lower evaporite subunit 2b
- Top Unit 3



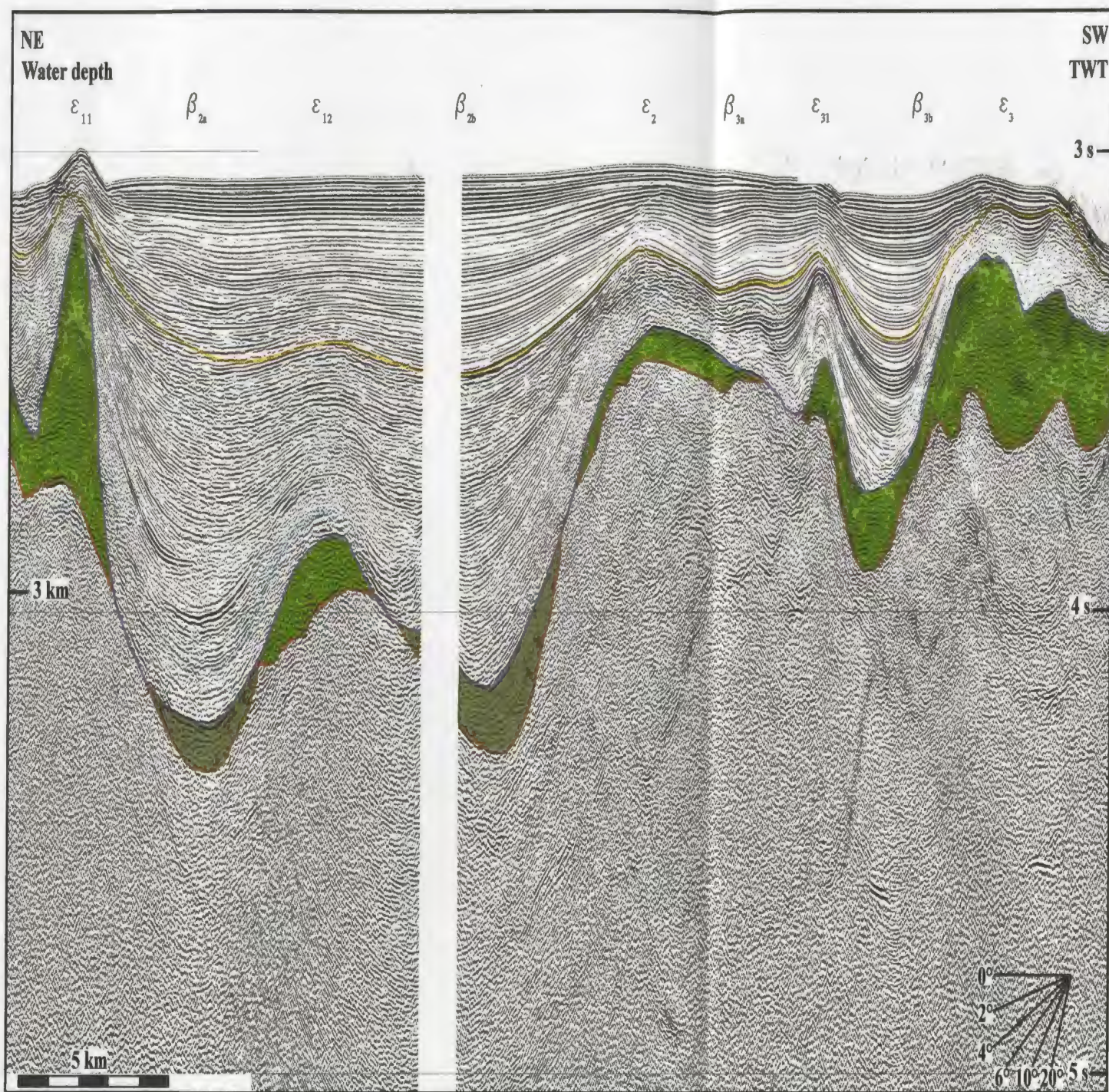
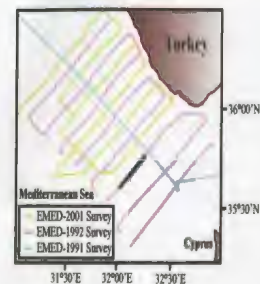


Fig. 5.13. Seismic reflection profile (FLX 1719-1735).

- Top middle Plio-Quaternary subunit
- Upper evaporite subunit 2a
- Top basal Plio-Quaternary subunit
- Lower evaporite subunit 2b
- M-reflector
- Top Unit 3



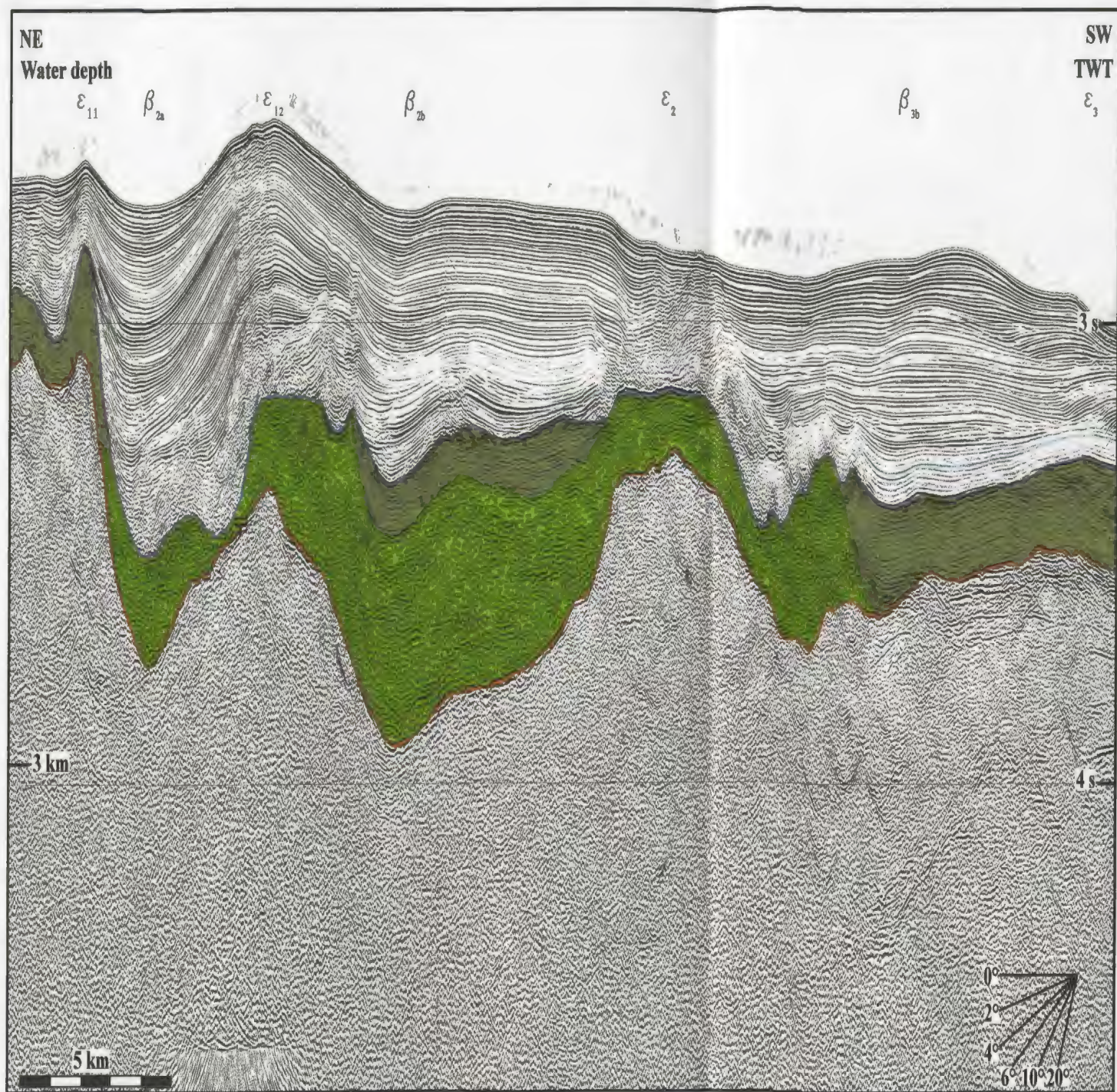
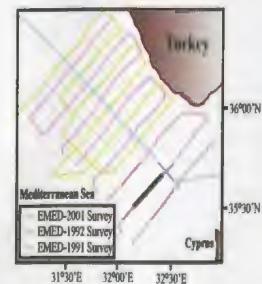


Fig. 5.14. Seismic reflection profile (FIX 1638-1655).

- Top basal Plio-Quaternary subunit
- Lower evaporite subunit 2b
- M-reflector
- Top Unit 3
- Upper evaporite subunit 2a



evaporite Unit 2 is notably thinner in this portion of the study area (Fig. 5.13): the lower evaporite subunit 2b is absent and the upper evaporite subunit 2a forms a thin and patchy veneer over the flanks and crests of ridge ϵ_2 with only a mild thickening toward the axes of basins β_{2b} and β_{3a} . Here, Unit 3 either immediately underlies subunit 2a where present, or the M-reflector. Unit 2 thickens considerably in the easternmost portion of the study area, where the upper evaporite subunit 2a is only confined to beneath basin β_{2b} and pinches out towards ridge ϵ_2 (e.g. Fig. 5.14). The lower evaporite subunit 2b extends below the M-reflector across ridge ϵ_2 with uniform thickness, but shows thickening towards both basins β_{2b} and β_{3a} (Fig. 5.14). A minor depression of the sea floor occurs above the crestal region of ϵ_2 . In the eastern portion of the study area, the internal architecture of Unit 3 is characterized by a series of large asymmetrical folds consisting of long north-dipping back limbs and shorter and steeper south-dipping forelimbs. (Figs. 5.13, 5.14).

5.1.3. Ridge ϵ_3

Ridge ϵ_3 is a large, generally double-crested anticlinal structure situated to the south of ridge ϵ_2 (Figs. 5.1, 5.2). In the western portion of the study area, it stands as a ~3 km wide structure with a nearly symmetrical cross-sectional geometry, rising ~750 ms above basins β_{3a} and β_{4a} , in the north and south, respectively (Fig. 5.15). The upper evaporite subunit 2a, is generally thickest (<100 ms) beneath the axes of basins β_{3a} and β_{4a} and shows a rapid thinning towards ridge ϵ_3 , attained by convergence of reflectors with minor inter-stratal onlap. Subunit 2a is either underlain by the lower evaporite subunit 2b

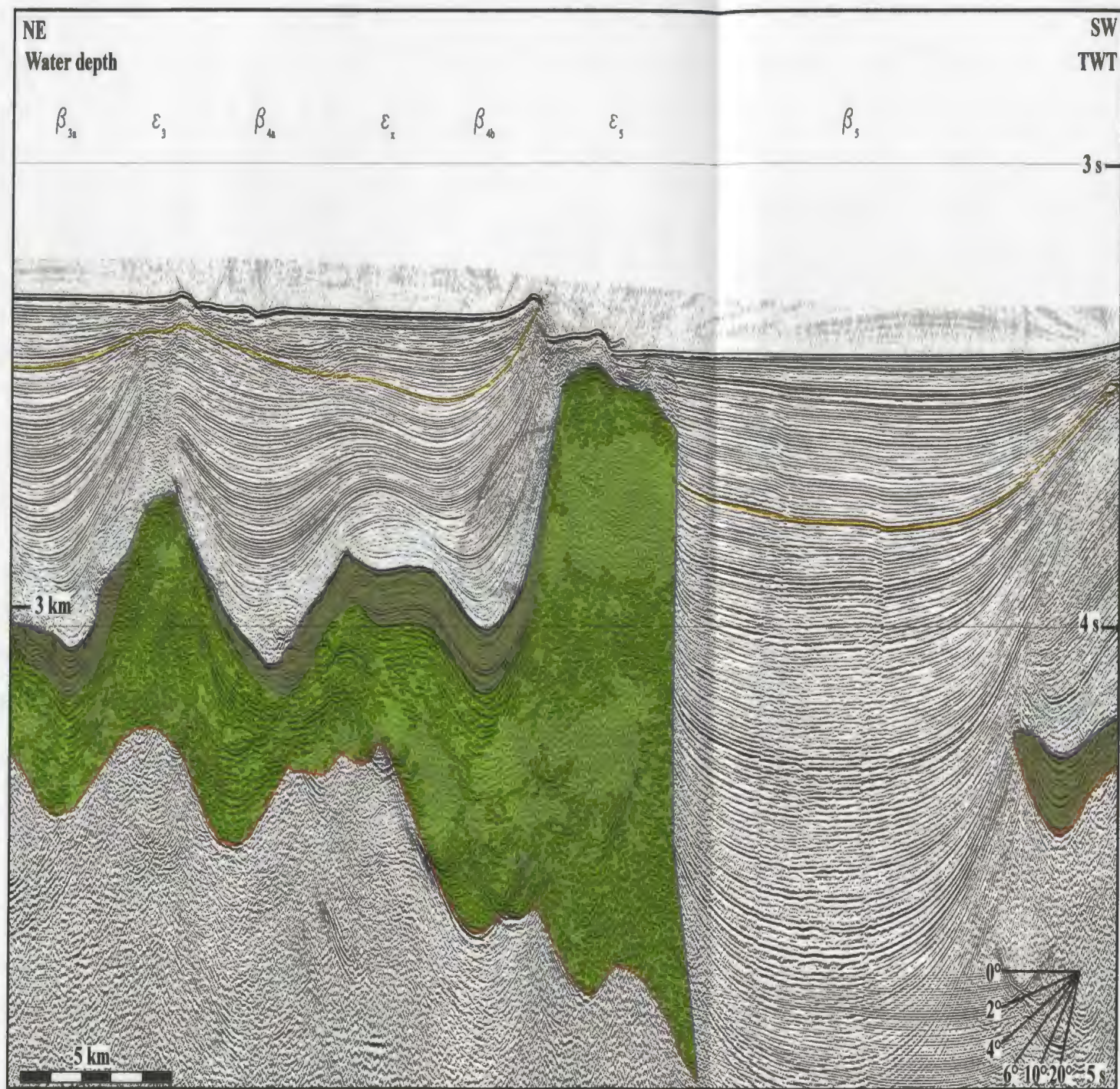
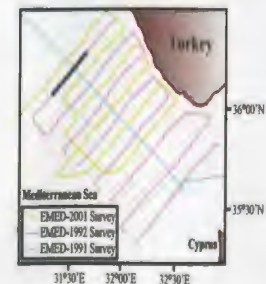


Fig. 5.15. Seismic reflection profile (FLX 1946-1963).

- Top middle Plio-Quaternary subunit
- Top basal Plio-Quaternary subunit
- M-reflector
- Upper evaporite subunit 2a
- Lower evaporite subunit 2b
- Top Unit 3



(Fig. 5.15) or by Unit 3 (Fig. 5.16). Where present, subunit 2b blankets the folded strata of Unit 3 with little thickness variations (Fig. 5.15). In Figure 5.16, the base of subunit 2a is marked by a strong reflector, which truncates the folded strata of Unit 3. Here, a detached package of subunit 2a occurs over the crest of ridge ϵ_3 . The morphotectonic architecture of the core of ridge ϵ_3 is delineated by a series of symmetrical fold structures in Unit 3 consisting of generally longer, gently north-dipping back limbs, and shorter and steeper south-dipping forelimbs (Fig. 5.15)

In the central portion of the study area ridge ϵ_3 is a prominent structure displaying an asymmetrical cross-sectional geometry defined by a long northern flank and a shorter southern flank (Fig. 5.17). The structure rises 1100 ms and 550 ms from the floor of basins β_{3a} and β_4 , respectively. The upper evaporite subunit 2a is thickest (300 ms) beneath the floor of basin β_{3a} and shows a dramatic thinning toward the crest of the ridge, further southward, it continues as a uniform-thickness package (<100 ms) along the southern flank as well as beneath the axial trough of basin β_4 (Fig. 5.17). The observed thinning of subunit 2a is accomplished by the southward convergence of reflectors with minor inter-stratal onlap. The lower evaporite subunit 2b appears as a 700 ms thick lenticular package nestled in the crestal region of ridge ϵ_3 and shows a dramatic northward thinning and pinch-out towards the center of basin β_{3a} . This package also displays a milder southward thinning and continues with a nearly uniform thickness (~200 ms) beneath the floor of basin β_4 (Fig. 5.17). In the seismic reflection profiles, the morphotectonic architecture of the core of ridge ϵ_3 is defined by a series of tight, asymmetrical fold

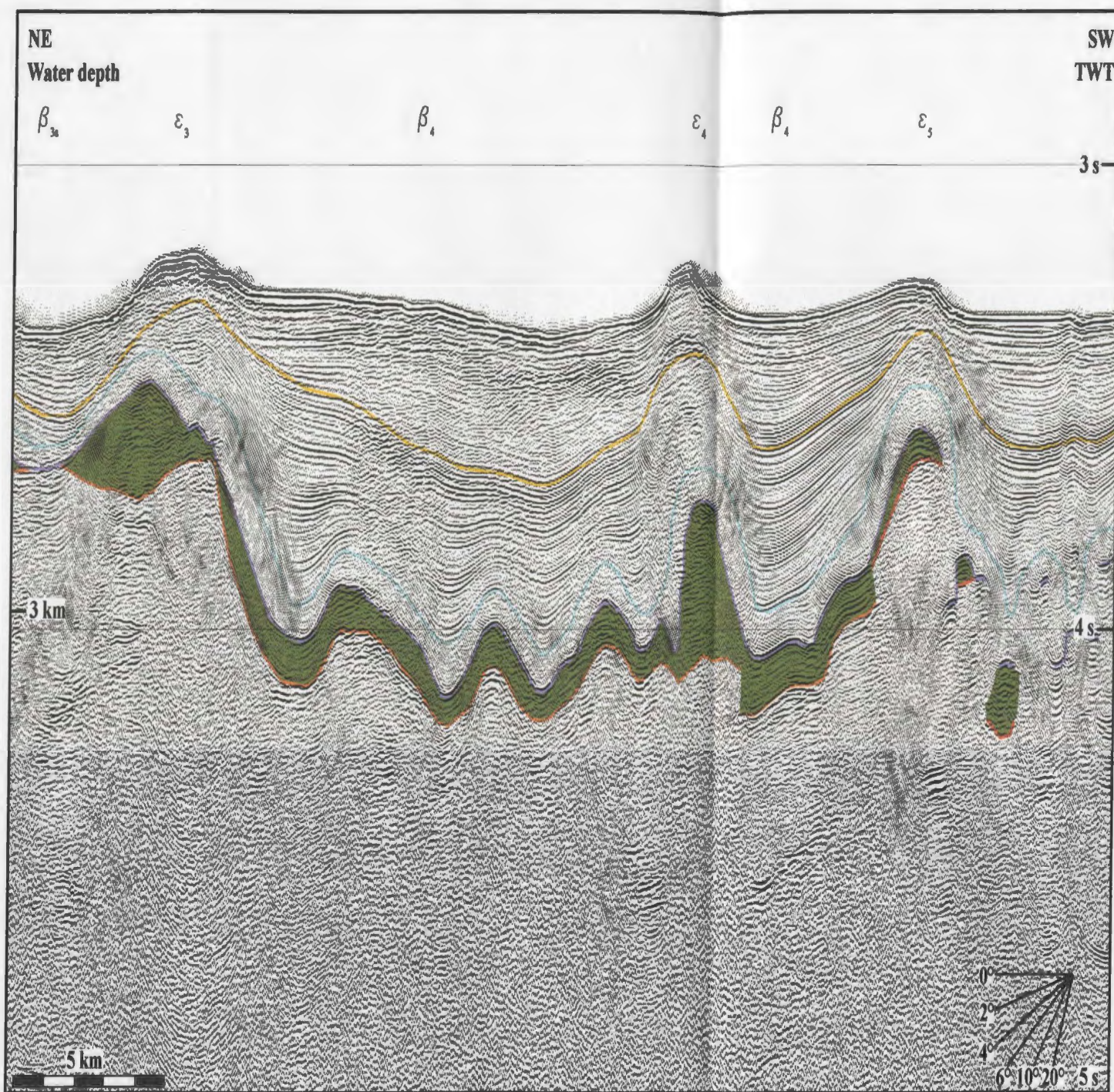
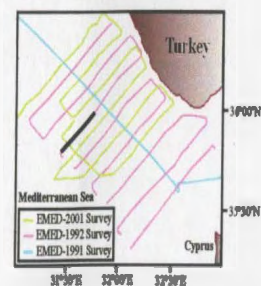


Fig. 5.16. Seismic reflection profile (FIX 1855-1873).

- Top middle Plio-Quaternary subunit
- Upper evaporite subunit 2a
- Top basal Plio-Quaternary subunit
- Top Unit 3
- M-reflector



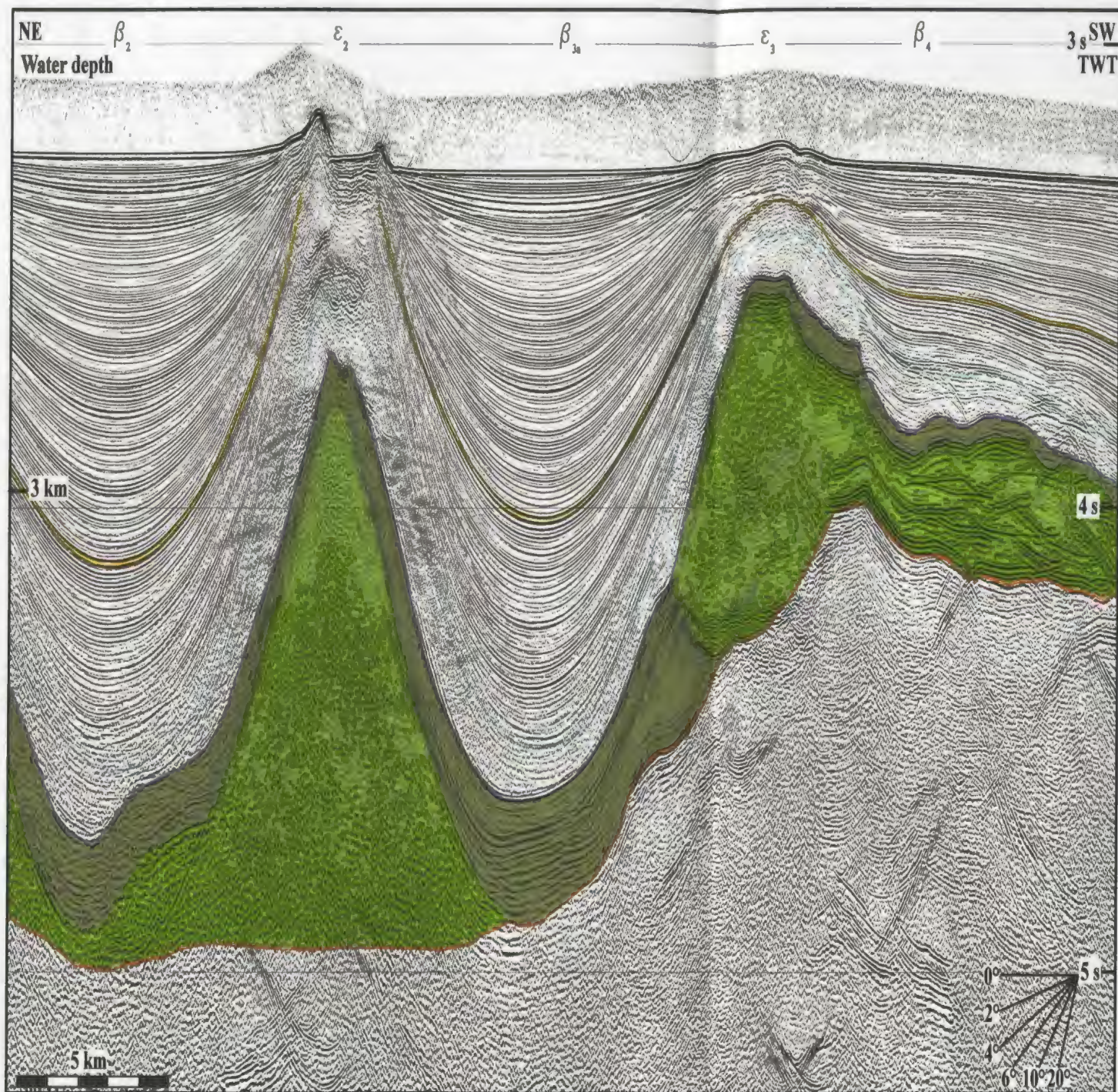
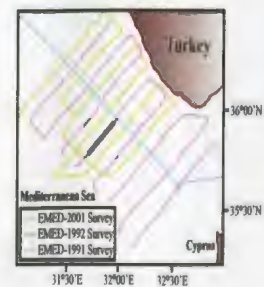


Fig. 5.17. Seismic reflection profile (FLX 1829-1844).

- Top middle Plio-Quaternary subunit
- Top basal Plio-Quaternary subunit
- M-reflector
- Upper evaporite subunit 2a
- Lower evaporite subunit 2b
- Top Unit 3



structures in Unit 3, mimicking the general trend of the overlying base Unit 2, although with gentler slopes along both southern and northern limbs (Fig. 5.17).

Further to the east, ridge ϵ_3 becomes a broad structure (~ 4 km) with the southern segment being separated from its northern counterpart (i.e., ϵ_{31}) by a shallow basin (i.e., β_3 ; Fig. 5.12). The boundary between the upper and lower evaporite subunits, 2a and 2b, is not well-defined, although the base of Unit 2 can be traced through a relatively continuous reflector (Fig. 5.12). Unit 2 blankets the folded successions of Unit 3 with minor thickness variations (~ 300 ms) in the central and southern portion of ridge ϵ_3 , as well as beneath the floor of basin β_4 , while it shows a northward thinning towards the axial trough of basin β_{3b} (Fig. 5.12).

In the eastern portion of the study area, ridge ϵ_3 rises to a <200 ms below-sea-floor depth and displays a triple-crested morphology (Fig. 5.18). It exhibits an asymmetrical cross-sectional geometry across its width with a relatively gently dipping northern flank rising 650 ms above the floor of basin β_{3b} and a mildly steeper southern flank rising 700 ms from the floor of basin β_4 . Here, the upper evaporite subunit 2a is thickest (~ 200 ms) beneath the axes of basins β_{3b} and β_4 and shows rapid thinning towards the flanks of ridge ϵ_3 , attained by the southward and northward convergence of the reflectors with minor inter-stratal onlap. Whereas, it shows a discontinuous character in the crestal area of ridge ϵ_3 and lies with a nearly uniform thickness (< 75 ms) beneath the M-reflector (Fig. 5.18). Subunit 2b defines a lenticular body that underlies subunit 2a within the upper portion of ridge ϵ_3 . It exhibits a prominent pinch-out towards both south

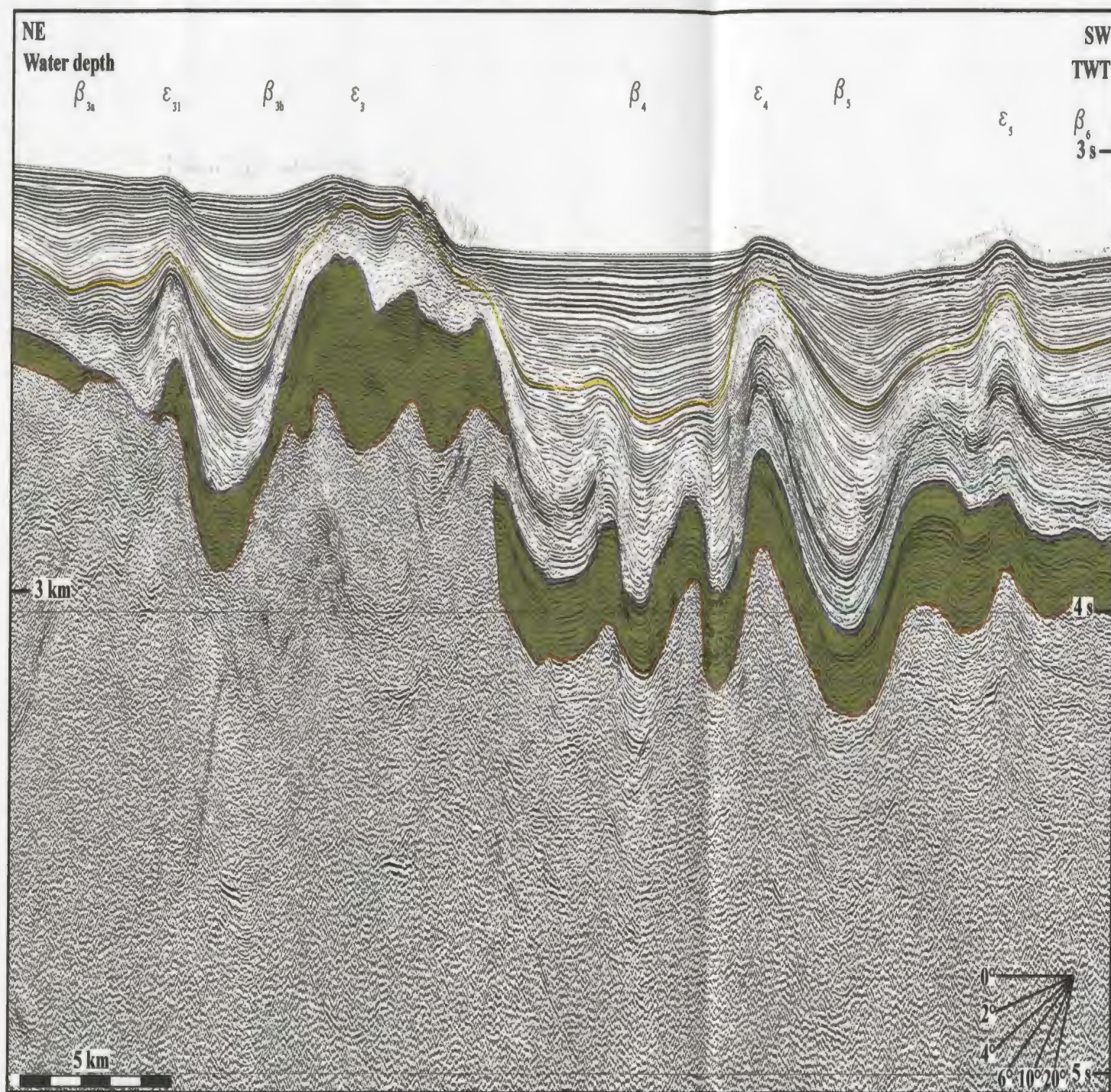
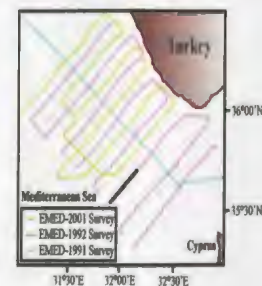


Fig. 5.18. Seismic reflection profile (FIX 1729-1745).

- Top middle Plio-Quaternary subunit
- Upper evaporite subunit 2a
- Top basal Plio-Quaternary subunit
- Top Unit 3
- M-reflector



and north, and is not present beneath the floor of adjacent basins, β_{3b} and β_4 (Fig. 5.18). Here, the boundary between subunits 2a and 2b is well-defined by the abrupt change in the seismic character. The morphotectonic architecture of the core of ridge ϵ_3 is defined by an asymmetrical fold structure, which shows a clear parallelism to the morphology of the overlying M-reflector (Fig. 5.18). Further to the east, ridge ϵ_3 appears attenuated (Fig. 5.19). Here, the gently folded morphology of the M-reflector does not reflect the large-scale morphotectonic architecture of the core of ridge ϵ_3 , which consists of a series of folds with long, gently north-dipping back limbs and a shorter, steeper south-dipping forelimbs (Fig. 5.19). In this portion of the study area, the upper evaporite subunit 2a extends beneath ridge ϵ_3 with a uniform thickness (250 ms), but subunit 2b is absent.

5.1.4. Ridge ϵ_4

Ridge ϵ_4 is a large generally cylindrical anticlinal structure situated to the south of ridge ϵ_3 (Figs. 5.1, 5.2). In the westernmost portion of the study area, the structure stands as a huge wall, rising ~650 ms and >1300 ms from the floors of basins β_{4b} and β_5 , respectively (Fig. 5.15). The upper evaporite subunit 2a is only present beneath the floor of basin β_{4b} and shows a rapid thinning towards ridge ϵ_4 , attained by the southward convergence of reflectors. The base of subunit 2a is delineated by a strong and continuous reflector. In this area, the lower evaporite subunit 2b appears as a sizable package, which is thickest in the crestal region of ridge ϵ_4 but thins beneath basin β_{4b} . Unit 3 exhibits an internal geometry characterized by a series of tight asymmetrical folds consisting of long

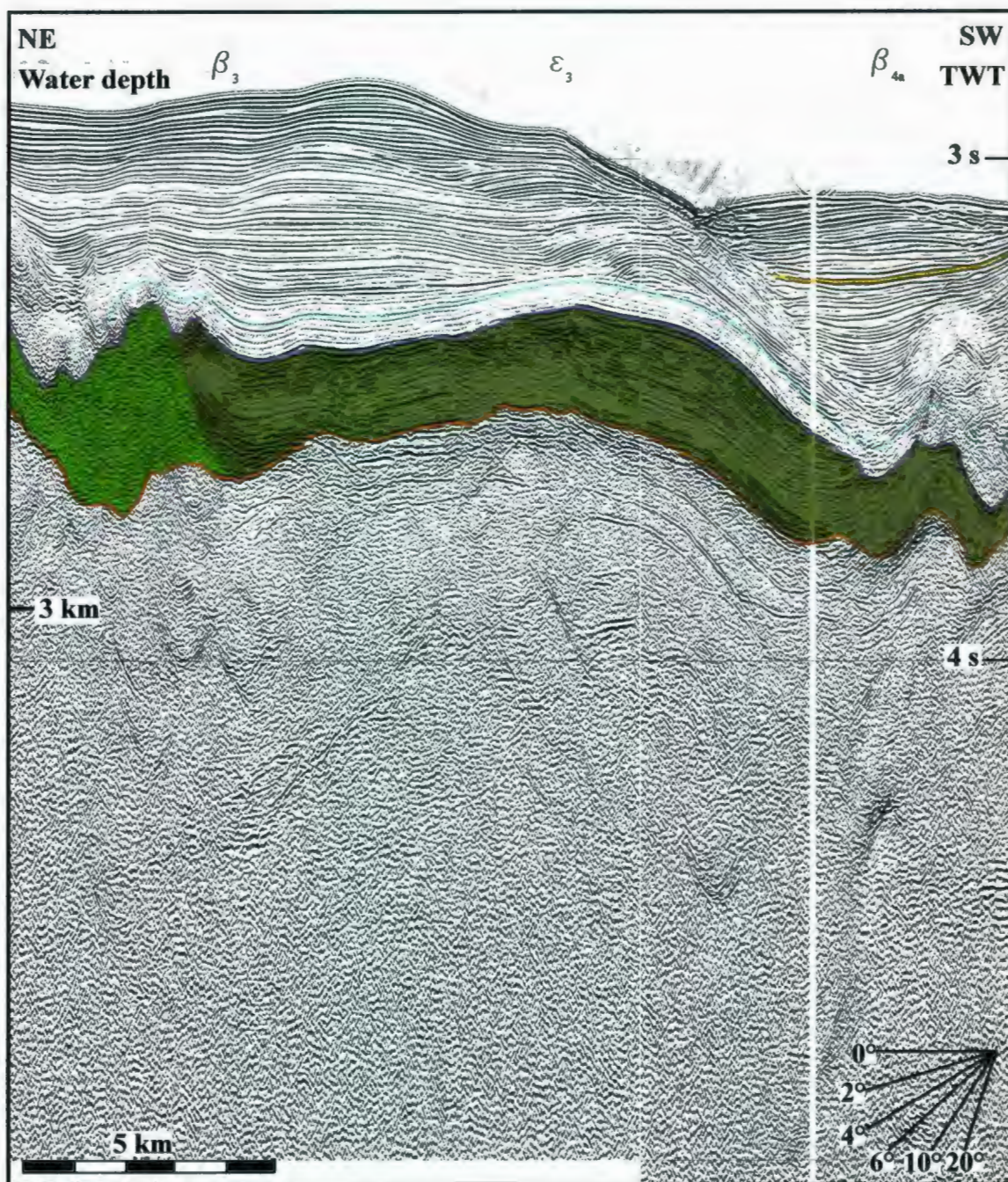
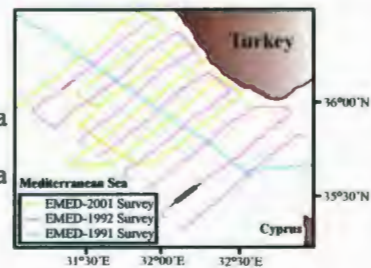


Fig. 5.19. Seismic reflection profile (FIX 1631-1648).

- | | |
|--------------------------------------|------------------------------|
| — Top middle Plio-Quaternary subunit | ■ Upper evaporite subunit 2a |
| — Top basal Plio-Quaternary subunit | ■ Upper evaporite subunit 2a |
| — M-reflector | — Top Unit 3 |



north-dipping back limbs and shorter south-dipping forelimbs (Fig. 5.15). In this portion of the study area, the succession extending beneath basin β_5 is not fully imaged in the seismic reflection profile. Further to the east, ridge ϵ_4 remains as a prominent structural high, although it appears narrower and displays a shorter southern flank rising 600 ms from the floor of basin β_5 (Fig. 5.16). Here, the upper evaporite subunit 2a is confined to beneath basins β_{4b} and β_5 , where it extends with a uniform thickness, but rapidly pinches out at the northern flank of ridge ϵ_4 . The lower evaporite subunit 2b appears as a prominent sub-rectangular package in the crestal area of ridge ϵ_4 and gradually thins northward beneath subbasins β_{4a} and β_{4b} . The geometry of subunit 2b beneath basin β_5 is situated beyond the limit of seismic profiles, thus remains undetermined. The internal architecture of Unit 3 consists of a largely symmetrical fold structure, which generally mimic the morphology of the reflector defining the base of subunit 2b (Fig. 5.16).

In the central portion of the study area, ridge ϵ_4 loses expression and becomes a part of a composite basin nestled between ridges ϵ_3 and ϵ_6 (Fig. 5.20). A thin veneer of upper evaporite subunit 2a and the underlying thicker package of lower evaporite subunit 2b extend across this composite basin with no significant variation in thickness (Fig. 5.20). In this portion of the study area, Unit 3 directly underlies the lower evaporite subunit 2b and displays a complex character associated with the interference of a set of off-plane diffractions. However, the overall folded architecture of the unit is still visible in seismic profiles. Further to the east ridge ϵ_4 displays a symmetrical cross-sectional geometry and rises ~100 ms and 350 ms from the floors of basins β_4 and β_5 , respectively (Fig. 5.21).

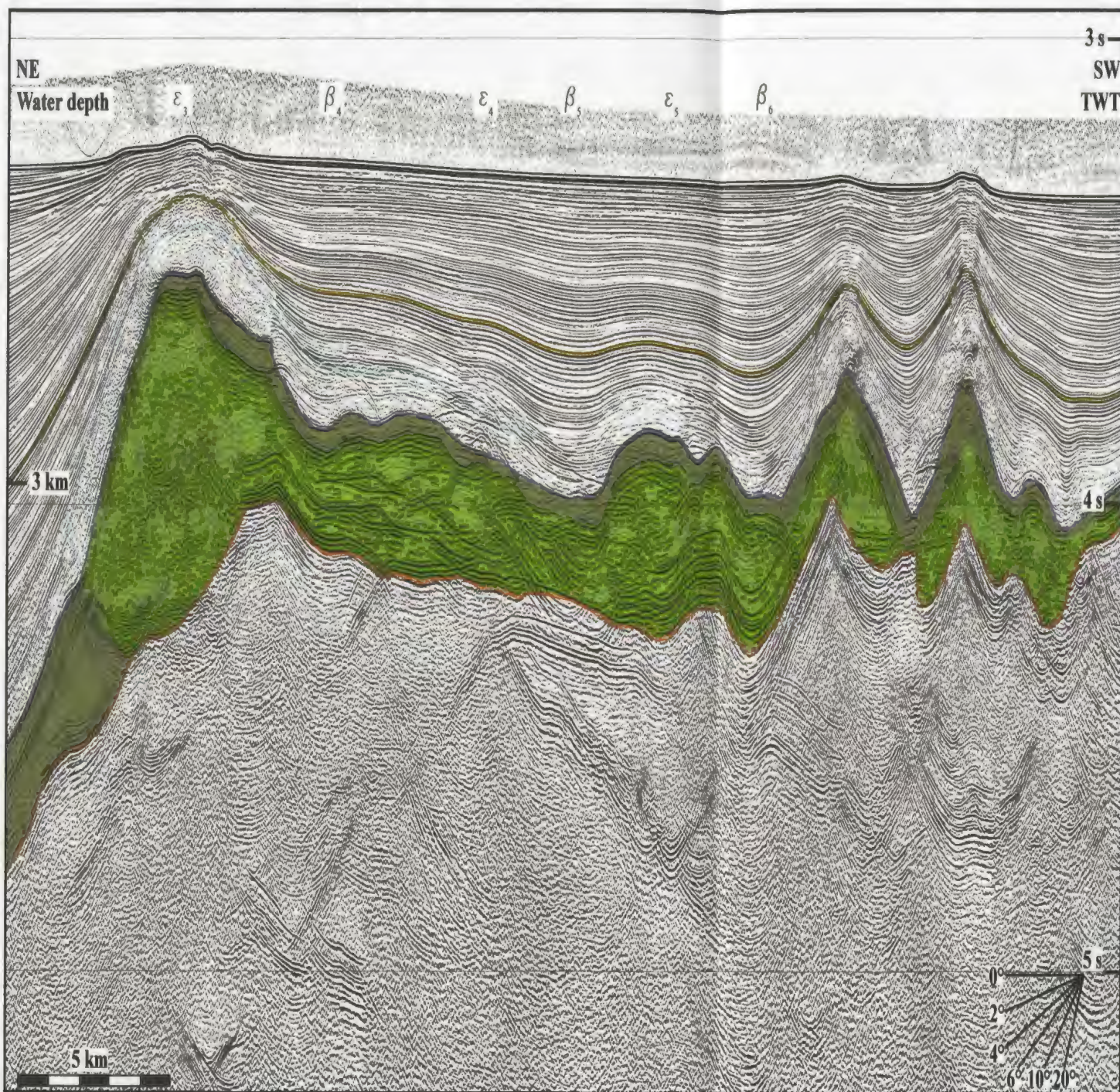
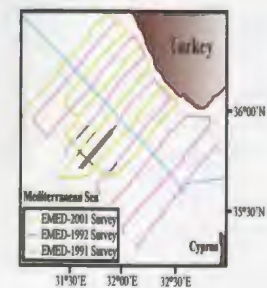


Fig. 5.20. Seismic reflection profile (FIX 1838-1853).



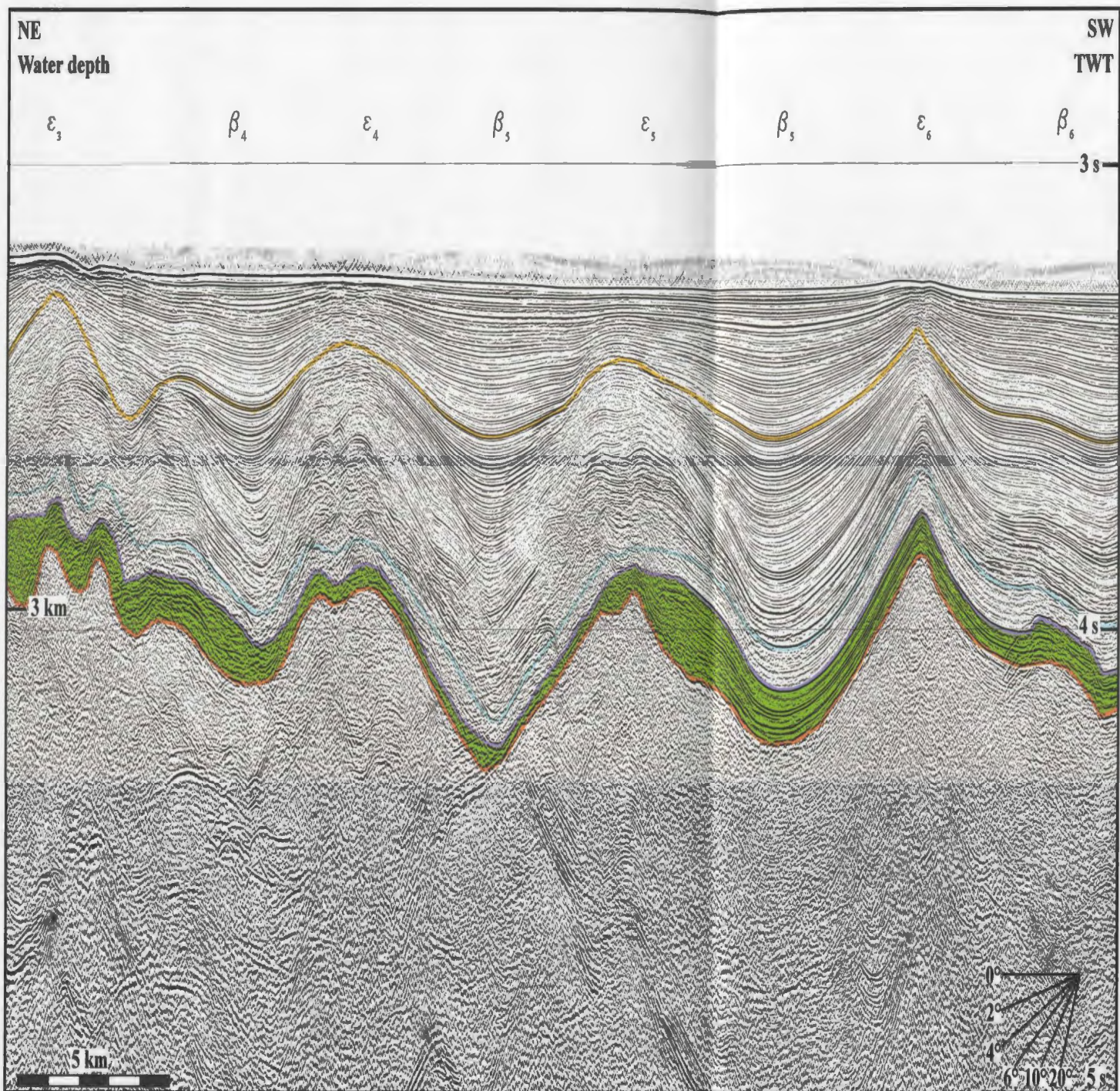
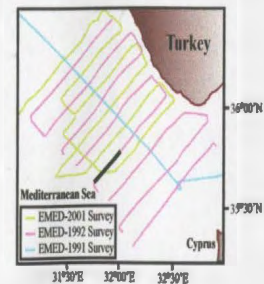


Fig. 5.21. Seismic reflection profile (FLX 1747-1762).

- Top middle Plio-Quaternary subunit
- Lower evaporite subunit 2b
- Top basal Plio-Quaternary subunit
- Top Unit 3
- M-reflector



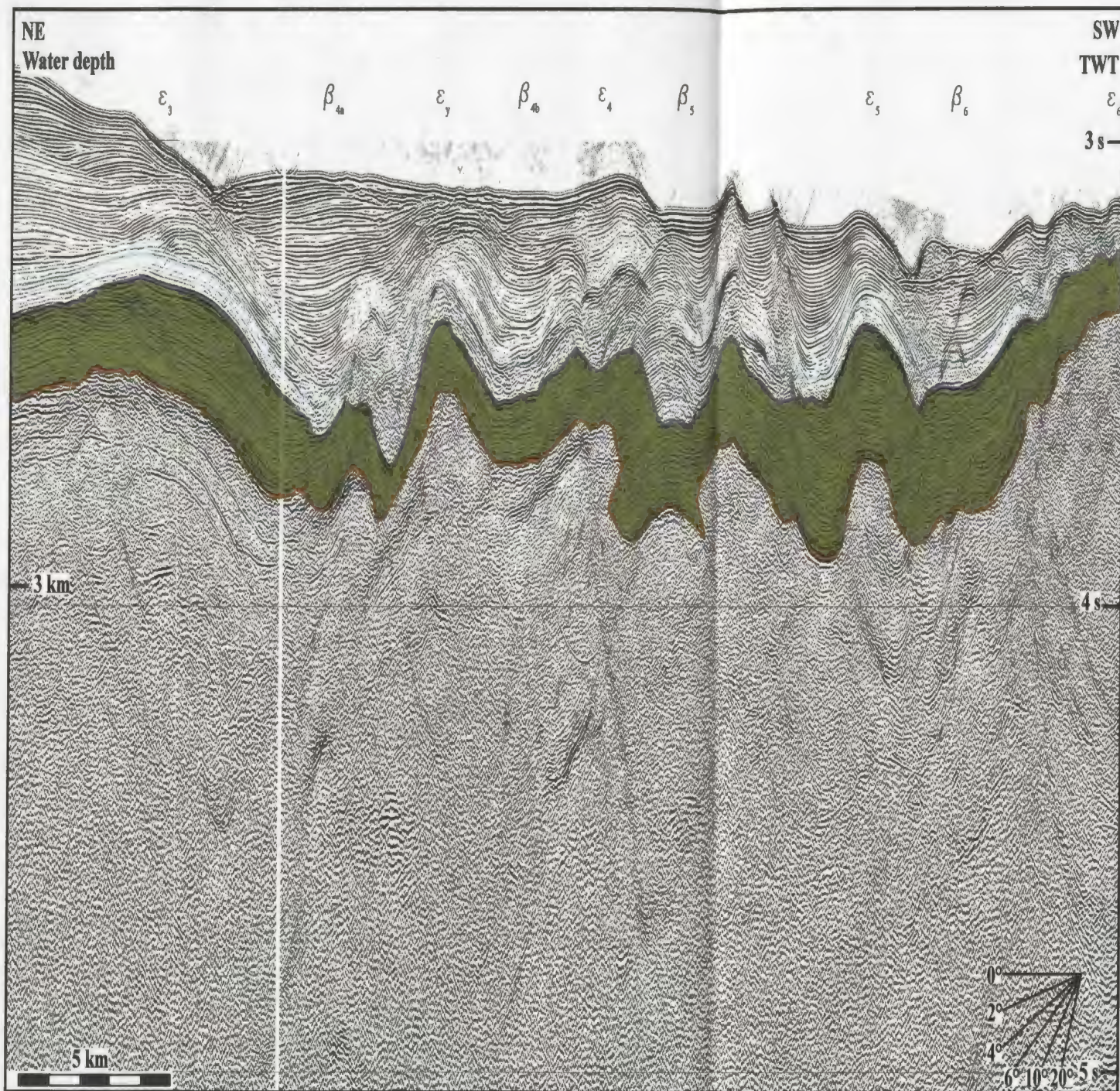
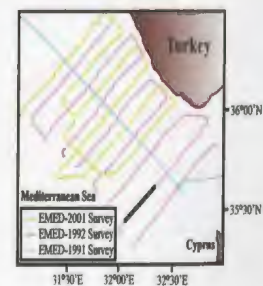


Fig. 5.22. Seismic reflection profile (FIX 1622-1639).

- Top basal Plio-Quaternary subunit
- Upper evaporite subunit 2a
- M-reflector
- Top Unit 3



Here, a thin package of upper evaporite subunit 2a extends across ridge ϵ_4 and basin β_5 and continues northward towards basin β_{4b} with a mild thickening. In this portion of the study area, lower evaporite subunit 2b appears to be missing and Unit 3 directly underlies subunit 2a, the base of which is marked by a strong and continuous reflector. The internal architecture of Unit 3 is characterized by a number of asymmetrical tight fold structures with long north-dipping back limbs and shorter south-dipping forelimbs (Fig. 5.21).

In the eastern portion of the study area, ridge ϵ_4 appears to be narrower and displays a north-slanted asymmetric cross-sectional geometry. The ridge crest rises 250 and 300 ms from the floor of basins β_4 and β_5 , respectively (Fig. 5.18). Here, the sea floor above the crest of the ridge is marked by a minor erosional high. The upper evaporite subunit 2a extends with a uniform thickness across ridge ϵ_4 as well as beneath the floor of basins β_4 and β_5 . The lower evaporite subunit 2b is absent and Unit 3 directly underlies subunit 2a. The base of the upper evaporite subunit 2a is delineated by a remarkable reflector, which truncates the folded strata of the underlying Unit 3. The fold structures that characterize Unit 3 exhibit a corrugated internal architecture which mimics the morphology of the overlying M-reflector (Fig. 5.18). In the easternmost portion of the study area ridge ϵ_4 is poorly defined because of the intensity of the interference of the off-plane diffractions; however the corrugated and folded internal architecture of Unit 3 is clearly visible in seismic profiles (Fig. 5.22).

5.1.5. Ridge ϵ_5

Ridge ϵ_5 is a major anticlinal structure situated to the south of ridge ϵ_4 (Figs. 5.1, 5.2). In the westernmost portion of the study area, it displays an asymmetrical cross-sectional geometry, rising >1000 ms and 500 ms from the floor of basins β_5 and β_6 , respectively (Fig. 5.23). It creates a minor inflection on the sea floor. Detailed examination of seismic profiles show that this region of the sea floor immediately above the crest of ϵ_4 is erosional. The upper evaporite subunit 2a extends across ridge ϵ_5 and beneath basin β_6 with a nearly uniform thickness, although it shows a local thickening beneath the southern flank of the ridge. The upper portion of ridge ϵ_5 exhibits a complex internal architecture consisting of two distinct but identical packages of subunit 2a, which is superimposed on one another separated by a detachment surface (Fig. 5.23). In the crestal region of ridge ϵ_5 , the lower evaporite subunit 2b is missing and subunit 2a directly overlies Unit 3. Here, the internal architecture of Unit 3 is not well imaged and the deep floor of basin β_5 and the underlying older successions remain beyond the limit of seismic reflection profiles. Further to the east, ridge ϵ_5 rises 500 ms and 400 ms above the floor of basins β_5 and β_6 , respectively (Fig. 5.16). The upper evaporite subunit 2a extends with a uniform thickness beneath basin β_5 . It shows an initial thinning towards the northern flank of ridge ϵ_5 , but becomes thicker across the crestal portion of ridge ϵ_5 . Subunit 2a pinches out towards the southern flank of ridge ϵ_5 . Here, the lower evaporite subunit 2b is absent and Unit 3 directly underlies the upper evaporite subunit 2a (Fig. 5.16). The internal architecture of Unit 3 is characterized by a gently northerly dipping homoclinal succession

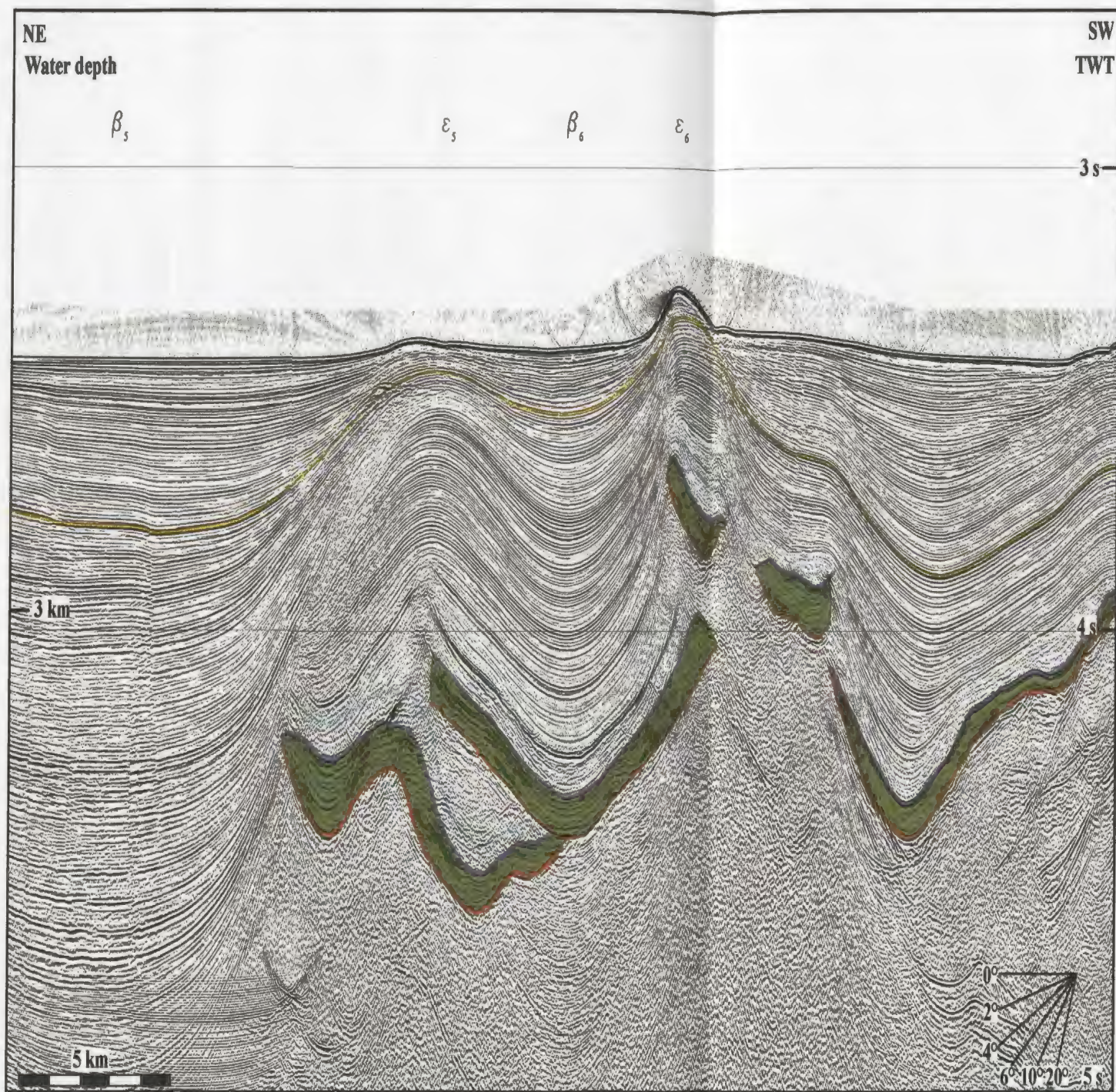
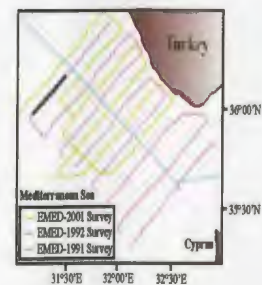


Fig. 5.23. Seismic reflection profile (FIX 1959-1974).

- Top middle Plio-Quaternary subunit
- Upper evaporite subunit 2a
- Top basal Plio-Quaternary subunit
- Top Unit 3
- M-reflector



with minor folds.

In the central portion of the study area, ridge ϵ_5 rises 100-400 ms and 100-250 ms from the floors of basins β_5 and β_6 (Figs. 5.20, 5.21). The upper evaporite subunit 2a extends beneath the M-reflector across ridge ϵ_5 as well as the adjacent basins β_5 and β_6 with generally a uniform thickness. The lower evaporite subunit 2b is present only in the seismic reflection profile closer to the western portion of the study area (Fig. 5.20) and cannot be traced further to east (Fig. 5.21). Where present, it exhibits a constant thickness all across ridge ϵ_5 and beneath the floors of both basins β_5 and β_6 (Fig. 5.21). Unit 3 underlies the upper evaporite subunit 2a and, where present, the lower evaporite subunit 2b (Fig. 5.21). The boundary between Unit 2 and Unit 3 is marked by a strong and continuous reflector. The internal architecture of Unit 3 is delineated by a series of broad open asymmetrical folds; however the lack of resolution in seismic profiles prevent delineation of the detailed architecture of Unit 3 (Fig. 5.21).

In the eastern portion of the study area, ridge ϵ_5 displays a highly asymmetrical external geometry, rising 150-400 ms and <100 ms from the floors of basins β_5 and β_6 (Figs. 5.18, 5.22). The upper evaporite subunit 2a extends with a constant thickness across ridge ϵ_5 as well as beneath the floors of basins β_5 and β_6 (Figs. 5.18, 5.22). The overall thickness of subunit 2a appears to be slightly higher in the easternmost portion of the study area (Fig. 5.22). The lower evaporite subunit 2b is absent and subunit 2a lies directly over Unit 3. The internal architecture of Unit 3 is defined a series of asymmetric folds, which mimic the trend of the overlying M-reflector (Figs. 5.18, 5.22).

5.1.6. Locally Emerging Ridges (referred to as $\epsilon_x, \epsilon_y, \epsilon_{13}, \epsilon_{12}, \epsilon_{31}$)

5.1.6.1. Ridge ϵ_{12}

Ridge ϵ_{12} is a major anticlinal structure, which locally emerges from the floor of basin β_2 in the eastern portion of the study area, separating the larger depocentre β_2 into two smaller subbasins, β_{2a} and β_{2b} (Figs. 5.1, 5.2). The structure shows an asymmetrical cross-sectional geometry, rising 450 ms and 300 ms from the floor of subbasins β_{2a} and β_{2b} , respectively (Figs. 5.13, 5.14). Further to the east and west, the crest of the anticline rapidly plunges and the structure becomes indistinguishable from the adjacent basins (Fig. 5.1, 5.2). The evaporite succession Unit 2 exhibits different characters across the seismic reflection profiles imaging ridge ϵ_{12} . In Fig. 5.13, the upper evaporite subunit 2a is ~100 ms thick beneath the floor of subbasin β_{2a} and shows rapid thinning and pinch-out towards ridge ϵ_{12} . The lower evaporite subunit 2b forms a lenticular package in the crestal area of ridge ϵ_{12} and is separated from the underlying strata of Unit 3 by a prominent reflector (Fig. 5.13). Whereas, further to the east, Unit 2 displays a dramatic thickening. The upper evaporite subunit 2a is confined to beneath the floor of subbasin β_{2b} , where it is thickest along the basin axis, and shows pinch-out towards the southern flank of ridge ϵ_{12} (Fig. 5.14). Here, the lower evaporite subunit 2b can be traced all across ridge ϵ_{12} as well as beneath subbasins β_{2a} and β_{2b} . It is thickest beneath the axial trough of subbasin β_{2b} , shows a mild thinning in the crestal area of ridge ϵ_{12} followed by an abrupt thinning towards subbasin β_{2a} (Fig. 5.14). Both the top and base of the lower evaporite succession is well marked by a strong reflector across the seismic reflection profiles (Figs. 5.13, 5.14). The

internal architecture of the core of ridge ϵ_{12} is characterized by a large asymmetrical fold structure of Unit 3 strata (Figs. 5.13, 5.14).

5.1.6.2. Ridge ϵ_x

Ridge ϵ_x is a wide, low-amplitude anticlinal structure limited to the westernmost portion of the study area (Figs. 5.1, 5.2). The crest of the structure displays a concave geometry and rises 250 ms and 150 ms above the floor of basin β_4 , separating it into two smaller subbasins, referred to as β_{4a} and β_{4b} (Fig. 5.15). A thin, constant-thickness layer of upper evaporite subunit 2a extends below the M-reflector all across ridge ϵ_x as well as subbasins β_{4a} and β_{4b} . It blankets the lower evaporite subunit 2b, which is thickest beneath subbasin β_{4b} and shows a northward thinning towards ridge ϵ_x . The boundary between these two evaporite subunits is well defined along the southern flank of ridge ϵ_x and beneath subbasin β_{4b} , but becomes less clear further to the north (Fig. 5.15). Unit 3 underlies the lower evaporite subunit 2b and exhibits an internal architecture consisting of largely asymmetrical fold structures with long north-dipping back limbs and shorter south-dipping forelimbs (Fig. 5.15).

5.1.6.3. Ridge ϵ_{31}

In the central portion of the study area ridge ϵ_{31} defines a locally prominent anticlinal structure rising 150-300 ms above basin β_3 and separating it into two smaller depocenters, β_{3a} and β_{3b} (Figs. 5.1, 5.2). The structure rises and broadens toward the east

(Figs. 5.12, 5.13). The upper evaporite subunit 2a extends across ridge ϵ_{11} as well as beneath the floor of subbasins β_{3a} and β_{3b} with minor thickness variation. In Fig. 5.12, the lower evaporite subunit 2b appears as a sizable package which directly underlie subunit 2a. It is thickest along the axis of basin β_{3a} and shows a mild thinning towards the crestal region of ridge ϵ_{31} , which is followed by a rapid thinning towards beneath the floor of basin β_{3b} . Unit 3 underlies subunit 2a, or where present subunit 2b and exhibits an internal architecture consisting of a series of fold structures with long northerly-dipping back limbs and shorter southerly-dipping forelimbs (Figs. 5.12, 5.13).

5.1.6.4. Ridge ϵ_y

Ridge ϵ_y is a major local anticlinal structure that emerges from the floor of basin β_4 in the eastern portion of the study area, separating this large basin into two smaller subbasins: β_{4a} and β_{4b} (Figs. 5.1, 5.2). The structure rises 200 ms and 300 ms from the floor of the subbasins β_{4a} and β_{4b} (Fig. 5.22) and display an erosional sea floor above its crest. The upper evaporite subunit 2a extends all across ridge ϵ_y as well as beneath the floors of the adjacent basins. It shows a gentle thinning towards the north accomplished by onlap of internal reflectors against the northern flank of ridge ϵ_y . The base of the upper evaporite succession is delineated by a moderately continuous reflector. The lower evaporite subunit 2b is absent, and Unit 3 directly underlies the upper evaporite subunit 2a. The internal architecture of Unit 3 is characterized by a series of open folds (Fig. 5.22).

5.1.6.5. Ridge ϵ_{13}

Ridge ϵ_{13} is a remarkable but local anticlinal structure, developing above the floor of basin β_2 in the western portion of the study area, separating it into two smaller subbasins, β_{2a} and β_{2b} (Figs. 5.1, 5.2). It is a 3 km wide structure with the crest rising 900 ms and 300 ms from the floor of the subbasins β_{2a} and β_{2b} (Fig. 5.9). The sea floor above the crest of the ridge is erosional in character and marks a minor depression. The upper evaporite subunit 2a is confined to beneath subbasins β_{2a} and β_{2b} , and is thickest along the hinge lines. It shows a pinch-out towards ridge ϵ_{13} , attained by the northward and southward convergence with minor inter-stratal onlap. The base of subunit 2a is marked by a prominent reflector. The lower evaporite subunit 2b is thickest across ridge ϵ_{13} (Fig. 5.9). The base of the lower evaporite succession is defined by a fairly continuous and strong reflector. Unit 3 directly underlies the evaporite succession of Unit 2 and displays and internal architecture consisting of folds with gently dipping back limbs and forelimbs

5.2. Pliocene-Quaternary Basins

The Pliocene-Quaternary sedimentary architecture of the central portion of the Antalya Basin is characterized by the morphology of the M-reflector which delineates a series of NW-SE trending, elongate deep depressions. Most of these basins are situated in deep Antalya Bay, seaward of the continental slope (i.e. abyssal plain basins); however, a few basins also occur between the present-day coastline and the base of continental slope (shelf and slope basins). Figure 5.1 shows the areal distribution of the abyssal plain basins,

referred to as β_1 to β_6 and their bounding ridges ε_1 to ε_5 . These basins are described in the following pages in terms of their stratigraphic architecture and their external geometries as defined by the isopach map of the Pliocene-Quaternary succession over the M-reflector (Fig. 5.2). The identification of the internal architecture is done using a seismic sequence stratigraphical analysis approach.

5.2.1. Shelf and Slope Basins

Several small isolated elongate basins occur nestled along the shelf and the continental slope of the Antalya Basin (Fig. 5.2). These basins are further subdivided based on their internal stratigraphic architecture into (1) shelf basins and (2) slope basins

The shelf basins occur between the present-day coastline and the shelf edge at ~120 m water depth, and are characterized by a seaward thickening Pliocene-Quaternary wedge over the M-reflector (Figs. 5.2, 5.24, 5.25). Laterally, these basins are bounded by the heads of submarine canyons which dissect the shelf edge and upper continental slope (e.g. Fig. 5.26). The internal architecture of the shelf basins is generally characterized by a seaward prograding clinoform package that shows vertical stacking of individual prograded units. The most prominent of these occur at the present-day shelf break where a distinct shelf-crossing unconformity delineates the top of the uppermost prograded package. Internally the oblique progradational clinoforms suggest that most sediments are used for seaward progradation with little or no vertical stacking for the middle-to-upper Pliocene-Quaternary (Fig. 5.24). A nearly uniform-thickness package with mainly gently

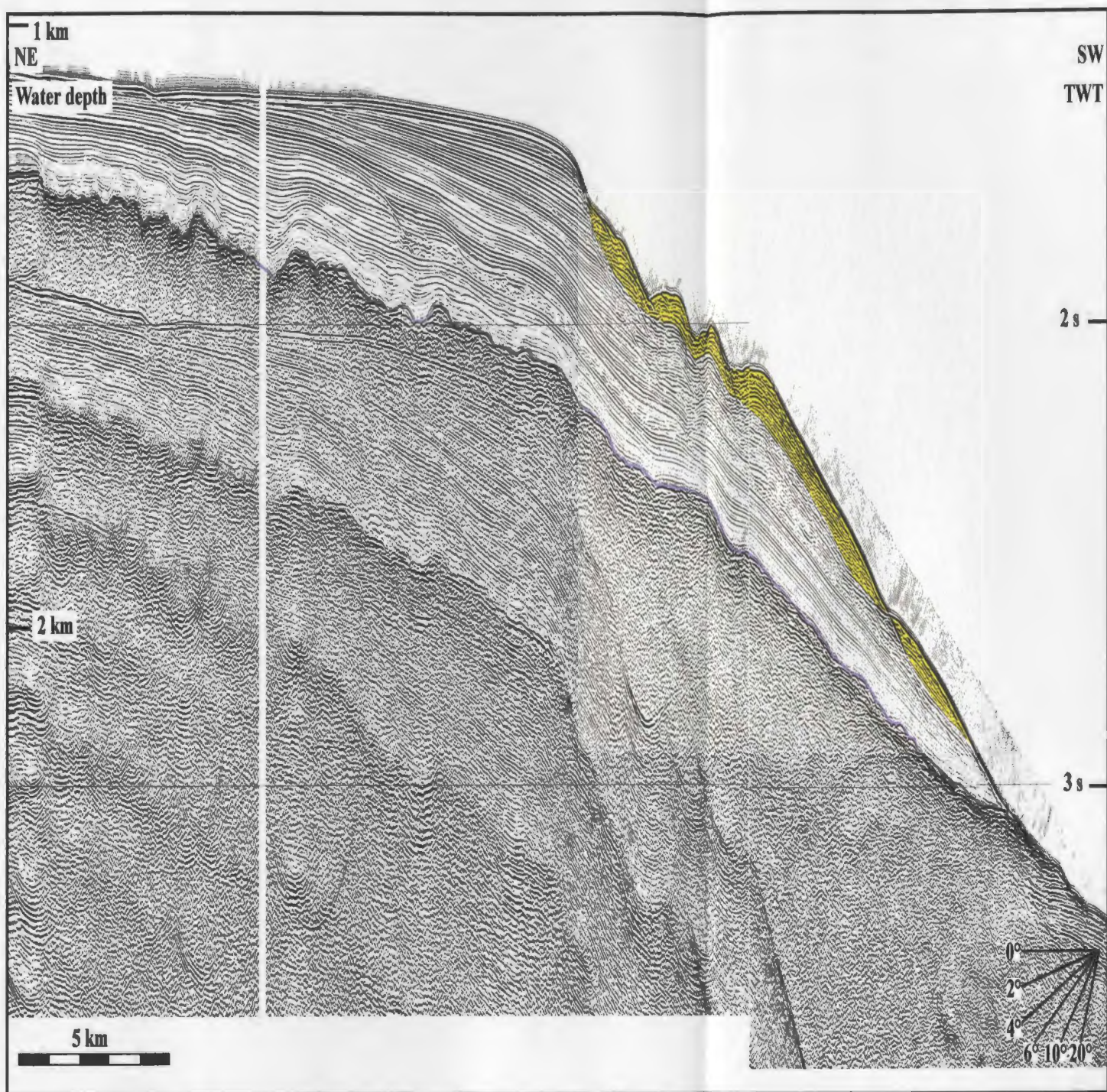
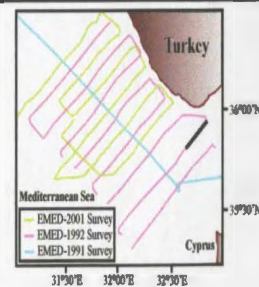


Fig. 5.24. Seismic reflection profile (FIX 1672-1684).



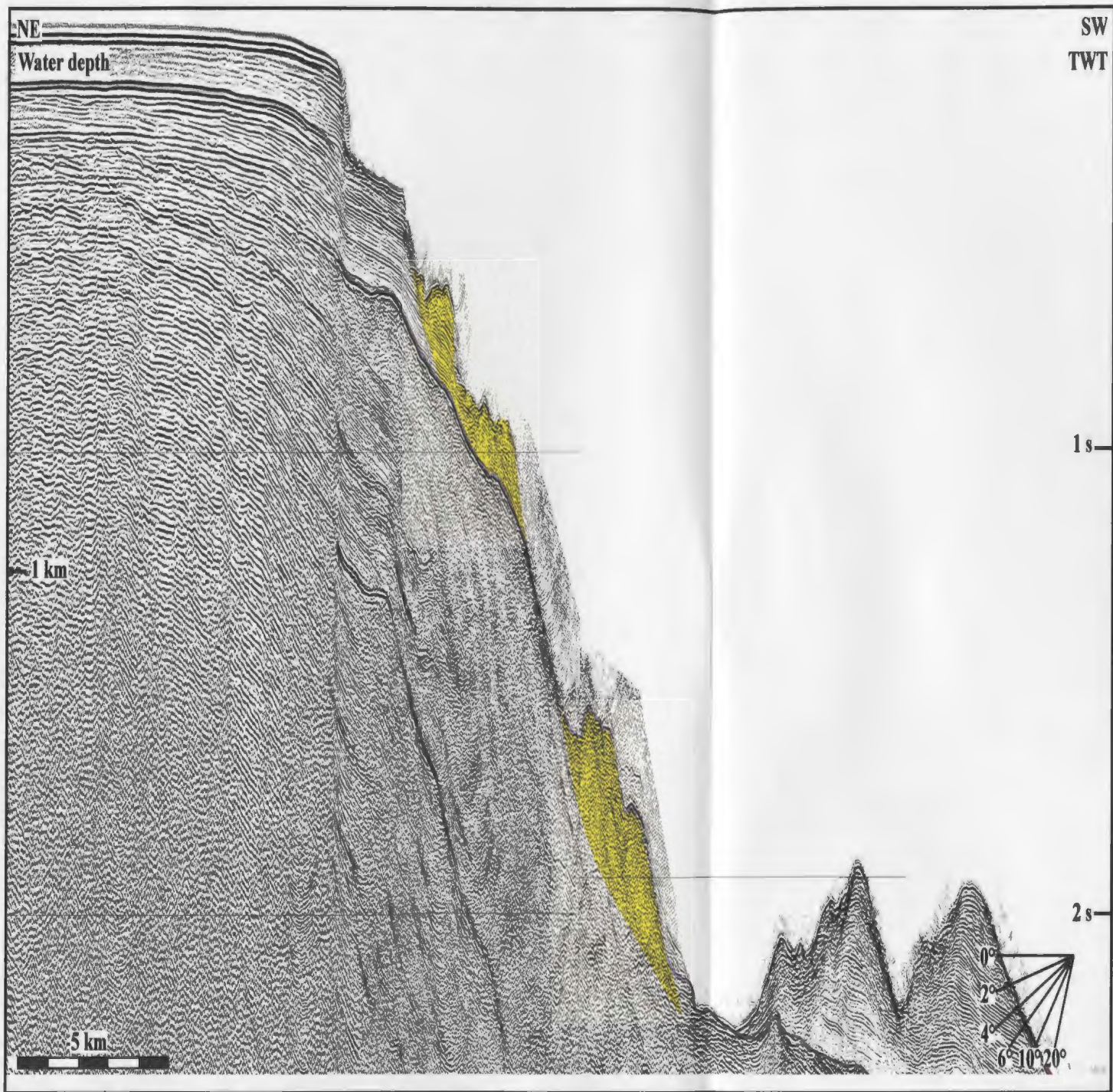
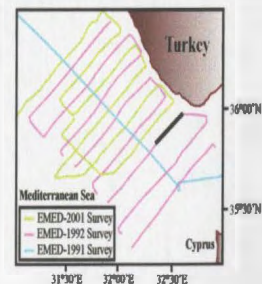


Fig. 5.25. Seismic reflection profile (FIX 1690-1705).

— M-reflector

Slide/slump masses



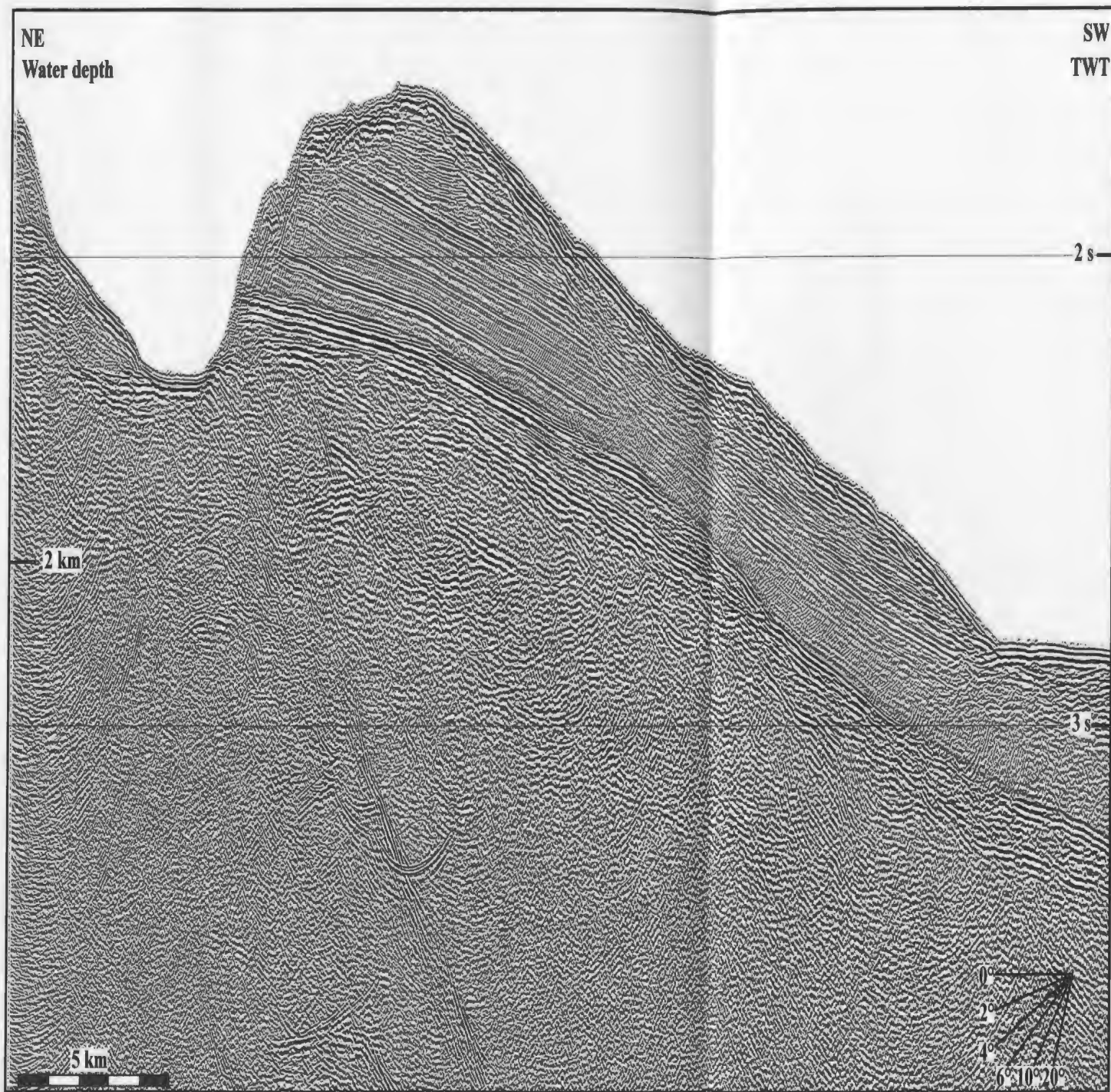
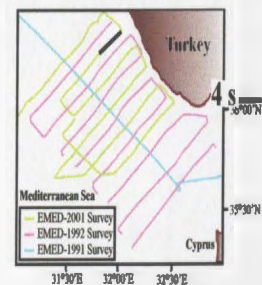


Fig. 5.26. Seismic reflection profile (FIX 481-491).

— M-reflector



seaward-dipping reflectors locally forms the base of the Pliocene-Quaternary succession and rests unconformably over the M-reflector.

In nearly all seismic profiles, the shelf edge is marked by a distinct set of moderately to steeply seaward-dipping detachment surfaces that truncate most of the upper to middle Pliocene-Quaternary succession, each detachment leaving a distinct scar and step on the sea floor (e.g. Figs. 5.24, 5.25). In some profiles these detachment surfaces display progressively flattened trajectories seaward, becoming emergent at the sea floor (e.g. Fig. 5.24). Yet in others, the detachment surfaces merge along common, bedding-parallel discontinuities (e.g. Fig. 5.25). As a result, the upper segment of the slope, immediately seaward of the shelf edge includes a series of tacked and seaward shingled wedge-shape bodies (Fig. 5.25).

Slope basins occur between the shelf edge and the base of slope, and are characterized by an interplay between deposition along the continental margin and gravity-driven slope processes, leading to the development of isolated Pliocene-Quaternary packages in the isopach map (Fig. 5.2). Slope basins are well-delineated throughout the continental slope, although, they are better developed along the lower slope where the slope gradient is significantly lower than the upper slope. In the steeply dipping upper portion of the slope, the architecture of the Pliocene-Quaternary succession is characterized by a number of wedge shaped bodies situated above bedding-parallel detachment surfaces that occur at various levels within the succession (Figs. 5.25, 5.27). These detachment surfaces have high-angle trajectories in the upper portion of the

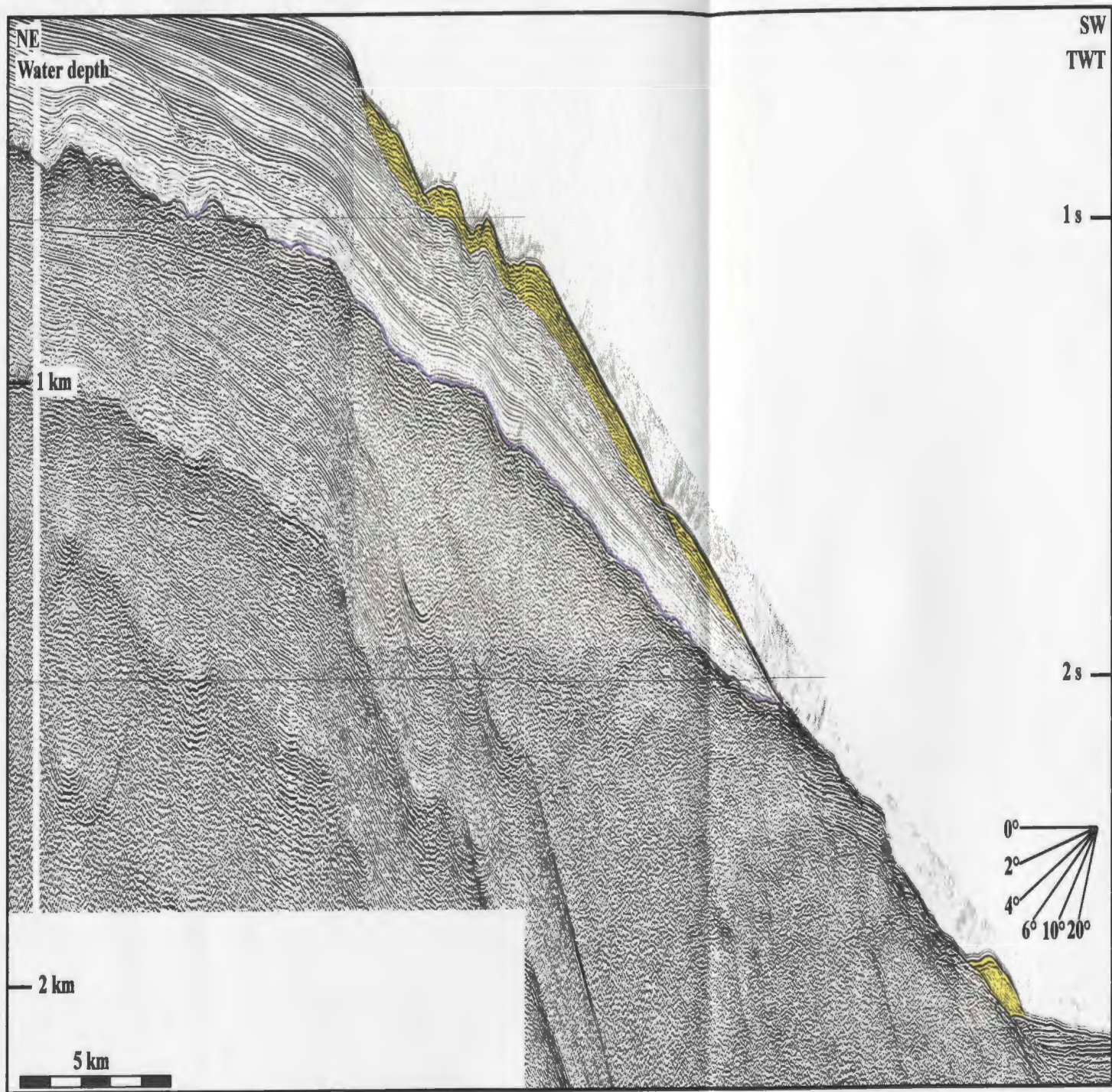
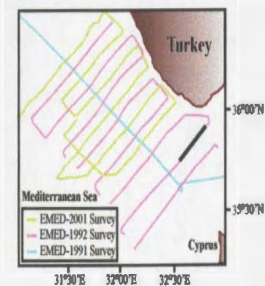


Fig. 5.27. Seismic reflection profile (FIX 1677-1662).

— M-reflector

Slide/slump masses



Pliocene-Quaternary succession, but become gentler as traced down section, where they merge in a common detachment surface. Where exposed on the sea floor, the M-reflector coincides with this common detachment surface. Generally, the internal architecture of the wedge-shaped packages display a chaotic seismic architecture with little coherent continuous reflections. Truncation of the upper strata at the sea floor is clearly visible across almost all seismic reflection profiles. In the lower slope regions where the slope gradient is small, a thicker, well-stratified package of Pliocene-Quaternary strata with an undisturbed internal architecture occurs (Figs. 5.28, 5.29, 5.30). Occasional small perched-basins occur along the lower slope (Fig. 5.31).

5.2.2. Abyssal Basins

All basins in the study area define northwest-southeast trending elongate synclines, nestled between the similar-trending ridges, with doubly-plunging synclinal axes (Fig. 5.1)

5.2.2.1. Basin β_1

Basin β_1 is a large depocentre situated between the base of Turkish continental slope in the north and ridge ϵ_1 in the south. Isopach map of the Pliocene-Quaternary succession shows that basin β_1 consists of three subbasins (Fig. 5.2). The western and central subbasins comprise the deep portion, whereas the eastern basin comprises the shallower portion of basin β_1 . The western subbasin is 30 km long and 12 km wide, and shows an asymmetrical cross-sectional geometry across its width with the axial trough in

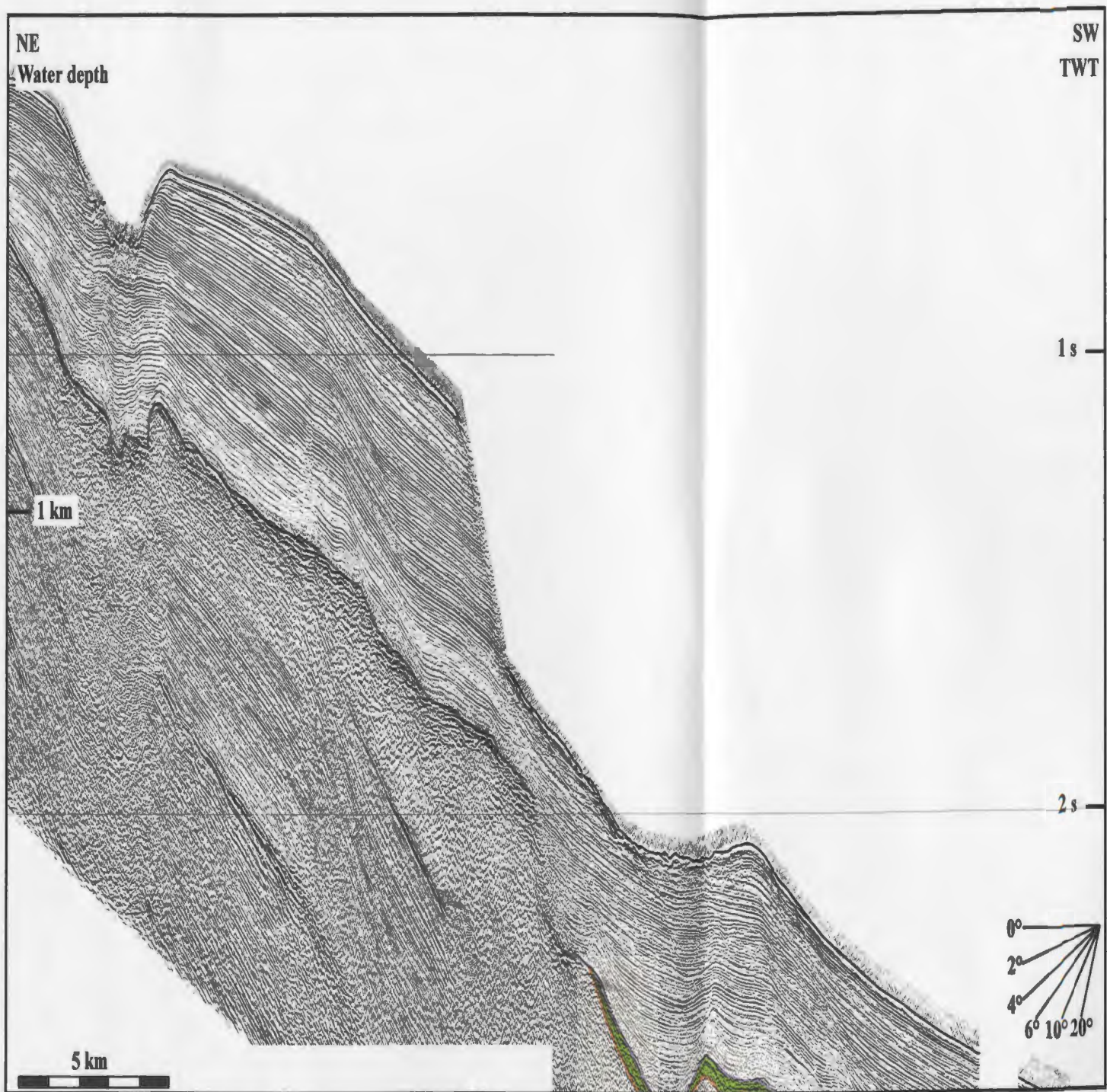
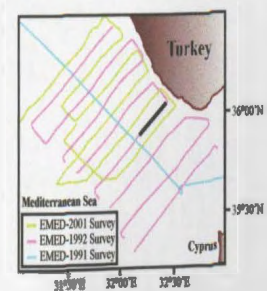


Fig. 5.28. Seismic reflection profile (FLX 1798-1782).

- M-reflector
- Top Unit 3
- Lower evaporite subunit 2b



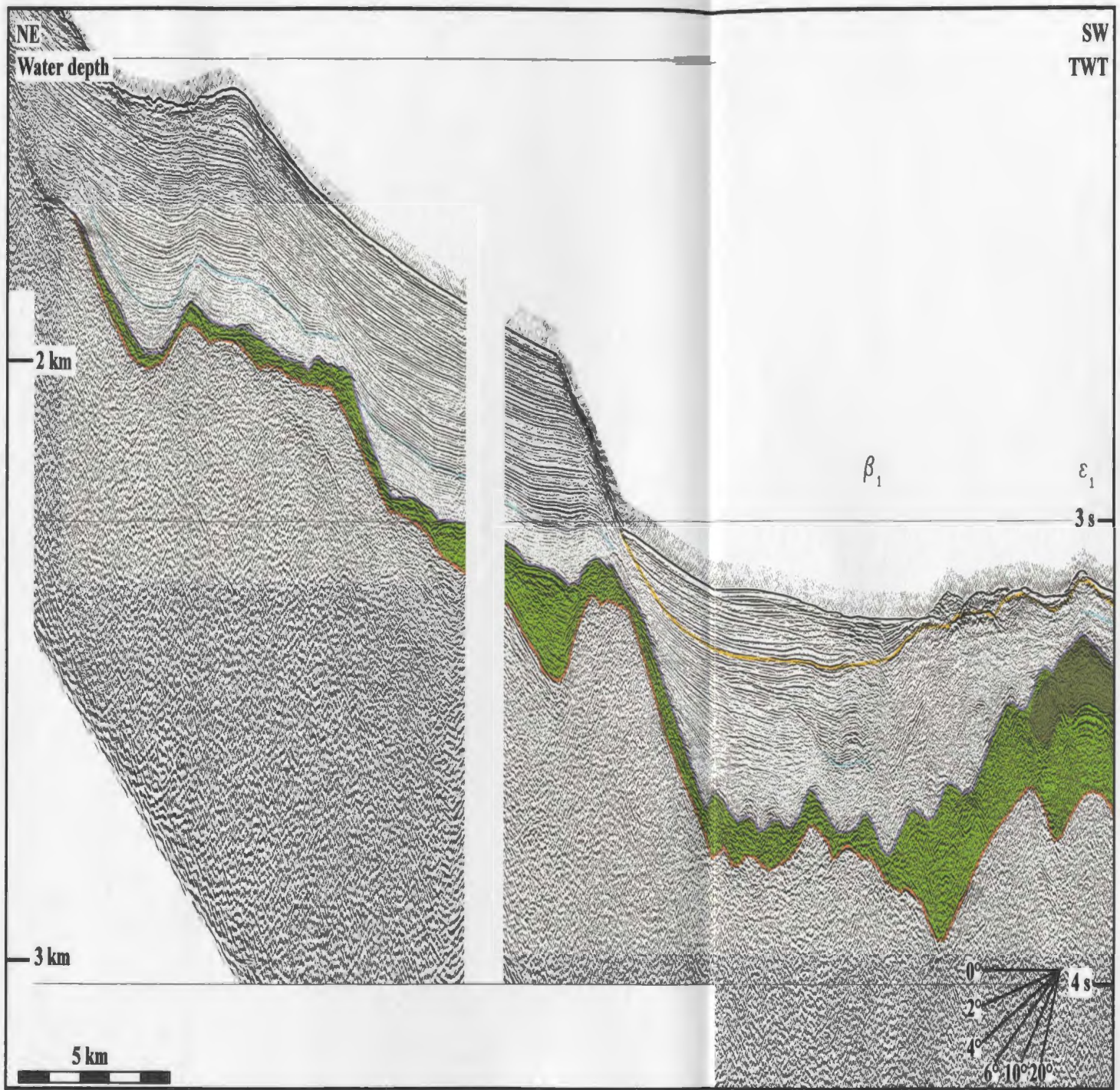
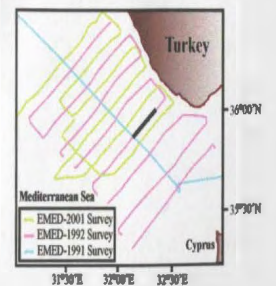


Fig. 5.29. Seismic reflection profile (FIX 1789-1773).

- Top middle Plio-Quaternary subunit
- Top basal Plio-Quaternary subunit
- M-reflector
- Upper evaporite subunit 2a
- Lower evaporite subunit 2b
- Top Unit 3



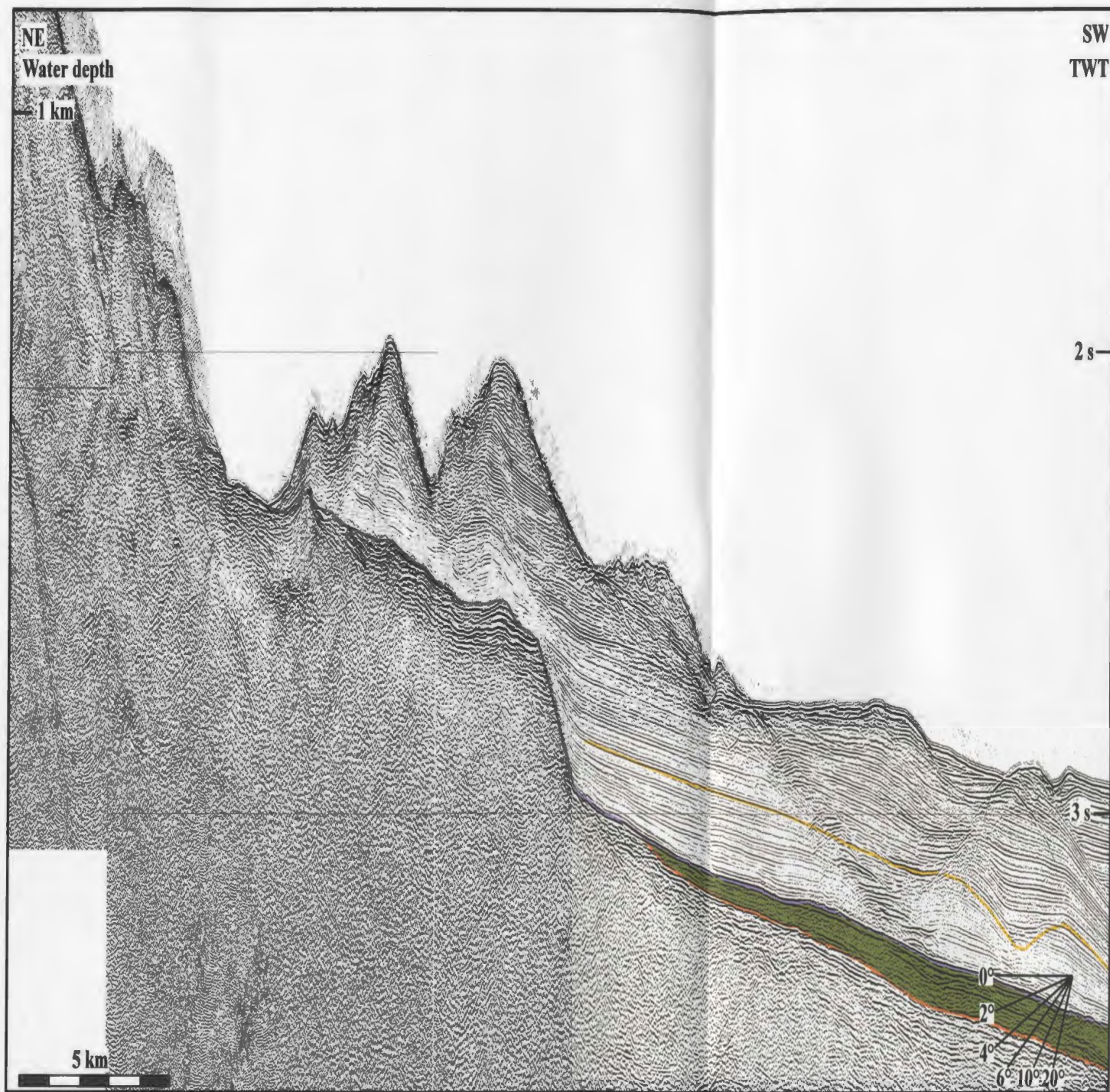


Fig. 5.30. Seismic reflection profile (FIX 1698-1709).

- Top middle Plio-Quaternary subunit
- Upper evaporite subunit 2a
- M-reflector
- Top Unit 3

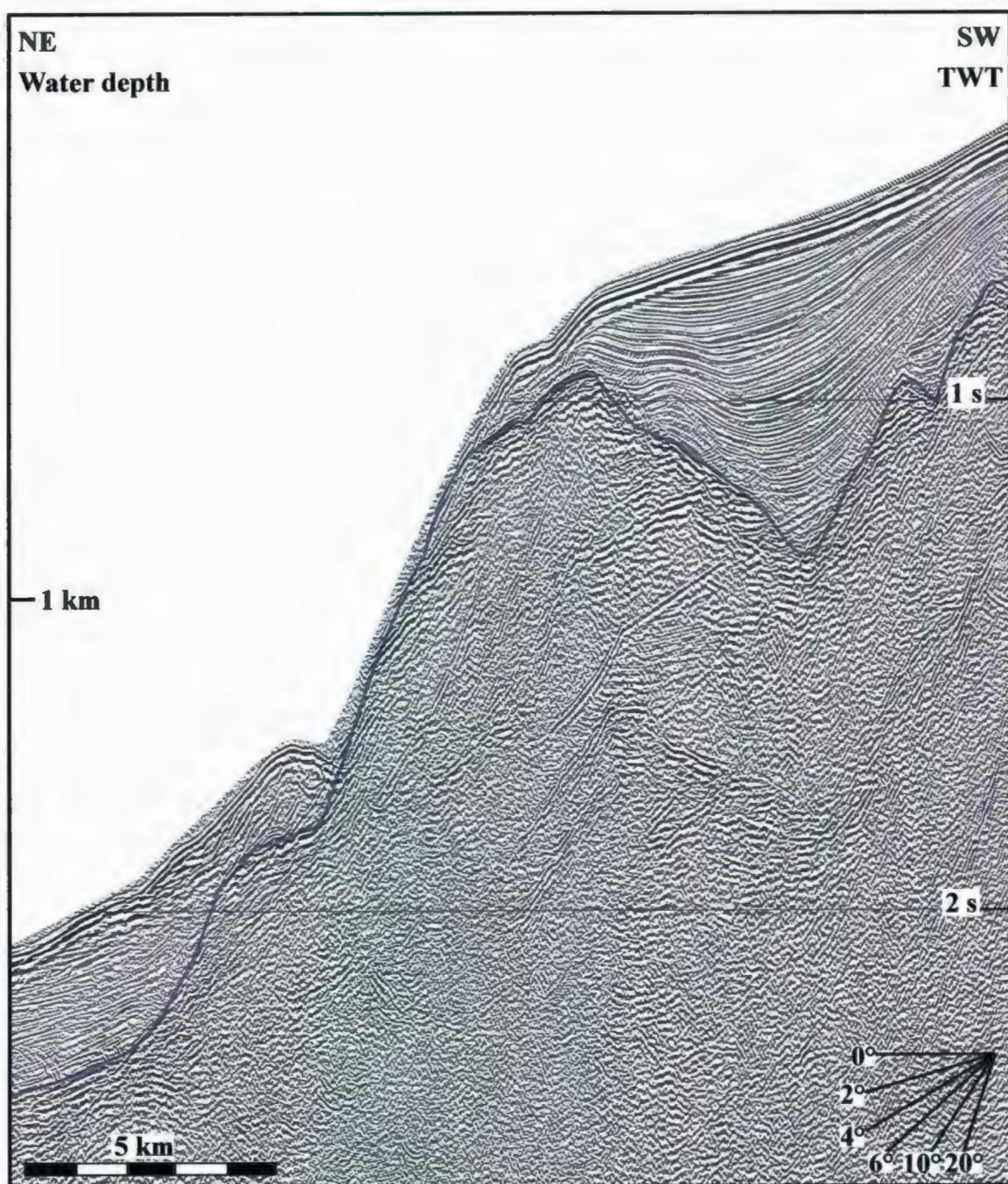
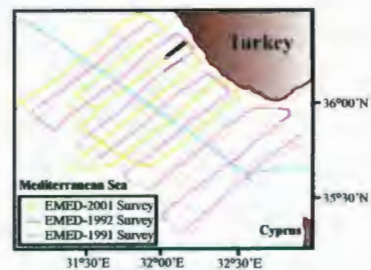


Fig. 5.31. Seismic reflection profile (FIX 569-579).

— M-reflector



the lowest portion of the Pliocene-Quaternary succession being located in the southern segment of the basin (Figs. 5.3, 5.4). The central subbasin is 20 km long and 7 km wide, and displays a symmetrical cross-sectional geometry across its width. These two subbasins are connected with each other through a narrow sill. The eastern subbasin is 30 km long and is considerably narrower than the northern and central subbasins, although its northern boundary is not well-defined in seismic profiles.

All three subunits of the Pliocene-Quaternary succession are present throughout basin β_1 . The thickness variation and the internal architecture of the Pliocene-Quaternary basin fill in western and central subbasins show notable similarities (Fig. 5.2). Across these subbasins, the M-reflector defines a gently south-dipping erosional surface marking the northern flanks of these depocentres. It extends as high as the depositional surface along the continental slope, locally becoming exposed on the seafloor where it creates a sharp boundary between the basin β_1 and the slope basins at higher elevations. Further in the central portion of these subbasins, the M-reflector shows a concave geometry delineating a narrow trough. Traced toward the south, the M-reflector defines a steeply northeast-dipping surface along the northern flank of the ridge ϵ_1 (Figs. 5.3, 5.4, 5.5). The Pliocene-Quaternary succession is thickest in the south-central portions of the western and central subbasins and shows dramatic overall thinning to the northeast and southwest. Within the deepest portion and along the axial trough of both the western and central subbasins the lowermost portion of the Pliocene-Quaternary succession exhibits a conformable contact with the underlying M-reflector. A similar relationship is generally

observed along the northeastern slope of ridge ϵ_1 , where the lower and middle Pliocene-Quaternary subunits define a northeast-dipping homoclinal succession (Figs. 5.3, 5.5, 5.7, 5.8). In both the western and central subbasins, the lower to upper subunits of the Pliocene-Quaternary succession show a remarkable northward progressive onlap over the M-reflector. The total thickness of the Pliocene-Quaternary succession lost to onlap ranges from 900 ms in central subbasin to 1100 ms in western subbasin. Within the western and eastern subbasins, the upper Pliocene-Quaternary subunit also displays a prominent south-directed progressive onlap over a local unconformity developed at the top of middle Pliocene-Quaternary subunit along the northeastern flank of ridge ϵ_1 (Figs. 5.3, 5.6, 5.8). In the southern portion of the western subbasin, the Pliocene-Quaternary succession is characterized by a symmetrically-corrugated internal architecture, which is also reflected on the morphology of the sea floor (Fig. 5.4). One of the most prominent elements of this architecture is the moderately southwest-dipping internally parallel detachment surfaces that frequently curve into bedding-parallel surfaces. This corrugated morphology of the Pliocene-Quaternary succession is not represented by the morphology of the M-reflector. Along the northernmost portion of the basin β_1 , a number of thin (10 ms-thick) wedge-shaped and/or lenticular seismic packages are identified within the upper Pliocene-Quaternary succession (Figs. 5.3, 5.5). The base of these thin units are often marked by small, local unconformities. These units are generally stacked one on top of the other and display weak and/or chaotic internal seismic expression (e.g. Fig. 5.5).

5.2.2.2. Basin β_{1a}

Basin β_{1a} is a small depocentre situated between ridges ε_1 and ε_{11} (Figs. 5.1, 5.2, 5.3, 5.4). It can only be traced from the northwestern to the central segment of the study area through a strike length of 47 km and a width of 20 km. It shows an asymmetrical cross-sectional geometry across its width. The basin loses its expression in the eastern segment of the study area, where ridges ε_1 and ε_{11} merge (Figs. 5.1, 5.2). The floor of the basin β_{1a} is well-imaged in seismic profiles where the M-reflector defines a narrow depression (Fig. 5.3). Traced from the northwest to the southeast, the overlying Pliocene-Quaternary succession shows an abrupt thickening to 1050 ms, followed by a gradual thinning to 350 ms.

In the northwestern segment of β_{1a} , the lowermost portion of the Pliocene-Quaternary succession shows a prominent northeast-directed downlap over the M-reflector along the axis of the basin (Fig. 5.8). However, the lower-to-upper subunits of the Pliocene-Quaternary succession show a notable southwest-directed onlap against the M-reflector along the northern flank of ridge ε_{11} , while along the southern flank, they display a conformable contact with the underlying M-reflector. The overall northeast-dipping character of the reflectors within the Pliocene-Quaternary succession defines a 'roll-over' geometry. This unique internal geometry is more pronounced in the northwestern segment of the study area, where, the reflectors within the upper subunit of the Pliocene-Quaternary succession are truncated at the seafloor. Towards the southeast where the roll-over starts to lose its expression, the tilted character of the reflectors

becomes confined to the lower portion of the Pliocene-Quaternary succession and the middle to upper subunits follow the morphology of the seafloor (Figs. 5.3, 5.4).

5.2.2.3. Basin β_2

Basin β_2 is a very large depocentre situated between ridge ϵ_{11} in the north and ridge ϵ_2 in the south (Figs. 5.1, 5.2). In the survey area, basin β_2 consists of three subbasins: the 46 km long and 32 km wide western subbasin, the 26 km long and 15 km wide central subbasin, and the 40 km long and 18 km wide eastern subbasin. The development of ridges ϵ_{13} in the west and ϵ_{12} in the east partitioned the larger depocentre β_2 into two prominent subbasins: β_{2a} and β_{2b} (Figs. 5.1, 5.2, 5.9, 5.13). In the northwestern portion of the study area the axial trough of basins β_{2a} and β_{2b} progressively converge toward the southeast associated with the southeast plunge of the crest of ridge ϵ_{13} (Fig. 5.1). Similarly, in the southern portion of the study area, the axis of basins β_{2a} and β_{2b} converge toward the northwest associated with the northwest plunge of the crest of ridge ϵ_{12} (Fig. 5.1). The merging of these basins resulted in the development of a somewhat narrower, but remarkably deep basin within the central segment of the study area (Figs. 5.1, 5.2, 5.6, 5.10, 5.11). Isopach map of the Pliocene-Quaternary succession clearly shows this basin architecture (Fig. 5.2).

In the southeastern portion of the study area there are two internally parallel subbasins (β_{2a} and β_{2b}) which contain 650-1100 ms of Pliocene-Quaternary sediments over the M-reflector. The northern of these two subbasins, β_{2a} , is significantly deeper than its

southern counterpart β_{2b} . The Pliocene-Quaternary succession rapidly thin northward in subbasin β_{2a} from ~1100 ms along the axial trough to <200 ms over the crest of ridge ϵ_{11} (Figs. 5.13, 5.14). This dramatic thinning is accomplished by rapid north-directed onlap of the lower to upper Pliocene-Quaternary subunits over the southern flanks of ridge ϵ_{11} , but also aided by a noticeable north-directed convergence of the middle and upper Pliocene-Quaternary subunits (Fig. 5.13). The Pliocene-Quaternary succession in subbasin β_{2b} also thins toward the south over the crest of ridge ϵ_{12} . The lower subunit show very mild thinning and generally drapes over ridge ϵ_{12} with a uniform thickness, whereas the middle and/or upper Pliocene-Quaternary subunits show a south-directed onlap and convergence (Figs. 5.13, 5.14). Along the southeastern portion of the study area the lower Pliocene-Quaternary subunit forms a nearly uniform thickness drape over the ridges ϵ_{12} and ϵ_2 , as well as across the subbasin β_{2b} (Fig. 5.13). However, the middle subunit displays a very prominent south-directed progressive onlap over the northern flank of ridge ϵ_{11} , with only the uppermost strata of the middle subunit and the lowermost strata of the upper subunit overstepping the crestal region of ϵ_2 . The upper Pliocene-Quaternary subunit also thins toward ridge ϵ_2 , where thinning is largely accomplished by south-directed convergence and minor onlap (Fig. 5.13). Further to the south, the near uniform drape geometry of the lower Pliocene-Quaternary subunit is still visible across subbasin β_{1b} , with a mild thinning toward the crest of ridge ϵ_2 (Fig. 5.14). Here, the Pliocene-Quaternary subunits exhibit a dramatically different internal stratigraphic architecture than that observed further to the north. The reflectors within the middle subunit show an apparent, south-directed

progressive downlap either on reflectors of the lower subunit or over a prominent reflector within the middle Pliocene-Quaternary subunit (Fig. 5.14). The middle and upper Pliocene-Quaternary subunits display mild thinning over the ridge ϵ_2 , where the gentle rise in the elevation of the M-reflector is matched by concomitant lowering of the sea floor. This thinning is accomplished by south-directed convergence of the upper and middle subunits (Fig. 5.14).

In the southwestern portion of the study area, the floor of the subbasins β_{2a} and β_{2b} , progressively rise toward the northeast where they converge over a narrow sill situated at ~700-800 ms elevation below the sea floor (Figs. 5.1, 5.2). Further to the northwest, the axial trough of the combined subbasins β_{2a} and β_{2b} (i.e., basin β_2) within the central portion of the study area sharply deepens, but rises again near the region of southward converge of the axis of subbasins β_{2a} and β_{2b} in the northwestern portion of the study area (Figs. 5.1, 5.2). Basin β_2 exhibits a symmetrical cross-sectional geometry across its width with the axial hinge line of the depocentre remaining stationary throughout the deposition of the entire Pliocene-Quaternary succession (Fig. 5.11).

The Pliocene-Quaternary succession is >1400 ms thick within the deepest portion of basin β_2 , but shows a remarkable south- and north-directed thinning to < 300 ms across ridges ϵ_2 and ϵ_{11} , respectively (Figs. 5.2, 5.6, 5.11). Similar to subbasins β_{2a} and β_{2b} , the lower portion of the lower Pliocene-Quaternary subunit defines a nearly uniform thickness drape succession blanketing the ridges ϵ_{11} and ϵ_2 , as well as the floor of basin β_2 , thus, does not contribute to the observed variations in the Pliocene-Quaternary thickness (Figs

5.6, 5.11). The observed dramatic thinning of the Pliocene-Quaternary succession is accomplished by a marked convergence of mainly the middle and upper subunits toward the ridges, which is associated with multiple phases of onlap over internally-converging reflectors. Thus, a number of stacked unconformities are developed across the northern as well as southern flanks of ridges ϵ_2 and ϵ_{11} , with the amount of section missing due to onlap progressively increasing toward the central region of the ridges (Figs. 5.6, 5.11). These unconformities can be readily traced toward the basin β_2 where they form an invariably conformable sequence. Detailed examination of seismic reflection profiles shows that the sea floor is locally erosional over the crest of both ridges ϵ_2 and ϵ_{11} (Figs. 5.6, 5.11).

Isopach map and seismic reflection profiles show that subbasins β_{2a} and β_{2b} in the northwestern portion of the study area constitute two large and deep depocenters containing ~900-1200 ms of Pliocene-Quaternary sediments over the M-reflector (Figs. 5.2, 5.9, 5.10). The northern subbasin β_{2a} is noticeably narrower, but deeper than the southern subbasin β_{2b} . In subbasin β_{2a} the Pliocene-Quaternary succession thins toward the bounding ridges to <800 ms and < 700 ms, where thinning is achieved by progressive north- and south-directed inter-stratal onlap toward the ridges ϵ_{11} and ϵ_{13} , respectively as well as a pronounced convergent reflection configuration toward the bounding ridges. Similar to that observed in the southeastern portion of the study area, a number of stacked unconformities are identified along the flanks of ridges ϵ_{11} and ϵ_{13} , which themselves display a convergent pattern toward the ridges (Figs. 5.9, 5.10). Detailed examination of

seismic reflection profiles shows that the sea floor is clearly locally erosional over the crests of ridges ϵ_{11} and ϵ_{13} (Figs. 5.9, 5.10). Subbasin β_{2a} is clearly asymmetric in cross-section across its width, with the center of depocenter in the lower Pliocene-Quaternary subunit being located furthest to the north, shifting southwards during the deposition of the middle and upper Pliocene-Quaternary subunits.

The broad internal stratigraphic architecture of subbasin β_{2b} is largely controlled by the elevation of its bounding ridges ϵ_2 and ϵ_{13} . In the westernmost segment of the study area, ϵ_{13} define a prominent ridge with a clear sea floor expression. Here, ridge ϵ_2 is much attenuated and is barely perceptible within the deep basin. In fact, a clear boundary does not exist between subbasin β_{2b} and β_1 (Fig. 5.9). Whereas further to the southeast, ridge ϵ_2 becomes a very prominent structure rising to a much shallower subbottom depth, where it also displays a notable expression on the sea floor. Here, a small early Pliocene-Quaternary strata onlap the southern flank of the ridge ϵ_{13} . However the lower portion of the middle Pliocene-Quaternary subunit oversteps the crest of ridge ϵ_{13} , merging subbasins β_{2a} and β_{2b} into a larger depocenter. In regions where ridges define prominent structures, the Pliocene-Quaternary succession is notably thin. The thinning is achieved by progressive south-directed onlap over ridge ϵ_2 such as seen in Figure 5.10, or north-directed onlap over ridge ϵ_{13} , such as seen in Figure 5.9. In both cases a number of stacked unconformities are also clearly visible in these regions.

5.2.2.4. Basin β_3

Basin β_3 consists of two internally parallel northwest-southeast trending depocentres that are situated between ridges ε_2 and ε_3 (Figs. 5.1, 5.2). A small ridge with limited lateral extent, ε_{31} , separates the northern basin β_{3a} from the southern basin β_{3b} . Isopach map shows that basin β_{3a} includes three subbasins which are separated from one another by shallower sills created by the higher elevation of the basinal hinge line relative to the deeper segments in the subbasins (Fig. 5.2). The eastern and western subbasins are narrow (<5 km) and contains a thin Pliocene-Quaternary fill of ~700 ms, whereas the central subbasin is broader (~10 km) and contains a greater thickness (~1300 ms) of Pliocene-Quaternary sediments (Figs. 5.2, 5.9, 5.10, 5.12, 5.13, 5.14, 5.17). In the western portion of the study area, basin β_{3a} constitutes the southern segment of a larger composite basin ($\beta_{3b} + \beta_{3a}$) which extends between ridges ε_{13} and ε_3 (Fig. 5.9). Further to the east, ridge ε_2 defines a prominent structural feature with a notable expression on the sea floor (Figs. 5.10, 5.17). Here, the Pliocene-Quaternary succession shows dramatic thickness variations across the width of basin β_{3a} , as well as longitudinally along its axis, deduced from comparisons of thicknesses in consecutive seismic profiles (e.g. Figs. 5.10, 5.12, 5.17). Within the deepest portion of basin β_{3a} , the observed thinning toward ridges ε_2 and ε_3 is attained by spectacular north- and south-directed convergence where thickness reduction from ~1400 ms to ~300 ms is achieved by thinning of individual reflection cycles rather than onlap or erosion (Fig. 5.17). Stacked multiple unconformities are only observed along the steep flanks as well as over the crestal regions of ridges ε_2 and ε_3 . The

sea floor over the crestal regions of both ridges ϵ_2 and ϵ_3 is erosional (Fig. 5.17). One of the most striking attributes of basin β_{3a} is its cross sectional symmetry illustrated by the spatial stability of the basinal hinge line throughout the deposition of the entire Pliocene-Quaternary succession (Fig. 5.17).

Further to the east, the floor of basin β_{3a} climbs over the combined ridges ϵ_2 , ϵ_{31} and ϵ_3 , east of which basin β_{3a} can no longer be traced in seismic reflection profiles (Figs. 5.12, 5.13). But here, another basin (i.e. β_{3b}) emerges between ridges ϵ_{31} and ϵ_3 . The southern basin, β_{3b} , includes two subbasins, of which the western one is narrow (<4 km) and well-defined by ridge ϵ_{31} in the north and ridge ϵ_3 in the south, whereas the eastern subbasin is a wider (~10 km) depocentre bounded by ridges ϵ_2 and ϵ_1 (Figs. 5.2, 5.12, 5.13, 5.14). Basin β_{3b} is asymmetrical in cross-section across its width, with the center of depocentre in the lower Pliocene-Quaternary subunit being located in the south, shifting northwards during the deposition of the middle-to-upper subunits (Figs. 5.12, 5.13). The thickness of the Pliocene-Quaternary sediments in the deepest portion of basin β_{3b} is ~600 ms and do not show any major variation throughout the study area (Fig. 5.2).

In the central segment of the study area ridge ϵ_{31} defines a minor structural high and comprises the northern boundary of basin β_{3b} (Figs. 5.1, 5.2, 5.12, 5.13). Here, the sea floor over the crestal region of ridge ϵ_{31} is erosional (Fig. 5.12). The Pliocene-Quaternary succession overlying the M-reflector along the hinge line of the basin β_{3b} thins to 50-300 ms towards ridge ϵ_{31} in the north and to 50-150 ms towards ϵ_3 in the south. The thinning is mostly accomplished by north- and south-directed convergence as well as

the onlap of the lower-to-upper subunits over ridge ϵ_3 , with the contribution of inter-stratal onlap observed at various levels within the Pliocene-Quaternary succession (Figs. 5.12, 5.13).

In the easternmost segment of the study area, ridge ϵ_{31} becomes attenuated and ridge ϵ_2 delineates the northern basin boundary (e.g. Fig. 5.14). Here basin β_{3a} is still visible as a narrow depression, north of a deep seated ridge ϵ_{31} , but it is clearly merged with the larger basin β_{3b} (Figs. 5.2, 5.14). In this region the internal architecture of the Pliocene-Quaternary deposits differ from that in the western continuation of the basin (see Fig. 5.14). The lower subunit of the Pliocene-Quaternary succession is thickest in the central portion of basin β_{3b} , but thins over ridge ϵ_{41} , abutting the lower southern slope of ridge ϵ_2 . The subunit gradually thins to the south over ridge ϵ_3 , but continues thinning into basin β_{4a} (Fig. 5.22). The middle portion of the Pliocene-Quaternary succession is thickest in the central portion of basin β_{3b} , thinning both north and south. However, the reflectors defining the upper portion of the subunit form a convex geometry immediately above the concave floor of the basin β_{3b} , broadly delineating a lenticular package (Fig. 5.14). The uppermost Pliocene-Quaternary subunit is thinnest within the central portion basin β_{3b} , but thickens notably to the south over the ridge ϵ_3 , and mildly over ridges ϵ_{31} and ϵ_2 . Three prominent detachment surfaces are developed over ridge ϵ_3 , where the upper and middle Pliocene-Quaternary subunits show prominent northward progressive onlap

5.2.2.5. Basin β_4

Basins β_4 consists of a large depocentre situated between ridge ε_3 in the north and ridge ε_4 in the south. The development of ridges ε_x in the westernmost and ε_y in the easternmost portions of the survey area partitioned basin β_4 into two subbasins, β_{4a} and β_{4b} (Figs. 5.1, 5.2, 5.15, 5.22). In the west, the axial troughs of these subbasins progressively converge toward the southeast associated with the southeast plunge of the crest of ridge ε_x , and in the east, converge toward the northwest associated with the northwest plunge of the crest of ridge ε_y (Figs. 5.1, 5.2). The resultant single depocentre, β_4 , in the central portion of the study area is much deeper than subbasins β_{4a} and β_{4b} , and extends from ridge ε_3 to ridge ε_5 in the southern portion of the study area (Figs. 5.1, 5.2, 5.16, 5.18, 5.20). The overall width of basin β_4 varies between 2 km and 7 km through a length of 120 km across the seismic profiles (Fig. 5.1, 5.2).

In the western portion of the study area, each of subbasins β_{4a} and β_{4b} contains ~750 ms of Pliocene-Quaternary sediments over the M-reflector. In subbasin β_{4a} , the Pliocene-Quaternary succession thins northward from 750 ms along the basin axis to 400 ms over the crest of ridge ε_3 (Figs. 5.15, 5.16). This thinning is mostly accomplished by northward convergence of the middle subunit with minor inter-stratal onlap, mainly in the upper subunit, while the lower subunit drapes over ridge ε_3 with an almost uniform thickness. The Pliocene-Quaternary deposits also thins southward to 550 ms over the crest of ridge ε_x , accommodated by the southward convergence of the middle subunit (Fig. 5.15, 5.16). The lower subunit gently thickens over the crest of ridge ε_x where the M-

reflector delineates a minor low. Here, the reflectors within the lower subunit to lower portion of the middle subunit exhibit a transition from a synformal to an antiformal character when traced up section (Fig. 5.15). In basin β_{4b} , the mild northward thinning of the Pliocene-Quaternary succession is accomplished by the northward convergence of the middle-to-upper subunits, while the lower subunit maintains its thickness along the floor of the basin, but becomes thicker over ridge ϵ_x , similar to that observed in basin β_{2a} . In the northwestern portion of the study area, ridge ϵ_4 is a large, high amplitude structural feature with the crest lying near or at the sea-floor, where it creates two prominent erosional steps on the sea floor (Fig. 5.15). The Pliocene-Quaternary succession rapidly thins southward in subbasin β_{4b} from 650 ms along the basin axis to <10 ms over the crest of ridge ϵ_4 . This dramatic thinning is attained by rapid south-directed convergence of the lower to upper subunits of the Pliocene-Quaternary succession, as well as prominent south-directed onlap over a series of stacked unconformities particularly within the upper subunit. Further to the east, subbasins β_{4a} and β_{4b} merge to form a larger and deeper basin β_4 as the anticlinal axis of ridge ϵ_x plunges toward the southeast (Figs. 5.1, 5.2, 5.16). Here, 550 to 800 ms of Pliocene-Quaternary sediments overlie the floor of basin β_4 defined by a corrugated M-reflector. The Pliocene-Quaternary succession thins northward from ~650 ms along the axial trough to 300 ms over the crest of ridge ϵ_3 (Fig. 5.16). This thinning is accomplished by a north-directed convergence of the middle subunit as well as the onlap of the upper subunit reflectors over a converging middle subunit package. Across the floor of basin β_4 , the lower subunit and the lower portion of the middle subunit

drapes over the wavy M-reflector with minor thinning over the crestal regions of the minor anticlines delineated by the corrugated M-reflector. The southward thinning of the Pliocene-Quaternary sediments to <250 ms is realized by the abrupt termination of the lower to middle subunits against the northern flank of ridge ϵ_4 (Fig. 5.16). Here, the upper subunit maintains its thickness and drapes over ridge ϵ_4 (Fig. 5.16).

In the central portion of the study area, basin β_4 loses its distinct expression and merges with basins β_5 and β_6 as both ridges ϵ_4 and ϵ_5 plunge towards the southeast, and thus losing their expression, and becoming a larger composite basin. Here, the Pliocene-Quaternary succession is >550 ms thick along the axial trough of the composite basin β_4 , but shows a notable north-directed thinning to 300 ms across ridge ϵ_3 (Figs. 5.2, 5.20). Several stacked unconformities that are marked by progressive onlap delineates northward converging packages of middle-upper Pliocene-Quaternary subunits in the northern portion of basin β_4 , which accommodate the observed thinning of the Pliocene-Quaternary deposits. The lower Pliocene-Quaternary subunit appears undisturbed and basically drapes over ridge ϵ_3 as well as the rugged M-reflector across the floor of basin β_4 .

In the eastern portion of the study area, ridge ϵ_5 rises again and stands as a major structural high marking the southern boundary of basin β_4 (Figs. 5.1, 5.2, 5.21). The Pliocene-Quaternary succession thins northward and southward from 600 ms along the basin axis to <10 ms and ~350 ms over the crest of ridge ϵ_3 and ϵ_4 , respectively (Fig. 5.21). This notable thinning is achieved mainly by north- and south-directed onlap of the lower to middle portion of the middle Pliocene-Quaternary subunit over ridges ϵ_3 and ϵ_4 ,

with significant contributions from northward- and southward-converging middle-to-upper Pliocene-Quaternary packages, which also show inter-stratal onlap. Further to the east, a structural high with double hinge, ridge ϵ_y partitioned the larger depocentre β_4 into two prominent subbasins, β_{4a} and β_{4b} (Figs. 5.1, 5.2, 5.18, 5.22). The 750 ms thick Pliocene-Quaternary succession along the axial trough of the basin rapidly thins to ~500 ms over the crests of ridge ϵ_y . The succession further dramatically thins to ~200 ms over ridges ϵ_x and ϵ_4 further to the north and south, respectively (Fig. 5.22). This thinning is mostly accommodated by the progressive north- and south-directed onlap of the middle-to-upper subunits of the Pliocene-Quaternary succession over the lower subunit, which blankets the rugged M-reflector across basin β_4 with little or no thickness variation (Fig. 5.18). The reflectors within the upper portion of the middle subunit as well as the upper subunit of the Pliocene-Quaternary succession show progressive onlap over a prominent reflector which can be traced across basin β_4 , and defines a clear unconformity (Fig. 5.18). The sedimentary package situated above this unconformity also exhibits inter-stratal onlap.

In the easternmost portion of the study area, the crests of ridge ϵ_x rises to a depth of ~250 to 300 ms below sea floor (Fig. 5.22). Here, the lower subunit drapes over the structural highs with little or no thickness variation. However, the internal architecture of the middle to upper Pliocene-Quaternary subunits display a highly deformed character. The thinning of the Pliocene-Quaternary succession from 550 ms along the axis of basin β_{4a} to 250 ms and 200 ms over the crests of ϵ_3 and ϵ_y , respectively, is accomplished by a series of very complex onlap and erosional truncation (Fig. 5.22). Along the southern

flank of ridge ϵ_3 , a diverging package of middle subunit reflectors show north-directed onlap over an unconformity surface developed within the upper portion of the lower subunit. When traced up section toward the crest of the ridge, the reflectors within this package roll over the prominent unconformity surface displaying a higher angle onlap (Fig. 5.22). The top of this prominent package is defined by another notable unconformity, over which middle to upper subunits of the Pliocene-Quaternary deposits show onlap. These unconformities, as well as the complex internal architecture of the middle-to-upper subunits can be traced into the southern half of subbasin β_{4a} and over the crest of ridge ϵ_4 . The southern subbasin, β_{4b} , is shallower (~350 ms) than its northern counterpart (Figs. 5.2, 5.22). Here, the upper portion of the middle subunit and the upper subunit show north- and south-directed progressive onlap over an unconformity identified within the middle Pliocene-Quaternary subunit, although the exact stratigraphic relationship within Unit 1 is not certain (Fig. 5.22). The base of this subunit clearly truncates the entire lower Pliocene-Quaternary succession across the crest of ridge ϵ_5 (Fig. 5.22). In the eastern portion of the study area, the crests of ridges ϵ_3 and ϵ_4 is an erosional surface on the sea floor.

5.2.2.6. Basin β_5

Basin β_5 is a major depocenter situated between ridges ϵ_4 and ϵ_5 in the north and south, respectively (Fig. 5.1). Isopach map shows that it includes three to four subbasins, separated from one another by shallower sills (Fig. 5.2). The largest subbasin is situated in

the western portion of the study area and shows a maximum width of ~ 15 km along a length of 40 km. It displays a symmetrical cross-sectional geometry across its width. Here, basin β_5 contains ~ 1600 ms of Pliocene-Quaternary sediments in the westernmost portion of the study area, which rapidly decreases to ~ 700 ms to the east, associated with the eastward emergence of the M-reflector along the axial trough of the basin (Figs. 5.2, 5.15, 5.16). The Pliocene-Quaternary succession also shows a marked thinning from >1600 ms in central basin β_5 northward to <100 ms over the crest of ridge ϵ_4 . Although there is a gentle northward convergence of the lower and middle Pliocene-Quaternary succession, this dramatic northward thinning is achieved by a radical abutting of the Pliocene-Quaternary succession on the southern wall of ridge ϵ_4 (Fig. 5.15). Whereas to the south, the succession shows a gentle thinning toward the crest of ridge ϵ_5 where thinning is the result of south-directed convergence associated with a number of stacked unconformities, which either progressively truncate the underlying successions or a gentle south-directed progressive onlap of the overlying reflectors is observed (Fig. 5.15). As the basin shallows to the east, it also becomes asymmetrical with the axial trough situated to the north during the deposition of the entire basin fill (Fig. 5.16). Here, the Pliocene-Quaternary succession exhibits northward and southward thinning from 700 ms along the hinge line of basin β_5 to <100 ms and <300 ms over ridges ϵ_4 and ϵ_5 , respectively. The observed thinning is attained by the progressive onlap of the almost the entire Pliocene-Quaternary succession over the M-reflector (Figs. 5.15, 5.16). Various unconformities developed between these onlapping packages can be traced into the central portion of the

basin where they become correlative conformities. Although one particular unconformity observed within the middle subunit of the Pliocene-Quaternary succession differs from the others as it continues in the form of an unconformity all across the basin (Figs. 5.15, 5.16). Additionally, minor fracturing associated with faulting is recognized within the lower to upper subunits of the Pliocene-Quaternary succession (Figs. 5.15, 5.16; also see chapter 6).

In the central portion of the survey area, basin β_5 merges with the adjacent basins β_4 and β_6 as the result of southeastward-plunging of ridges ε_1 and ε_2 (Fig. 5.20). Thus, here, basin β_5 comprises the central portion of a larger depocentre nestled between ridges ε_3 in the north and ε_5 (or possibly ε_6) in the south. Whereas, in the eastern portion of the study area, basin β_5 is well-delineated by ridges ε_4 and ε_5 . It exhibits a symmetrical cross-sectional geometry across its width (Figs. 5.2, 5.21). Here, the thickness of the Pliocene-Quaternary sediments is ~750 ms along the axial trough of the basin, which thins to ~350 ms over the crests of ridges ε_4 and ε_5 (Fig. 5.21). This thinning is mainly attained by north- and south-directed onlap of the middle-to-upper subunits of the Pliocene-Quaternary succession over the flanks of the ridges ε_4 and ε_5 with the exception of a <50 ms thin strata of upper portion of the upper subunit that lies undisturbed above the crest of ridge ε_5 . A number of unconformities delineate the onlap packages. The lower subunit drapes over the structural highs without any major thickness variation, hence do not contribute to the observed thinning. Here, the sea floor above the crest of ridge ε_4 is erosional. Further to the east, the external geometry of the basin changes and it displays

an asymmetrical cross-sectional geometry across its width with the hinge line of the depocentre situated to the north during the deposition of lower to middle Pliocene-Quaternary subunits, shifting to the south during the deposition of younger sediments (Fig. 5.18). The observed change in the external geometry of the basin is associated with the mild partitioning of ridge ϵ_5 into two connected structural highs. Here, the Pliocene-Quaternary succession is ~650 ms at the deepest portion of the basin. The lower to middle subunits of the Pliocene-Quaternary succession show notable north- and south-directed onlap against the M-reflector along the flanks of ridges ϵ_4 and ϵ_5 , while the middle to upper subunits show onlap over a prominent unconformity delineating the top of the older sediment package (Fig. 5.18). Inter-stratal onlap is observed through the entire Pliocene-Quaternary deposits of the eastern subbasin. In the easternmost portion of the study area, the floor of basin β_5 rapidly emerges accompanied by remarkable narrowing of the basin to 3 km (Figs. 5.2, 5.22). Here, the basin shows an asymmetrical cross-sectional geometry across its width with the hinge line being situated to the south. The thickness of the Pliocene-Quaternary succession is ~300 ms along the basin axis which sharply decreases to ~200 ms over ridges ϵ_4 and ϵ_5 as a result of north- and south-directed onlap over the uniform lower subunit that drapes over the surrounding ridges.

5.2.2.7. Basin β_6

Basin β_6 is a large depocentre situated between ridges ϵ_5 and ϵ_6 in the north and south, respectively. It comprises the southernmost depocentre within the study area (Fig.

5.1, 5.2).

In the western portion of the study area, the floor of basin β_6 mimics the highly corrugated morphology of the M-reflector (Figs. 5.20, 5.23). Here, the Pliocene-Quaternary succession is ~650 ms thick along the axial trough of the basin and shows thinning to ~350 ms above the crest of ridge ϵ_5 . This thinning is attained by northward convergence of the upper and to a lesser extent the middle Pliocene-Quaternary subunits with minor inter-stratal onlap confined to the upper subunit. Whereas, the lower Pliocene-Quaternary subunit drapes over ridge ϵ_5 , as well as the crestal regions of the corrugated M-reflector in the central portion of the basin (Fig. 5.23). The Pliocene-Quaternary succession also thins southward from ~650 ms in central basin β_6 to <150 ms over the crest of ridge ϵ_6 (Figs. 5.15, 5.20, 5.23). The observed thinning is achieved either by dramatic south-directed convergence and associated intra-stratal onlap of the middle and upper subunits (e.g. Figs. 5.16, 5.20) or a distinct abutting and truncation of the lower and middle subunits over the northern flank of ridge ϵ_6 (Fig. 5.23), where only the uppermost portion of the upper subunit barely oversteps the crest of ridge ϵ_6 . Many profiles from the westernmost portion of the study area the sea floor is clearly erosional over ridge ϵ_6 (Figs. 5.16, 5.20, 5.23). Here, ridge ϵ_6 is situated outside the coverage of the seismic profiles.

Further to the east, ridge ϵ_5 plunges and becomes much attenuated while ridge ϵ_6 stands as a major structural high (Fig. 5.20). The Pliocene-Quaternary succession is 650 ms thick along the hinge line of the basin and thins to 550 ms and <300 ms over ridges ϵ_5 and ϵ_6 , respectively. The northward thinning is accomplished by the north-directed onlap

of the lower portion of the middle Pliocene-Quaternary subunit over ridge ϵ_5 , while the lower subunit as well as the upper portion of the middle subunit and the upper subunit blanket ridge ϵ_5 without any significant variation in thickness. The southward thinning is attained by the convergence of the middle-to-upper Pliocene-Quaternary subunits with minor inter-stratal onlap in the upper portion of the upper subunit. The sea floor above the crest of ridge ϵ_6 is erosional (Figs. 5.16, 5.20).

In the central portion of the study area, basin β_6 is well-delineated by ridges ϵ_5 and ϵ_6 and shows a symmetrical cross-sectional geometry across its width (Figs. 5.18, 5.21). Over this deepest portion of the basin, the Pliocene-Quaternary succession is 850 ms thick along the axial trough and shows thinning to <300 ms above the crests of the surrounding ridges. The northward thinning is accomplished by the convergence of the middle to upper Pliocene-Quaternary subunits as well as the progressive onlap of the middle subunit over the top of the lower subunit along the southern flank of ridge ϵ_6 (Figs. 5.18, 5.21). The southward thinning is also attained mainly by the convergence of middle to lower Pliocene-Quaternary subunits, but with only minor inter-stratal onlap in the upper portion of the upper subunit. The lower Pliocene-Quaternary subunit drapes over both ridges ϵ_5 and ϵ_6 in the central portion of the study area.

In the eastern portion of the study area, basin β_6 is dissected by a narrow structural high rising to a depth of 100 ms below sea floor (Fig. 5.22). The lower Pliocene-Quaternary subunit shows little thickness variation across the entire basin β_6 , including its bounding ridges ϵ_5 and ϵ_6 . However, the middle Pliocene-Quaternary subunit

shows a rapid thinning by onlap and convergence toward both bounding ridges ϵ_5 and ϵ_6 , with the uppermost reflectors overstepping the narrow high situated on the southern portion of the ridge ϵ_5 . The upper subunit clearly abuts a prominent intra-Pliocene-Quaternary unconformity along the northern slope of ϵ_5 .

CHAPTER 6. Structural Geology of the Antalya Basin

On the basis of style and age of deformation, as well as the stratigraphic architecture of the Miocene to Pliocene-Quaternary successions, the structural framework of the Antalya Basin is divided into three structural domains. Each domain comprises of distinctive families of structures and structural associations and is confined to a specific geographical region within the basin. Furthermore, each structural association is related to deformation during a restricted time interval during the evolution of the Antalya Basin. These structural domains are as follows (Fig. 6.1): Domain 1 includes the northwest-trending listric extensional faults involving the Pliocene-Quaternary succession as well as the similarly trending transtensional faults involving the Miocene to Pliocene-Quaternary successions, which occupy the northeastern portion of the study area extending from the present-day shoreline to the innermost portion of the deep Antalya Basin (Fig. 6.1). Domain 2 consists of the northwest-trending, southwest-directed fold-thrust structures involving the Miocene Units 3 and 2, which occupy the entire Antalya Basin, as well as the northwest-trending, southwest-directed fold-thrust structures involving the Pliocene-Quaternary Unit 1, which occupy the northern and central segment of deep Antalya Basin (Fig. 6.1). Domain 3 includes the northwest-trending transpressional structures involving the Miocene to Pliocene-Quaternary Units 3, 2 and 1, which occupy the southwestern segment of the deep Antalya Basin (Fig. 6.1). The age of deformation is assumed to be Miocene if the associated sedimentary growth of the structures is confined to seismic stratigraphic Units 3 and 2, whereas those confined to Unit 1 are designated as Pliocene-

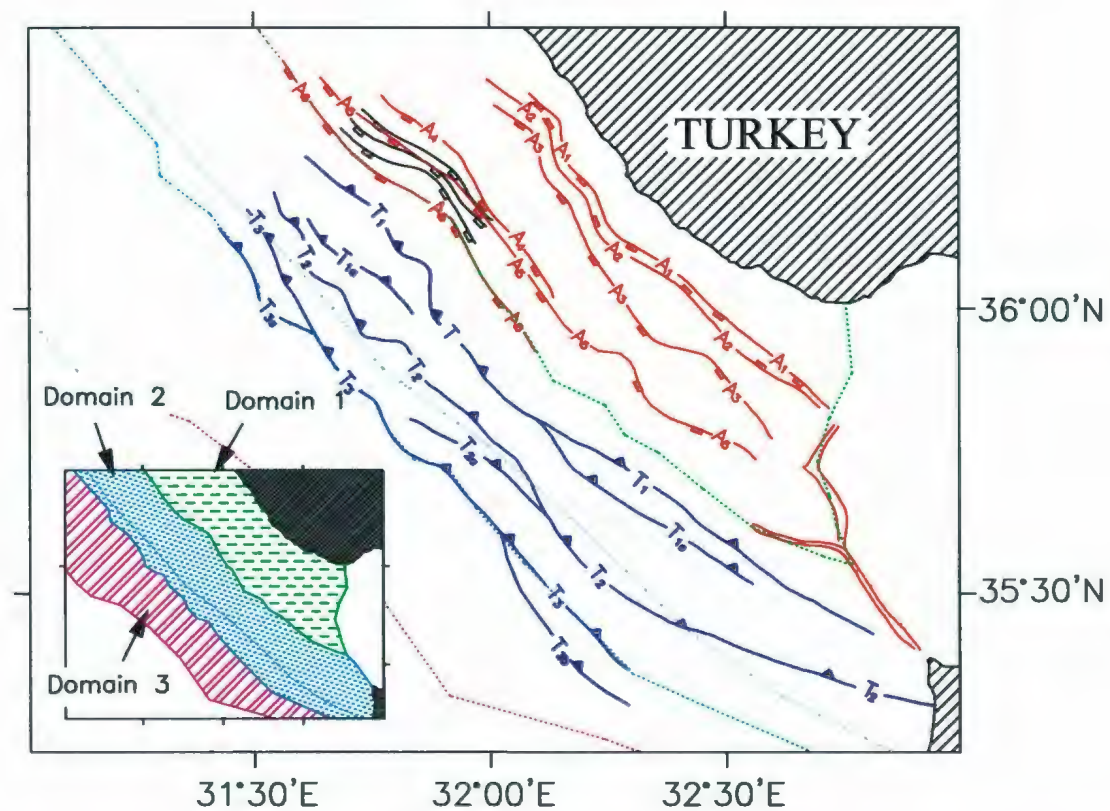


Fig. 6.1. Map showing major structural elements in Antalya Basin. Ticks on thrusts and normal faults are on the hanging wall. Normal faults with open and closed ticks are explained in text. Inset illustrates the structural domains, their boundaries are also shown in the main map with dotted lines.

Quaternary. However, several structures show a protracted deformation involving both the Miocene as well as the Pliocene-Quaternary successions.

6.1. Domain 1

Domain 1 constitutes the northeastern portion of the offshore Antalya Basin within the study area and encompasses the continental shelf, the shelf-break, the upper-lower slopes and the northernmost segment of the abyssal plain, extending across basin β_1 to ridge ϵ_1 (Figs. 5.1, 5.2 and 6.1). The structure of this domain is characterized by four families of extensional faults, three of which are geographically restricted, while the fourth extends throughout the study area.

The first family comprises an imbricate fan of northwest-southeast striking, southwest-dipping listric extensional faults, which can be traced from the upper continental slope in the north into basin β_1 in the south. These faults are confined to the Pliocene-Quaternary succession with most of the tip points lying near or at the sea-floor. Where emergent, the faults display a 10-400 ms step-like morphology on the sea-floor. The faults in this family have high-angle trajectories in the vicinity of the tip points, which become gentler as traced down-section into the middle to lower Pliocene-Quaternary succession. Individual faults of the fan merge with a common southwest-dipping bedding-parallel detachment surface, which lies within the lower portion of the Pliocene-Quaternary succession. This detachment surface can readily be traced southward into basin β_1 where it becomes indistinguishable from any of the laterally continuous reflectors

which constitutes the upper Pliocene-Quaternary succession in basin β_1 (Fig. 6.2). Above the common detachment surface, the Pliocene-Quaternary sediments form wedge-shaped bodies bounded by the listric extensional fault trajectories (Figs. 6.3, 6.4). Locally, the common detachment surface appears exposed on the sea-floor where it also coincides with the M-reflector (Figs. 6.3, 6.4). The reflectors within the Pliocene-Quaternary succession do not show any variation in thickness (i.e. growth), suggesting that the deposition of the succession pre-dates the fault activity. Three major faults of this family could be correlated across the seismic reflection profiles in the northwestern portion of the study area (Fig. 6.1). Based on the similarities to the previously defined slide structures (Reading, 1986), the faults of this family are interpreted to represent detachment surfaces associated with gravity-driven slide structures. The chaotic seismic expression of the internal architecture of the sediment masses resemble the internal architecture of the previously defined slump structures (Reading, 1986). Sliding and slumping causes lateral displacement of a semi-consolidated sediment mass along a basal shear plane while restraining some internal coherence (Reading, 1986). The sediment bodies transported by sliding show little internal disturbance while slumping yields disturbed sediment masses related with rotation accompanying shear failure. The morphology of the slope, the physical properties of slope sediments including shear strength, bulk density and the type and rate of deposition are described as the primary factors that control slumping and sliding (Reading, 1986). The slump/slide structures in this domain may be the result of rapid deposition of the Pliocene-Quaternary strata along the shelf edge and upper slope

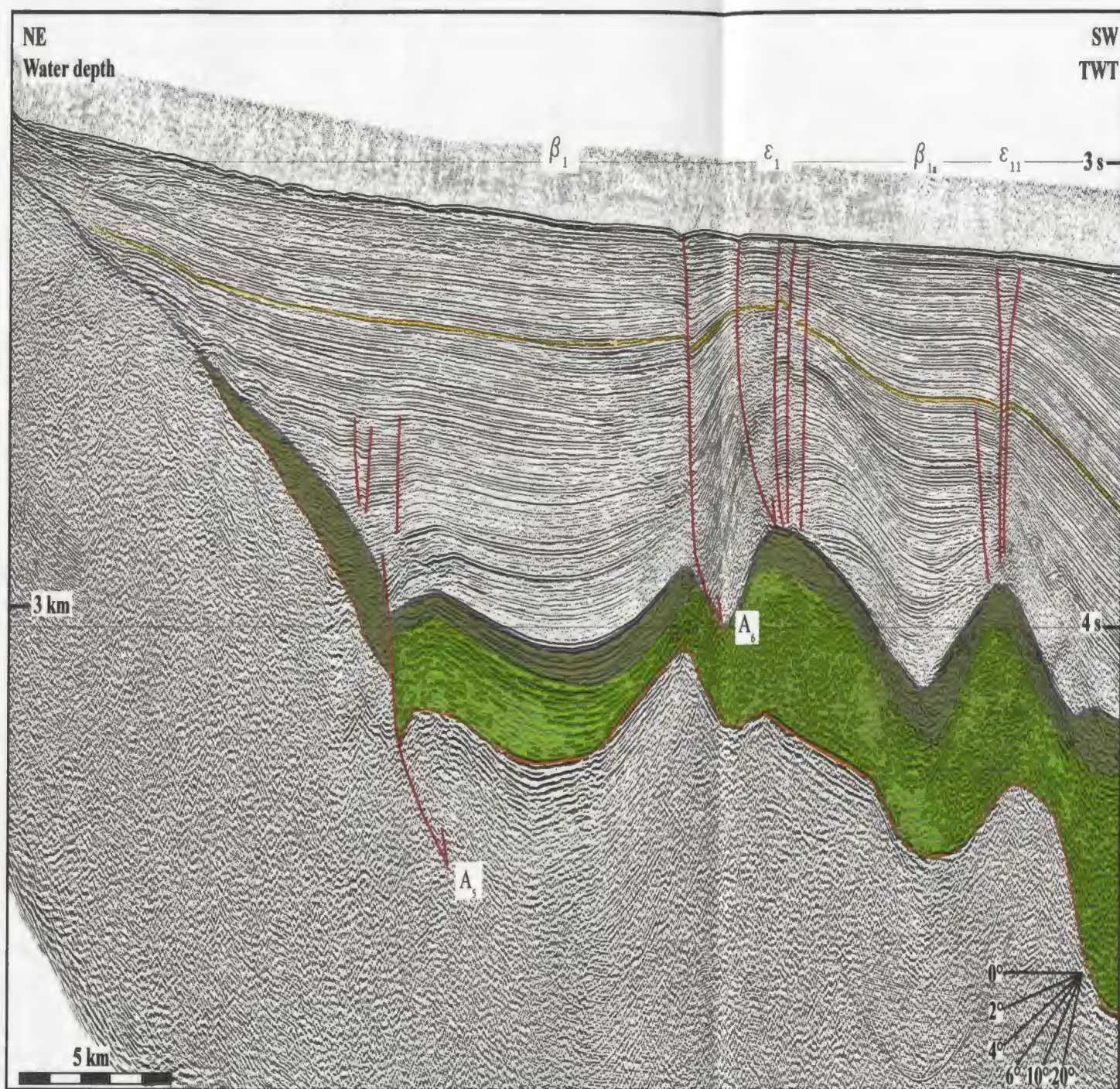
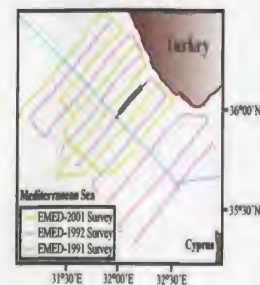


Fig. 6.2. Seismic reflection profile (FIX 1813-1828).

- Top middle Plio-Quaternary subunit
- Top basal Plio-Quaternary subunit
- M-reflector
- Upper evaporite subunit 2a
- Lower evaporite subunit 2b
- Top Unit 3



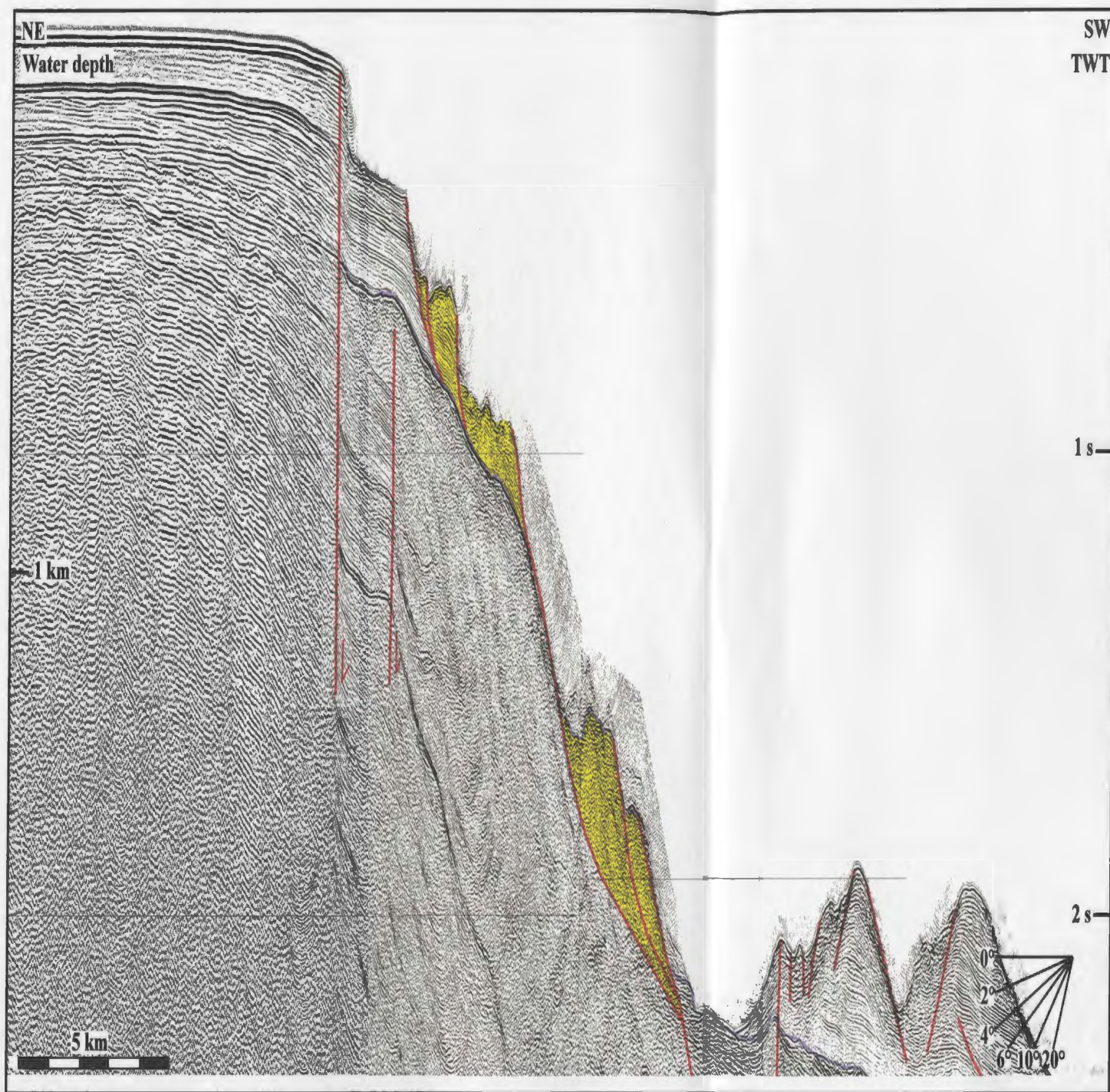
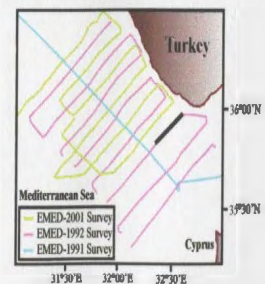


Fig. 6.3. Seismic reflection profile (FLX 1690-1705).

— M-reflector Slide/slump masses



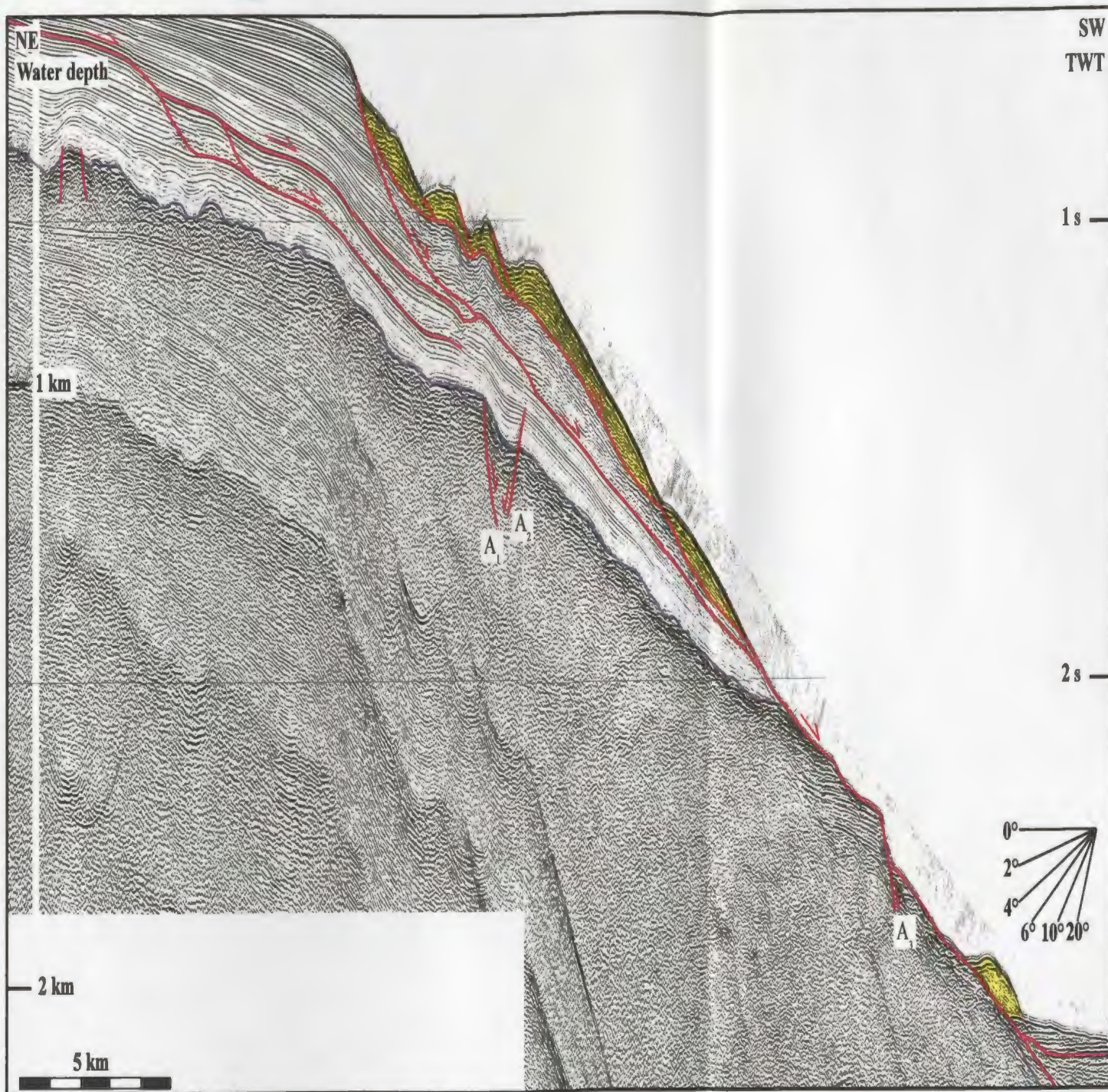
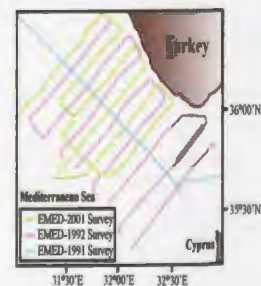


Fig. 6.4. Seismic reflection profile (FIX 1662-1677).

— M-reflector

Slide/slump masses



during the oscillating sea-level conditions of the Quaternary and their resedimentation caused by slope as the result of southward movement of the leading thrusts of the Tauride Mountains may have contributed to the mass wasting along the Antalya margin

The Pliocene-Quaternary fill of basin β_1 is dominated by a series of stacked, northwest-southeast-trending, southwest-dipping listric extensional faults (Fig. 6.5). The tip points of these faults are situated within the middle to upper Pliocene-Quaternary succession. These faults are connected with one another along listric trajectories, yielding wave-shaped geometries (i.e., the lower elevation faults have tip points at the detachment surface of the overlying faults; Figs. 6.5, 6.6). They carry internally transparent lens-shaped bodies on their hanging-walls (Fig. 6.6), which are interpreted as debris flow deposits based on their similarities with the previously-described debris flow deposits (e.g. Aksu and Hiscott, 1992; Hiscott and Aksu, 1994; 1996). Debris flow deposits are described as highly concentrated, viscous sediment masses with a plastic flow behaviour (Johnson, 1970; Hampton, 1972). These flows are developed as sediments are mobilized in the upper slope regions as failures (i.e. slides/shears) by either seismic events or by rapid dewatering and subsequent destabilization of the slope sediments. As the mass travel downslope, in-mixing of water occurs and the flow progressively become less viscous, thus increases in velocity. The debris flow is supported by its own matrix rather than the upward-moving pore pressure such as seen in turbidity currents; these flows are triggered by seismic events, slumping or sliding as well as high rates of sedimentation. The chaotic internal architecture displayed by debris flow deposits are related to their structureless

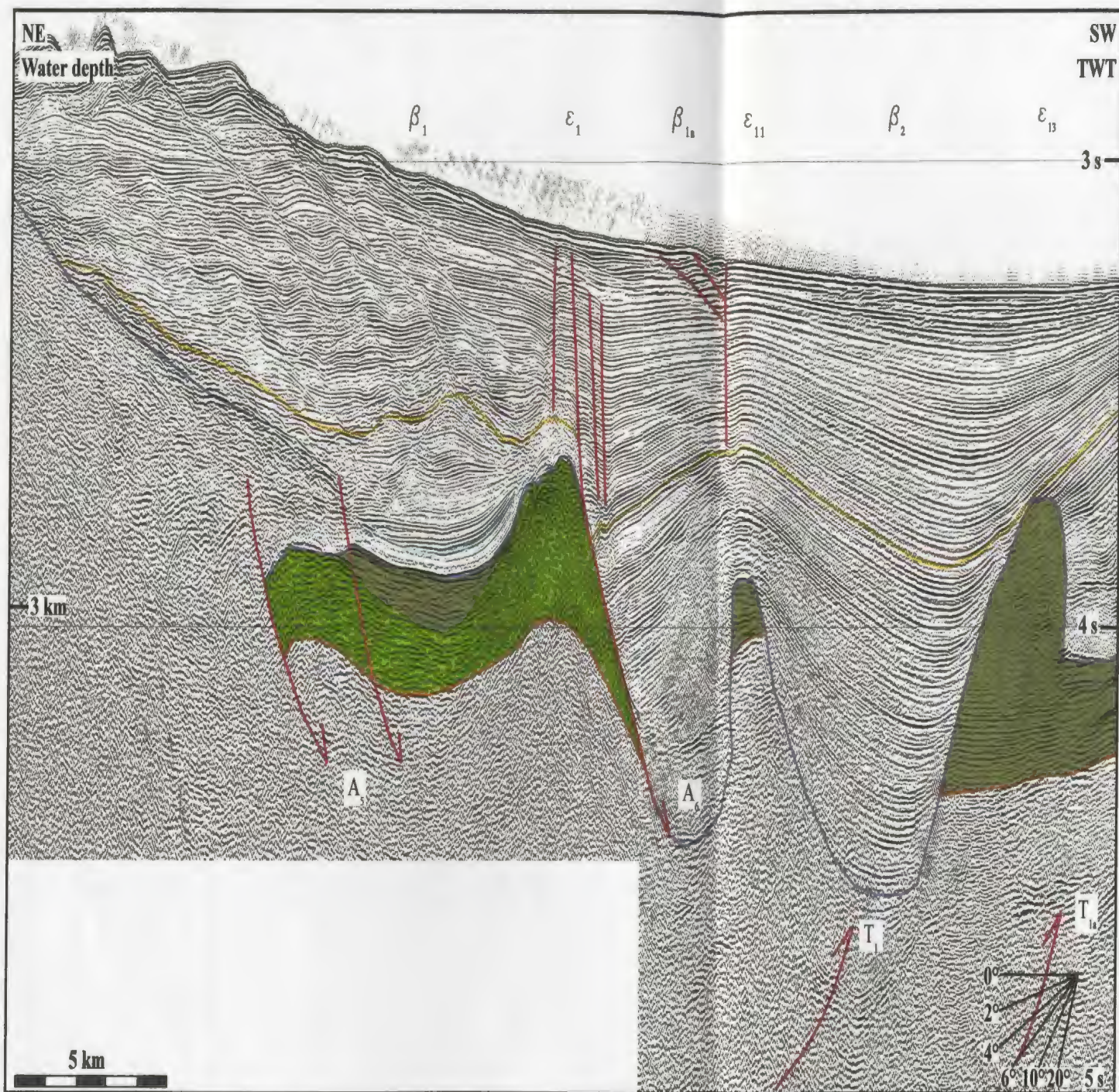
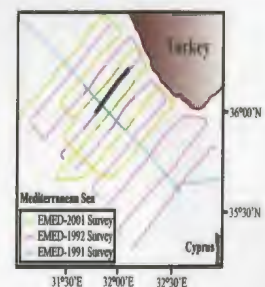


Fig. 6.5. Seismic reflection profile (FIX 1879-1897).

- Top middle Plio-Quaternary subunit
- Upper evaporite subunit 2a
- Top basal Plio-Quaternary subunit
- Lower evaporite subunit 2b
- M-reflector
- Top Unit 3



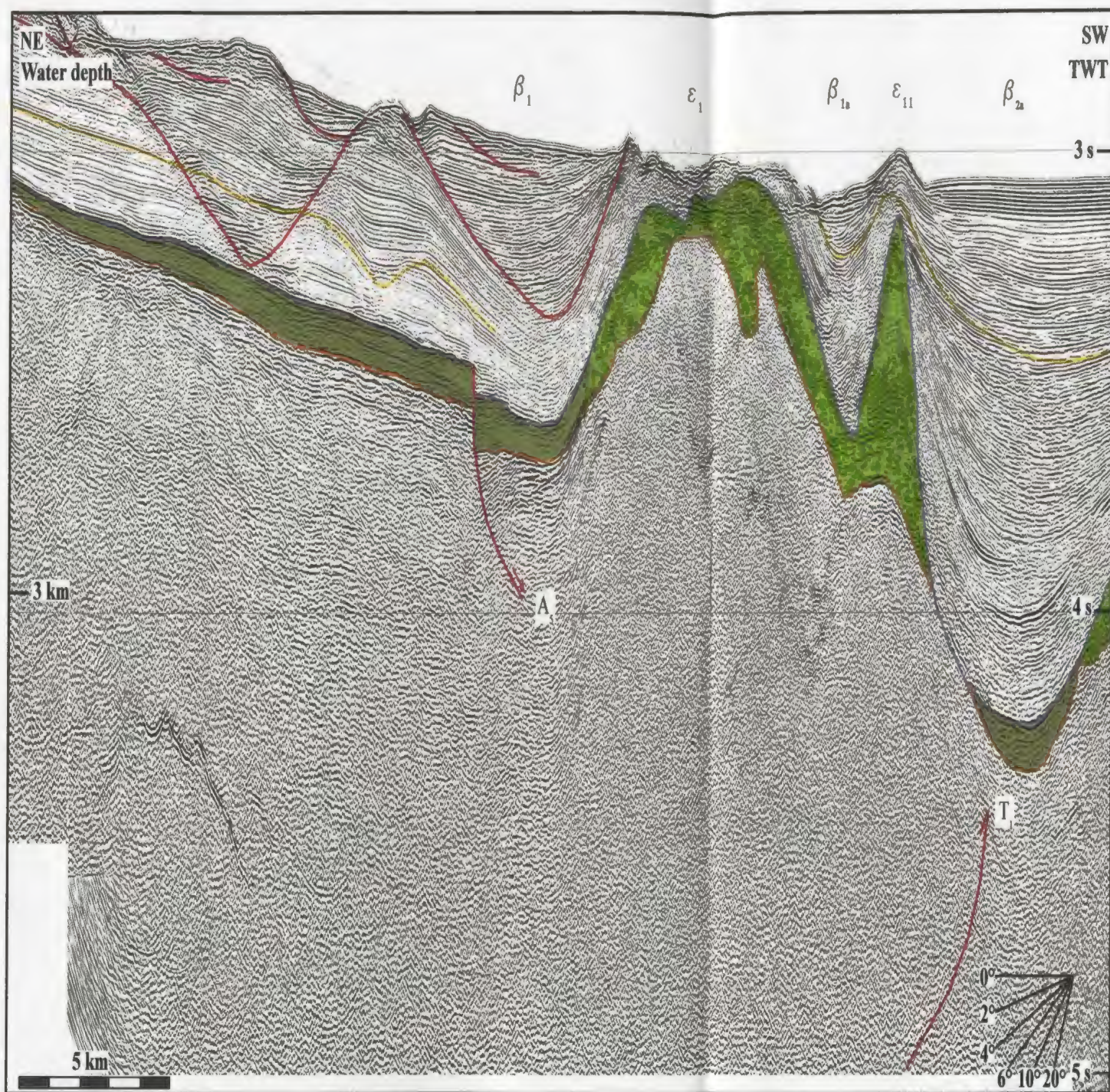
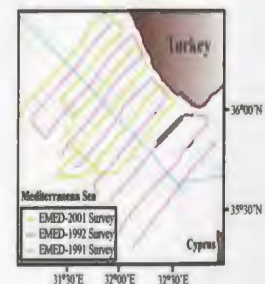


Fig. 6.6. Seismic reflection profile (FIX 1704-1723).

- Top middle Plio-Quaternary subunit
- Lower evaporite subunit 2b
- M-reflector
- Top Unit 3
- Upper evaporite subunit 2a



and disorganized character resulting from transport and reworking they underwent. This remarkable geometry of the strata in basin β_1 is best imaged in the northwestern portion of the study area, but it becomes less significant in the central to eastern seismic reflection profiles. The reflectors on the hanging-walls of the faults do not show evidence of growth suggesting that the movement along the fault trajectory post-dates the deposition of these sediments (Fig. 6.5).

The second family consists of northwest-southeast-trending, southwest- and northeast-dipping, deep-rooted extensional faults occurring along the continental shelf and slope, and at the base of basin β_1 (Fig. 6.1). These faults have high angle trajectories and their tip points lie in the lower to upper portion of the Pliocene-Quaternary succession (Figs. 6.3-6.5). They cut through the M-reflector and extend down-section into the Messinian and older strata. Vertical separations on the M-reflector range between 200 ms and 600 ms along the strike of the fault fan, with the largest separation occurring in the central portion of the study area (Fig. 6.7, 6.8). The fault pairs with opposite sense of dip (i.e. north- and south-dipping) define prominent horst and graben structures (Figs. 6.7-6.9). In general, no growth is observed on the hanging-walls of these faults. However, in a few faults the lower to middle portion of the Pliocene-Quaternary succession shows syn-depositional growth (Figs. 6.8, 6.9). The reflectors within the upper portion of the Pliocene-Quaternary succession display a uniform thickness, which indicates either post-growth or pre-growth deposition, depending on where the tip point of the fault is situated (Fig. 6.7). The most prominent faults of this family extending along the continental slope

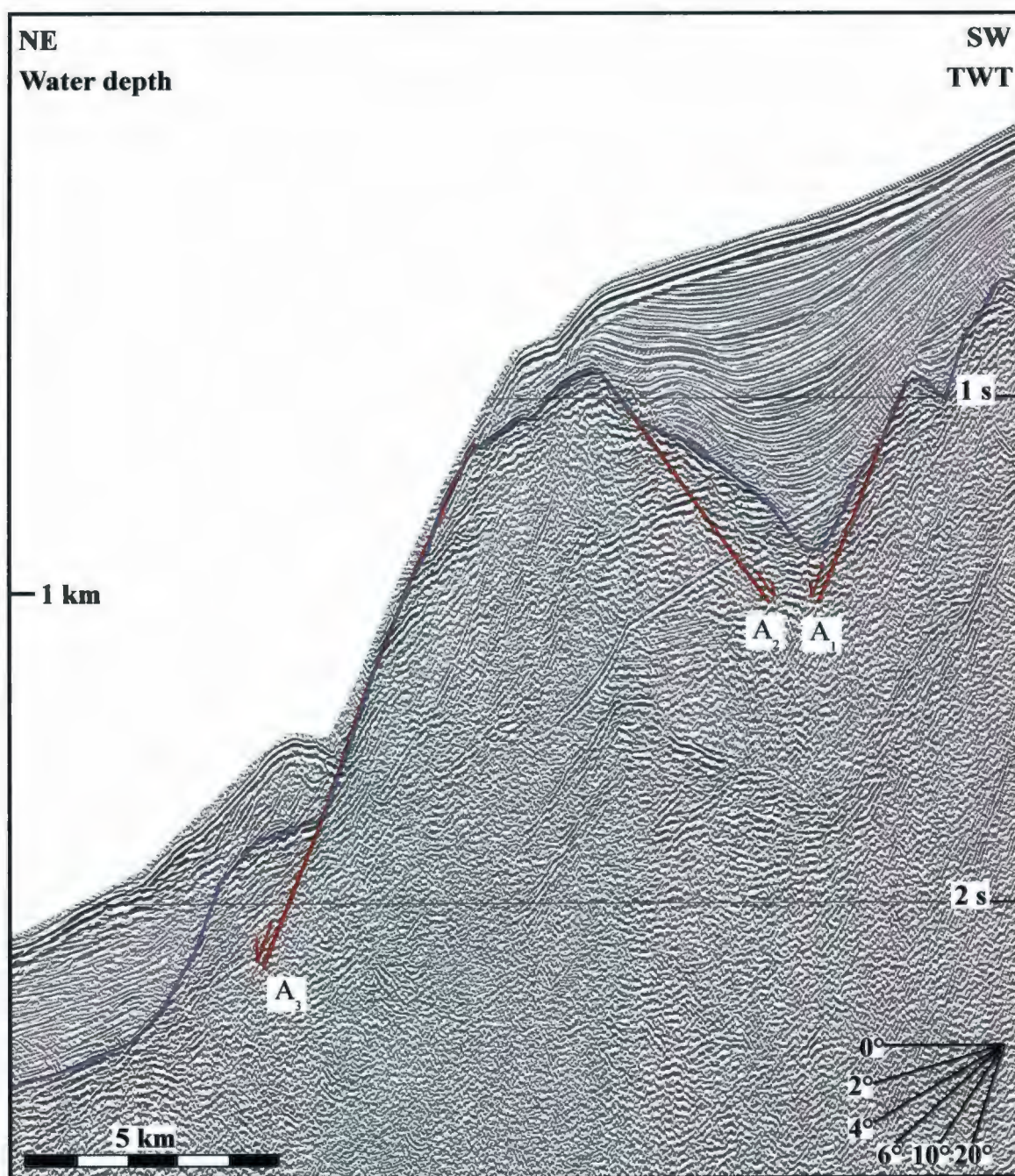
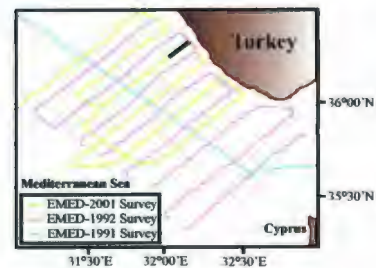


Fig. 6.8. Seismic reflection profile (FIX 569-579).

— M-reflector



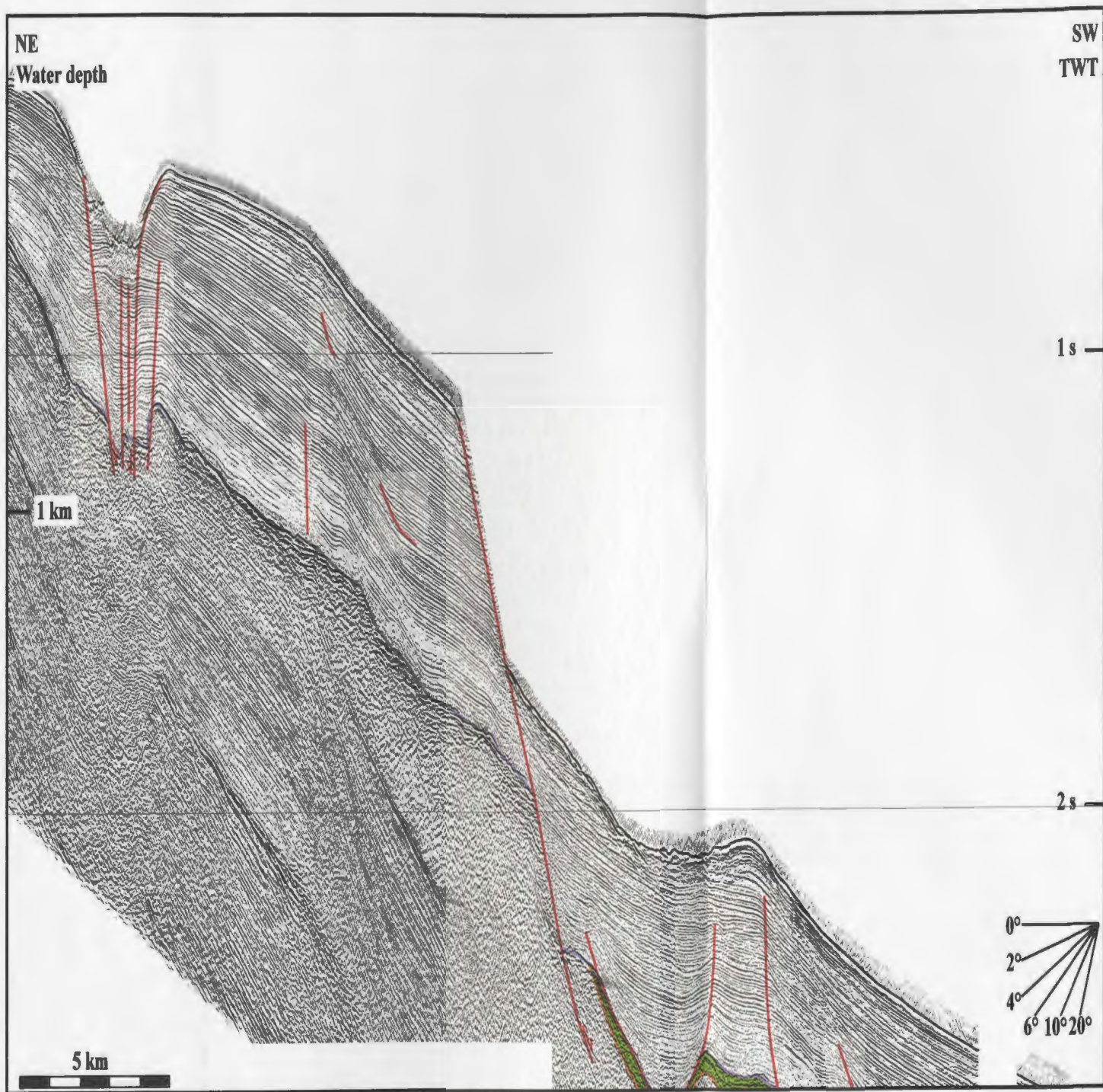
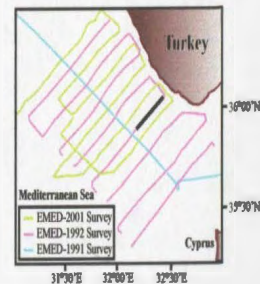


Fig. 6.9. Seismic reflection profile (FIX 1782-1798).

- M-reflector
- Top Unit 3
- Lower evaporite subunit 2b



are referred to as A_1 , A_2 , A_3 and A_4 from north to south, and could be mapped with confidence mostly throughout the study area based on correlations performed across seismic reflection profiles (Fig. 6.1)

The southernmost fault of this family is situated to the south of the axial trough of basin β_1 and is referred to as A_5 (Fig. 6.1). Its tip point lies in the lower portion of the Pliocene-Quaternary succession. The fault cuts through the M-reflector and extends down-section into the Messinian and older successions along a relatively shallow trajectory, creating an apparent vertical separation of 100 ms to 300 ms on the M-reflector along its strike (Fig. 6.2, 6.5, 6.10). The reflectors on the hanging-wall of this fault form south-thinning wedge-shaped packages in the upper portion of Unit 3, the entire Messinian and the lower portion of the Pliocene-Quaternary succession, and display minor onlap with roll-over against the fault surface (Fig. 6.9).

The third family is characterized by a major northwest-southeast-trending and southwest-dipping listric extensional fault system situated above ridge ε_1 (Fig. 6.1). The large fault at the northeastern segment of this system is referred to A_6 (Fig. 6.1). The fault is well-imaged in the northwestern portion of the study area, but becomes less evident in the seismic reflection profiles towards the southeast, where ridges ε_1 and ε_{11} merge (Fig. 6.1). The tip point of the fault lies near or at the sea floor. The fault displays a high-angle trajectory near the tip point, and extends down-section with little variation in dip until it meets the M-reflector, from where it soles into the Messinian evaporites of Unit 2 along a gentler trajectory (Figs. 6.2, 6.5, 6.6, 6.10). The fault creates a vertical separation on the

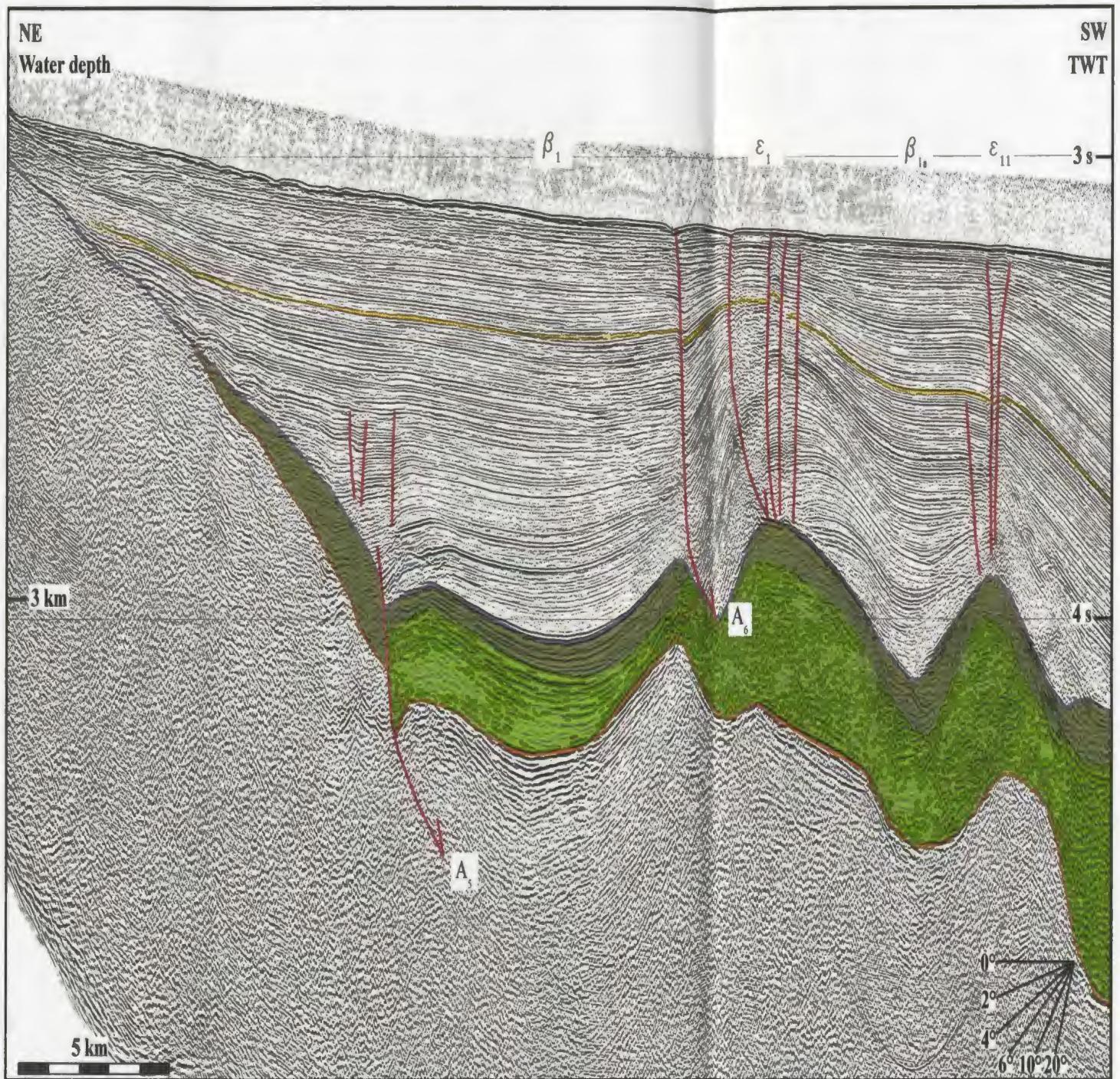
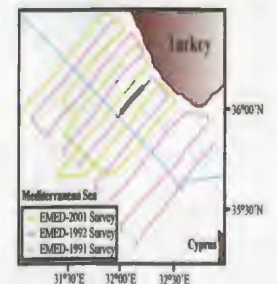


Fig. 6.10. Seismic reflection profile (FIX 1921-1935).

- Top middle Plio-Quaternary subunit
- Top basal Plio-Quaternary subunit
- M-reflector
- Upper evaporite subunit 2a
- Lower evaporite subunit 2b
- Top Unit 3



M-reflector ranging between 200 ms and 600 ms along the strike (Figs. 6.5, 6.6, 6.10). The reflectors within the Pliocene-Quaternary succession show clear onlap against the fault surface marking well-defined hanging-wall and footwall cutoffs (Figs. 6.5, 6.6, 6.10). A notable roll-over structure is observed on the hanging-wall, where the reflectors appear 2-10 degree tilted in a northeast direction. Along the fault plane, the cutoff angles of the reflectors become more pronounced towards the deeper portion. The reflector packages within the Pliocene-Quaternary succession delineate tilted wedge-shaped bodies (i.e. growth wedges), which show remarkable thickening towards the fault surface (Fig. 6.2). Several small-scale normal faults confined to Unit 1 are developed on the hanging-wall (Fig. 6.10) and to a lesser extent on the footwall. These faults are presumably formed as a result of breaking during the roll-over.

The fourth family consists of sub-vertical normal faults occurring above salt structures throughout the study area. These faults are confined to the Pliocene-Quaternary succession with tip points lying near or at the sea floor (Figs. 6.11-6.14). They develop as a result of collapse due to the rise or withdrawal of salt from the crestal region of the associated salt-cored anticlines.

6.2. Domain 2

Structures within Domain 2 consist of a series of at least three major northwest-trending, southwest-verging open and mildly asymmetric anticline-syncline pairs. These anticlines are represented by three prominent ridges $\varepsilon_1 + \varepsilon_{11}$, ε_2 and ε_3 , with the synclines

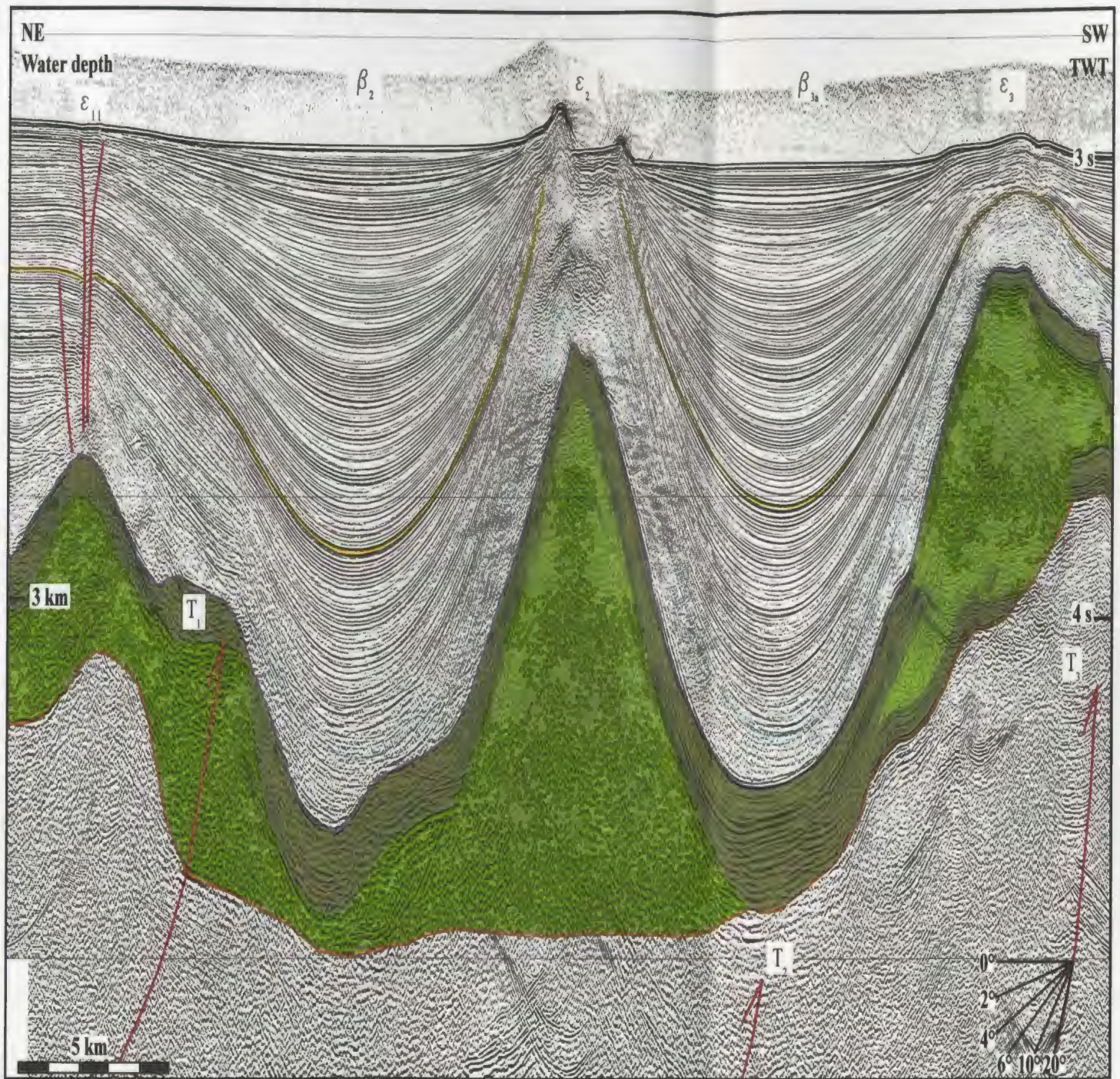
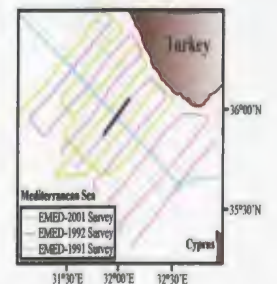


Fig. 6.11. Seismic reflection profile (FIX 1820-1835).

- Top middle Plio-Quaternary subunit
- Top basal Plio-Quaternary subunit
- M-reflector
- Upper evaporite subunit 2a
- Lower evaporite subunit 2b
- Top Unit 3



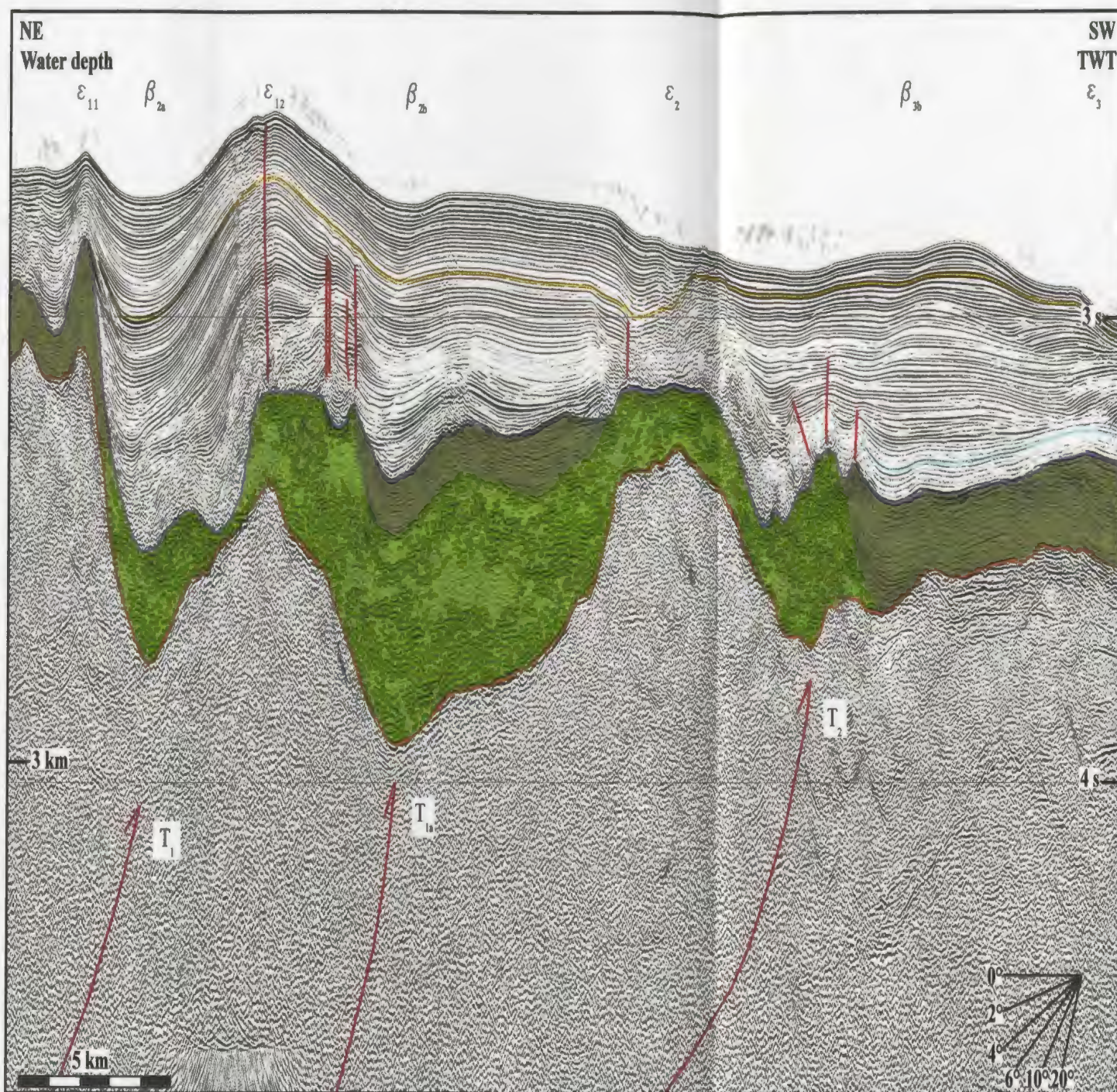
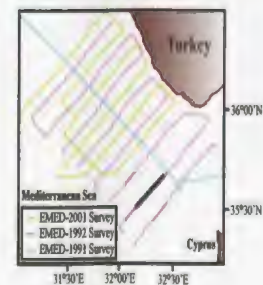


Fig. 6.13. Seismic reflection profile (FIX 1638-1655).

- M-reflector
- Upper evaporite subunit 2a
- Lower evaporite subunit 2b

— Top Unit 3



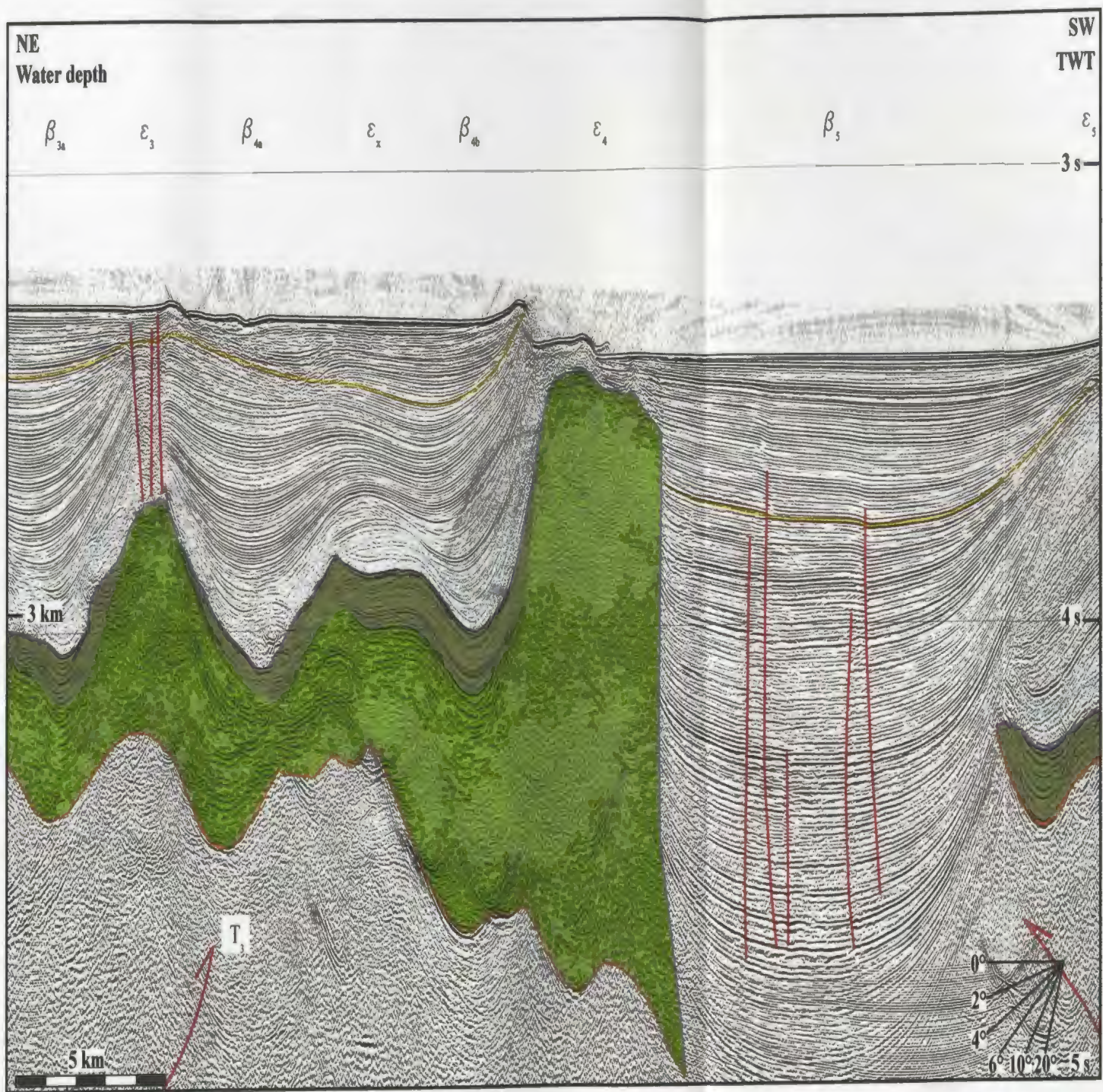
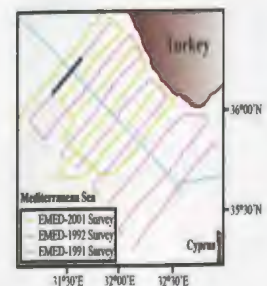


Fig. 6.14. Seismic reflection profile (FLX 1946-1963).

- Top middle Plio-Quaternary subunit
- Top basal Plio-Quaternary subunit
- M-reflector
- Upper evaporite subunit 2a
- Lower evaporite subunit 2b
- Top Unit 3



represented by the basins β_1 , β_2 and β_3 (also see Chapter 5). These structures trend parallel to the overall strike of the Florence Rise, which defines the western segment of the Cyprus Arc. Two smaller anticline-syncline pairs splay from the central anticline (i.e. ϵ_2), forming two prominent double-crested anticlines in the eastern and western segments of the study area (Fig. 6.1). The anticlines display notably long, gently northeast-dipping backlimbs and shorter, but steeply southwest-dipping forelimbs, suggesting that these structures define a large southwest-verging fold system. In seismic reflection profiles where the folds are well imaged, the hinge traces of the folds invariably show moderate to gentle northeast dips, further supporting the southwest vergence of the fold system.

The geometry of structures within the core of the anticlines is poorly resolved in most seismic reflection profiles. However, there are several key profiles where the geometry is better imaged, allowing the delineation of the structural architecture of the anticline-syncline pairs (Figs. 6.13, 6.14). The stratigraphic framework and the structural architecture observed within the syncline-anticline pairs resemble the geometries observed in the previously-described fold-thrust belts (McClay, 1981; Jackson and McKenzie, 1984; Ori and Friend, 1984). Therefore, the discontinuities imaged within the core of the ridges are interpreted to represent thrusts, with the ridges defining ramp anticlines. In this framework, the basins situated on the backlimb and forelimb of the thrust culminations represent the trailing and leading synclines, respectively. Careful correlation of seismic markers within Unit 3 between the leading syncline to the southwest and the crest of the anticline indicates ~ 500-600 ms vertical separation. Similarly, correlation of seismic

markers in Unit 3, as well as the M-reflector between the trailing syncline to the northeast and the leading syncline to the southwest, indicates ~ 300-400 ms vertical separation. This overall architecture of the anticlines, the stratal relationship within the leading and trailing synclines and the growth stratal architecture on both the backlimb and forelimb of the anticlines (see also Chapter 5) indicate the presence of northeast-dipping and southwest-verging thrusts seated deep in the core of the anticlinal structures. Where clearly imaged, the thrust surfaces are marked by narrow, higher amplitude reflector bundles (e.g. Figs. 6.13-6.16). However in many profiles thrust surfaces are not well-imaged or they extend well below five seconds in seismic reflection profiles (e.g. Figs. 6.5, 6.16). In these profiles, the vertical separations between marker reflectors between the leading and trailing synclines strongly suggest the presence of southwest-verging thrust faults in the core of these structures, even though the actual thrust surfaces are not always imaged.

In some profiles, the tips of the thrusts can be readily and invariably traced to the base of the M-reflector cutting the strata within the leading syncline, thus representing “break thrusts” (Fig. 6.17). Yet in others, the thrust tips are inferred to lie well within Unit 3 in the partially imaged leading syncline, suggesting that these represent “blind thrusts”. The ridges described in Chapter 5 are, thus interpreted to represent the apex of the hanging-wall ramp anticlines. Some well-imaged examples of these are illustrated in Figures 6.13-6.15 and 6.18. Note that in all these images, ridge ϵ_2 defines the crestal region of the hanging-wall ramp anticline of thrust T_2 , whereas the gently to moderately

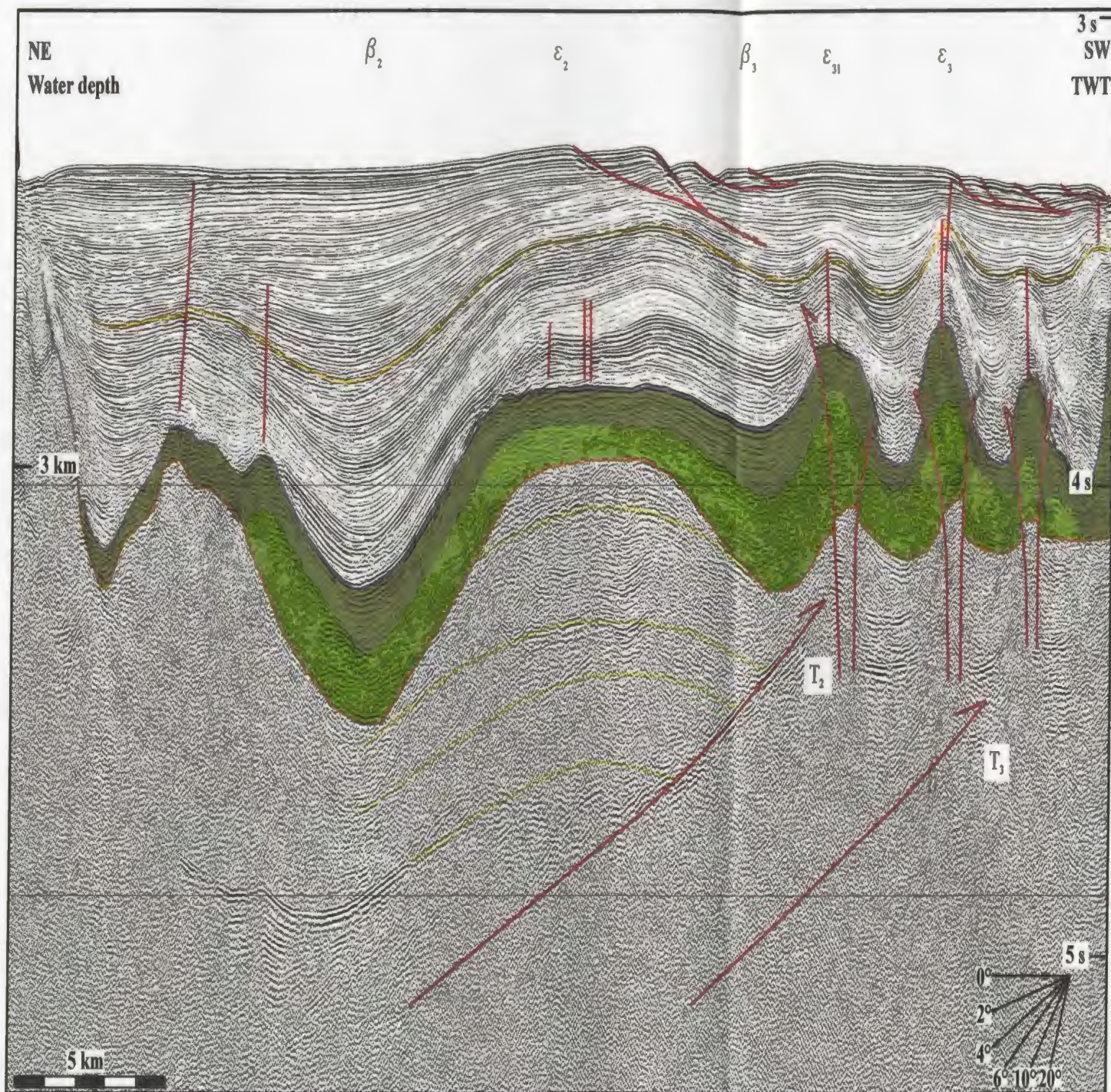
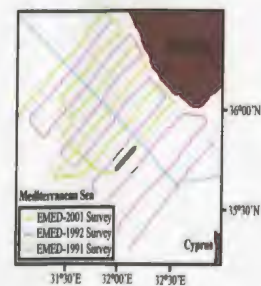


Fig. 6.15. Seismic reflection profile (FIX 765-774).

- Top middle Plio-Quaternary subunit
- Top basal Plio-Quaternary subunit
- M-reflector
- Upper evaporite subunit 2a
- Lower evaporite subunit 2b
- Top Unit 3
- Reflectors in Unit 3



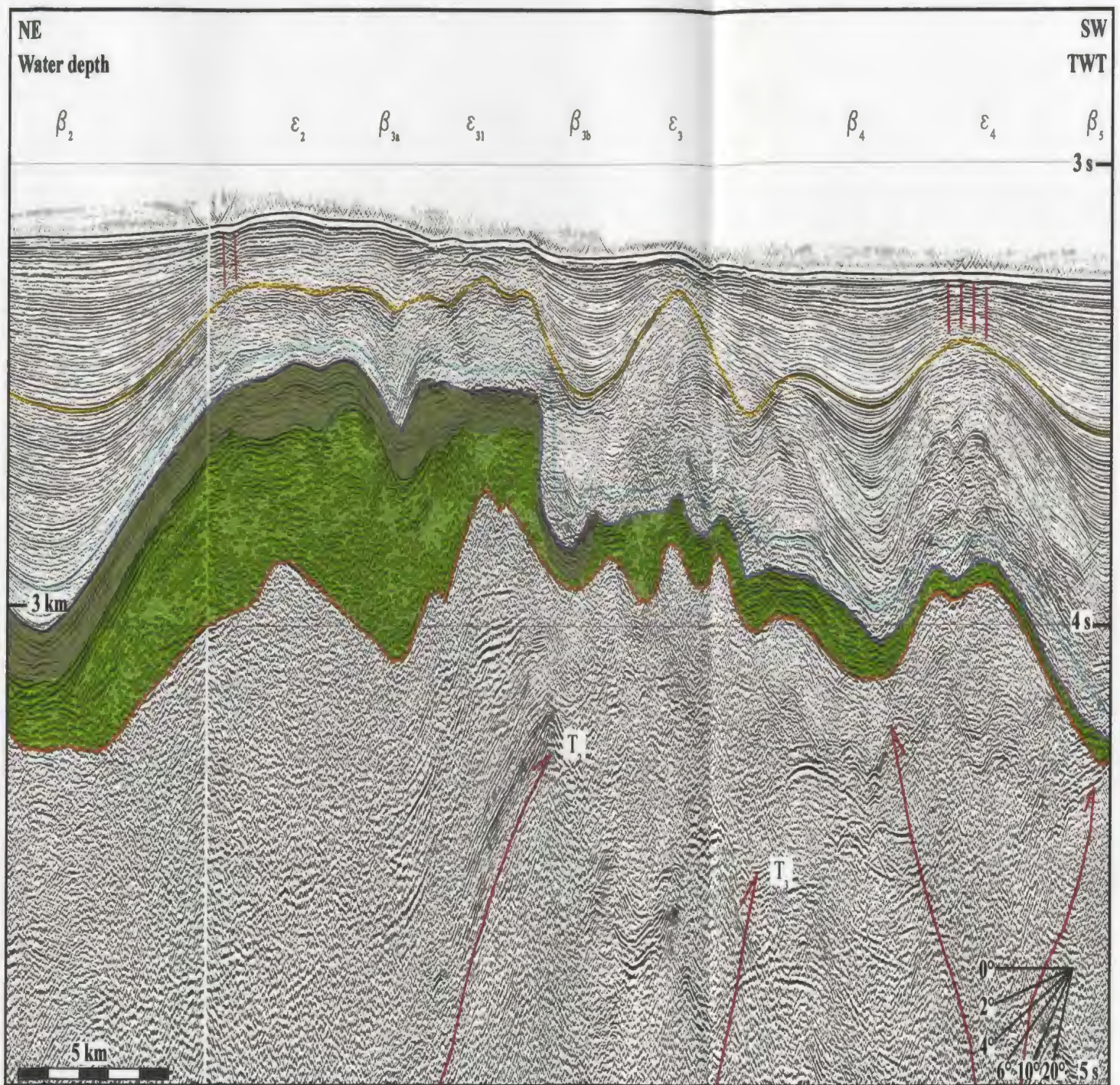
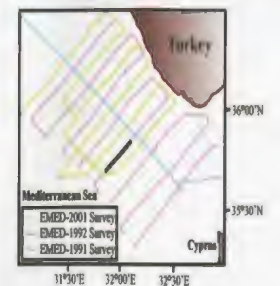


Fig. 6.16. Seismic reflection profile (FIX 1757-1772).

- Top middle Plio-Quaternary subunit
- Upper evaporite subunit 2a
- Top basal Plio-Quaternary subunit
- Lower evaporite subunit 2b
- M-reflector
- Top Unit 3



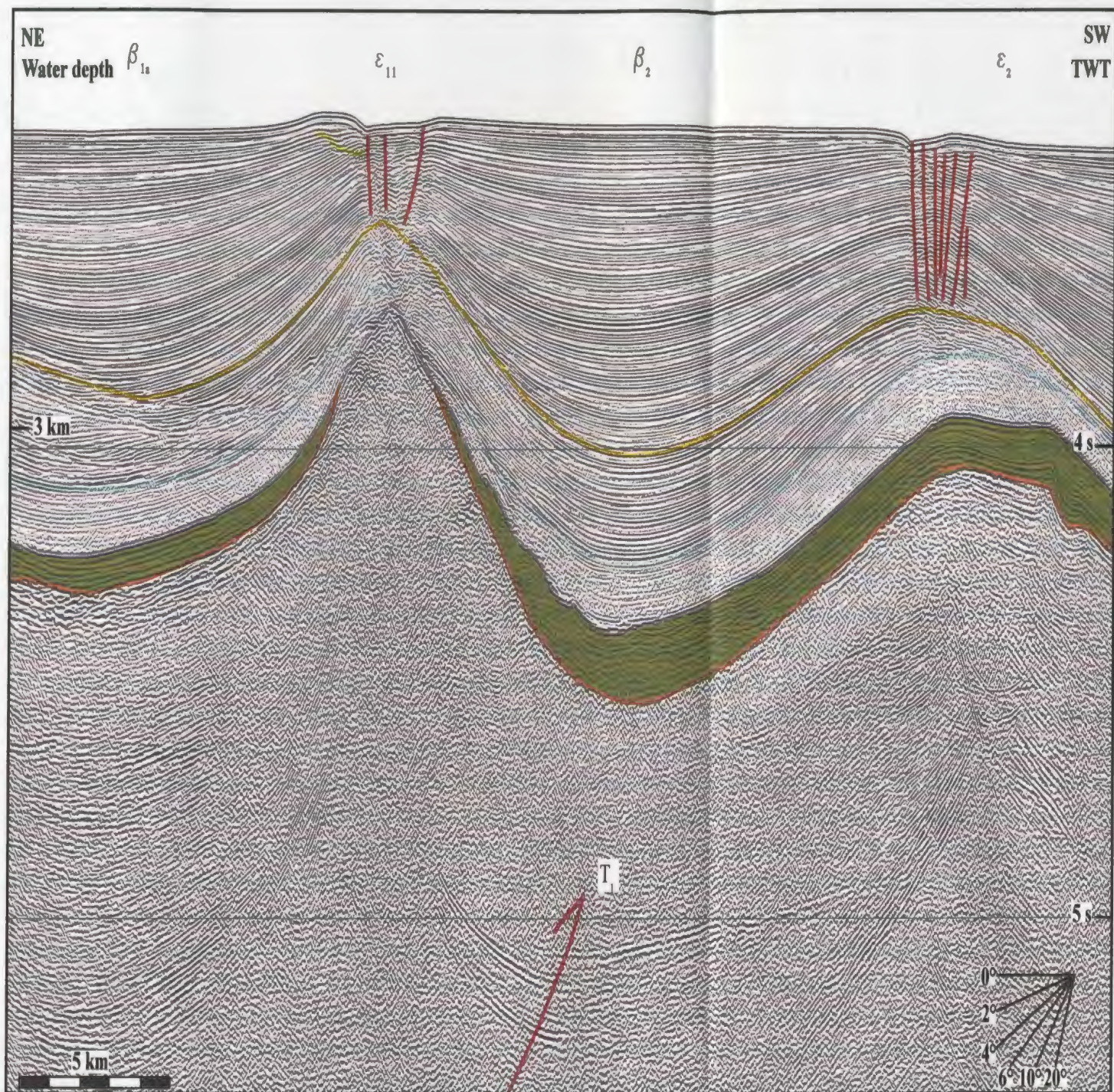
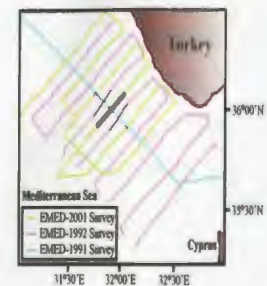


Fig. 6.17. Seismic reflection profile (FIX 612-620).

- Top middle Plio-Quaternary subunit
- Upper evaporite subunit 2a
- Top basal Plio-Quaternary subunit
- Top Unit 3
- M-reflector



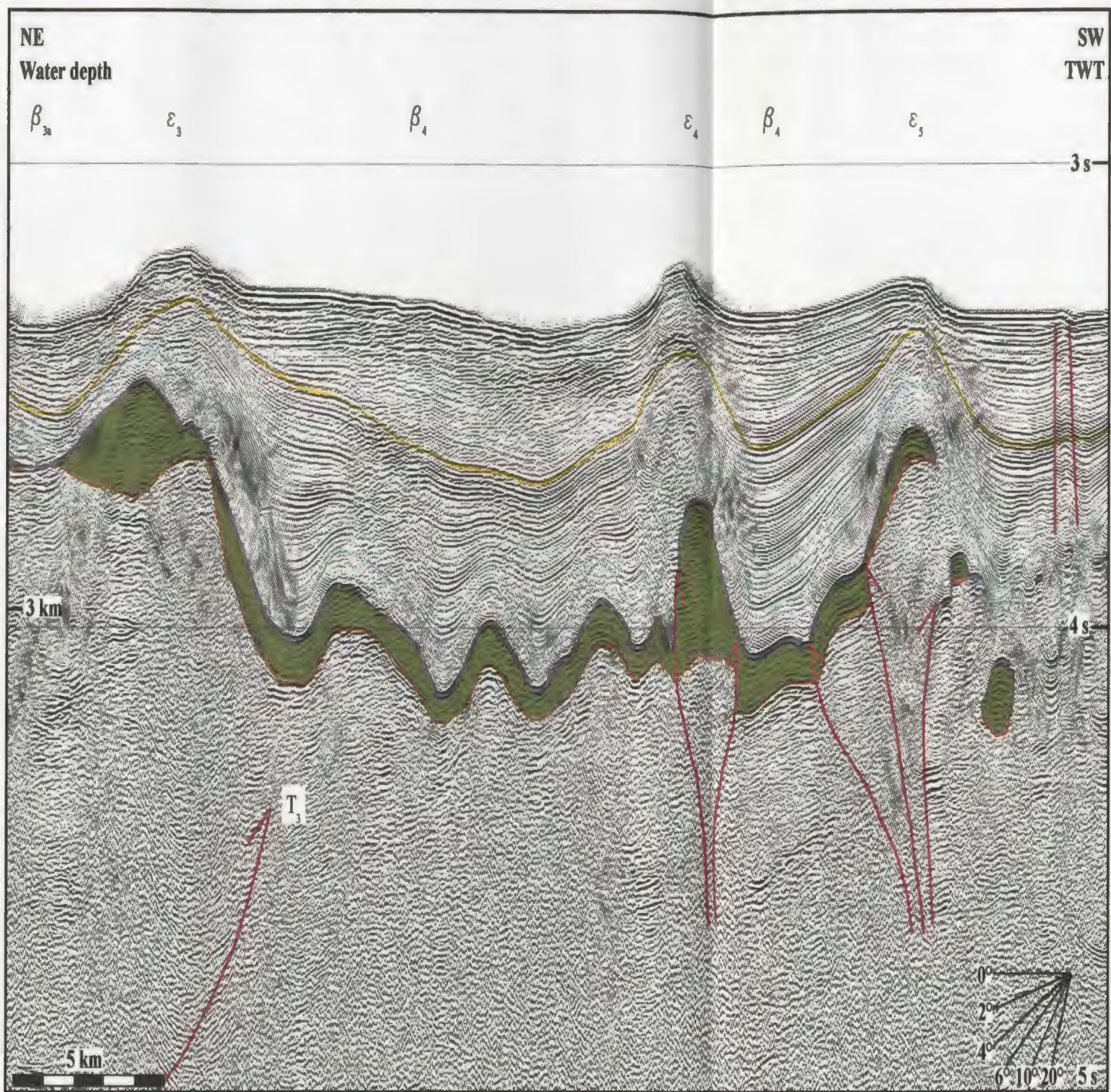
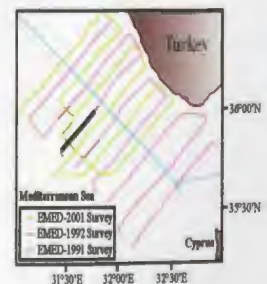


Fig. 6.18. Seismic reflection profile (FLX 1855-1873).

- Top middle Plio-Quaternary subunit
- Upper evaporite subunit 2a
- Top basal Plio-Quaternary subunit
- Top Unit 3
- M-reflector



northeast-dipping backlimbs represent hanging-wall flats above the thrust surfaces. The large Pliocene-Quaternary depocentre β_2 , which is nestled on the backlimb of the ramp anticline, thus represents a piggyback basin carried by thrust T_2 , whereas the depocentre β_3 represents the piggyback basin nestled on the backlimb of T_3 thrust.

The individual thrusts T_1 , T_2 and T_3 of the fold-thrust system occur beneath the most prominent ridges, $\epsilon_1 + \epsilon_{11}$, ϵ_2 and ϵ_3 , respectively (Fig. 6.1). Splays with southwest-verging sense stem from thrusts T_1 , T_2 in the northwest and southeast and from thrust T_3 in the central portion of the study area, and display map traces mostly parallel to the trend of the associated main faults (Fig. 6.1). They exhibit low-angle trajectories similar to that of the main thrusts and the tip points mostly lie below or at the M-reflector. Thrusts T_{1a} and T_{1b} form the western and eastern splays originating from thrust T_1 , which extend below ridges ϵ_{13} and ϵ_{12} , respectively. These thrusts both merge with the associated main thrust (T_1) in the central portion of the study area (Fig. 6.1). Thrust T_{2a} extends below ridge ϵ_{31} and comprises the splay stemming from thrust T_2 in the central portion of the study area. It displays a northwest-southeast strike, and merges with thrust T_2 and T_3 in the eastern and western portions of the study area, respectively (Fig. 6.1). In the southern portion of the study area, thrusts T_{3a} and T_{3b} carry ridges ϵ_x and ϵ_y and form the western and eastern splays originating from thrust T_3 , respectively (Fig. 6.1). Each splay merge with the main thrust T_3 in the central portion of the study area.

The intervening basins between the ramp anticlines, are referred to as piggy-back basins, which are carried above the imbricate thrust fault system. The sedimentary fill of

these piggy-back basins contain Messinian to Recent deposits. The deposition of the Messinian to Recent strata is mostly contemporary with the activity of thrust faults, suggested by the growth strata wedges recognized throughout the sedimentary column of the piggy-back basins. Although, the mainly undeformed character of the lower Pliocene-Quaternary subunit through most of the study area provides evidence of a period of quiescence in the fault activity. However, occasionally, this subunit locally shows thinning towards the crest of the ridges, suggesting that the faults continued to grow during the deposition of this succession (Fig. 6.16, 6.17). Various intra-stratal unconformities developed within the Pliocene-Quaternary succession separate growth strata packages and mark the stages of hiatus in the growth of the thrusts. These growth strata wedges developed on the backlimb and forelimb of the fold-thrust structures are bounded by several unconformities delineated by the prominent onlap of the mostly the lower/middle Pliocene to Recent succession over the flanks of the ridges or the underlying pre-growth strata (Fig. 6.16). This character of the unconformities show remarkable resemblance to that of progressive unconformities as described by Riba (1976). Progressive unconformities are inferred to develop associated with growth of the thrust-related folds during sedimentation (Suppe et al., 1992, Hardy and Poblet, 1994) and they represent changes in rate of uplift assuming constant sedimentation rate.

In summary, the overall structural framework of Domain 2 is characterized by three prominent northwest-southeast striking, southwest-verging thrust faults with several minor splays, which display curvilinear, south-convex traces on the map throughout the

study area (Fig. 6.1). The thrust sheets are 900-1200 ms thick and consist of sediments of Units 3 and 2. These thrusts override one another in the transport direction and define a stacked imbricate fan. The thrust faults exhibit low-angle trajectories, of which only the uppermost portion could be imaged in the seismic reflection profiles. Except a small number of break thrusts, most represent blind thrusts with tip points located mostly within Unit 3 below the M-reflector.

6.3. Domain 3

Domain 3 constitutes the southeastern portion of the Antalya Basin within the study area bounded by ridge ε_2 in the north and by the southern limit of the seismic grid in the south (Fig. 6.1). The internal architecture of the Miocene to middle to upper portions of the Pliocene-Quaternary succession within this domain is characterized by five northwest-southeast-trending fold structures, which exhibit north- and south-tilted asymmetrical cross-sectional geometries (Figs. 6.18-6.20; also see Chapter 5). Here, ridges ε_3 , ε_4 , ε_5 , ε_6 and the locally emerging ridge ε_{31} represent these fold structures delineated by the M-reflector. Ridges ε_4 , ε_6 and ε_{31} are identified by their long, gently southwest-dipping backlimbs, and shorter, but steeply northeast-dipping forelimbs, which contradict the common south-tilted asymmetrical cross-sectional geometry of the structures recognized throughout the study area (Figs. 6.18-6.21). Whereas, ridges ε_3 and ε_5 are characterized by their long, gently northeast-dipping backlimbs, and shorter, but steeply southwest-dipping forelimbs (Figs. 6.18, 6.19). The structures within Units 3 and

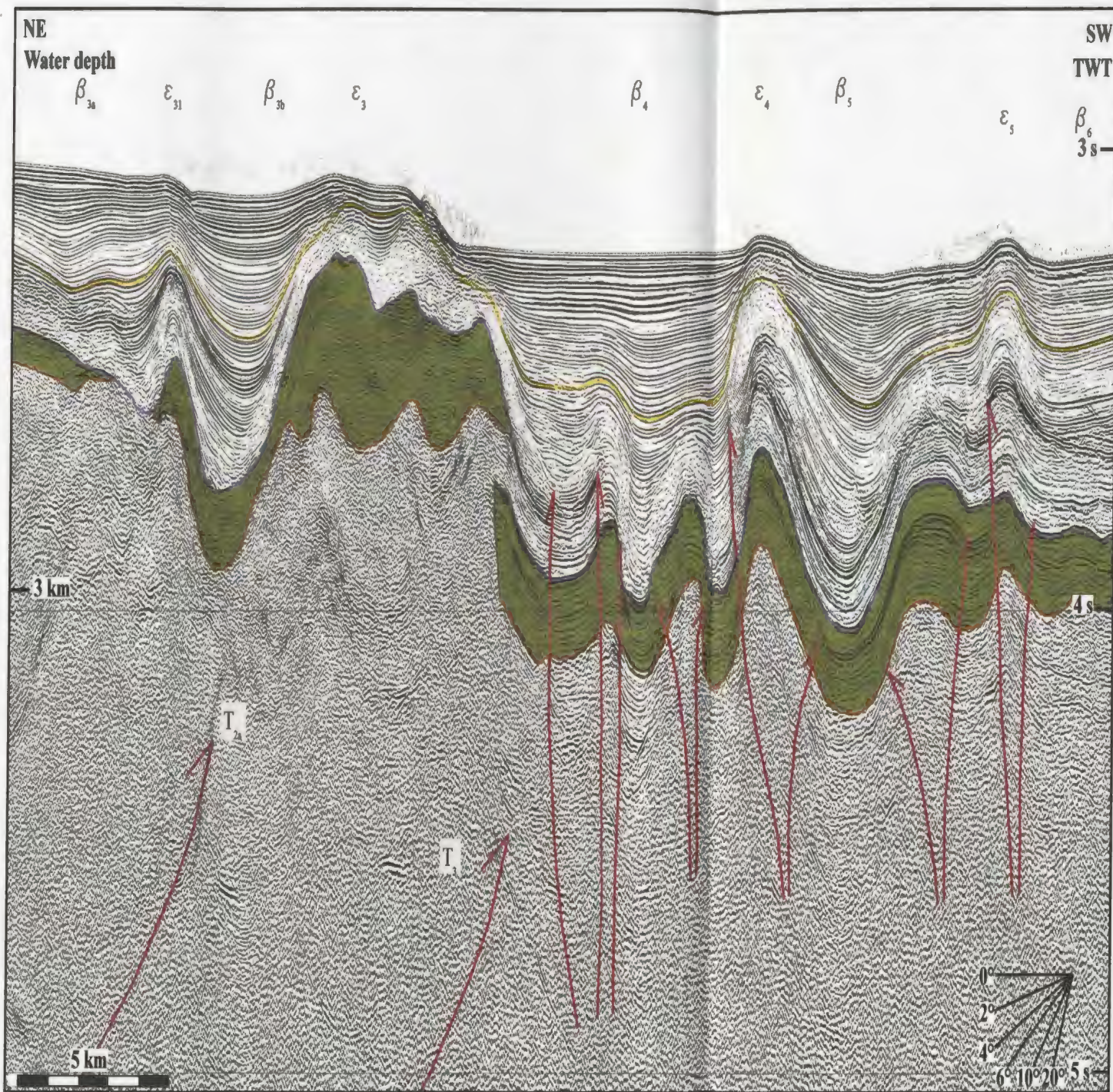
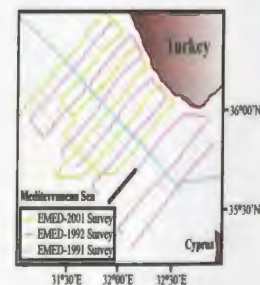
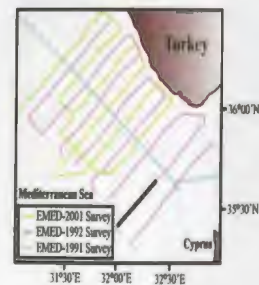


Fig. 6.19. Seismic reflection profile (FIX 1729-1745).

- Top middle Plio-Quaternary subunit
- Upper evaporite subunit 2a
- Top basal Plio-Quaternary subunit
- Top Unit 3
- M-reflector





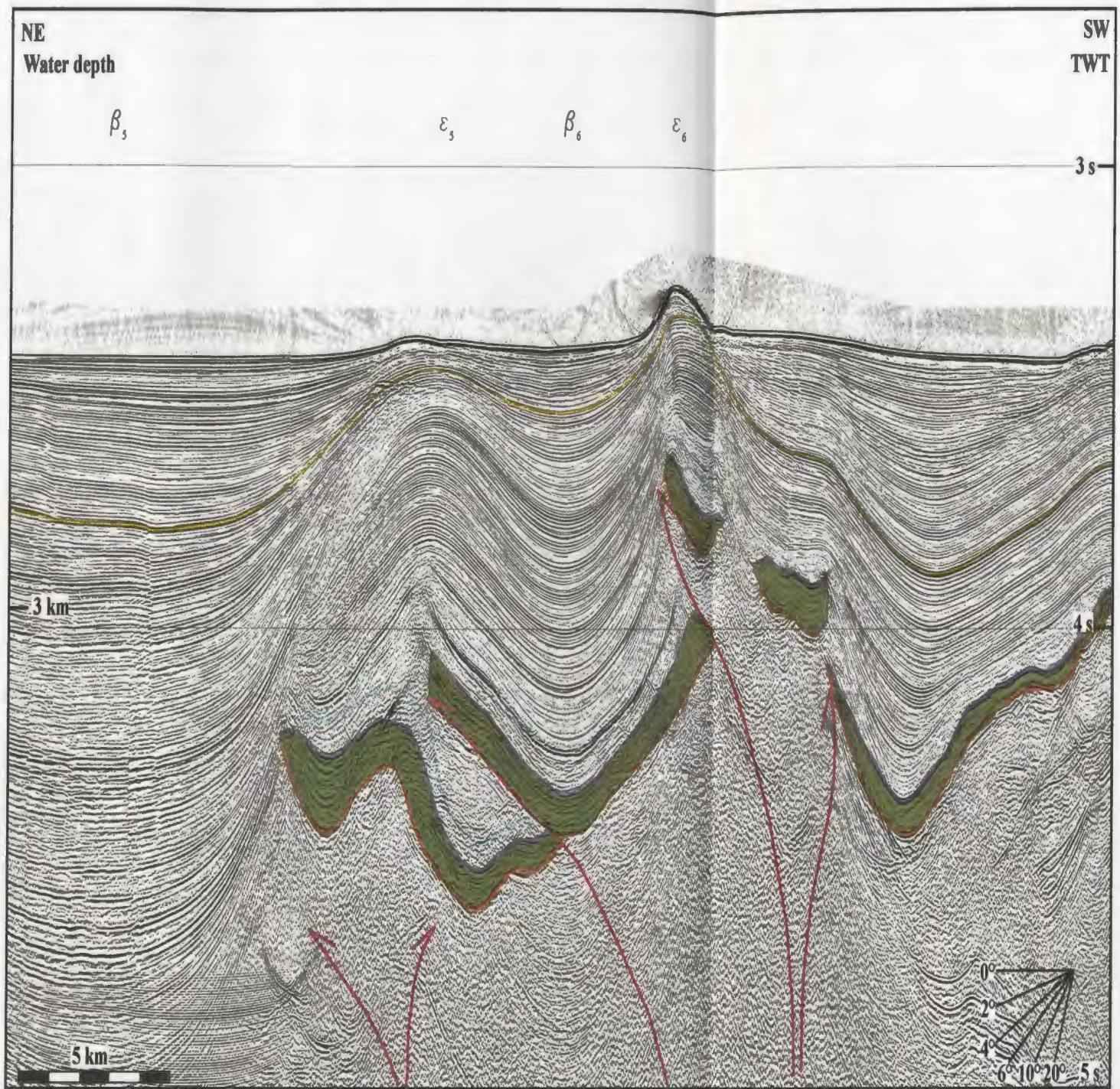


Fig. 6.21. Seismic reflection profile (FIX 1959-1974).

- Top middle Plio-Quaternary subunit
- Upper evaporite subunit 2a
- Top basal Plio-Quaternary subunit
- Top Unit 3
- M-reflector

2, which constitute the core of these ridges, show parallel trends to the morphology of the M-reflector, although the wavelength of the fold structures tend to decrease as traced down-section (Fig. 6.18). The external geometry of the Miocene ridges are still preserved in the lower to upper Pliocene-Quaternary succession with the reflectors draping over the M-reflector. Additionally, a number of low-amplitude and short-wavelength ridges locally emerge on the floor of intervening basins β_4 and β_6 , and display similar characteristics in terms of the internal architecture as well as the external geometry, to that of the major ridges within this domain (Figs. 6.18, 6.20, 6.22).

The overall internal architecture of Domain 3 suggests that the ridges developed in this portion of the study area are associated with a family of narrowly-spaced, thrust faults with markedly curved north- and south-verging trajectories. The thrusts of each fault pair are rooted deep in Unit 3 with tip points lying between the upper portion of Unit 3 and the lower to middle portion of Unit 1 (Figs. 6.18, 6.20, 6.21). They display sub-vertical trajectories in the vicinity of the roots, but as traced up-section, they curve away from each other along progressively gentler trajectories (Figs. 6.20, 6.21). The doubly-verging character of the thrust pairs and the north- and south-tilted asymmetrical cross-sectional geometry of the ridges bounded by these thrusts suggest that these thrust pairs represent positive flower structures. Similar structures are described by Calon et al (submitted) from the Cyprus Basin. Such structures are generally associated with transpressional deformation (e.g. Harding et al., 1983).

The reflector packages within the middle to upper portion of the Pliocene-

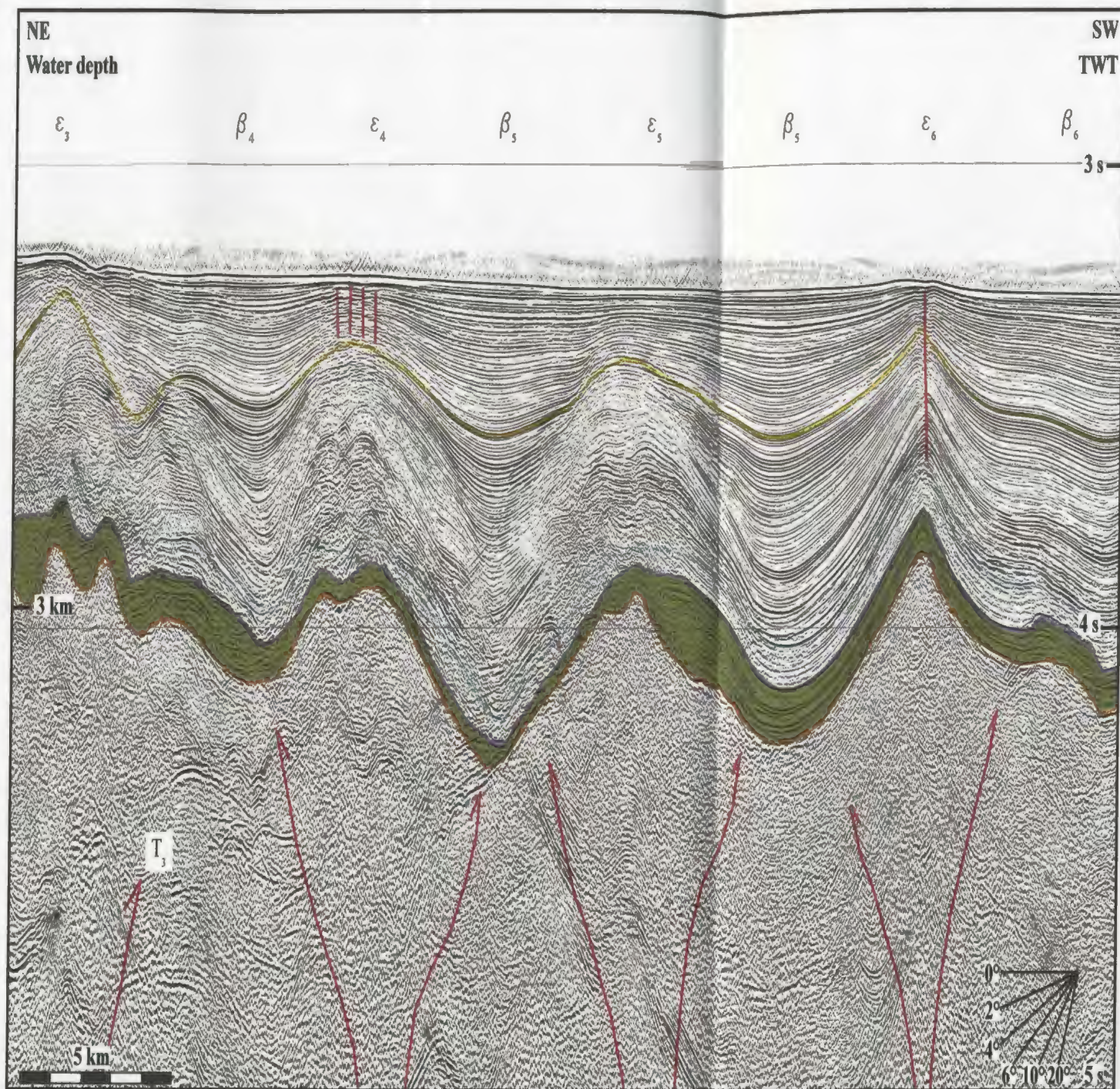
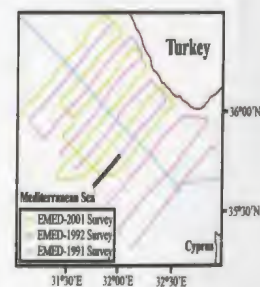


Fig. 6.22. Seismic reflection profile (FIX 1747-1762).

- Top middle Plio-Quaternary subunit
- Upper evaporite subunit 2a
- Top basal Plio-Quaternary subunit
- Top Unit 3
- M-reflector



Quaternary succession show north- and south-directed thinning and progressive onlap against the older folded strata overlying the Miocene ridges. This stratigraphic architecture represents growth strata wedges and suggests that the activity of thrust faults of the flower structures is contemporaneous with the deposition of the middle to upper portion of the Pliocene-Quaternary succession (Figs. 6.18-6.20, 6.22). The sea floor above the crestal area of the ridges truncates the underlying reflectors of the Quaternary succession and occasionally displays small scale inflections, which together suggests that the thrust faults of Domain 3 continue to be active in the present-day (Figs. 6.18-6.22). Thrusts with tip points situated below the middle Pliocene-Quaternary succession represent “blind thrusts”, while the others with tip points reaching the middle portion of the Pliocene-Quaternary succession represent “break thrusts”.

Due to the poor resolution in the deeper portions of the seismic reflection profiles as well as the limited record length, the internal architecture of the core of the positive flower structures could only be imaged in a small number of profiles within the existing seismic grid (Figs. 6.18, 6.20). However, the relief created by the doubly-verging thrust faults is prominent throughout the study area and is diagnostic of flower structures (e.g. Harding et al., 1983; Biddle and Christie-Blick, 1985) which enabled a tentative assignment of the domain boundaries. The detailed mapping and understanding of these structures require a denser seismic grid and critical structural geological analysis involving detailed cross-section balancing, which will be the focus of the author’s PhD research.

CHAPTER 7. Discussion

The Antalya Basin is situated in a forearc setting north of the African-Aegean/Anatolian convergent plate boundary and comprises several structural elements, which are commonly associated with plate tectonic activity. Several hypotheses have been proposed for the Neogene evolution of the Antalya Basin as well as its role within the regional tectonic setting of the eastern Mediterranean. Despite a number of previous studies (e.g. Woodside, 1977; Sage and Letouzey, 1990; Robertson 1998, Calon et al. submitted a, b); the Miocene to Recent kinematic evolution of the Antalya Basin is still not well understood, primarily because most previous investigations have been exploratory in nature, and lack the rigorous systematic mapping of large-scale structural elements, necessary to delineate the kinematic history.

7.1. Kinematic evolution of the Antalya Basin

Detailed analysis of the seismic stratigraphic architecture of the Pliocene-Quaternary basins and the Miocene ridges, as well as the spatial and temporal trend of the structural culminations reveal a tectonic model that explains the Miocene to Recent evolution of the Antalya Basin within the context of the factors that shaped the eastern Mediterranean. The deformation in the Antalya Basin occurred primarily as the result of compressional stresses and to a lesser extent extensional, transpressional and transtensional stresses (Figs. 6.1 and 7.1). Mobilization of the Messinian evaporites also played an important role in basin evolution, although it is not yet possible to quantify the

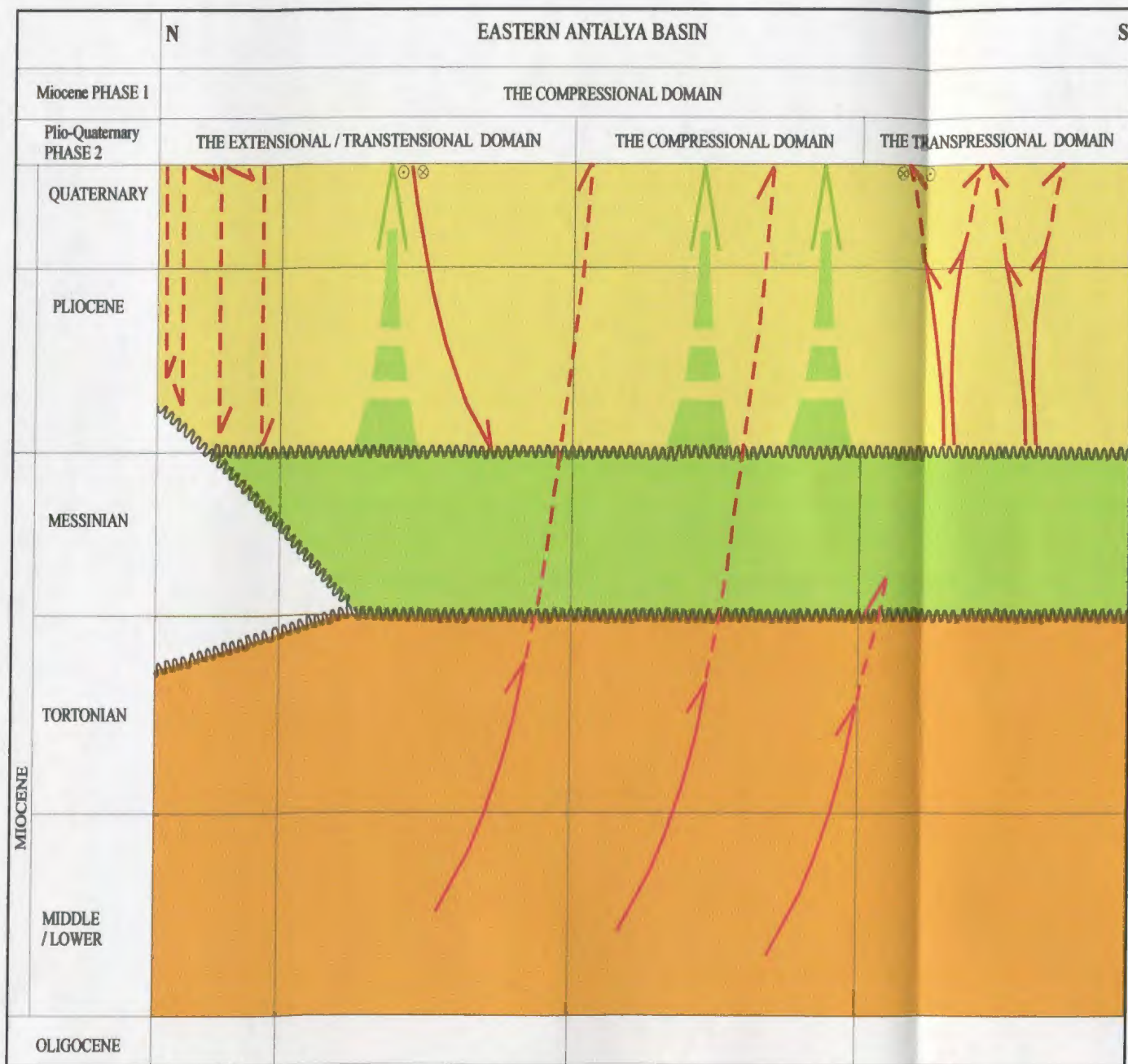


Fig. 7.1. The tectonostratigraphic chart showing the two main phases of deformation (i.e. Miocene and Pliocene-Quaternary) in the eastern Antalya Basin. Refer to the map displayed in Figure 6.1 for the locations of the structural domains.

amount of deformation caused by halokinesis.

7.1.1. Miocene (pre-Messinian)

During the middle-late Miocene, the marine Antalya Basin, as well as the onland Darıören, Beydağları and Antalya Basins, were situated within a forearc setting located between the evolving Tauride culminations in the north and the subduction zone in the south. Miocene (Serravallian to Tortonian) successions of the Karpuzçay and Aksu formations and their equivalents in seismic stratigraphic Unit 3 were deposited within a large east-west-trending foredeep which extended from the Bitlis Ocean in the east (Şengör, 1985), across the Iskenderun, Adana, Inner Cilicia (Aksu et al., submitted; Burton et al., submitted) and Inner Latakia (Hall et al., submitted a) basins in the centre, to the Kyrenia Range of northern Cyprus (Calon et al., submitted a, b) and the Antalya Basin in the west. Middle to late Miocene regional compression led to the development of a major northwest-southeast-oriented arcuate fold-thrust belt, which can be traced all across the forearc region north of Cyprus Arc (Fig. 7.2). The structures associated with this late Miocene compression are clearly documented in the Antalya Basin.

Large imbricate thrust sheets T_1 , T_2 and T_3 and their associated ramp anticlines ϵ_1 , ϵ_2 and ϵ_3 carrying piggyback basins β_1 , β_2 and β_3 collectively show a protracted contractional deformation throughout the deposition of Miocene Unit 3. The Antalya Basin remained as a foredeep during this phase of contraction, while the Kyrenia foredeep became progressively inverted leading to the development of the Kyrenia fold/thrust belt in

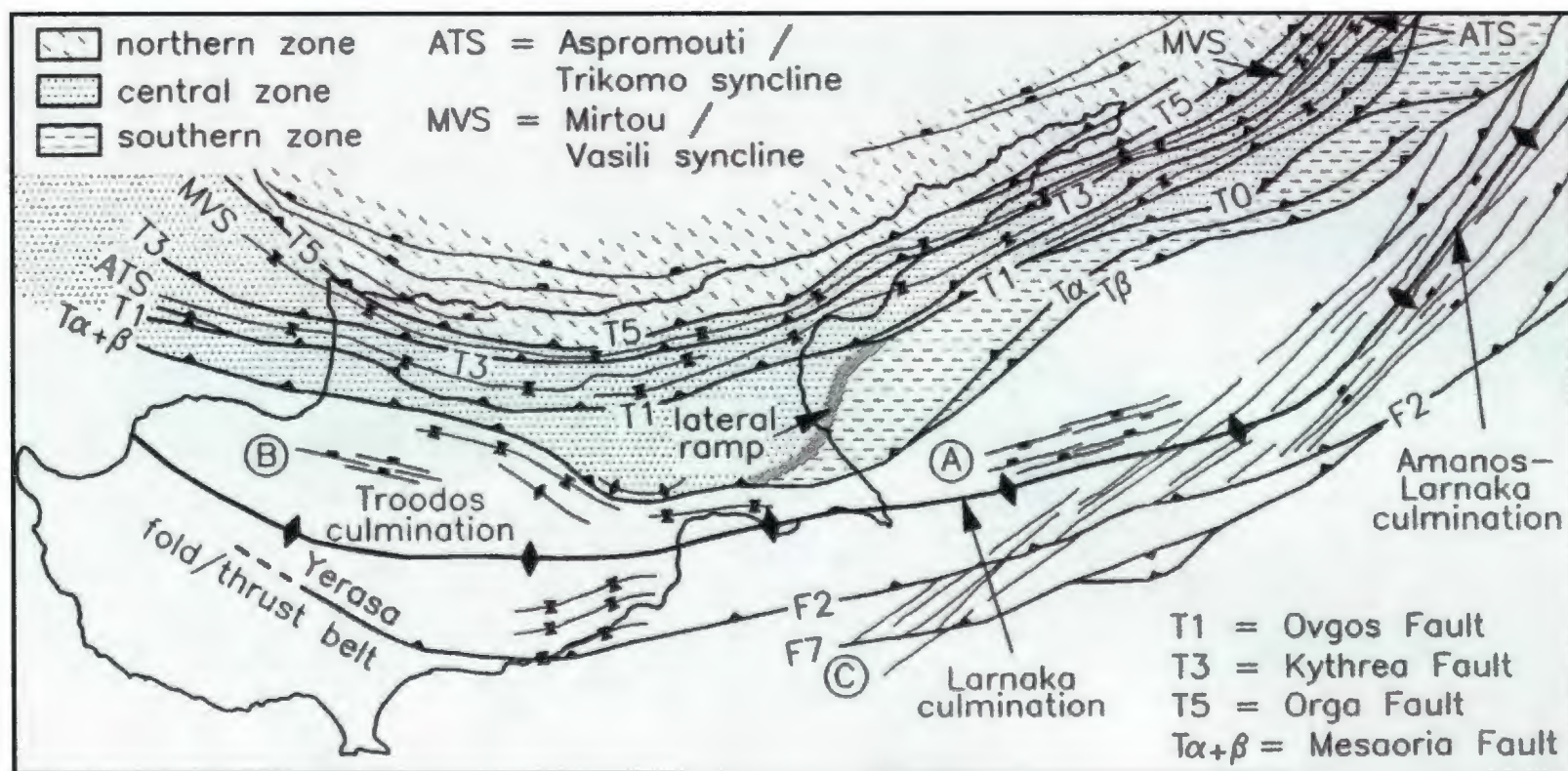


Fig. 7.2. Map showing the major faults and piggy-back basins in northern Cyprus (Calon et al., submitted a and b)

the Pliocene-Quaternary (Calon et al., submitted a or b).

Progressive northward movement of the Arabian Microplate resulted in the collision and subsequent suturing of the Arabian Microplate with the Aegean-Anatolian Microplate in the late Miocene. During this time the last relics of the Bitlis Ocean closed, and the eastern connection of the Neotethys with the Indo-Pacific Ocean was ruptured by the evolving Bitlis-Zagros fold/thrust belt. Towards the end of Tortonian the progressive northeast-directed motion of the African Plate relative to the Eurasian Plate also narrowed and eventually closed the connection between the Neotethys (i.e. Mediterranean) and the Atlantic Ocean to the west. At the end of Tortonian the Mediterranean Sea was situated at approximately the same subtropical latitudes as today and was completely isolated both from the Atlantic Ocean as well as the Indian Ocean.

7.1.2. Messinian

Subareal exposure and the significant lowering of the base level associated with the evaporative drawdown led to the profound erosion of the desiccated Mediterranean basins (i.e. the Mediterranean Salinity Crisis, Hsu et al., 1978). This erosional event in Antalya Basin is represented by the N-reflector, which is an angular unconformity truncating the folded strata of the Miocene Unit 3 (Fig. 7.3). The erosional nature of the unconformity and the stratal relationships of the overlying and underlying reflectors indicate that the present-day N-reflector largely preserves the paleo-relief associated with the pre-Messinian deformation. Deposition of the evaporitic succession in a shallow marine

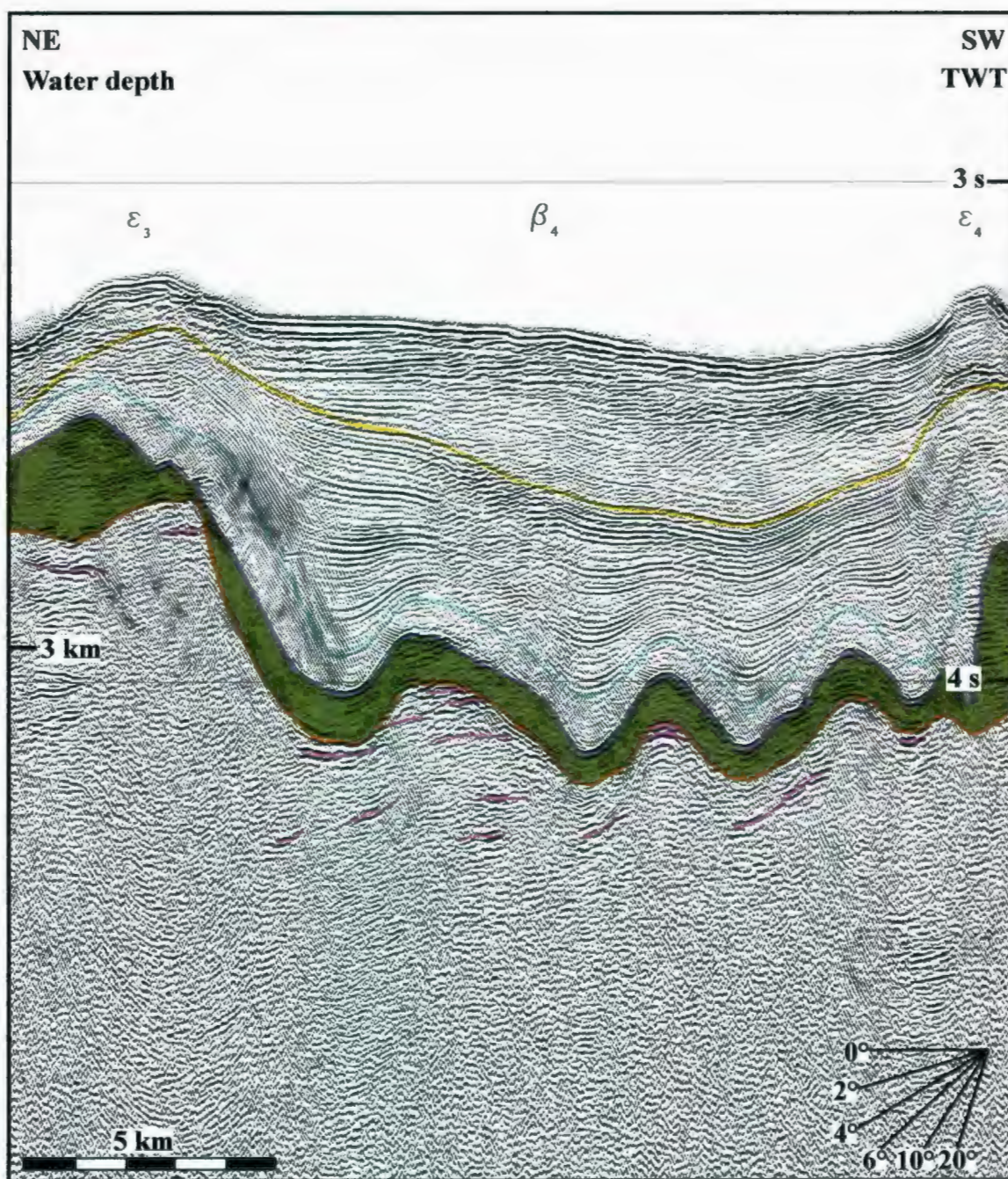


Fig. 7.3. Seismic reflection profile showing the erosional character of the N-reflector. The folded Unit 3 strata is truncated by the N-reflector.

- | | |
|------------------------------------|----------------------------|
| Top middle Plio-Quaternary subunit | Upper evaporite subunit 2a |
| Top basal Plio-Quaternary subunit | Top Unit 3 |
| M-reflector | Reflectors in Unit 3 |

environment followed the development of the N-reflector. The observed thickness of the Messinian evaporites range from 3000 m in the Herodotus Basin to ~2500 m in Antalya Basin (Biju-Duval et al., 1978), to ~1000 m in the Cilicia and Latakia Basins (Aksu et al., submitted; Hall et al., submitted). The present-day volume of the Mediterranean Sea of 3.77×10^6 km with an average salinity of ~39 ‰ would produce ~40 m thick evaporite deposits if desiccated completely. This first order calculation suggests that ~70 times the volume of the Mediterranean Sea is needed to produce the 3000-2500 m thick evaporites in deep basins. The floor of the Cilicia and Latakia Basins are situated 1200-2000 m above the floor of the adjacent deep Antalya and Levantine Basins, respectively. Thick evaporite deposits in these basins provide additional evidence for the multiple filling and desiccation of the deep Mediterranean basins during the Messinian. The initial depositional distribution of the evaporites cannot be derived by only analyzing the seismic reflection profiles and interpreting the reflector terminations because what is observed today represents the structures formed following halokinesis.

The generally north- and south-thinning geometry of the relatively well-stratified Messinian subunit 2a on the flanks of the early Messinian subunit 2b highs or Miocene fold structures where subunit 2b is absent, show that local re-activation of the fold-thrust belt occurred during the deposition of the upper evaporitic subunit 2a (Fig. 7.4). Further evaluation of the behavior of the evaporites during the evolution of the basin is going to be a subject of the author's PhD thesis.

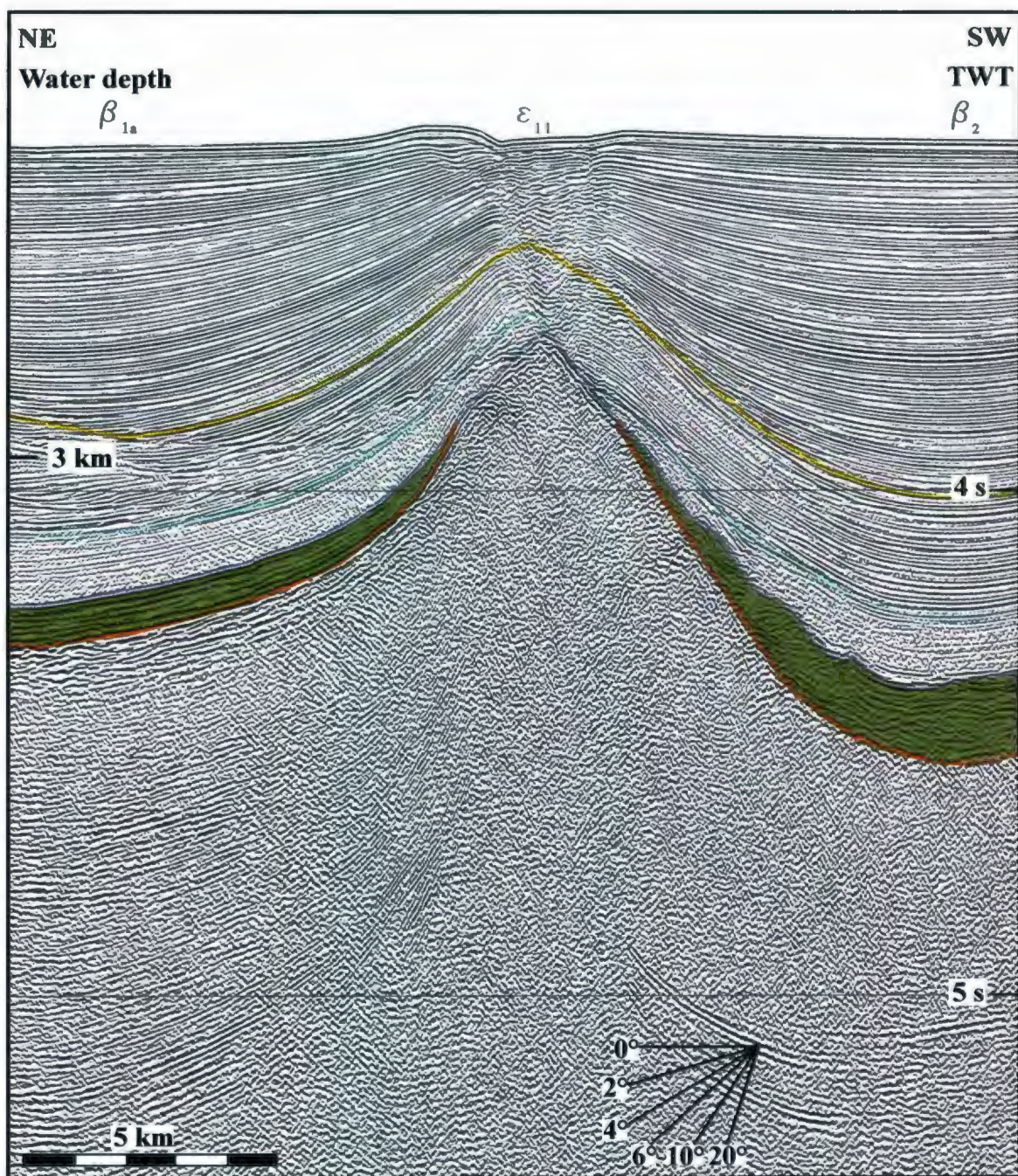


Fig. 7.4. Seismic reflection profile showing the north- and south-thinning geometry of Subunit 2a towards the crestal area of ridge ϵ_{11} .

- Top middle Plio-Quaternary subunit
- Top basal Plio-Quaternary subunit
- M-reflector
- Upper evaporite subunit 2a
- Top Unit 3

7.1.3. Pliocene-Quaternary

Interpretation of the existing seismic reflection profiles demonstrates a fundamental change in kinematic regime during the transition from the Miocene to the Pliocene. The desiccation of the Mediterranean Sea at the end of the Miocene (Hsü et al., 1978) and the related exposure of the sea-floor at the time resulted in the development of an erosional surface, represented by a well-defined angular unconformity on the seismic reflection profiles, the M-reflector. The M-reflector truncates the underlying folded strata of Unit 3, or Unit 2 where the Messinian evaporites are present, suggesting that the fold-thrust activity continued into the Messinian and that this activity pre-dates the development of the M-unconformity (Fig. 7.5). The erosional nature of the unconformity further implies that the initial thickness of the Miocene sedimentary fill of the piggy-back basins were greater than what is observed on the seismic reflection profiles.

The basal Pliocene-Quaternary subunit was deposited above the M-reflector as the post-growth strata relative to the Miocene fold/thrust activity. The re-filling of the Mediterranean Sea during the early Pliocene caused the landward retreat of the shoreline and initiated an interval dominated by hemipelagic deposition throughout the eastern Mediterranean Sea. The early Pliocene marls of Unit IV encountered in the DSDP sites 375 and 376 (Hsü et al., 1978), the Mirtou Formation of the Kyrenia Range and Mesaoria Basin in Cyprus (Robertson and Woodcock, 1986), and the Handere Formation of the Adana and Cilicia Basins (Yalçın and Görür, 1984) all represent this hemipelagic phase.

During the deposition of the early/middle Pliocene to Recent strata, the fault

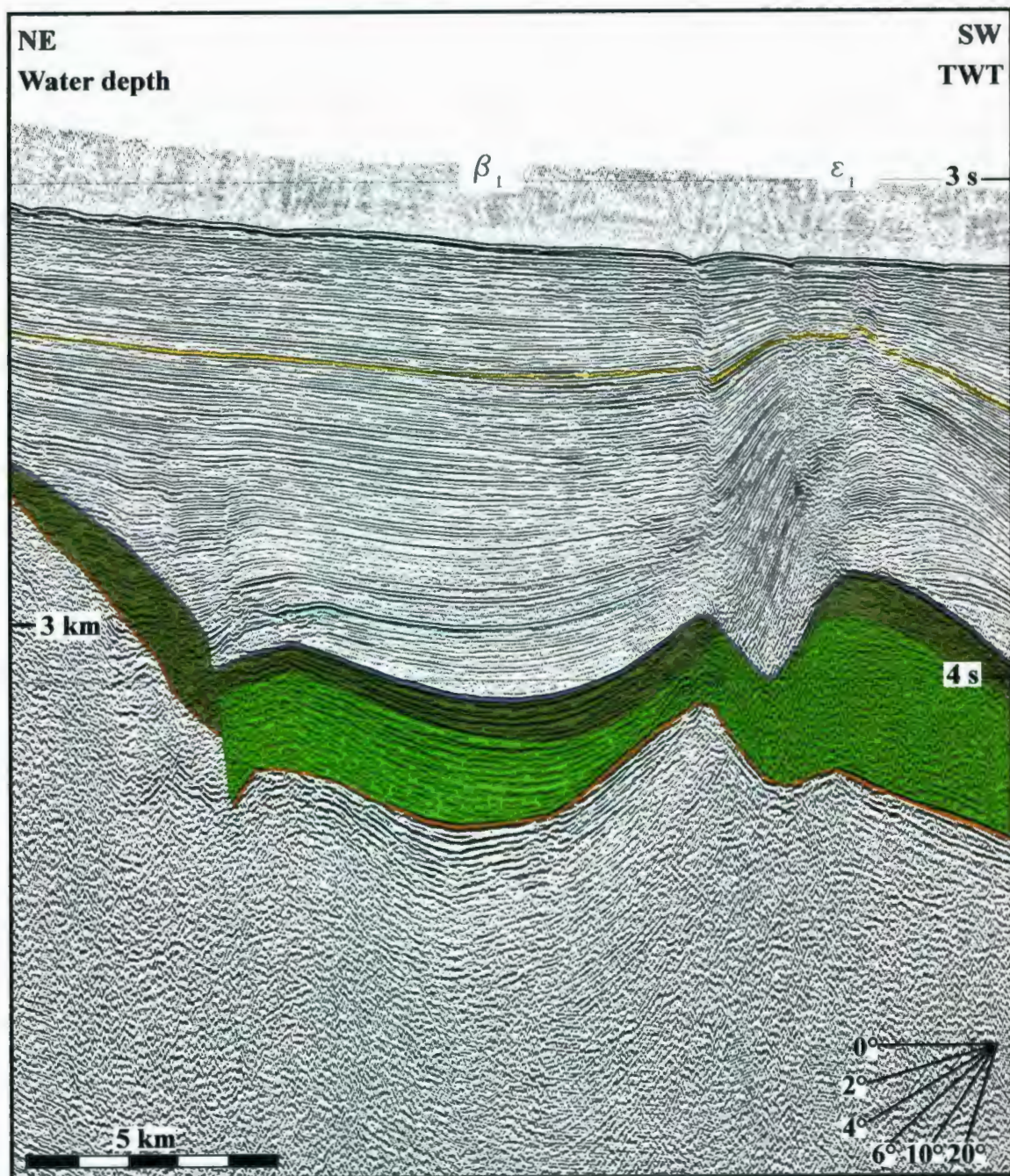


Fig. 7.5. Seismic reflection profile showing the erosional character of the M-reflector. Unit 2 strata is truncated by the M-reflector.

- | | |
|------------------------------------|----------------------------|
| Top middle Plio-Quaternary subunit | Upper evaporite subunit 2a |
| Top basal Plio-Quaternary subunit | Upper evaporite subunit 2a |
| M-reflector | Top Unit 3 |

activity in the Antalya Basin is constrained to three geographical domains comprising the northern, central and southern portions of the Antalya Basin.

In the northern and central portions of the deep Antalya Basin, the north- and south-thinning growth strata wedges developed on the backlimb and forelimb of the fold-thrust structures indicate thrust fault activity continued from early-middle Pliocene to Recent (Fig. 7.6). The relatively thicker growth packages imaged within the middle Pliocene-Quaternary interval suggest that the fold-thrust belt displays a protracted activity with intervals of accelerated growth during this interval (Fig. 7.6). The upper Pliocene-Quaternary succession homoclinally oversteps some culminations while showing onlap against the flanks of others (Fig. 7.7). The overstep of the upper Pliocene-Quaternary succession over the crests of the ridges shows that the thrust activity locally slowed down or even ceased during this interval (Fig. 7.7). Where present, any fold/thrust activity extending into the Recent is expressed by the small scale inflections on the seafloor (Fig. 7.6).

In the northern portion of the Antalya Basin, the stratal architecture of the Pliocene-Quaternary succession on the hanging-wall of the listric extensional fault A6 (Fig. 7.8) indicates that growth has been taking place since the beginning of Pliocene essentially acting concurrently with the fold/thrust activity to the south. This listric extensional fault is interpreted to represent a major transtensional zone, which must have developed in relation to the westward displacement of the Tauride block as the Anatolian Microplate initiated its westward escape in the latest Miocene to early Pliocene. This

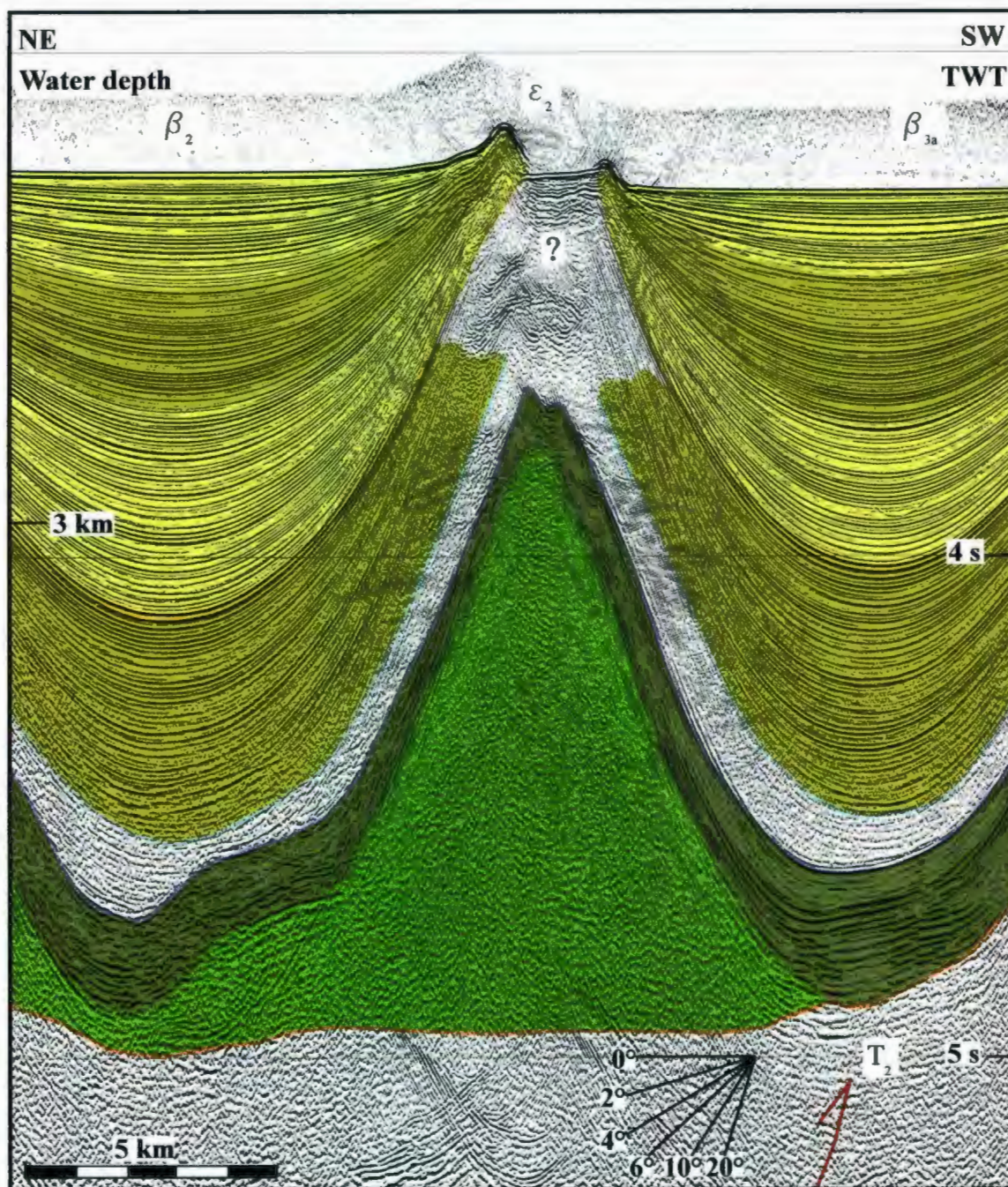


Fig. 7.6. Seismic reflection profile showing the north- and south-thinning growth strata packages in Unit 1.

- | | | |
|------------------------------------|----------------------------|----------------------|
| Top middle Plio-Quaternary subunit | Upper evaporite subunit 2a | Growth strata wedges |
| Top basal Plio-Quaternary subunit | Lower evaporite subunit 2b | Growth strata wedges |
| M-reflector | Top Unit 3 | |

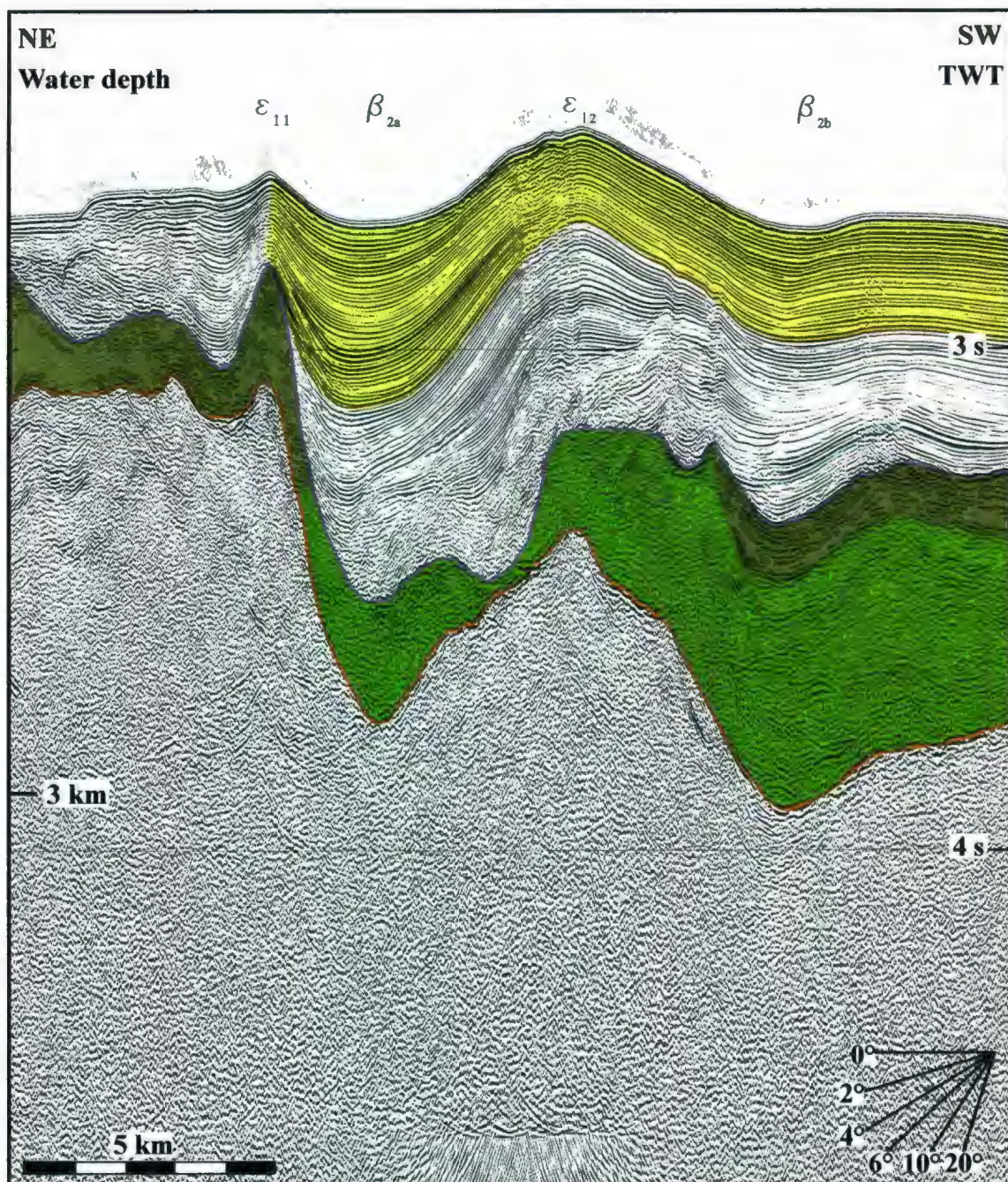


Fig. 7.7. Seismic reflection profile showing the upper Plio-Quaternary subunit homoclinally overstepping a culmination while showing onlap against the other.

- | | | |
|------------------------------------|----------------------------|-------------------------------|
| Top middle Plio-Quaternary subunit | Upper evaporite subunit 2a | Upper Plio-Quaternary subunit |
| Top basal Plio-Quaternary subunit | Lower evaporite subunit 2b | |
| M-reflector | Top Unit 3 | |

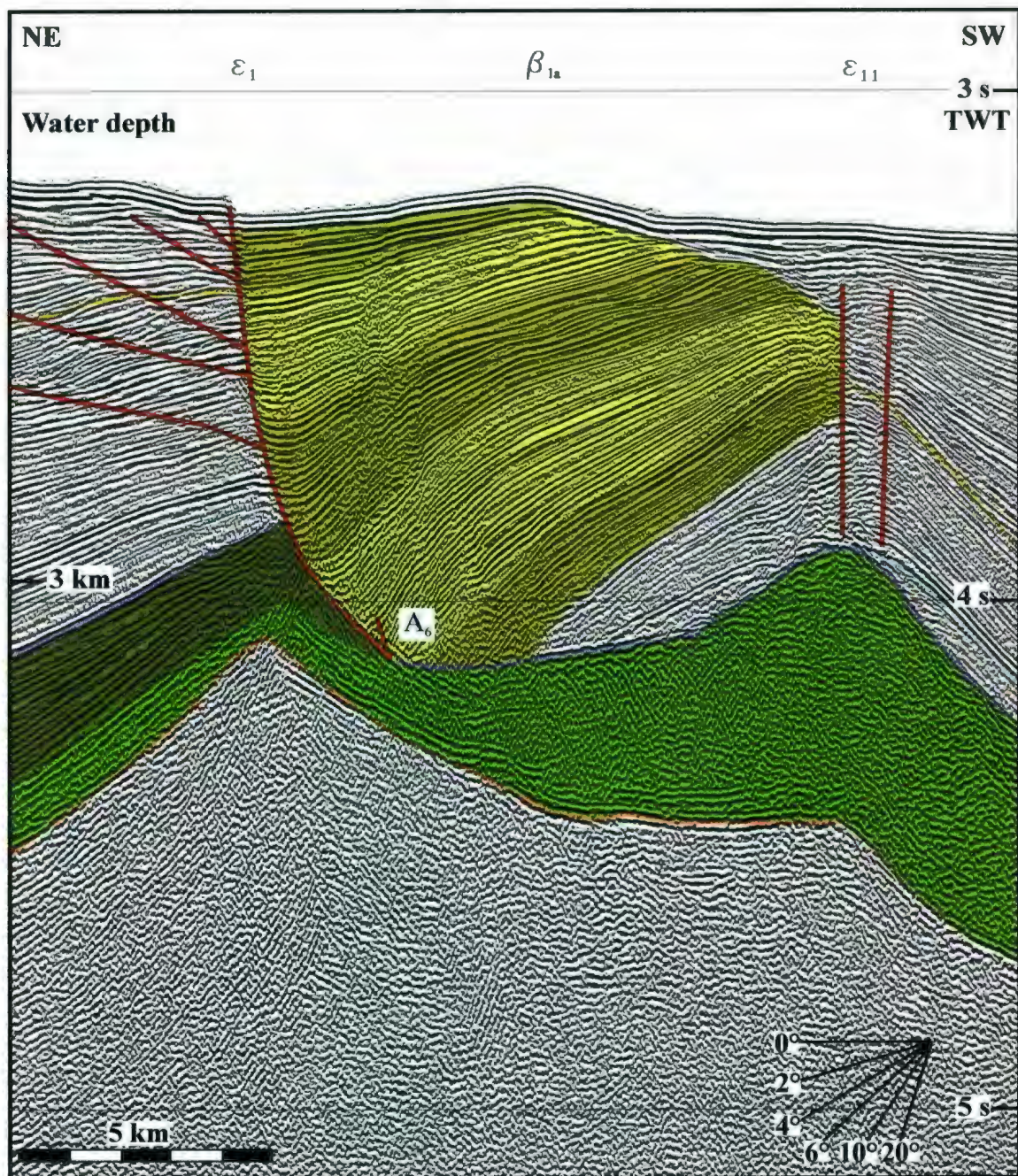


Fig. 7.8. Seismic reflection profile showing tilted growth wedges in Unit 1.

- | | | |
|------------------------------------|----------------------------|----------------------|
| Top middle Plio-Quaternary subunit | Upper evaporite subunit 2a | Growth strata wedges |
| Top basal Plio-Quaternary subunit | Lower evaporite subunit 2b | Growth strata wedges |
| M-reflector | Top Unit 3 | |

westward displacement continued during the Pliocene-Quaternary and still persists today (Dewey et al., 1986). GPS data show that the motion of the eastern segment of the Aegean-Anatolian Microplate relative to a fixed Eurasian Plate is invariably west directed east of 30°E longitude with no evidence of rotation or fragmentation in this region. The data presented in this thesis suggest that the west escape of the eastern segment of the Aegean-Anatolian Microplate is accommodated in its southern boundary by an arcuate splay of the East Anatolian Transform Fault, which is represented by a major fault zone extending from the Misis Mountains of southern Turkey to the Kyrenia Range of northern Cyprus and further west to the northern segment of the Antalya Basin. The fact that GPS data show no rotation of the microplate requires that the sense of movement along this arcuate zone with respect to the African Plate to the south must be sinistral. The overall data further suggest that the southern margin of the Aegean-Anatolian Microplate is being fragmented during its westward escape. The linkage of the crustal scale structures mapped in the Antalya Basin to the Isparta Angle on land is not done with any degree of certainty but will be another important aspect of the author's PhD thesis. Therefore, the kinematic implications of the suggested fragmentation of the southern microplate boundary cannot be fully evaluated at this stage. Along the slope of the Antalya margin, the extensional faults A4-A6 clearly have a strike-slip component and fault A6 defines the boundary between the extensional/transensional structural domains to the north from the pure contractional domain in the central portion of the basin. Apparent differences in the timing of the growth strata along the strike of the culmination is likely to relate to

diachroneity in activity.

In the southern portion of the deep Antalya Basin the cessation of the fold/thrust activity occurred during the transition from the latest Miocene-early Pliocene and the transpressional fault activity represented by narrow-stemmed positive flower structures dominated this portion of the study area in the early-middle Pliocene to Recent (Fig. 7.9). Moreover, the comparison of seismic reflection profiles shows that the period of activity on the flower structures is highly variable spatially and temporally. Where present, the Recent fault activity is represented by small-scale inflections on the sea-floor (Fig. 7.10). The transpressional fault activity is interpreted to be related to the collision of the Eratosthenes Seamount with Cyprus during the early Pliocene to Recent (Ben Avraham et al., 1988). Eratosthenes Seamount is continental in character (Robertson, 1998), thus, has choked the subduction along the Cyprus Arc, generating a transpressional stress field (Harding et al., 1983). The overall deformation history of the Pliocene-Quaternary strata suggests that the plate strain is strongly partitioned in the Pliocene-Quaternary

7.2. Correlations with western Cyprus

The main thrusts of the fold-thrust culmination in the Antalya Basin, T_1 , T_2 and T_3 , and their leading piggy-back basins, β_2 , β_3 and β_4 can be readily traced to western Cyprus in the southeast.

The western marine extension of the Mesaoria Basin of Cyprus constitutes the easternmost portion of the study area. This region is critical because it allows direct

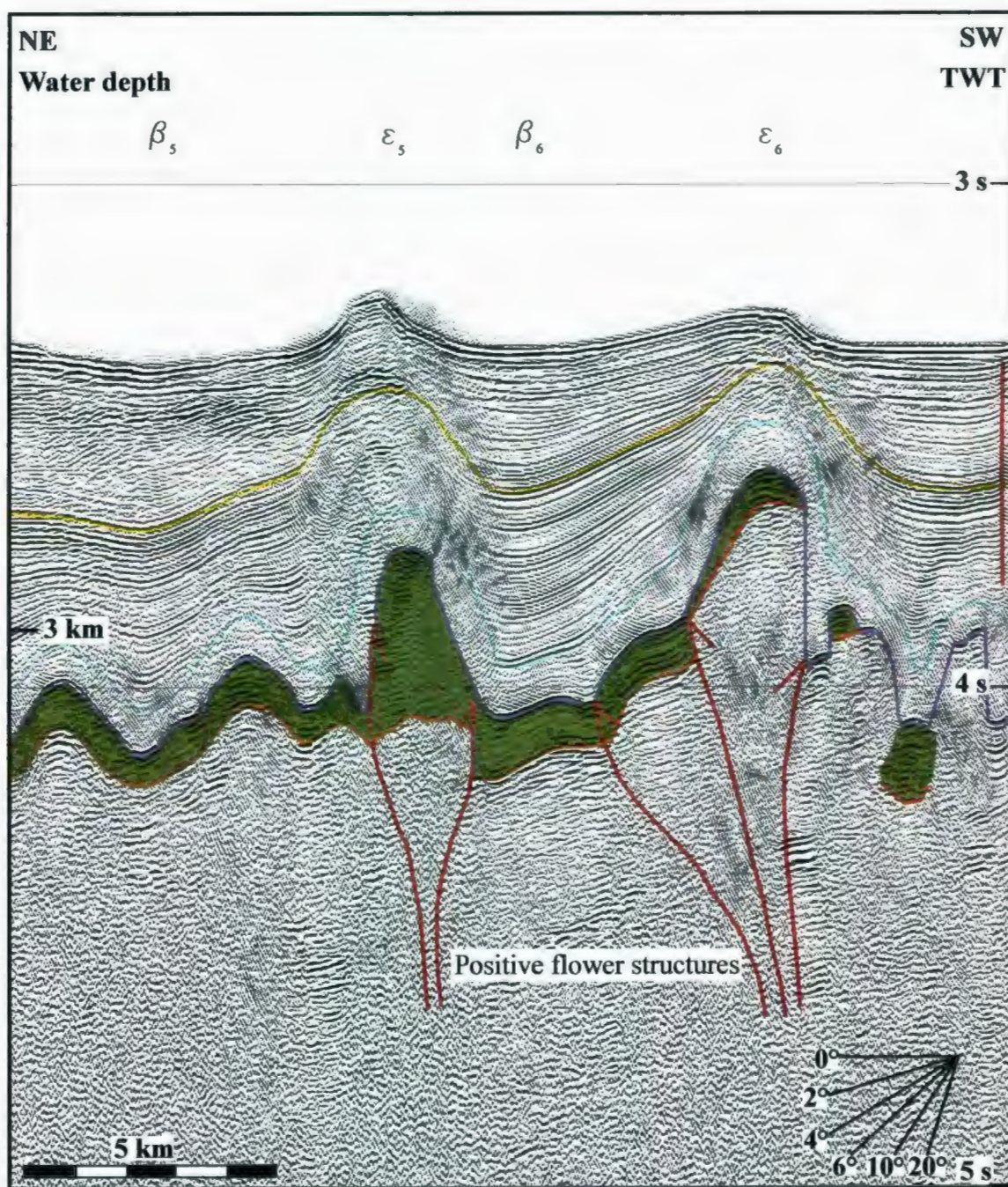


Fig. 7.9. Seismic reflection profile showing the positive flower structures.

- Top middle Plio-Quaternary subunit
- Top basal Plio-Quaternary subunit
- M-reflector
- Upper evaporite subunit 2a
- Top Unit 3

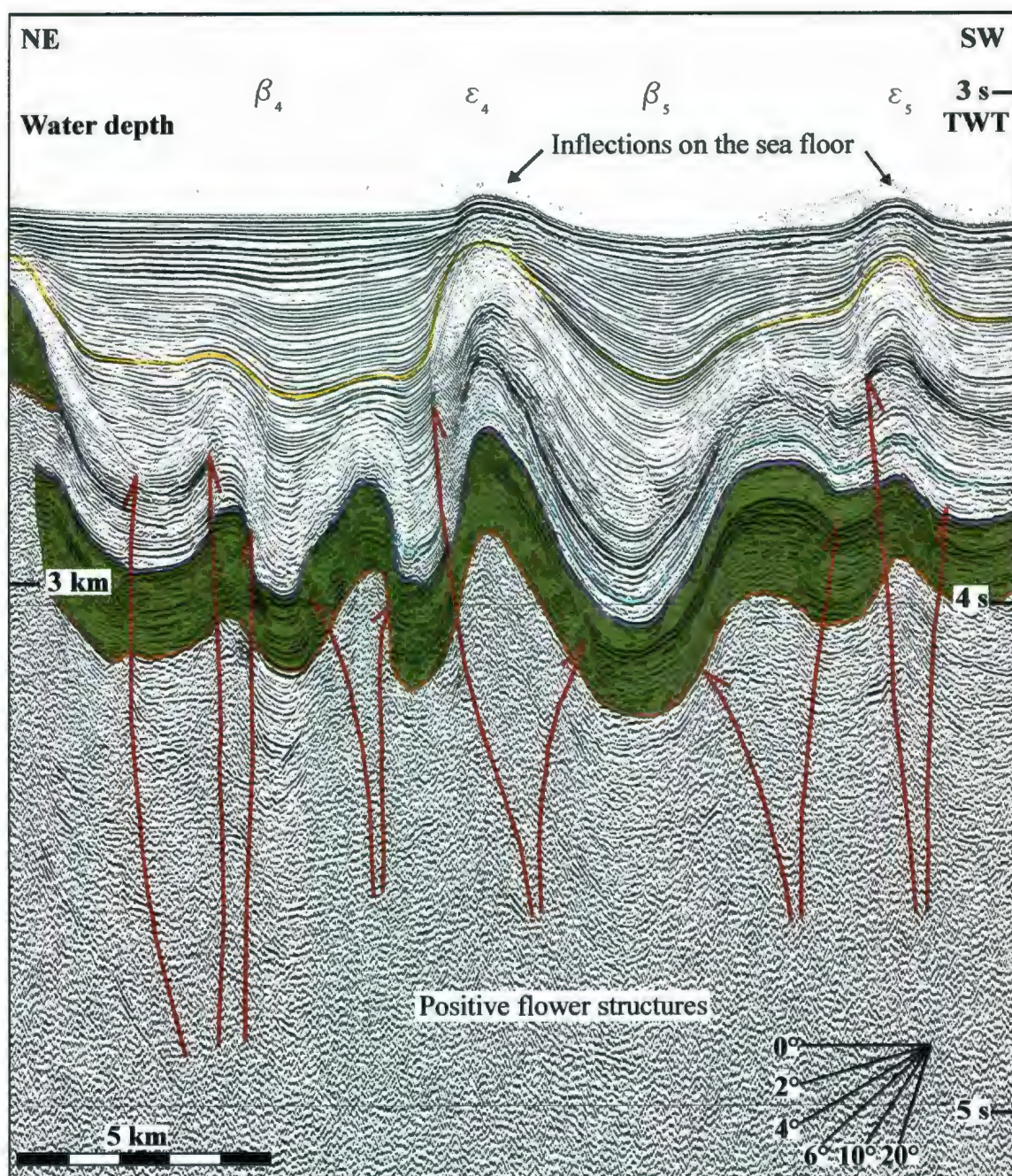


Fig. 7.10. Seismic reflection profile showing the positive flower structures .

- Top middle Plio-Quaternary subunit
- Upper evaporite subunit 2a
- Top basal Plio-Quaternary subunit
- Top Unit 3
- M-reflector

correlations to be made between the large scale structures delineated in the Mesaoria Basin and Kyrenia range, and those mapped in the Antalya Basin. The Mesaoria-Latakia-Iskenderun Basin Complex evolved in Eo-Oligocene to Present as a large east-west trending piggy-back basin carried over a prominent south-verging thrust system, the Troodos-Larnaka culmination (Calon et.al., submitted a, b). From early Oligocene until middle Miocene, present-day northern Cyprus was the site of a large foredeep with the Kyrenia foredeep forming the northern segment and the Mesaoria Basin constituting the southern segment of this depocentre. This foredeep was receiving a predominantly deep water turbiditic deposition (i.e. the Kythrea Group of Cyprus; Robertson, 1998), which represents the eastern correlative of the seismic stratigraphic Unit 3 of the Antalya Basin. During the middle-late Miocene, contractional deformation affected the entire forearc region north of Cyprus Arc, including the Kyrenia foredeep, and the northern segment of the Mesaoria Basin underwent progressive inversion in response to contraction (Calon et al., submitted a, b). The present-day structural framework of the Kyrenia Range is characterized by an imbricate fold/thrust system consisting of four major thrust panels: the northernmost Orga thrust, the central Kythrea and Ovgos thrusts and the southern Mesaoria thrust (Cleintuar et al., 1977). The Orga Fault defines a north-dipping, south-verging fold-thrust system that forms the spine of the Kyrenia Range, while the Kythrea and Ovgos Faults define north-dipping, south-verging imbricate fold-thrust systems and form the central zone of the Kyrenia Range (Fig. 7.2). A north-south running seismic reflection profile shot across the western marine extension of the Kyrenia Range and the

northern Mesaoria Basin, images the northernmost three thrust panels as well as the prominent Mirtou and Aspromouti piggy-back basins (Fig. 7.9; Calon et al., submitted a, b). On the basis of similarity in strike, and stratigraphic architecture, the three northernmost prominent thrust panels of the imbricate fold/thrust system in the Antalya Basin, T_1 , T_2 , and T_3 are correlated with confidence with the Orga, Kythrea and Ovgos faults of Cyprus, respectively (Figs. 6.1 and 7.2).

The piggy-back basins nestled between the major culminations of the Kyrenia Range are carried over the Kythrea and Ovgos Faults (Calon et al., submitted a, b). The northern Mirtou syncline is a west-northwest-east-southeast-trending depocentre carried by Kythrea Fault. The southern Aspromouti syncline is carried by the Ovgos Fault. The fill of both basins comprise mildly folded successions of Pakhna, Lapatza, Mirtou and Nicosia formations. The piggy-back basins β_2 and β_3 of Antalya Basin are correlated with the Mirtou and Aspromouti synclines of northern Cyprus (Figs. 6.1 and 7.2).

Previous studies clearly documented that the Miocene to Pliocene transition is marked by a major change in plate kinematics (e.g. Aksu et al. submitted; Calon et al. submitted; Hall et al., submitted), where the Miocene is differentiated by a pervasive contractional phase characterized by south-directed thrusting, whereas the Pliocene-Quaternary is marked by a phase of extensional and transtensional deformation in the eastern portion of the Mediterranean Sea with strain clearly partitioned geographically into distinct domains. Aksu et al. (submitted) showed that the northern fringes of the Kyrenia range are cut by a family of east-west-trending, north-dipping extensional faults which

show 500-1000ms offset on the M-reflector. Calon et al. (submitted, a,b) and Aksu et al. (submitted) indicated that Kyrenia Range clearly extends northeast into the Misis Mountains of southern Turkey, with this extensional fault family marking the western segment of the Misis-Kyrenia Horst block. To the west, this extensional fault system can be tentatively correlated with the horst and graben forming extensional faults along the Antalya Margin. Therefore, it appears that the fault system marking the western margin of the Misis Mountains, Misis-Kyrenia Horst and the northern portion of the Kyrenia Range extending into the Antalya Basin must delineate a major intra-plate fault zone

7.3. Previous Models and Comparisons with the Author's Model

Woodside (1977) used widely-spaced single channel seismic reflection profiles and gravity data across the eastern Mediterranean Sea to show that the large scale tectonic elements, such as the Florence Rise, the Kyrenia-Misis Mountains and the Eratosthenes Seamount partitioned the eastern Mediterranean into several separately-evolving basins. He combined other geological and geophysical data to show that the crust across the eastern Mediterranean is transitional in character (i.e., between oceanic and continental) and suggested that it probably represents the thinned and attenuated northern margin of the African Plate. He pointed out the presence of several prominent features of the African-Anatolian convergence, which suggest underthrusting of the Turkish Plate by the African Plate, such as the morpho-tectonic character of the Florence Rise and Anaximander Mountains, the northward tilting and subsidence of the Antalya and Finike

Basins and the apparent continuation of the Strabo Trench south of the Florence Rise. However, he further noted that there is insufficient seismicity across the African-Anatolian Plate boundary, no active volcanic arc and that the trench is rather poorly developed to confirm active subduction. Thus, he speculated that normal subduction probably ended within the past 5 Ma, and that along the northern fringe of the African Plate former oceanic crust has since disappeared. Woodside argued that today plate convergence continues with only limited underthrusting of African Plate along the Cyprus Arc, with regional deformation along zones of weakness within a ~300 km wide band stretching from the Herodotus Basin eastward along the northern edge of the African/Arabian Plates.

The model presented in this study partially supports the findings of Woodside (1977). For example, the broad northwest-southeast trending imbricate thrust sheets showing a protracted contractional deformation from Miocene until Recent is compatible with the continued, although limited, convergence and contraction between the African Plate and the Aegean-Anatolian Microplate. However, the present study clearly documents that the strain in the Antalya Basin and environs is partitioned temporally and that the major phase of northeast-southwest-directed contraction in the Miocene was replaced in the Pliocene-Quaternary by a phase involving mild, similarly-directed contraction, which is overprinted by the extensional/transtensional and transpressional tectonism associated with the westward-escape of the Aegean-Anatolian Microplate and the collision of the Eratosthenes Seamount with Cyprus during the early Pliocene to Recent. This strain partitioning is not observed and discussed in the Woodside model.

Sage and Letouzey (1990) used ~6500 km of industry seismic reflection data and documented the presence of at least two northwest-trending, north-dipping, south-verging crustal-scale thrust panels in Antalya Basin north of the Florence Rise. They linked these thrust panels with the schematic stratigraphic cross-sections of Bijou-Duval and Dercourt (1980) and further correlated these crustal-scale elements with the major onland Upper Cretaceous to Recent thrusts of the Kyrenia Range of Cyprus, which dominate the geology of the onland segment of the north-eastern Mediterranean. They further suggested that this arcuate imbricate thrust belt defines the basement of the Oligocene to Quaternary deep basins such as the Rhodes, Antalya, Cilicia and Adana Basins. They also delineated several south-verging crustal-scale thrust panels across the present-day boundary of the African Plate and Aegean-Anatolian Microplate and suggested that the Florence Rise constitutes the topographic expression of the accretionary prism.

The crustal-scale contractional deformation presented by Sage and Letouzey (1990) is entirely compatible with the model presented in this study. However, the detailed architecture of the contractional deformation in the Antalya Basin marked by 4-5 imbricate thrust panels presented in this study is not found in the Sage and Letouzey (1990) maps. Furthermore, they only presented an instantaneous kinematic solution, thus, the temporal and spatial partitioning of strain is not discussed by these authors. The proposed correlations of the crustal-scale thrust panels with similar structures onland Cyprus are also largely compatible with Sage and Letouzey (1990), although the details of the linkages with the known thrust sheets of northern Cyprus (i.e. Orga, Kythrea and

Ovgos Faults) were not included in their study.

Glover and Robertson (1998) used fault data from the onland segment of the Antalya Basin and Isparta Angle, together with a limited number of shallow seismic reflection profiles from offshore western Antalya Basin to suggest that the present tectonic framework of the region is dominated by extension. They showed that both the north-south and the northwest-southeast trending limbs of the Isparta Angle consist of large Miocene thrust faults, which are initially overprinted by dextral strike slip faults in the latest Miocene and early Pliocene and subsequently by extensional faults in the Pliocene-Quaternary. They further suggested that the tectonic framework of the marine Antalya Basin is characterized by a northwest-southeast trending widely-spaced normal faults that locally define an asymmetric horst and graben system and the authors linked this system with the extensional faults bounding the limbs of the Isparta Angle. They related the latest Miocene to earliest Pliocene dextral strike slip to shear along the eastern termination of a zone of extension and rotation that characterizes the western Aegean region. Glover and Robertson (1998) further related the switch of the tectonism from dextral strike slip in the Miocene to northeast-southwest extension in the Pliocene-Quaternary, to a regional change in stress direction throughout the Aegean region. They concluded that there is no data to support the notion that the present-day Antalya Bay and Isparta Angle represent a regional compressional zone related to plate collision.

The results of the detailed and systematic mapping of structures in the marine Antalya Basin together with the careful analysis of geometric relationships and growth

stratal architecture of the late Miocene as well as the Pliocene-Quaternary fill within several northwest-southeast trending piggy-back basins show a much more complex kinematic evolution than the simple model presented by Glover and Robertson (1998). The data presented in this study clearly document a Miocene phase dominated nearly exclusively by compressional tectonism, followed by a Pliocene-Quaternary phase when strain was partitioned into a northern zone of extension/transtension along the inner portion of the Antalya Basin, a central zone of contractional deformation and a southern zone of distinct transpression. Thus, the data presented here cannot be reconciled with the statement of Glover and Robertson (1998) that the Antalya bay area is presently dominated by extensional tectonism. The strong partitioning of strain documented in this study was interpreted as the consequence of the west-directed tectonic escape of the Aegean-Anatolian Microplate, rather than the extension and rotation of the Aegean region as suggested by Glover and Robertson (1998). Within the context of detailed stratigraphic and structural evolution, this study is not in agreement with the findings of these authors

Robertson and Woodcock (1986) documented three crustal-scale south-verging thrust faults (i.e. Orga, Kythrea and Ovgos Faults) which characterized the core of the Kyrenia Range, with a fourth leading thrust (i.e., the Mesaoria Fault) of this system situated beneath the Mesaoria Basin to the south. McCallum and Robertson (1990), Robertson et al (1991, 1995), Robertson (1998) have proposed that the Orga, Kythrea and Ovgos Faults acted as fundamental south-dipping extensional growth faults during the Oligocene to Miocene associated with the period of forearc extension. They further

proposed that these extensional faults were re-activated as contractional faults and rotated to steeply north-dipping structures during the Pliocene thrusting (i.e. the D3 event of Robertson and Woodcock, 1986).

Detailed mapping of the large northwest-southeast trending thrusts T_1 , T_2 , and T_3 in Antalya Basin shows that they readily link with the Orga, Kythrea and Ovgos Faults of the Kyrenia Range. Careful analysis of the multi-channel seismic reflection profiles presented in this study shows no evidence for the existence of a south-dipping and south-verging extensional growth fault system that can be correlated with any onland structure within the eastern segment of the study area. Note that the strata associated with the growth of the major structural culminations imaged throughout the study area display wedge like geometries thinning towards the forelimb and backlimb of the ramp anticlines. In addition, these growth strata packages observed mostly within the Pliocene-Quaternary succession are enveloped by progressive syn-tectonic unconformities. Both the geometry of the growth strata and the presence of progressive syn-tectonic unconformities clearly imply the characteristics of growth analogous to thrust-related fold structures. Therefore, the interpretation of these faults as having an extensional character is not possible primarily because of the geometry of the associated growth strata. The extensional growth faults require a wedge-like geometry with stratal thickening towards the fault plane on their hanging-walls; this is not the case, as demonstrated clearly on our seismic reflection profiles. For the hypothesis that these faults were re-activated as contractional faults and rotated to steeply north-dipping structures during the regional Pliocene

thrusting to be true, one expects to see the growth strata associated with extensional faulting on the deeper portions of the hanging-walls of these rotated faults. The seismic data presented in this study do not exhibit any growth architecture analogue to extensional fault activity on the hanging-walls of the thrust structures. Calon et al. (submitted a, b) clearly documented that they also cannot find any tangible evidence for extensional faulting and subsequent inversion. They further stated that " ... for both mechanical and kinematic reasons these structures cannot be thrust-inverted extensional faults because of the opposite directions of the superposed structures...".

Calon et al (submitted b) used high resolution seismic reflection profiles from the western offshore extension of the Kyrenia Range and linked main thrusts delineating the core of the Kyrenia range, the Orga, Kythrea and Ovgos Faults, with three prominent thrust culminations and their intervening piggy-back basins (i.e. the Mirtou and Aspromouti synclines) in the easternmost Antalya Basin (Fig. 7.2). They interpreted these faults in easternmost Antalya Basin as north-dipping, south-verging thrusts based on the structural architecture of the associated growth strata and further argued that they define an west-northwest-east-southeast striking imbricate fold/thrust system. As for the activity of this fold/thrust system, they proposed a Late Miocene to Recent age for thrusting with increased tectonic activity in late Miocene and middle Pliocene, interrupted by a period of quiescence coinciding with the development of the M-reflector and the deposition of the basal Pliocene-Quaternary subunit. However, apart from this initial correlation Calon et al. did not carry these structures westward into Antalya Basin.

Papazachos and Papaioannou (1999) used the spatial distribution of shallow-and intermediate-depth earthquake data and documented a continuous boundary between the Eurasian and African Plates across the eastern Mediterranean Sea. They calculated fault plane solutions using recent earthquake data and determined the character of relative plate motion. Papazachos and Papaioannou (1999) plotted the focal depth of intermediate earthquakes along a line that crosses the Antalya Basin in a southwest-northeast direction and observed that the plot points out the presence of a well-defined Benioff Zone dipping in a northeast direction. They also demonstrated the presence of a north-northeast striking dextral transform fault with a thrust component west of Cyprus, the Paphos Transform Fault. They suggested that this fault connects two concave segments of the plate boundary: the east-northeast trending Cyprean Arc which links with the Eastern Anatolian Transform Fault in southeastern Turkey, and the west-northwest striking Florence Rise which joins with the Rhodes Fault further northwest.

Mascle et al. (2000) used multibeam swath bathymetry in conjunction with single channel seismic reflection profiles from offshore Egypt and showed the presence of a belt of N145°E trending, crustal-scale right-lateral transtensional faults that obliquely transect the eastern Nile deep-sea fan. Mascle and his co-workers interpreted this fault zone as to define the western boundary of a newly-defined Sinai-Levantine Microplate which represents a segment of the African craton disconnected from the African plate as a consequence of the collision between the Eratosthenes Seamount and Cyprus. They showed that this microplate moves independently from the surrounding Arabian and

African Plates, and the Anatolian-Aegean Microplate, along the Dead Sea Transform Fault to the east, the Cyprus Arc to the north and the Suez Rift System in the west-southwest.

Mascle et al. (2000) described the northwestern boundary of the Levantine-Sinai Microplate as defined by a N145°E trending transtensive faults with an apparent right-lateral component. Papazachos and Papaioannou (1999) suggested the presence of a north-northeast striking transform right-lateral fault with a thrust component in the offshore southwestern Cyprus. Although these two faults do not overlap geographically, they display similar characteristics in terms of their relative sense of movement, hence yield a possibility that they may represent a common boundary (Fig. 7.11). Despite considerable efforts, the anatomy of this complex plate boundary is still not fully understood. The data presented by Papazachos and Papaioannou (1999) and Mascle et al. (2000) bring us a step closer to resolving geometric relationships of large tectonic elements in this region. Clearly, new data are needed to confirm the linkage between the Paphos Transform Fault, the unnamed western boundary fault of the Levantine-Sinai Microplate and the Florence Rise. The transpressional deformation documented in the southern segment of the study area is believed to be somehow related to these right-lateral faults, although a better understanding of these structures again requires denser seismic grid as well as additional seismic coverage further south.

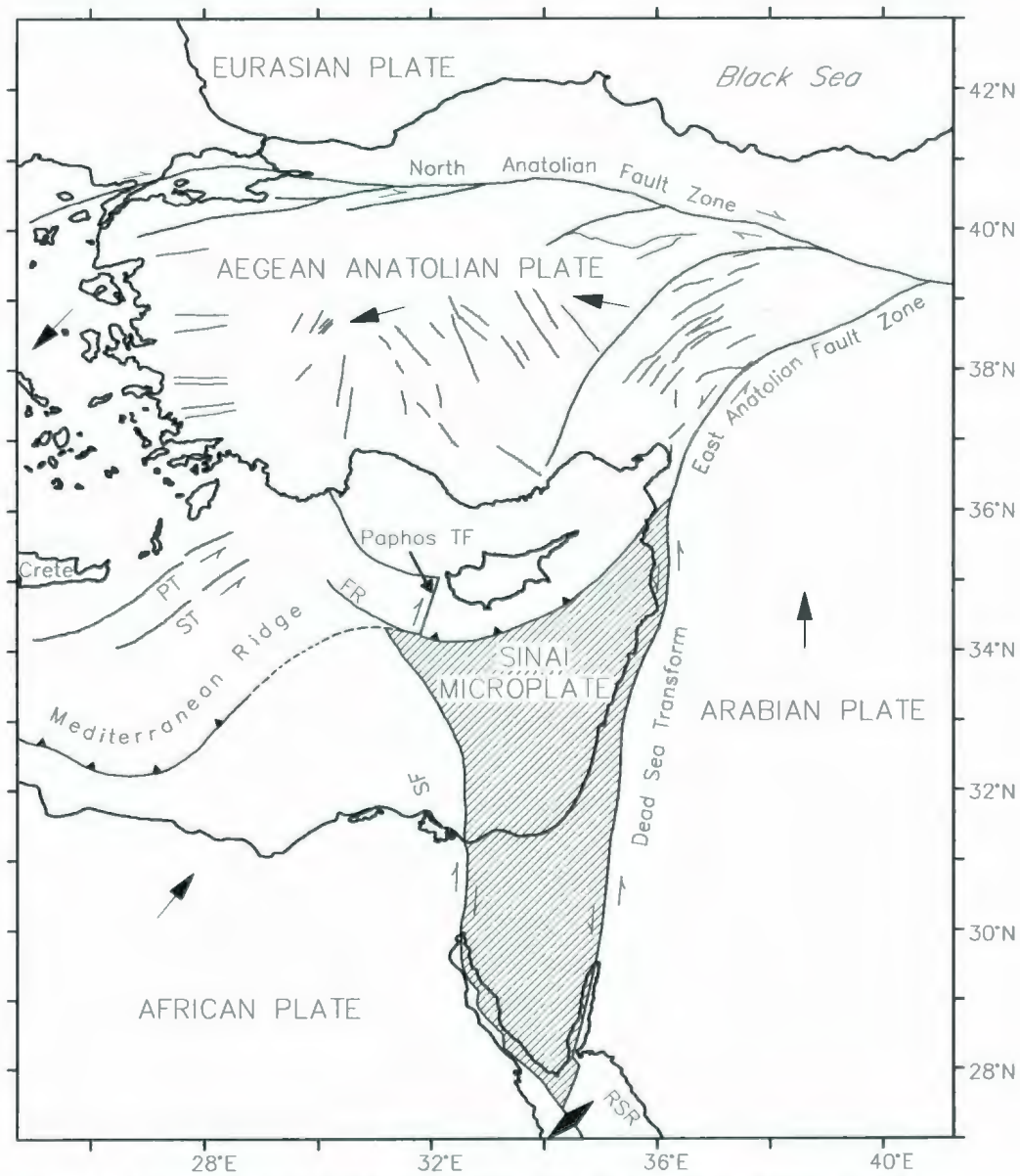


Fig. 7.11. Map showing the right-lateral transform Paphos Fault (Papazachos and Papaioannou, 1999) and the right-lateral transform fault defining the north-western boundary of the Sinai microplate (Masle et al., 2000).

CHAPTER 8. Conclusions

Detailed mapping of the major structural culminations of the Antalya Basin and the intervening basins, the thorough interpretation of the temporal and spatial development of these structural elements, and the analysis of the seismic stratigraphic architecture of the Pliocene-Quaternary basins reveal the following salient conclusions for the Miocene to Recent tectonic evolution of the Antalya Basin:

1. Antalya Basin evolved as part of the leading syncline in front of the central Tauride fold/thrust belt during the middle-late Miocene in a forearc setting north of the African-Eurasian convergent plate boundary. The Miocene fill (i.e. Unit 3) of the basin probably consists of deep-water siliciclastic deposits.
2. During the middle-late Miocene regional compression, several major northwest-southeast-striking, north-dipping and south-verging thrust culminations developed in the Antalya Basin and split the large depocenter into several smaller basins. These culminations define the ramp anticlines of the underlying buried thrust faults, while the intervening basins represent the piggyback basins carried by these thrust faults. This overall structural architecture is interpreted to define a crustal-scale imbricate fold/thrust belt.
3. The transition from late Miocene (Tortonian) to Messinian is marked by a prominent reflector in the Antalya Basin, the N-reflector, and records a period of erosion associated with the initial desiccation of the Mediterranean Sea. The deposition of the evaporites

(Unit 2) in the Antalya Basin took place during the Messinian. The final desiccation of the Mediterranean Sea at the end of the Miocene and the subaerial exposure of the sea-floor at that time resulted in the development of a major erosional surface, represented by the well-defined angular unconformity on the seismic reflection profiles, the M-reflector.

4. The stable south-verging character of the fold/thrust belt throughout the study area suggested a major phase of contractional deformation during the middle-late Miocene. A fundamental change in kinematic regime occurred during the transition from the Miocene to Pliocene-Quaternary. In the northern-central portion of the deep Antalya Basin, the fold-thrust belt displayed a protracted activity from the early Pliocene to Recent with intervals of accelerated growth during the middle Pliocene-Quaternary. During its early Pliocene to Recent growth, the fold-thrust belt was overprinted by the concurrent extensional/transensional fault activity developed in relation to the westward displacement of the Tauride block as the eastern segment of the Aegean-Anatolian Microplate initiated its westward escape in the latest Miocene to early Pliocene. Whereas, in the southern portion of the deep Antalya Basin the cessation of the fold/thrust activity occurred in the latest Miocene and the transpressional fault activity exclusively dominated this portion of the study area in the early Pliocene to Recent. The transpressional fault activity is interpreted to be related to the collision of the continental fragment Eratosthenes Seamount with Cyprus during the early Pliocene to Recent, which as a result has choked the subduction along the Cyprus Arc, generating a transpressional stress field.

5. The stratigraphic and structural architecture of the Antalya Basin with a distinctive set

of north-dipping, south-verging imbricate thrusts in conjunction with the basin's geographic setting between the boundary of the African Plate and the Aegean-Anatolian Microplate to the south and the volcanism documented in the Isparta Angle area to the north, are interpreted to suggest that Antalya Basin represents an accretionary prism at least since the middle Miocene.

References

- Akay, E. and Uysal, S., (1985). Orta Toroslarin batısındaki (Antalya) Neojen çökellerinin stratigrafisi, sedimentolojisi ve yapısal jeolojisi. MTA.
- Akay, E. and Uysal, S. (1988). Orta Toroslarin post-Eosen tektonigi. MTA Dergisi, 108, 57-68.
- Akay, E. and Uysal, S., Poisson, A., Cravatte, J., Müller, C., (1985). Stratigraphy of the Antalya Neogene Basin. Bulletin of the Geological Society of Turkey, 28, 105-119.
- Akbulut, A., (1977). Etude géologique d'une partie du Taurus occidental au Sud d'Eğridir (Turquie): Thèse 3^e Cycle Univ. Paris Sud (Orsay), 203 s., unpublished
- Ambraseys, N. N., (1970). Some characteristic features of the Anatolian Fault zone. Tectonophysics, 9, 143-165
- Ambraseys, N. N., (1988). Engineering seismology. Earthq Engineer Struct Dyn., 17 1-105.
- Ambraseys, N. N. and Finkel, C. F., (1987). Seismicity of the Northeast Mediterranean region during early 20th century. Annal. Geophys., 5B, 701-726
- Ambraseys, N.N., and Adams, R. D., (1993). Seismicity of the Cyprus region Terra Nova, 5:8-94.
- Anastasakis, G., and Kelling, G., (1991). Tectonic connection of the Hellenic and Cyprus arcs and related geotectonic elements. Marine Geology, 97, 261-277
- Barazangi, M., and Dorman, J. (1969) World seismicity maps compiled from ESSA.

- Coast and Geodetic Survey, epicenter data 1961-1967 Bull. Seismol. Soc. Am., 59, 369,-380.
- Barka, A., and Kadinsky-Cade, K., (1988). Strike-lip fault geometry in Turkey and its influence on earthquake activity Tectonics, 7, 663-684.
- Barka, A., Reilinger, R., Şaroğlu, F., Şengör, A.M.C., (1997). The Isparta Angle: its importance in the Neotectonics of the Eastern Mediterranean region In: Pişkin, O., Ergun, M., Savaşçın, M.Y., and Tarcan, G. (Eds.), International Earth Sciences Colloquium on the Aegean Region, 9-14 October, 1995, İzmir, Göllük, Turkey, 1:3-18.
- Ben-Avraham, Z., Tibor, G., Limonov, A.I.F., Leybov, M.B., Ivanov, M.K., Tokarev, M.Y., and Boray, A., Şaroğlu, F. and Emre, O., (1985). Isparta büklümünün kuzey kesiminde D-B daralma için bazı veriler. Jeoloji Mühendisliği Dergisi 23, 9-20.
- Büyükaşikoğlu, S., (1980b). Sismolojik verilere göre doğu Akdenizin kuzeyinde ve güneydoğu Anadolu'da Avrasya-Afrika levha sınırının özellikleri. Bull. Earthquake Res. Inst., Ministry of Reconstruction and Resettlement, 29, 58-74.
- DeMets, C., Gordon, R.G., Argus, D.F., and Stein, S., (1990). Current plate motions, Geophys. J. Int., 101, 425-478.
- DeMets, C., Gordon, R.G., Argus, D.F., and Stein, S. (1994). Effects of recent revisions to the geomagnetic reversal time scale on estimates of current plate motions, Geophys. Res. Lett., 21, 2191-2194.
- Dewey, J.F., and Şengör, A.M.C., (1979). Aegean and surrounding areas: complex multi-

- plate and continuum tectonics in a convergent zone. *Geol. Soc. Am. Bull.*, 90:84-92.
- Dilek, Y. and Rowland, J.C., (1993). Evolution of a conjugate passive margin pair in Mesozoic southern Turkey. *Tectonics*, vol. 12, No. 4, Pages 954-970.
- Dumont, J.F., (1976). Études géologiques dans les Turides occidentales les formations Paleozoïques et Mézozoïques de la coupole de Karacahisar (Isparta, Turquie) : Thèse 3^e Cycle Université du Paris Sud (Orsay), 213 p., unpublished.
- Eroskay, O., (1968). Geological investigation of the Köprüçay-Beşkonak reservoir area: E.I.E. (Elektrik İşleri Etüd İdaresi-Water Works Department), 69-23, unpublished.
- Glover, C., Robertson, A.H.F., (1998)b. Role of regional extension and related uplift on the Plio-Pleistocene evolution of the Aksu Basin, SW Turkey. *Journal of the Geological Society of London*, vol. 155, pp. 365-387.
- Hadımlı, L., (1968). Manavgat-Akkuşlar bentyeri ve rezervuarının jeolojisi: İ.Ü.F.F. Tatbiki Jeoloji Kürsüsü, diploma çalışması, yayınlanmamış (İstanbul University Faculty of Science, Geology Department, diploma study, unpublished).
- Hayward, A.B., (1984). Miocene clastic sedimentation related to the emplacement of the Lycian Nappes and the Antalya Complex, southwest Turkey. In: Dixon, J.E., and Robertson, A.H.F. (Eds.), *The Geological Evolution of the Eastern Mediterranean*. *Geol. Soc. Spec. Publ. London*, 17:287-300.
- Hsü, K.J., Montadert, L., Bernoulli, D., Cita, M.B., Erickson, A., Garrison, R.E., Kidd, R.B., Melières, F., Müller, C., and Wright, R., (1978). History of the

- Mediterranean Salinity Crisis / In: Hsü, K J., Montadert, L., et al. (Eds.), Init. Repts. DSDP, 42 (Pt.1): Washington (U.S. Govt. Printing Office), 1053-1078.
- Jackson, J., and McKenzie, D., (1984). Active tectonics of the Alpine-Himalayan belt between western Turkey and Pakistan. *Geophys. J. R. Astron. Soc.*, 77, 185-246.
- Jackson, J., and McKenzie, D., (1988). The relationship between plate motions and seismic moment tensors, and the rates of active deformation in the Mediterranean and Middle East. *Geophys. J. R. Astron. Soc.*, 93, 45-73
- Jackson, J., (1992). Partitioning of strike-slip and convergent motion between Eurasia and Arabia in eastern Turkey. *J. Geophys. Res.*, p. 471- 479.
- Jackson, J., (1994). Active Tectonics of the Aegean Region. *Annu. Rev. Earth Planet. Sci.* 239-271
- Kempler, D., and Ben-Avraham, Z., (1987). The tectonic evolution of the Cyprian Arc. *Ann. Tecton.*, 1:58-71.
- Ketin, İ., (1969). Über die nordanatolische horizontal verschiebung. *Bull. Mineral. Res. Explor. Inst. Turkey*, 72, 1-28.
- Kissel, C. and Poisson, A., (1987) Etude paléomagnétique préliminaire des formations Cénozoïques des Beydağları (Taurides occidentales, Turquie). *C. R. Acad. Sci. Paris* 304 (8), 343-348.
- McClusky, S., Balassanian, S., Barka, A. A., Demir, C., Ergintav, S., Georgiev, I., Gürkan, O., Hamburger, M., Hurst, K., Kahle, H., Kastens, K., Kekelidze, G., King, R., Kotzev, V., Lenk, O., Mahmoud, S., Mishin, A., Nadariya, M.,

- Ouzounis, A., Paradissis, D., Peter, Y., Prilepin, M., Reilinger, R., Şanlı, I., Seeger, H., Tealeb, A., Toksöz, M. N. and Veis, G., (2000). Global positioning system constraints on plate kinematics and dynamics in the eastern Mediterranean and Caucasus. *Journal of Geophysical Research*, 105, B3, 5695–5719.
- McKenzie, D.P., (1970). Plate tectonics of the Mediterranean region. *Nature*, 226, 1-15.
- McKenzie, D.P., (1972). Active tectonics of the Mediterranean region. *Geophys. J.R. Astron. Soc.*, 30:109-185
- Monod, O., (1977). Recherches géologiques dans de la Taurus occidental au sud de Beysehir (Turquie). Thèse, Université du Paris Sud Orsay. 442 p.
- Morris, A., and Robertson, A.H.F., (1993). Miocene remagnetism of carbonate platform and Antalya Complex units within the Isparta Angle, southwest Turkey. I. *Tectonophysics*, 220:243-266.
- Nur, A., and Ben-Avraham, Z., (1978). The eastern Mediterranean and Levant: tectonics of continental collision. *Tectonophysics*, 46:297-311.
- Nowroozi, A.A., (1971). Seismotectonics of the Persian Plateau, eastern Turkey, Caucasus, and Hindu-Kush regions. *Bull. Seismol. Soc. Am.*, 54, 1927-1940.
- Oral, M.B., Reilinger, R.E., Toksöz, M. N., King, R.W., Barka, A.A., Kınık, I., (1995). Coherent plate motions in the eastern Mediterranean continental collisional zone. *Eos, Trans. AGU*, 76(2), 9-11.
- Özgül, N., (1984). Stratigraphy and tectonic evolution of the central Taurus. *In: Tekeli, O., and Göncüoğlu, M.C. (Eds.), Geology of the Taurus Belt: Proceedings Int.*

- Sym., 26-29 Sept. Ankara, Turkey, p. 77-90.
- Öztin, F., and Bayülke, N., (1990). Historical earthquakes of İstanbul, Kayseri and Elazığ. Report, Earthquake Research Department, General Directorate of Disaster Affairs, Ministry of Public Works and Settlement, Ankara, Türkiye, p. 22.
- Parejas, E., Pamir, H.N., (1939). 19/4/1938 orta Anadolu depremi. İstanbul Üniversitesi Fen Fakültesi, 3/4.
- Poisson, A., Akay, E., Dumont, J.F., and Uysal, Ş., (1984). The Isparta Angle (western Taurides-Turkey): a Mesozoic paleorift. *In*: Tekeli, O. and Göncüoğlu M.C. (Ed.), Geology of Taurus Belt: Proceedings Int. Sym., 26-29 Sept. Ankara, Turkey, p. 11-26.
- Price, S. and Scott, B., (1994). Fault-block rotations at the edge of a zone of continental extension; southwest Turkey. *J. Struct. Geol.*, 16, 381-392.
- Reilinger, R.E., McClusky, S.C., Oral, M.B., King, R.W., Toksöz, M.N., Barka, A.A., Kınık, I., Lenk, O., and Şanlı, I. (1997). *Journal of Geophysical Research*, Vol. 102, No. B5, Pages 9983-9999.
- Richter, I., and Strobach, K., (1978). Benioff zones of the Aegean Arc, Alps, Apennines, Hellenides. *Inter. Union Comm. Geodyn. Sci. Rep.*, 38.
- Rotstein, Y. and Kafka, A.L., (1982). Seismotectonics of the southern boundary of Anatolia, eastern Mediterranean region: Subduction, collision, and arc jumping. *Journal of Geophysical Research*, 87, B9, 7694-7706.
- Rotstein, Y. and Ben-Avraham, Z., (1985). Accretionary processes at subduction zones in

- the Eastern Mediterranean. *In*: Kobayashi and I.S. Sacks (Eds.). Structures and Processes in Subduction Zones. Tectonophysics, 112: 551-561
- Sage, L. and Letouzey, J., (1990). Convergence of the African and Eurasian Plate in the eastern Mediterranean. Petroleum and Tectonics in Mobile Belts. Letouzey, J. (Editor), p. 49-68
- Straub, C. and Kahle, H., (1994). Global Positioning system (GPS) estimates of crustal deformation in the Marmara Sea region, northwest Anatolia. Earth. Plan. Sci. Lett., 121, 495-502.
- Straub, C. and Kahle, H., (1995). Active crustal deformation in the Marmara Sea region, NW Anatolia, inferred from GPS measurements. Geophysical Research Letters, 22, 2533-2536.
- Şaroğlu, F., Boray, A. and Emre, O., (1987). Active faults of Turkey, Mineral Res. Explor. Inst. Turkey. Unpubl. Report, 8643, 394 pp.
- Şenel, M., (1997). 1:250 000 ölçekli Türkiye Jeoloji Haritaları, No:4, Isparta paftası, MTA Genel Müdürlüğü, Jeoloji Etüdler Dairesi, Ankara.
- Şengör, A.M.C., (1979). The North Anatolian Transform Fault: its age, offset and tectonic significance. J. Geol. Soc. Lond., 136, 269-282.
- Şengör, A. M. C. and Yılmaz, Y., (1981). Tethyan evolution of Turkey: a plate kinematic approach. Tectonophysics, v. 75, p. 181-241.
- Taymaz, T., Eyidoğan, H. and Jackson, J., (1991). Source parameters of large earthquakes in the East Anatolian Fault Zone (Turkey). Geophys. J. Int., 106,

537-550.

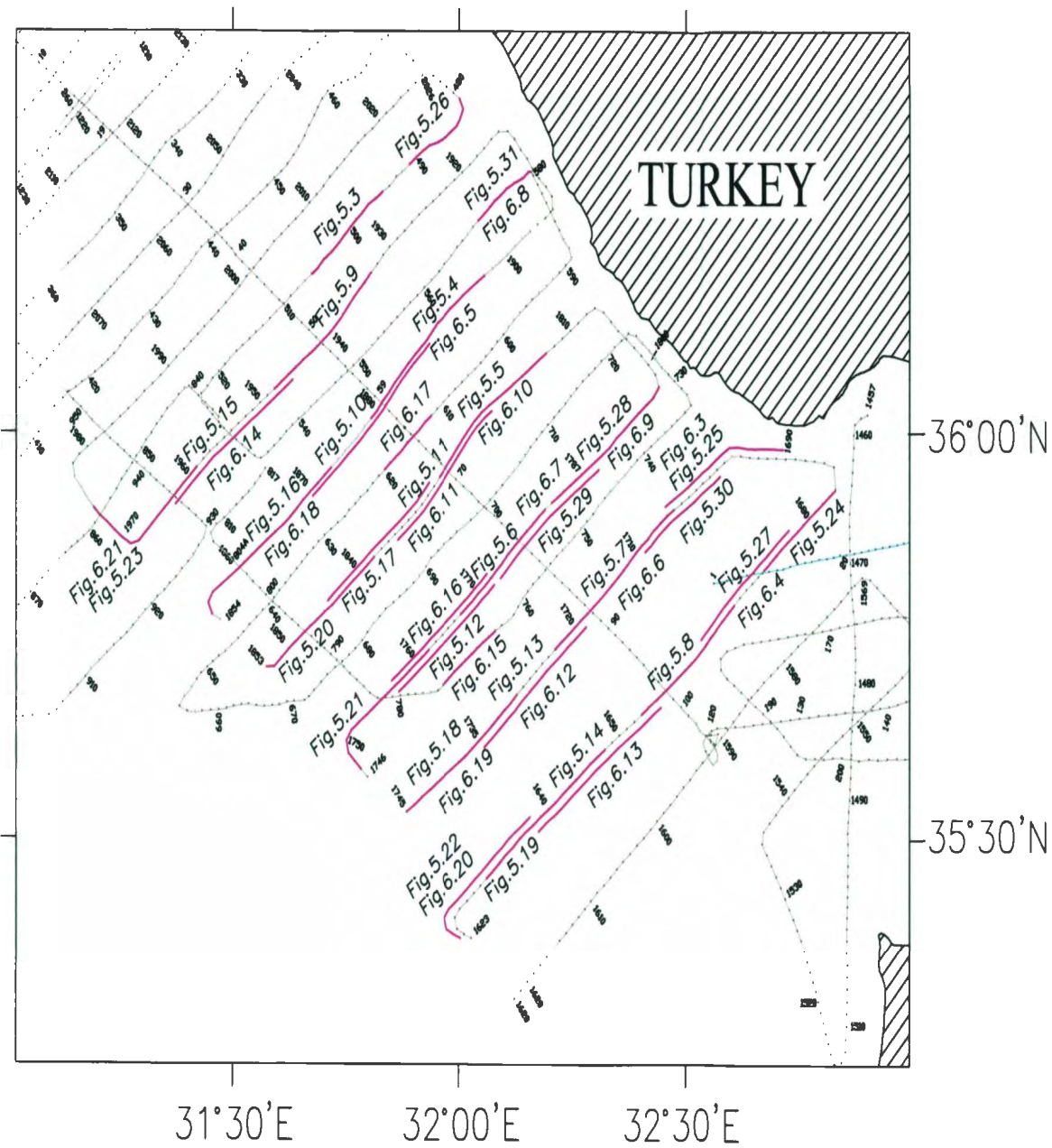
Vidal, N., and Alvarez-Marrón, J., (2000). The structure of the Africa-Anatolia plate boundary in the eastern Mediterranean. *Tectonics*, 19, (4), 723-739.

Westaway, R., (1994). Present-day kinematics of the Middle East and eastern Mediterranean. *J. Geophys. Res.*, 99, 12, 071-12, 090.

Woodside, J.H. (1976). Regional vertical tectonics on the eastern Mediterranean. *Geophys. J.R. Astron. Soc.*, 47: 493-514.

Woodside, J.H., (1977). Tectonic elements and crust of the eastern Mediterranean Sea. *Marine Geophysical Researches* 3, 317-354.

Woodside, J.M., (1995). Structure and tectonics of the eastern Cyprus Arc. *Mar. Pet. Geol.*, 12: 263-271.



Appendix: Map of the study area showing the locations of seismic reflection profiles illustrated in Chapters 5 and 6.



